DEVELOPMENT OF A NOVEL HIGH THROUGHPUT ASSAY: IMPAIRED MANGANESE TRANSPORT KINETICS AND HOMEOSTASIS IN HUNTINGTON'S DISEASE

By

Gunnar F. Kwakye

Dissertation

Submitted to the Faculty of the

Graduate School of Vanderbilt University

in partial fulfillment of the requirements

for the degree of

DOCTOR OF PHILOSOPHY

in

Neuroscience

December 2011

Nashville, Tennessee

Approved by:

Michael Aschner, Ph.D.

Kevin Currie, Ph.D.

Judy Aschner, M.D.

Aaron B. Bowman, Ph.D.

For all those in my life that have inspired and supported my dreams and aspirations:

my wife (Dr. Leslie Kwakye), mother (Rose Kwakye), family, and God. I love you all.

ACKNOWLEDGEMENTS

The work contained in this document would not have been possible without the generous funding support by the National Institutes of Health/National Institute of Environmental Health Sciences: RO1ES016931 (A.B.B.), American Recovery and Reinvestment Act (ARRA) supplement - ES016931S2 (G.F.K.), Vanderbilt University Interdisciplinary Graduate Program (IGP), Vanderbilt Neuroscience Graduate Program, Vanderbilt Brain Institute (VBI), Vanderbilt Neurology Department, Vanderbilt Kennedy Center, and the Society for Neuroscience (SfN) Neuroscience Scholars Program.

I am deeply grateful to my beautiful wife, best friend, and statistician, Dr. Leslie Kwakye, for her unending support and encouragement. I am very grateful to all those with whom I have had the pleasure of working with during my graduate studies. I would like to thank Dr. Blairanne Williams for the discovery of the novel gene-environment interactions in Huntington's disease that made it possible for me to investigate the exciting scientific questions discussed in my thesis. Dr. Michal Wegrzynowicz has been a great friend and colleague with whom I have discussed and shared great scientific ideas. Heather Tanner is one of the best research assistants that I have ever encountered in my life. Her positive attitude and enthusiasm for science created the perfect collegial atmosphere for research. Daphne Li is a wonderful and outstanding undergraduate student that I mentored in my graduate studies. Her commitment, passion, and creativity made her invaluable during the development of the novel Mn detection assay. I have the utmost faith that she will be a phenomenal physician. I will absolutely miss all the great scientific discussions that I had with the hardworking and intelligent fellow graduate

students (Jennifer Madison, Terry Jo Bichell, Andrew Tidball, and Kevin Kumar) in the Bowman laboratory. I am very grateful to Olympia Kabobel, Michael Scott Cardone, and Christopher Jetter for all their assistance. Dr. Diana Neely, Asad Aboud, and Bingying Han have been wonderful colleagues, and I know this is just the beginning of a lifetime friendship with them. The positive and supportive contributions of all my wonderful graduate school friends (Dr. Albert Russell Powers III, Sudipta Chakraborty, Zeqiang Ma, Dr. Weiguang Wang, Dr. Vera Blau-McCandliss and Dr. Bruce McCandliss) would be forever cherished.

I am eternally grateful to Dr. Aaron Bowman for his untiring support, mentorship, and my professional development. His dedication and enthusiasm for science, perseverance, ability to propose logical hypothesis to answer novel scientific questions, and critical interpretation of experimental results were a few of the countless qualities that I count myself incomparably fortunate to have gained under his mentorship. Dr. Bowman has been the perfect role model for a young upcoming scientist. I am honored to have him as my life-long mentor and friend.

Finally, I would like to express my heart field gratitude to my thesis committee. To Dr. Kevin Currie and Dr. Judy Aschner, who have inspired, provided constructive feedback, and whose doors have always been opened to me; and Dr. Michael Aschner, whose expertise in metals and neurotoxicology has helped shape the way I think about my work and constant mentorship I still rely. Thank you all for the insightful discussions, support, and mentorship.

TABLE OF CONTENTS

LIST OF TABLES

Table Page

LIST OF FIGURES

Figure Page

CHAPTER I

GENE-ENVIRONMENT INTERACTIONS AND NEURODEGENERATION: ASSOCIATION BETWEEN HUNTINGTON'S DISEASE AND METALS

Introduction

Synergism of genes and environment in neurodegenerative diseases

We live in a world where we are constantly bombarded with a plethora of toxic substances that converge on genetically regulated pathways to modify the susceptibility, age of onset, and progression of neurodegenerative diseases. Neurodegenerative diseases affect millions of people worldwide and is estimated to insidiously cause considerable financial and emotional burdens on the society[1]. There are several neurodegenerative diseases, but the most common progressive forms include Huntington's disease (HD), Parkinson's disease (PD), Alzheimer's disease (AD), and Amyotrophic lateral sclerosis (ALS). The familial forms of the aforementioned diseases are caused by discrete mutations in susceptibility genes and/or resistance alleles[2]. For example, mutations in the glutamine encoding triplet repeat (CAG) region of the Huntingtin (*HTT*) gene is associated with HD, single nucleotide polymorphism in α-synuclein and mutations in parkin, PINK1, DJ-1, and other genes cause PD, mutation in β-amyloid precursor protein (APP) gene has been implicated in AD, and mutations in the copper-zinc superoxide

dismutase (SOD1) gene is associated with ALS[3-6]. Although HD, PD, AD, and ALS exhibit different genetic mutations and distinct pattern of selective neuronal degeneration, they all display common and broad disease symptoms, for example; motor, cognitive, and psychiatric deficits, and others. In fact, since Archibold Garrod first suggested that some of the inborn errors of metabolism may be masked by diet and diseases, there has been an increasing acceptance of a combinatorial effect of genes and other causative factors to modulate the susceptibility, age of onset, and progression in neurodegenerative diseases[7].

Emerging evidence from association studies has identified modulators/factors that influence disease-causing genes to induce idiopathic neurodegenerative diseases. Importantly, the modulators/factors in neurodegenerative diseases can be classified as genetic (single nucleotide polymorphisms), environmental (extrinsic neurotoxins, e.g. metals, pesticides), excitotoxic (intrinsic neurotoxins, e.g. excitatory amino acids and altered metal homeostasis), autoimmunity, ageing, metabolic (oxidative injury), and biological (accumulation of aberrant proteins)[8]. Unfortunately, it is still unclear which of the above modulators/factors are the predominant initiators of gene-environment interactions in neurodegenerative diseases. Furthermore, the segregation and examination of only genes and environment in neurodegenerative diseases, and ignoring their pathophysiological interactions has for several decades limited our understanding of neurodegenerative diseases. The rationale that gene-environment interactions are essential in the development of common neurodegenerative diseases has been supported by the following experimental observations. First, incomplete penetrance of some monozygotic forms of HD, PD, AD, and ALS; second, similarities in disease phenotypes caused by neurotoxicants and genetic mutations; third, the ability of genetic factors to

dictate disease risk following exposure to environmental toxins; fourth, discordance in disease diagnosis, for example, age of disease onset amongst monozygotic twins; finally, the effects of environmental enrichment on motor and cognitive deficits, synaptogenesis, transcription, and development[9-15]. All these observations highly suggest the involvement of environmental factors to modulate the risk association of a genetic mutation. Despite the hypothetical and suggested ideas that gene-environment interactions may underlie neurodegenerative and other diseases, there has been paucity of studies that have directly provided experimental evidence to support it.

Exemplary studies that strongly argue in favor of gene-environment interactions in neurodegenerative diseases are summarized below. Emerging evidence in AD research has identified a genetic association between a single nucleotide polymorphic form of the lipoprotein metabolism gene, ε4 allele of the *apolipoprotein E* gene (APOE4), and cholesterol levels that increase the risk of AD. Specifically, possession of one or two alleles of APOE4 is sufficient to increase the risk of AD to approximately two or five fold, respectively[16,17]. Secondly, a conventional example of environmental influence in PD is the ability of the neurotoxin, 1-methyl-4-phenyl-1, 2,3,6-tetrahydropyridine (MPTP) to induce PD-like symptoms in rodents, non-human primates, and humans. MPTP is a non-toxic compound that possess toxic properties once metabolized by the glial enzyme, monoamine oxidase B (MAO-B), to 1-methyl-4-phenylpyridinium (MPP+). The toxic MPP+ cation selectively annihilates dopaminergic neurons in the substantia nigra pars compacta[18,19]. Impairment in metal ions and metal-dependent enzymes has been reported in HD. For example, Dexter and colleagues have provided evidence for elevated copper (Cu) and iron (Fe) levels in the corpus striatum of

postmortem human brain tissues[20,21]. In fact, several metal-dependent enzymes have also been shown to be altered in the striatum of HD patients[22]. Furthermore, the full-length Huntingtin protein (HTT) has been reported to interact with Cu^{2+} ions in mouse brains. This interaction decreases the solubility of HTT and induces aggregation[23]. Finally, the inclusion bodies formed by CAG expansion in mutant HTT fragments are associated with iron-dependent oxidative events[24].

Metals have also been suggested to exhibit gene-environment interactions in other neurodegenerative diseases[20,21,25-27]. Thus, it is not surprising that a recurring theme in neurodegenerative disease research has been to understand how neurotoxic metals modulate disease-causing genes to modify the age of disease onset, susceptibility, and disease progression.

Role of metals in neurodegenerative diseases

Over the past decade, there has been a growing interest to understand the metabolism of neurotoxic metals and their influence on various neurodegenerative diseases, including manganism, Wilson's disease (WD), PD, and AD. However, less attention has been focused on the role of metals in HD. Occupational and environmental exposures to neurotoxic metals, including, Mn^{2+}, Hg^{2+}, Cu^{2+}, Zn^{2+}, As^{2+}, Cr^{2+}, Pb^{2+}, and Al^{3+} have been associated with neurodegeneration and modulation of the age of disease onset and severity in neurodegenerative diseases. Metals play a critical role as cofactors of enzymes required for cellular processes, but can exert deleterious effects in the brain

and peripheral tissues when not properly regulated. Metals exposure may occur in large or trace quantities via diet, drinking water, auto exhaust, cosmetics, toothpaste, and many others. The brain is capable of efficiently regulating these metals under physiological conditions. However, excessive exposure to neurotoxic metals can accumulate in the brain. The distribution of metals throughout the brain is not uniform, albeit specific brain region accumulation of metals insinuates neurotoxicity. For example, Mn accumulation and neurotoxicity in the globus pallidus results in manganism. Alterations in metal homeostasis have been suggested to cause neurodegeneration via its association with proteins and subsequent induction of aggregate formation. Moreover, metals can cause neurodegeneration through a vicious cycle by disrupting mitochondrial function, which would deplete ATP, induce reactive oxygen species (ROS) production, and ultimately cause cell death by apoptotic and/or necrotic mechanisms.

It has been recently reported that acute exposure of a transgenic *C. elegans* model of PD to Mn results in degeneration of dopaminergic neurons[28]. Experimental studies in PD postmortem brain tissues have elucidated a strong link between oxidative stress and PD through increased Fe levels, markers of oxidative stress, and lipid peroxidation in the substantia nigra. Interestingly, pharmacological chelation of elevated Fe levels in an MPTP-induced neurotoxicty model of PD prevents and delays degeneration of midbrain dopaminergic neurons[29]. These studies indicate the potential neurotoxic contributions of metals (Fe, Mn) in PD neuropathology. On the other hand, Zn has been proposed to have distinct functions as an enzyme cofactor and involvement in normal neurological functions based on its significant levels (10 μM) present in the brain[30]. While some of the brain Zn levels are associated with proteins, the neocortex and hippocampus possess a

substantial amount of Zn that exist in its chelatable form[30-33]. The defined physiological functions of Zn are currently unclear, but it has been suggested to play an important role in the stabilization of glutamate-containing vesicles at the synapse of secretory cells[34,35]. In addition, *in vitro* experimental studies have elucidated Zn's ability to attenuate NMDA induced toxicity[36]. However, intracerebroventricular administration of Zn in rats causes epileptic seizure-induced hippocampal neurodegeneration[37].

In fact, other studies have also shown that Mn and other metals (e.g. Cu, Al, Zn) can interact and promote amyloid fibrillogenesis and aggregation of proteins such as prion protein (PrP) and α-synuclein[8]. These proteins are metal binding proteins that interact with metals and contribute to their altered conformational state, solubility, and aggregation[38-42]. However, in vitro analysis of PrP aggregates has demonstrated that Mn can promote aggregation independent of the PrP metal binding site[41]. In AD, Cu has been shown to bind Aß peptides with high affinity and modulate its conformational state and peptide length[43,44]. Other *in vitro* studies have demonstrated that Aß interacts with Fe and Zn to promote amyloidogenesis. Interestingly, these findings have been corroborated in AD postmortem brains that show elevated Fe and Zn in the neocortex and amyloid plaque deposits compared to control patients[44]. All these studies indicate that metal interactions with PrP, α-synuclein, and Aß proteins can cause cell death by inducing the formation of aberrant and toxic aggregates as well as activating redox cycling via Fenton and Haber-Weiss reactions, which depletes cellular antioxidants, including glutathione and trigger ROS ($\cdot O_2^-$, $OH\cdot$, or H_2O_2) production. The generation of these highly reactive species can cause oxidative stress that would damage lipids, proteins, and DNA and further deplete ATP to cause cell death. In spite of the reports that have implicated metals in

neurodegenerative diseases, including; PD and AD, there has been paucity of evidence to support a functional role of metals in the pathophysiological mechanisms and neuropathology of HD. HTT has been demonstrated to be essential in the regulation of vesicular compartmentalization of Fe and its metabolism[45]. Finally, Williams and colleagues have recently reported a gene- environment interaction between mutant HTT and Mn[46,47]. The rationale and findings of the mutant HTT and Mn interaction would be discussed in depth in the discovery of a gene-environment interaction: PolyQ-expanded HTT and manganese sub-chapter of this thesis.

Huntington's disease

Overview

Huntington's disease (HD) is a late-onset and progressive neurodegenerative disorder that was first described by George Huntington in 1872. HD is inherited in an autosomal dominant pattern whereby an affected individual has one mutated and one normal gene on a pair of chromosomes and possesses a 50/50 chance of transmitting the mutant gene and disorder to their offspring. Prevalence of HD is approximately 5 in 100,000 worldwide and 1 in 10,000 in the United States with a median age of onset at thirty-nine[3]. HD is characterized by motor impairment, cognitive deterioration, emotional disturbance, and psychiatric deficits. Some of the early motor symptoms include chorea, postural imbalance, dystonia, incoordination, and oculomotor apraxia. Conversely, akinesia is observed in HD patients at the later stages of the disease. HD patients also

exhibit depression, temper, apathy, and irritability during the course of the disease. The cognitive deficits observed in HD include short-term memory, attention, and learning. In fact, it has been reported that the cognitive and emotional features of HD precede the motor symptoms by several years[48,49]. The development of drugs and other therapeutic strategies to combat HD progression is still in its infancy. Tranquilizers and lithium have been used to control the anxiety and severe mood instability symptoms respectively in HD patients. Furthermore, antipsychotic drugs such as the dopamine receptor antagonist, haloperidol, alleviate some of the disabling abnormal movements, emotional, and psychological deficits albeit, the side effects that it causes including sedation[50]. Current strategies to improve the lives of HD patients have combined a multidisciplinary approach including medication, nutrition, psychosocial support, genetic counseling, physical, occupational, and speech therapies. Unfortunately, there is currently no effective treatment to halt or reverse the course of the disease. Life expectancy from the age of disease onset usually spans between 10 to 30 years. Moreover, cause of death is usually through complications such as pneumonia.

HD Neuropathology

The neuropathology of HD is characterized by selective degeneration of GABAergic medium-sized spiny neurons (MSNs) in the corpus striatum that innervate the globus pallidus and substantia nigra. The highly selective loss of the MSNs results in the symptoms observed in HD. The striatum is a 'master regulator' and a subset of the basal ganglia nuclei, which includes the subthalamic nucleus, globus pallidus, substantia

nigra, thalamus, and cortex. These subcortical nuclei are involved in the generation and integration of complex information to initiate voluntary movements through a large-scale neural circuit referred to as the basal ganglia circuitry. In the early stages of HD, the first neurons to degenerate are the dopamine expressing MSNs (D2-like). This results in a loss of inhibitory input to the thalamus from the globus pallidum externa (indirect pathway) and enhanced stimulation of the cortex, which causes the excessive movements observed in HD. However, as the disease progresses, the striatal dopamine receptor 1 (D1) expressing MSNs that project to the globus pallidus interna (direct pathway), other striatal neuronal populations, including the cholinergic and nitric-oxide synthase containing interneurons, and cortical pyramidal neurons in layers III, V, and VI are lost, whereas the brainstem, cerebellum and hippocampus remain unaffected[3,51,52]. In the late stages of HD, broad brain atrophy occurs in the basal ganglia nuclei, pons, medulla, hippocampus, cerebellum, and other brain regions[53]. However, the most striking neuronal loss (95%) in the brain is in the corpus striatum[54]. Although the impaired basal ganglia circuitry underlying HD is fairly understood, it is still unclear why the MSNs are the most vulnerable in HD.

Huntingtin protein function

The Huntingtin protein (HTT) is a large soluble cytoplasmic protein of 3,144 amino acids that is ubiquitously expressed in all regions of the brain and peripheral tissues[55]. The protein is enriched in the soma, dendrites, and synaptic terminals of neurons with similar expression patterns for wild-type and mutant HTT[3,56,57]. Mutated

HTT causes progressive degeneration of the MSNs in the corpus striatum. Expansion of the polyglutamine (polyQ) tract alters the conformational state and biophysical properties of mutant HTT and modifies its fragmentation by proteolytic processing. The HTT protein has several domains and binding partners (Figure I.1.). Importantly, *in vivo* and *in vitro* HD models have demonstrated and suggested that HTT has multiple roles in development, vesicular and axonal transport, gene transcription, anti-apoptosis, synaptic function, and metal homeostasis. Three independent studies have demonstrated that wild-type HTT is essential for normal embryonic development and neurogenesis. Its complete inactivation in *HTT*-knockout mice (*Hdh*-/-) results in embryonic lethality before E7.5 in mouse (prior to gastrulation and the formation of the nervous system)[58-60]. In addition, Lumsden and colleagues have reported that morpholino knockdown of wild-type HTT results in developmental defects and premature death in zebrafish[45]. Wild-type HTT is also essential for the vesicular transport of brain-derived neurotrophic factor (BDNF) along microtubules. Finally, wild-type HTT has functional roles in post-mitotic brain development[61].

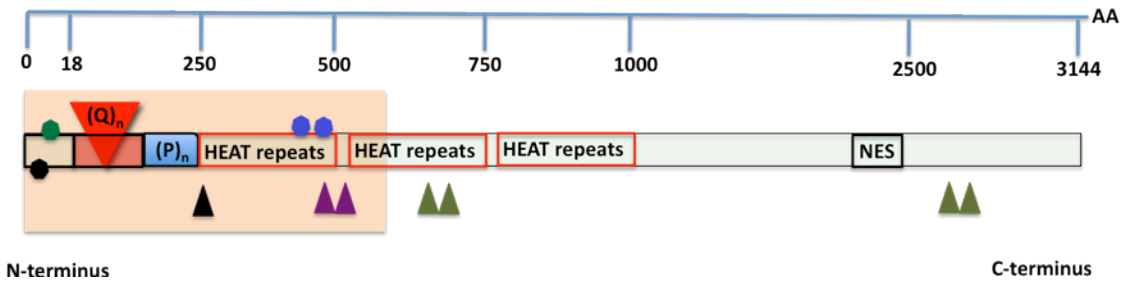

Figure I. 1. Schematized representation of the HTT protein amino acid sequence. The above markings on the HTT protein indicate the following: $(Q)_n$ (number of polyglutamine (polyQ) repeats in the poly Q domain); $(P)_n$ (polyproline sequence rich domain). Red boxes (HEAT repeat clusters); Black box (NES - nuclear export sequence); Brown shaded area (Huntingtin interacting protein, HIP14-interaction domain); Green arrowhead (palmitoylation site); Purple arrowheads (calpain cleavage sites); Red arrows (caspase cleavage sites); blue octagons (clusters of phosphorylation); Green and black octagons (post-translational modifications: ubiquitination and sumoylation). Modified from[62].

Genetics of HD

The *HTT* gene that encodes a ubiquitously expressed HTT protein is located on human chromosome 4, position 16.3[63]. In the first exon of the *HTT* gene are trinucleotide repeats (CAG) that encode for the amino acid, glutamine (Q), in the HTT protein[64,65]. HD is one of nine neurodegenerative diseases that are caused by an expansion in the trinucleotide-encoding region of the disease-causing gene. HD is caused by an expansion in the glutamine-encoding triplet repeat (CAG) of the normal *HTT* gene[3,64,65]. The majority of HD patients have repeat lengths between 40 and 50 CAGs [66]. Importantly, there is an inverse correlation between age of disease onset and repeat length[66,67]. However, the correlation between repeat length and age of disease onset is significantly weaker in HD patients with 40-50 CAGs[66]. Although HD is thought to be an adult-onset

neurodegenerative disease, approximately 5% of HD patients have the juvenile form of the disease with patients exhibiting symptoms in their early teens. In addition, the juvenile form of HD is characterized by increased repeat length (70 or more) in comparison to adult HD onset (40-60). Juvenile HD patients show early cerebellar degeneration and enhanced disease progression compared to adult-onset. The largest CAG repeat that has been documented so far is approximately two hundred and fifty[60,68]. Importantly, most *in vivo* (e.g. YAC128) and *in vitro HD* models (e.g. mutant ST*Hdh*$^{Q111/Q111}$) currently used in HD research and in our studies express a longer repeats length similar to what is observed in the juvenile form of HD. The longer repeats length provides an efficient and practicable experimental duration to observe disease phenotypes[69]. In unaffected individuals, the HTT protein contains between 6 to 37 CAGs. Alleles of CAG between 36 and 39 increase the likelihood of developing HD. In fact, CAGs above 40 are fully penetrant and cause HD[70]. HD and other polyQ diseases share a genetic anticipation phenomenon. In this phenomenon, successive generations of mutant *HTT* inheritance result in an increase polyQ length and a concomitant earlier age of disease onset. HD patients exhibit a striking variability in age of disease onset and severity.

Genetic and environmental modifiers of HD

The autosomal dominant inheritance pattern in HD follows Mendelian genetics. Affected individuals have at least one mutated allele and a 50% probability of transmitting the mutant gene and disorder to their offspring. The CAG repeat length

increases through successive generations. Interestingly, inheritance of the mutated *HTT* allele does not follow an equal sex transmission rate. Specifically, same-sex (mother to daughter or father to son) has a greater sex transmission rate compared to different-sex (mother to son or father to daughter) transmission. In addition, same-sex siblings have been reported to have a greater tendency to have higher transmission rates[66]. Although HD is caused solely by mutation in *HTT* and expansion in the CAG tract, the susceptibility and precise age of onset is modified by other genetic and/or environmental factors. Interestingly, kindred studies have reported that the length of the polyQ repeat in the HTT protein accounts for approximately 60% of the variance in age of disease onset and severity. Importantly, Wexler and colleagues show that repeat lengths between 40 and 50 CAGs account for 44% of the variability and exhibit decreased correlation between CAG repeat length and age of disease onset. In essence, the shorter the repeat length (<50), which is prevalent in majority of HD cases, the greater the influence of genetic and environmental influence on age of onset and susceptibility[66]. Furthermore, the kindred studies have also indicated that a significant segment of the variability in age of onset is familial and accounts for as much as 84% of the residual variance[66].

Importantly, twin studies have demonstrated that siblings with the same CAG repeat length may have striking differences in their symptoms, clinical manifestation, and over 20 year difference in age of disease onset[66,71-73]. Moreover, after accounting for the effect of CAG repeat length, other twin studies have reported a high degree of heritability (h=0.56) in the residual variance. These studies have implicated genetic modifiers as the potential modulators of residual variability in age of onset and severity in HD[74-76]. The findings from the kindred and twin studies strongly suggest that the variability in age of

disease onset and susceptibility may be due to other genetic/and or environmental factors and not the HD gene itself.

Current strategies including, linkage analysis, candidate approach, and genetic screens have been utilized to explore genetic modifiers in HD. Despite the identification of several genetic modifiers in HD, for example genes implicated in lipoprotein metabolism (APOE), axonal trafficking (HAP1), energy metabolism ($PPARGC_1A$), and many others, it is still unclear how they modify the pathogenesis of HD. However, several positive findings of polymorphic genes that modify age of onset in HD have been negated in subsequent studies. For example, APOE, HAP1, UCHL, MTHFR, and $GRIN_2B$. The discrepancies in the modifier investigation and identification has been proposed to be due to sample size, failure to account for multiple hypotheses when many genes are involved, and confounding factors of population stratification and relatedness of the samples used in the study[77]. Conversely, one of the earliest identified genetic modifiers, *GRIK2*, which is a glutamate receptor gene, has been demonstrated to have an effect on age of onset in multiple studies. Specifically, modifications in a particular allele of the 3' untranslated region TAA trinucleotide repeat of GRIK2 that encodes for the GluR6 subunit of the kainate receptor is associated with earlier age of onset than expected[77-79]. Unfortunately, the Venezuelan kindred studies failed to identify any association between *GRIK2* and age of onset. This discrepancy has been attributed to the rareness of *GRIK2* in the Venezuelan kindred[80]. Nevertheless, Andresen and colleagues have reported that the Venezuelan kindred has a genetic polymorphism in the NR2A and NR2B subunits of the NMDA receptor that modify the age of disease onset[80]. Finally, recent genetic modifier studies have also demonstrated that a genetic polymorphism in

$hOGG_1$, a DNA repair gene, increases the CAG repeat length and decreases the age of disease onset in HD[81,82].

Environmental factors, including, exercise and environmental enrichment has been implicated in HD progression using animal models[83-85]. In fact, exercise and environmental enrichment is known to exhibit neuroprotective effects, including, memory enhancement and neurogenesis through *in vivo* alterations of brain derived neurotrophic factor (BDNF) levels[86,87].

The Venezuelan kindred studies have reported that the environment accounts for 63% of the residual variance in age of onset that is not attributed to repeat length. Despite the earlier age of onset in the Venezuelan kindred compared to Canadian and American HD patients, they do not exhibit significant differences in life expectancy. Wexler and colleagues have postulated that the destitute sanitation conditions along Lake Maracaibo where the Venezuelan kindred reside may potentially increase their likelihood of being exposed to environmental factors, such as pollutants that may modify age of disease onset[76]. Unfortunately, the nature of the environmental factor(s) is still unknown. Given the previous reports of occupational neurotoxicity of mercury in Japan and Sweden, which causes Parkinsonian phenotypes in cats and humans, it is highly likely that the suggested environmental factors that modify age of onset may potentially be metals.

Association between metals and HD

Due to the essentiality of metals in the brain, alteration in their homeostasis is

detrimental. Out of all the metals that have been hypothesized to possibly influence HD pathophysiology, it is only Fe and Cu that have been extensively examined to substantiate their potential roles in HD. In fact, magnetic resonance imaging (MRI) studies have demonstrated a significant increase in *in vivo* Fe levels in the basal nuclei, specifically; caudate, putamen, and globus pallidus of HD patients[88]. Fe levels have been reported to be elevated in the caudate and putamen of HD postmortem tissues by 56% and 44% above controls, respectively, albeit no significant changes in ferritin, an intracellular iron storage protein, levels in the aforementioned regions[20,21]. Conversely, other studies have demonstrated elevated ferritin levels in HD brains and animal models of HD[89,90]. The discrepancies in ferritin level reports may possibly be due to experimental and technical issues used to assess ferritin levels in the tissues. Although ceruloplasmin, a ferroxidase enzyme and copper transport protein, levels is increased in HD brains, emerging reports have demonstrated a significant decrease in ceruloplasmin ferroxidase activity in the cerebrospinal fluid of HD patients[91]. Interestingly, other studies have suggested that Fe may influence the expression of HTT, as chelation of Fe by deferoxamine results in increased HTT expression[92]. Thus, it is possible that loss of wild-type HTT function may elevate the levels of free Fe pools in the brain to induce oxidative injury through the Harber-Weiss fenton reactions, which would ultimately result in cell death. Nevertheless, the formation of inclusion bodies by CAG expansion in mutant HTT protein fragments have also been suggested to be associated with iron-dependent oxidative events[24].

Current experimental reports aimed at elucidating the molecular mechanisms underlying altered Fe homeostasis in HD patients, postmortem tissues, and animal models have suggested a possible regulatory role of HTT in Fe compartmentalization. In

fact, wild-type HTT has been demonstrated to be important for Fe metabolism and oxidative energy production in zebrafish. Specifically, morpholino knockdown of HTT causes Fe-deficiency albeit the availability of cellular Fe pools. In addition, there are enhanced transcript levels of transferin receptor 1, a trivalent Fe uptake transporter, in the HTT knockdown zebrafish[45]. HTT protein has been implicated in the modulation of Fe release from endocytic vesicles into the cytosol via the transferrin-mediated pathway[45,93]. Nevertheless, myelination impairments are known to occur in HD patients[94]. Interestingly, the differentiation and proliferation of oligodendroglia, myelinating cells in the CNS, have been reported to be dependent on the availability of Fe[93,95]. In addition, HD patient brains exhibit elevated oligodendrocyte density[96]. Interestingly, the increased Fe levels in the HD brains have been suggested to mediate the sustainment of oligodendrocyte-mediated myelination in the brain[94].

Fe-dependent enzymes, including; the energy metabolism enzymes, mitochondrial complexes I-IV and aconitase are decreased in HD patients and animal models[97,98]. The activity of aconitase, an Fe-sulfur (Fe-S) containing enzyme, essential for Fe homeostasis and the conversion of citrate to isocitrate in the tricarboxylic acid cycle[99,100] as well as the mitochondrial complexes II and III are inhibited by ROS production[101,102]. Thus, it is possible that elevated Fe levels in HD brains may impair energy production and induce ROS production, which would inhibit aconitase and mitochondrial complexes II and III to cause cell death.

Alterations in Cu homeostasis have been implicated in HD. A regional comparison of the concentration of ceruloplasmin in HD patients showed a significant

increase in the hippocampus, parietal cortex, and substantia nigra compared to control patients[103]. In addition, Dexter and colleagues have reported increased Cu levels in the putamen of HD postmortem tissues compared to controls[21]. Finally, recent evidence has demonstrated that the wild-type HTT protein interacts with Cu and decreases its solubility[23]. Although Dexter and colleagues observed no alterations in Mn levels in HD postmortem brains, several Mn-dependent enzymes, including transglutaminase, arginase, gluatmine synthetase, pyruvate carboxylase, and Mn superoxide dismutase 2 (SOD2) are impaired in human HD postmortem brains and toxicant models of HD[22,104,109].

In essence, the above studies elucidating the association of metals in HD pathophysiology strongly insinuate that alterations in metal homeostasis may modify age of onset and disease progression in HD. Thus, future studies would have to focus on the possible influence of other metals in HD neuropathology.

Discovery of a gene-environment interaction: PolyQ-expanded HTT and manganese

Over a decade after the identification of the HD mutation, there has been conflicting reports linking complete or incomplete penetrance of HD to triplet repeat expansion length. Although longer repeat length has been associated with earlier onset, repeat length only accounts for 60% of the variability in age of disease onset and severity. Emerging reports have suggested the possibility of both genetic and environmental factors in playing important roles in HD neuropathology, with environmental factors being the

largest share of the residual variability in age of disease onset and severity[66,110]. Moreover, Gómez-Esteban and others have implicated environmental influences to modify age of disease onset and clinical presentation in monozygotic twin studies that have the same number of expanded repeats[71-73,111]. Unfortunately, these twin studies failed to reveal the nature of the environmental factors involved. Furthermore, animal models of HD have provided further support for the influence of environmental factors on HD onset and progression[110,112]. Indeed, exercise, environmental enrichment, and dietary changes have demonstrated neuroprotective effects in HD. With the increasing and compelling evidence to support a strong association between metals and protein aggregation, altered metal ion homeostasis in HD, and the differential accumulation of various metals across neuronal subtypes, it is highly rationale to propose that metals with neurotoxic properties are the strongest candidates for the largest residual environmental variability in HD that modify age of onset, severity, and selective neuropathology.

In an attempt to identify the metals that contribute or share pathophysiologial mechanisms and potentially modify the age of disease onset, severity, and neuropathology in HD, our lab has previously performed a disease-toxicant screen. We evaluated the potential effects of Mn^{2+}, Fe^{3+}, Cu^{2+}, Zn^{2+}, Pb^{2+}, Cd^{2+}, Co^{2+}, and Ni^{2+} to modify cell survival in an established knock-in immortalized murine striatal cell line model of HD that express either wild-type HTT (ST*Hdh*$^{Q7/Q7}$) or the polyQ-expanded form of the protein (ST*Hdh*$^{Q111/Q111}$)[113-115]. We discovered a novel gene-environment interaction between the mutant HTT protein and Mn. Specifically, acute Mn exposure of the cultured striatal cells produced an unexpected result, wherein mutant (ST*Hdh*$^{Q111/Q111}$) expressing cells showed decreased vulnerability to Mn cytotoxicity compared to wild-

type (ST*Hdh*$^{Q7/Q7}$)[47]. Furthermore, a measurement of total intracellular Mn levels following Mn exposure by graphite furnace atomic absorption spectrometry (GFAAS) in ST*Hdh*$^{Q7/Q7}$ and ST*Hdh*$^{Q111/Q111}$ cells showed a significant decrease in net accumulated Mn levels in mutant compared to wild-type cells. Moreover, the mutant HTT–Mn interaction was corroborated *in vivo* using the YAC128 mouse model of HD. Specifically, we demonstrated a striatal specific decrease in Mn uptake in the YAC128 compared to wild-type animals following subcutaneous injections with 50mg/Kg of Mn chloride tetrahydrate[46,47,116]. Finally, we have reported a significant decrease in basal Mn levels in mutant compared to wild-type cells[46]. Furthermore, recent evidence from Madison and colleagues has demonstrated an *in vivo* impairment effect of Mn exposure on medium spiny neuron morphology and architecture in the YAC128 mouse model of HD (*personal communication*). In essence, while the studies by Williams and Madison are the first to demonstrate a gene-environment interaction between mutant HTT and Mn as well as the ability of Mn to alter neuronal architecture in the corpus striatum respectively, they strongly suggest that Mn may be one of the environmental factors proposed to modify the age of disease onset, progression, and severity in HD. However, it is still unknown how mutant HTT protein expression modulates Mn homeostasis. Hence, further studies that we have performed and would be discussed in subsequent chapters would focus on deciphering the regulatory function of mutant HTT protein on Mn transport, transporter systems, and homeostasis to elicit decreased susceptibility to Mn toxicity.

Manganese

Overview

Mn is an essential ubiquitous trace element required for normal growth, development and cellular homeostasis[117]. Specifically, Mn is important in bone formation, fat and carbohydrate metabolism, blood sugar regulation, and calcium absorption. In humans and animals, Mn functions as a required cofactor of several enzymes necessary for neuronal and glial cell function, as well as enzymes involved in neurotransmitter synthesis and metabolism[22,118,119]. Furthermore, *in vitro* data has implicated Mn in the induction of stellate process formation of astrocytes[120]. Mn exists in various chemical properties including, oxidataion states (Mn^{2+}, Mn^{3+}, Mn^{4+} Mn^{6+}, Mn^{7+}), salts (sulfate and gluconate), and chelates (aspartate, fumarate, succinate). The versatile chemical properties of Mn has enabled for its industrial usage in making glass and ceramics, adhesives, welding, paint, and gasoline anti-knock additive [methylcyclopentadienyl manganese tricarbonyl (MMT)]. While uncommon, Mn deficiency can contribute to birth defects, decreased fecundity, bone malformation, weakness, and enhanced susceptibility to seizures[121,122]. The routes of Mn exposure are mainly through dietary intake, dermal, and inhalation. Moreover, Mn in the diet is found mostly in whole grains, nuts, and seeds, tea, legumes, pineapples, and beans. Despite its essentiality in multiple metabolic functions and industrial usage, excessive levels of Mn exposure can accumulate in the brain and has been associated with dysfunction of the basal ganglia system to cause an irreversible neurological disorder similar to PD[123].

Manganese neurotoxicity

The average Mn levels in brain tissue is approximately 1-2 μg/g dry weight[124]. The concentration of Mn in the brain is very heterogenous under excessive physiological exposures. Importantly, the highest Mn level is in the globus pallidum of humans and hypothalamus of rats[124,125]. Mn exposure is mediated through diet, inhalation, or the skin. Excessive and prolonged exposure to Mn via occupations including welding, mining, combustion products from the anti-knock agent in fuel, for example; MMT, and highly concentrated Mn concentrations in ground/well water results in its the accumulation in the dopamine rich regions of the basal ganglia. In fact, spectroscopy data in rats has demonstrated that the mitochondria accumulate the highest amount of Mn in the basal ganglia following exposure[126,127]. This causes a clinical disorder referred to as manganism that is characterized by extrapyramidal symptoms including, anorexia, apathy, muscle and joint pain, and many others that resemble idiopathic Parkinson's disease (IPD). Shortly after the onset of the symptoms, patients also exhibit memory loss, compulsive behavior, visual impairments, illusions and delusions, disorientation, which is clinically referred to as *locura manganica*, meaning manganese madness[128]. Two vital organs are affected following excessive Mn accumulation in the body, specifically; the brain and lungs, with the latter mediated through inhalation[129,130]. Elevated Mn levels in the brain is associated with impaired Fe homeostasis, excitotoxicity, mitochondrial dysfunction, oxidative stress, induction of protein aggregation, and alteration in the homeostatic conditions of other metals that share similar transporter systems with Mn. Although the relationship between increased Mn levels and its disruptive effects on the neurochemistry of neurotransmitters has been debatable, elevated Mn levels have been

suggested to alter γ-aminobutyric acid (GABA), dopamine, and glutamate neurotransmitters levels in the brain[131-133]. Mn associates with several proteins to facilitate its physiological functions.

Functions of Mn-binding proteins

Mn is a necessary cofactor of several physiological enzymatic activities. Although Cu and Mg can substitute the essential physiological roles of Mn, a subset of enzymes solely depend on Mn for their physiological roles in neuron and/or glial function. These discrete Mn-binding proteins (manganoproteins) include, the glutamine synthetase, superoxide dismutase 2 (SOD2), arginase, pyruvate carboxylase, serine/threonine phosphatase[125,134,135].

Glutamine synthetase (GS) is the most abundant manganoprotein and predominantly expressed in astrocytes. GS synthesizes glutamine through the conversion of glutamate to glutamine. Importantly, Mn has been reported or proposed to regulate GS activity. GS contains four Mn ions per octamer[136]. In fact, decrease GS activity in the brain has been proposed to increase the functional glutamate trafficking, glutamatergic signaling, and excitotoxicity[137]. Interestingly, it has been proposed that the increased susceptibility of seizures observed in individuals with Mn deficiency may be due in part to diminish or aberrant GS levels and/or activity[138]. SOD2 is a mitochondrial enzyme that detoxifies superoxide anions through the formation of hydrogen peroxide (H_2O_2). Although the concentration of Mn within neurons is low ($<10^{-5}$ M), its high mitochondrial energy demands is correlated with a propensity of increased SOD2 in

neurons compared to glia[124,129]. Furthermore, loss of SOD2 activity increases the susceptibility of cells to mitochondrial inhibitors induced toxicity and cause oxidative injury[109]. In the brain, arginase plays an important role in regulating the levels of L-arginine, an amino acid that helps eliminate ammonia from the body. Arginase catalyzes the production of L-ornithine and urea from L-arginine in the urea cycle. Moreover, L-arginine is converted to nitric oxide by the neuronal nitric oxide synthetase. Proper regulation of arginase has been demonstrated to promote neuronal survival by impairing nitric oxide signaling[139,140]. Pyruvate carboxylase is an essential enzyme required for glucose metabolism. It interacts with Mn for the generation of oxaloacelate, a precursor of the tricarboxylic acid (TCA) cycle[141,142]. Interestingly, in the brain, pyruvate carboxylase is predominantly expressed in astrocytes[143,144]. Protein phosphatase 1 is a manganoprotein that is essential for glycogen metabolism, cell progression, regulation of neurotrophin synthesis and release for neuronal survival, and synaptic membrane receptors and channels[145].

Regulation of plasma manganese homeostasis

The intricate regulation of Mn is crucial for its absorption and tissue specific accumulation. Furthermore, it contributes to our understanding of Mn essentiality and toxicity in the brain and periphery. Three major factors have been postulated to be highly important in the modulation of plasma Mn levels. First, given that the main source of Mn exposure is via diet, it is crucial to tightly regulate gastrointestinal absorption of Mn. Secondly, following Mn exposure and a concomitant increase in plasma Mn levels,

excretion of Mn to target organs, including the liver is necessary to prevent Mn induced toxicity in the periphery. Finally, although the liver detoxifies substances, the excreted Mn must be further eliminated from the plasma via shuttling to the bile[129]. The absorption of Mn by the gastrointestinal tract is highly dependable on the quantity of ingested Mn and the net accumulated levels in the plasma. *In vivo* data from mice and rats have reported a minimum variability (1-3.5%) in the GI absorption of plasma Mn[146,147]. While there is a simple diffusion-mediated transport of Mn in the large intestines, Mn is actively and efficiently transported in the small intestines[129]. The major organ required for eliminating accumulated Mn in the plasma is the liver. The concentration gradient-dependent Mn excretion into the bile suggests an active mode of transport[148]. Interesting, a plethora of plasma proteins or ligands have been implicated as specific Mn carrier proteins. These include $beta_1$-globuin, album, and transferrin[149,150]. In fact, Foradori and colleagues have reported that approximately 80% of plasma Mn is bound to $beta_1$-globuin[149]. Despite the demonstration that Mn preferentially binds to albumin in the plasma of both rabbits and humans, emerging evidence has challenged the Mn-albumin assertion and provided evidence for a poor binding of Mn to albumin compared to cadmium and zinc[151,152].

Manganese transport in the central nervous system (CNS)

Mn can cross the blood-brain barrier (BBB) and blood-cerebrospinal fluid barrier (BCB) on several carriers and different oxidation states. Given the essential physiological functions of Mn and the neurotoxicity associated with its homeostatic impairment, Mn

absorption, transport, and tissue levels are stringently regulated. Under normal physiological conditions, Mn is efficiently transported across the blood-brain barrier (BBB) in both the developing fetus and adults[129,153]. Although Mn transport across the BBB has been actively investigated, there has been a paucity of evidence and controversial findings to substantiate the identities of its transporter systems. However, over the past two decades, different Mn transporter systems have been identified; including active and facilitated diffusion modes of Mn transport[154-156]. For example: Mn can be transported via several transporters/channels and candidate proteins including the divalent metal transporter 1 (DMT1), transferrin (Tf) receptor (TfR) that mediates trivalent Fe uptake, calcium channels, zinc-interacting protein transporters, huntingtin-interacting proteins (HIP14 and HIP14L), PARK9, the transient receptor potential 7 (TRPM7) channels, and choline transporters as schematized in Figure I.2. While the tissue-specific expression of each of the aforementioned Mn transporters is yet to be determined, it is likely that the optimal tissue Mn levels are maintained through the involvement of all the above and other unknown Mn transporters. In addition, other cellular process in response to Mn deficiency or overload in tissues may regulate the activity of the above transporters. Of all the above listed polyvalent transporters, TfR and DMT1 are the most extensively documented[156]. Interestingly, it is estimated that approximately 80% of plasma Mn is associated with albumin and $beta_1$-globulin. However, a smaller fraction plasma Mn is bound to transferrin (Tf), an iron-binding protein[149].

The divalent metal transporter 1 (DMT1) is a member of the family of natural resistance-associated macrophage proteins (NRAMP) and crucial for the maintenance of

essential metal homeostasis in the brain[157-159]. It is best known for its ability to regulate Fe homeostasis in the gastrointestinal lumen[159]. DMT1 is also known as the divalent cation transporter (DCT1) due its ability to competently transport divalent metals including, Zn^{2+}, Mn^{2+}, Co^{2+}, Cd^{2+}, Cu^{2+}, Ni^{2+}, Pb^{2+}, and Fe^{2+}[157,160]. There are two alternative splice isoforms of DMT1 that are predominantly localized at the plasma membrane. However, depending on the cation requirements, the different splice isoforms can be localized in subcellular compartments[161]. The transcriptional regulation of the gene that encodes DMT1 protein is modulated by Fe concentration via an iron-response element (IRE) located on its mRNA[125,158]. DMT1 transports metals across the plasma membrane into the cytosol. The relative high affinity of DMT1 for Mn has been well established. Specifically, *in vivo* reports have demonstrated that mutations in the DMT1 gene of the Belgrade rats and microcytic anemia mouse results in significant decrease in Mn and Fe tissue levels[162-164]. Furthermore, the use of magnetic resonance imaging (MRI) in a recent study demonstrated the consistency of a shared transport mechanism (s) between Mn and Fe[165]. Other *in vitro* experiments have also elucidated the role of DMT1 in Mn transport across the BBB. In fact, DMT1 mediated metal transport across the rat brain endothelial cells in culture has been reported to be pH, temperature, and Fe-dependent[166,167].

The TfR is the major cellular receptor for Tf bound Fe, but can also mediate the transport of extracellular Mn with a 3+ valence. Once Mn^{3+} is internalized through the endocytic pathway, it is reduced to Mn^{2+} and transported through DMT1 to the cytosol. Mn binding to Tf is time-dependent and Tf receptors are also present on the surface of cerebral capillaries[156,168]. Additionally, the TfR is an active transporter that is pH and Fe-

dependent[168]. Both *in vivo* and *in vitro* studies have reported that Mn is efficiently transported via the TfR. For example, a spontaneous mutation in the murine gene that is linked to the TfR and referred to as hypotransferrinemic, results in a drastic serum TfR deficiency, impairs Mn transport, as well as disrupts Fe deposition[169,170]. Interestingly, autioradiography reports have indicated that the TfR is generally localized in the gray matter regions, but not the white matter tracts that contain Mn levels in humans and rodents[171-173].

The zinc-interacting protein 8 (ZIP8) and 14 (ZIP14) proteins are divalent metal/bicarbonate ion symporters known to transport Mn, Zn, and Cd under normal conditions[174,175]. ZIP8 and ZIP14 are members of the solute carrier-39[175,176] that are glycosylated and expressed on the apical surface of brain capillaries. Mn uptake through ZIP8 or ZIP14 is driven by the extracellular carbonate (HCO_3^-). The expression of ZIP8 and ZIP14 in the brain are relatively lower compared to the liver, duodenum, and testis[177]. On the other hand, the voltage-gated Ca^{2+} channels, including; L and P-types[178], ligand-gated Ca^{2+} channels, for example; store-operated Ca^{2+} channels (SOCCs)[179], and the ionotropic glutamate receptor Ca^{2+} channels[180] have been implicated in Mn transport across the BBB.

Over the past decade, there has been an increasing interest in the exploration and identification of novel candidate Mn transporters. Emerging experimental data has indicated the role of the magnesium transporter, huntingtin-interacting protein 14 and 14L (HIP14, HIP14L) in mediating Mn^{2+} and other divalent metals (Mg, Sr, Ni, Ca, Ba, Zn^{2+}) transport across cell membranes[181,182]. HIP14 is the mammalian ortholog of the

ankyrin repeat protein 1 (Akr1p) that is primarily expressed in neurons and not glia. HIP14 is involved in the palmitoylation of several neuronal proteins including HTT[183]. In addition, it is required for endo and exocytisis, as well as targeting of cysteine string protein (CSP) and synaptosomal-associated protein 25 (SNAP25) to the synapse[184,185]. HIP14 is predominantly expressed in the presynaptic terminal, golgi apparatus, and vesicular structures localized in the axon, dendrites, and soma of neurons[186]. Biochemical studies, including; yeast-two-hybrid has demonstrated that the interaction between HIP14 and HTT is inversely correlated to the poly-Q length in the HTT protein[185]. Furthermore, Gitler and colleagues have recently reported that the PARK9 gene responsible for early-onset Parkinsonism also transports Mn[182]. The PARK9 gene encodes a putative P-type transmembrane ATPase (ATP13A2) protein. Although the exact function of PARK9 is unknown, it is generally thought to be a transmembrane cationic metal transporter that shuttles cations, including Mn across the cell. Biochemical studies have demonstrated that the highest and lowest PARK9 mRNA levels are localized within the substantia nigra and cerebellum respectively[187].

In spite of the inhibitory roles of Mn on the choline transporter at the BBB, it has been suggested that Mn transport during periods of high-throughput may be mediated through the choline transporter. In addition, the choline transporter has a higher affinity for Mn compared to the other metals (Cd^{2+} and Al^{3+}) that it transports[188-190]. Mn transport across the choline transport is sodium-independent, carrier-mediated, and saturable[168].

The TRPM7 transporter is ubiquitously expressed in vertebrates as a Ca^{2+} selective channel, and a serine/threonine protein kinase. Transport of cations across

TRPM7 channel is energy dependent. Furthermore, the kinase activity is important for the TRPM7 metal transport function. Specifically, the kinase operates by regulating the intracellular Ca^{2+} levels and Mg^{2+} homeostasis through the creation of an inward current. Thus, contributing to the establishment of a cell membrane potential. The selective permeability of cations through TRPM7 has been reported to be as follows: Zn^{2+}, Ni^{2+}> Ba^{2+}, Co^{2+}> Mg^{2+}> Mn^{2+}> Sr^{2+}> Cd^{2+}> Ca^{2+}. Finally, physiological levels of Mg^{2+} and Ca^{2+} are necessary for maintaining the permeability of Mn^{2+}, Co^{2+}, and Ni^{2+} through TRPM7[168].

The homomeric purinorecptors, including P2X and P2Y have been suggested to participate in Mn transport. These receptors are ATP-dependent and ubiquitously expressed on endothelial cells[191-193]. Purinoreceptors have a relatively lower affinity for Mn compared to other divalent metals that it transports (Ca> Mg> Ba> Mn)[168]. Finally, the citrate transporter has been implicated in Mn transport across the BBB[194].

Intracellular Mn^{2+} is sequestered into the mitochondria of brain and liver via the Ca^{2+} uniporter[195,196]. There has been conflicting reports to support either the mitochondria or nuclei as the cellular organelle that accumulates the primary pool of Mn in the cell[143,197,198]. In fact, Suzuki and colleagues have reported that both brain mitochondria and lysosomes accumulate a substantial amount of unbound Mn following Mn administration[199]. The efflux mechanism of cellular mitochondrial Mn^{2+} is mediated preferentially through an active, but slow Na^{+}-independent mechanism with minimal transport over the Na^{+}-dependent efflux mechanism[125]. This slow Mn efflux is suggested to account for the net accumulation of Mn in the mitochondria. Nevertheless, the

cytoplasmic Fe^{2+} exporter, ferroportin-1, has been hypothesized and reported to be a candidate Mn exporter. Interestingly, ferroportin-1 surface localization and protein expression is perturbed following Mn exposure[200].

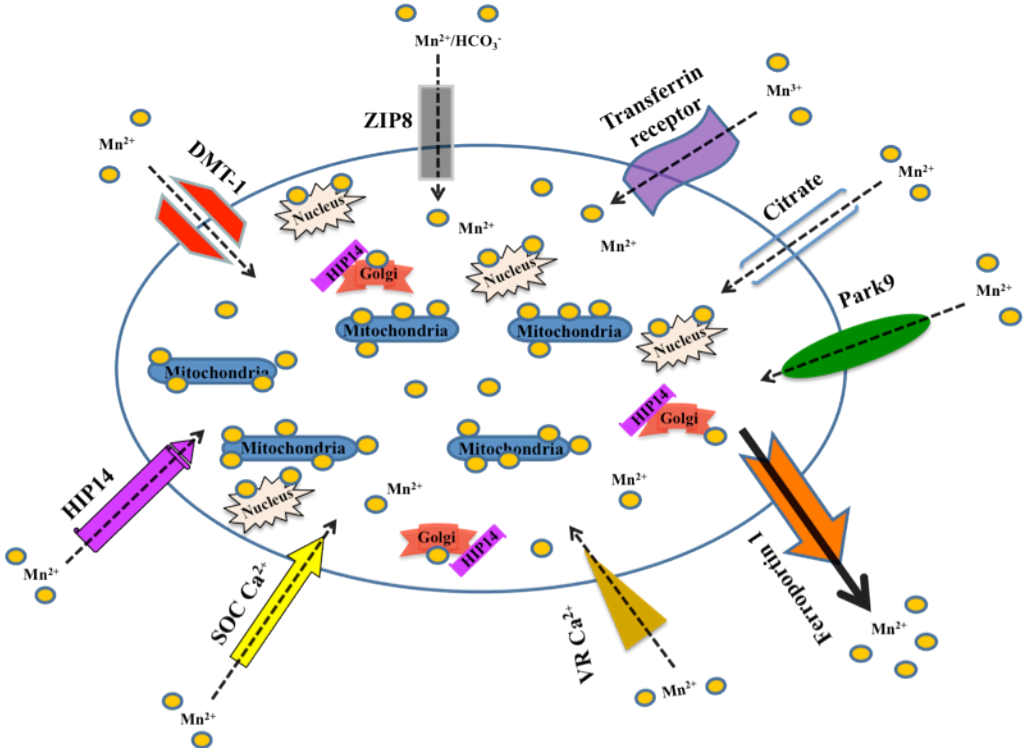

Figure I. 2. Identified and putative Mn transporters. These illustrated Mn transporters have been demonstrated to facilitate Mn trafficking (uptake, storage, efflux) between the extra and intra-cellular milieu. Each of these transporter proteins has also been implicated in the transport of other metals.

Methods for detecting manganese levels in biological specimens

Over the past two decades, several analytical methods have been developed for detecting Mn levels and monitoring Mn homeostasis in biological samples. Although

most methods used to detect Mn in biological samples require digestion of the organic matrix prior to analysis, a recently developed method has successively measured trace concentrations of metals without sample digestion[201]. In fact, the biological sample-type determines the method of digestion to be used. For example, blood or saliva may be digested by an ion exchange resin while tissue samples would require acid (nitric or sulfuric) digestion. Exogenous Mn can contaminate the accuracy of detecting and measuring Mn levels in biological samples, especially low Mn levels. The current methods used for measuring Mn levels in biological specimens include atomic absorption spectroscopy (AAS), atomic emission spectroscopy (AES), inductively coupled plasma-atomic emission spectrometry (ICP-AES) and mass spectrometry (ICP-MS), neutron activation analysis, x-ray fluorimetry, spectrophotometry, and radioactive trace assays.

AAS and ICP-MS are the most common methods used for measuring Mn levels in biological samples. AAS analysis requires aspiration of the sample into a flame or graphite furnace (GFAAS) that is further detected on a photoelectric detector for elemental measurements. GFAAS is mostly used for the determination of very low analyte levels as well as solid sample analysis[202]. ICP-MS provides multi-element analysis of biological specimens, including Mn. In fact, ICP-AES and ICP-MS can often measure analytes at the part per trillion levels[203]. In addition, ICP-AES and ICP-MS can be used to measure both liquid and solid analytes. While measurements of analytes in solid samples require a laser ablation system, liquid samples are introduced into the ICP by a nebulizer for analyte (Mn) measurements. Conversely, neutron activation analysis minimizes potential contamination of biological Mn levels through minimal sample handling and no reagent usage. Furthermore, neutron activation analysis has a low

detection limit and capable of accurate detection of 4ng/g of analytes in biological samples[202]. However, none of the above Mn detection methods is capable of distinguishing between different Mn compounds or oxidation states.

In spite of the several advantages that the current Mn detection techniques provide, for example; multi-elemental analysis, excellent specificity, extremely high sensitivity and limited chemical interference, they are not feasible to assess Mn transport kinetics in a high-throughput manner. This is mainly due to the large number of samples required, duration of experimental analysis and cost of analysis.

Rationale behind the development of a high-throughput manganese detection assay

We have previously identified a disease-toxicant interaction between mutant HTT and Mn, wherein expression of the mutant HTT protein decreases net Mn uptake in both cellular and mouse models of HD[46,47]. However, it is still unknown how expression of mutant HTT protein modulates Mn transport dynamics and homeostasis. Unfortunately, the current Mn detection methods described above are not feasible to assess Mn transport kinetics in a high-throughput manner. Therefore, we sought to develop a high-throughput assay that could accurately measure cellular Mn levels following detergent extraction and enable efficient assessment of Mn transport kinetics. The remaining chapters of this thesis would focus on the development of a novel high-throughput assay and its usage in the functional characterization of Mn transport kinetics and dissection of metal

transporter systems that underlie the Mn accumulation deficiency observed in a mutant expressing cellular model of HD.

Summary

The above-discussed chapters have elucidated and provided experimental evidence to support the idea of gene-environment interactions in modifying age of onset, progression, and severity in neurodegenerative and other diseases. Importantly, metals have been reported to exhibit gene-environment interactions in other neurodegenerative diseases, including HD[20,21,25-27]. Moreover, we have reported that acute Mn exposure of cultured mutant (ST*Hdh*$^{Q111/Q111}$) expressing cells exhibit decreased vulnerability and accumulate significantly less Mn levels compared to wild-type (ST*Hdh*$^{Q7/Q7}$) following Mn exposure[47]. Unfortunately, it is still unknown how mutant HTT expression modulates Mn homeostasis. Nevertheless, the current methods used to measure Mn levels in biological specimens lack the practicability to assess Mn transport kinetics in a high-throughput manner. Therefore, it is necessary to develop a high-throughput Mn detection assay that enables functional assessment of Mn transport dynamics and can be utilized to dissect the metal transporter systems that underlie the decreased Mn accumulation observed in mutant HTT expressing cells.

Overview of Specific Aims

Emerging evidence from the kindred and twin studies have indicated that the polyQ repeat length in the HTT protein accounts for approximately 60% of the variance in age of disease onset and severity. Interestingly, both genetic and environmental factors have been suggested to modulate the susceptibility, age of onset, and selective neuropathology in HD[66,110]. However, the nature of the environmental factor(s) is still unknown. Given that there is a strong association between metals and protein aggregation, similarities between metal cytotoxicity and cellular pathways of neurodegeneration, alterations in metal homeostasis, and the differential brain region accumulation of metals across neuronal subtypes, it is rationale to propose that metals with neurotoxic properties are the prime candidates for the largest residual environmental variability that has been indicated to modulate the age of onset, severity, and selective neuropathology in HD.

In fact, we have previously reported a disease-toxicant interaction between the polyQ-expanded HTT protein and Mn in an established knock-in immortalized murine mutant (ST*Hdh*$^{Q111/Q111}$) striatal cell line and the YAC128 mouse models of HD. We have demonstrated that mutant HTT protein (ST*Hdh*$^{Q111/Q111}$) expressing cells exhibit decreased vulnerability to Mn cytotoxicity compared to wild-type (ST*Hdh*$^{Q7/Q7}$) following $MnCl_2$ exposure[47]. Importantly, assessment of intracellular Mn levels by GFAAS has shown that mutant ST*Hdh*$^{Q111/Q111}$ cells exhibit a significant decrease in net accumulated Mn levels compared to wild-type ST*Hdh*$^{Q7/Q7}$ [46]. In essence, these findings imply that Mn is a major environmental factor that may potentially modify the susceptibility, age of onset, and progression in HD. Prominently, the discovery of the

disease-toxicant interaction between the glutamine-expanded HTT protein and Mn established the significance of deciphering how mutant HTT protein modulates Mn transport and transporter systems to elicit decreased susceptibility to Mn toxicity.

Our over-arching hypothesis is that mutant HTT alters the regulation of cellular Mn by aberrant interactions with the normal cellular Mn transport system. To test this hypothesis, we propose to do the following: 1) Develop a novel high-throughput assay to assess cellular Mn levels and transport dynamics in cultured striatal cells. 2) Measure Mn transport kinetics to functionally characterize the decreased Mn accumulation in mutant ST*Hdh* cells. 3) Dissect and examine metal transport pathways that contribute to the mutant HTT-Mn gene-environment interaction.

Specific Aim 1: Develop a novel high-throughput assay to assess cellular Mn levels and dynamics.

We have established and developed a novel high-throughput fluorescence-quenching extraction assay (Cellular Fura-2 Manganese Extraction Assay - CFMEA). Furthermore, we have validated CFMEA using two alternative Mn-supplementation or Mn-spike methods. In addition, we have utilized GFAAS to validate the accuracy and specificity of CFMEA to measure cellular Mn levels in the well-established HD cellular model (wild-type ST*Hdh*$^{Q7/Q7}$ and mutant ST*Hdh*$^{Q111/Q111}$ cells). Finally, we have developed a normalization assay (PicoGreen assay) to enable accurate normalization of cellular Mn levels in cell-extracts to dsDNA post CFMEA analysis.

Specific Aim 2: Assess Mn transport kinetics to functionally characterize the decreased Mn accumulation in mutant ST*Hdh* cells.

Here, we explored the nature of the Mn transport defect that we had previously discovered with the mutant HTT protein. To determine whether the decreased cellular Mn accumulation in mutant ST*Hdh*$^{Q111/Q111}$ compared to wild-type ST*Hdh*$^{Q7/Q7}$ cells is due to an impairment in Mn uptake, decreased cellular Mn storage capacity, or enhanced efflux processes, we utilized the CFMEA assay to measure net cellular Mn levels in the ST*Hdh* cell lines following Mn exposure. In addition, we used a kinetic fluorescence assay to assess real-time Mn transport kinetics in the ST*Hdh* cells.

Specific Aim 3: Dissect metal transport pathways underlying the mutant HTT-Mn gene-environment interaction.

We explored the transporter system(s) and pathway(s) underlying mutant HTT-Mn interaction by systematic dissection of various known and putative metal transporters and the cellular pathways that facilitate Mn uptake, cellular Mn storage, and efflux. We investigated the nature of the impaired metal transporter implicated in the Mn accumulation deficit observed in mutant HD cells. Furthermore, we explored the requirement of other metals for the establishment of a disease-toxicant interaction in the ST*Hdh* cells. Additionally, we utilized different metal transporter agonist or antagonists to examine their contributions in the disease-toxicant interaction. Moreover, we examined the protein and transcript expression levels of known and putative Mn transporters by

western blotting analysis. Finally, we examined the relationship between Mn induced cytotoxicity, cellular Mn pools, and changes in ROS levels in the ST*Hdh* cells.

References

1. Meek, P.D., McKeithan, K. & Schumock, G.T. Economic considerations in Alzheimer's disease. *Pharmacotherapy* **18**, 68-73; discussion 79-82 (1998).

2. Hunter, D.J. Gene-environment interactions in human disease. *Nature Reviews* **6**, 285-298 (2005).

3. Cowan, C.M. & Raymond, L.A. Selective neuronal degeneration in Huntington's disease. *Curr Top Dev Biol* **75**, 25-71 (2006).

4. Krüger, R., Kuhn, W., Müller, T., Woitalla, D., Graeber, M., Kösel, S., Przuntek, H., Epplen, J.T., Schöls, L. & Riess, O. Ala30Pro mutation in the gene encoding alpha-synuclein in Parkinson's disease. *Nat. Gen.* **18**, 106-108 (1998).

5. Goate, A., Chartier-Harlin, M.C., Mullan, M., Brown, J., Crawford, F., Fidani, L., Giuffra, L., Haynes, A., Irving, N., James, L. & et al. Segregation of a missense mutation in the amyloid precursor protein gene with familial Alzheimer's disease. *Nature* **349**, 704-6 (1991).

6. Rosen, D.R. Mutations in Cu/Zn superoxide dismutase gene are associated with familial amyotrophic lateral sclerosis. *Nature* **364**, 362 (1993).

7. Garrod, A.E. About Alkaptonuria. *Med Chir Trans* **85**, 69-78 (1902).

8. Gaeta, A. & Hider, R.C. The crucial role of metal ions in neurodegeneration: the basis for a promising therapeutic strategy. *Br J Pharmacol* **146**, 1041-59 (2005).

9. van Dellen, A., Blakemore, C., Deacon, R., York, D. & Hannan, A.J. Delaying the onset of Huntington's in mice. *Nature* **404**, 721-2 (2000).

10. Guilarte, T.R., Toscano, C.D., McGlothan, J.L. & Weaver, S.A. Environmental enrichment reverses cognitive and molecular deficits induced by developmental lead exposure. *Ann Neurol* **53**, 50-6 (2003).

11. Kempermann, G., Kuhn, H.G. & Gage, F.H. More hippocampal neurons in adult mice living in an enriched environment. *Nature* **386**, 493-5 (1997).

12. Horowitz, M.P. & Greenamyre, J.T. Gene-environment interactions in Parkinson's disease: the importance of animal modeling. *Clin Pharmacol Ther* **88**, 467-74 (2010).

13. Nithianantharajah, J., Levis, H. & Murphy, M. Environmental enrichment results in cortical and subcortical changes in levels of synaptophysin and PSD-95 proteins. *Neurobiol Learn Mem* **81**, 200-10 (2004).

14. Bennett, E.L., Diamond, M.C., Krech, D. & Rosenzweig, M.R. Chemical and Anatomical Plasticity Brain. *Science* **146**, 610-9 (1964).

15. Altman, J. & Das, G.D. Post-natal origin of microneurones in the rat brain. *Nature* **207**, 953-6 (1965).

16. Chandra, V. & Pandav, R. Gene-environment interaction in Alzheimer's disease: a potential role for cholesterol. *Neuroepidemiology* **17**, 225-32 (1998).

17. Jarvik, G.P., Wijsman, E.M., Kukull, W.A., Schellenberg, G.D., Yu, C. & Larson, E.B. Interactions of apolipoprotein E genotype, total cholesterol level, age, and sex in prediction of Alzheimer's disease: a case-control study. *Neurology* **45**, 1092-6 (1995).

18. Langston, J.W. The impact of MPTP on Parkinsons disease research: past, present, and future. in *Parkinson's Disease: Diagnosis and Clinical Management.* (eds. Factor, S.A. & Weiner, W.J.) (Demos Medical Publishing;, New York, 2002).

19. Vance, J.M., Ali, S., Bradley, W.G., Singer, C. & Di Monte, D.A. Gene-environment interactions in Parkinson's disease and other forms of parkinsonism. *Neurotoxicology* **31**, 598-602 (2010).

20. Dexter, D.T., Carayon, A., Javoy-Agid, F., Agid, Y., Wells, F.R., Daniel, S.E., Lees, A.J., Jenner, P. & Marsden, C.D. Alterations in the levels of iron, ferritin and other trace metals in Parkinson's disease and other neurodegenerative diseases affecting the basal ganglia. *Brain* **114 (Pt 4)**, 1953-75 (1991).

21. Dexter, D.T., Jenner, P., Schapira, A.H. & Marsden, C.D. Alterations in levels of iron, ferritin, and other trace metals in neurodegenerative diseases affecting the basal ganglia. The Royal Kings and Queens Parkinson's Disease Research Group. *Ann Neurol* **32 Suppl**, S94-100 (1992).

22. Butterworth, J. Changes in nine enzyme markers for neurons, glia, and endothelial cells in agonal state and Huntington's disease caudate nucleus. *J Neurochem* **47**, 583-7 (1986).

23. Fox, J.H., Kama, J.A., Lieberman, G., Chopra, R., Dorsey, K., Chopra, V., Volitakis, I., Cherny, R.A., Bush, A.I. & Hersch, S. Mechanisms of copper ion mediated Huntington's disease progression. *PLoS One* **2**, e334 (2007).

24. Firdaus, W.J., Wyttenbach, A., Giuliano, P., Kretz-Remy, C., Currie, R.W. & Arrigo, A.P. Huntingtin inclusion bodies are iron-dependent centers of oxidative events. *FEBS J* **273**, 5428-41 (2006).

25. Yasui, M., Kihira, T., Ota, K., Mukoyama, M. & Adachi, K. [Aluminum deposition in the central nervous system tissues of patients with Parkinson's disease]. *Rinsho Shinkeigaku* **31**, 1095-8 (1991).

26. Ward, N. & Mason, J. Neutron activation analysis techniques for identifying elemental status in Alzheimer's disease. *J. Radioanal. Nucl. Chem* **113**, 515-526 (1987).

27. McDermott, J.R., Smith, A.I., Iqbal, K. & Wisniewski, H.M. Brain aluminum in aging and Alzheimer disease. *Neurology* **29**, 809-14 (1979).

28. Martinez-Finley, E.J., Avila, D.S., Chakraborty, S. & Aschner, M. Insights from Caenorhabditis elegans on the role of metals in neurodegerative diseases. *Metallomics*, 271-279 (2010).

29. Kaur, D., Yantiri, F., Rajagopalan, S., Kumar, J., Mo, J.Q., Boonplueang, R., Viswanath, V., Jacobs, R., Yang, L., Beal, M.F., DiMonte, D., Volitaskis, I., Ellerby, L., Cherny, R.A., Bush, A.I. & Andersen, J.K. Genetic or pharmacological iron chelation prevents MPTP-induced neurotoxicity in vivo: a novel therapy for Parkinson's disease. *Neuron* **37**, 899-909 (2003).

30. Frederickson, C.J. Neurobiology of zinc and zinc-containing neurons. *Int Rev Neurobiol* **31**, 145-238 (1989).

31. Frederickson, C.J., Kasarskis, E.J., Ringo, D. & Frederickson, R.E. A quinoline fluorescence method for visualizing and assaying the histochemically reactive zinc (bouton zinc) in the brain. *J Neurosci Methods* **20**, 91-103 (1987).

32. Danscher, G., Howell, G., Perez-Clausell, J. & Hertel, N. The dithizone, Timm's sulphide silver and the selenium methods demonstrate a chelatable pool of zinc in CNS. A proton activation (PIXE) analysis of carbon tetrachloride extracts from rat brains and spinal cords intravitally treated with dithizone. *Histochemistry* **83**, 419-22 (1985).

33. Szerdahelyi, P. & Kasa, P. Histochemistry of zinc and copper. *Int Rev Cytol* **89**, 1-33 (1984).

34. Pattison, S.E. & Dunn, M.F. On the mechanism of divalent metal ion chelator induced activation of the 7S nerve growth factor esteropeptidase. Thermodynamics and kinetics of activation. *Biochemistry* **15**, 3696-703 (1976).

35. Zalewski, P.D., Millard, S.H., Forbes, I.J., Kapaniris, O., Slavotinek, A., Betts, W.H., Ward, A.D., Lincoln, S.F. & Mahadevan, I. Video image analysis of labile zinc in viable pancreatic islet cells using a specific fluorescent probe for zinc. *J Histochem Cytochem* **42**, 877-84 (1994).

36. Peters, S., Koh, J. & Choi, D.W. Zinc selectively blocks the action of N-methyl-D-aspartate on cortical neurons. *Science* **236**, 589-93 (1987).

37. Itoh, M. & Ebadi, M. The selective inhibition of hippocampal glutamic acid decarboxylase in zinc-induced epileptic seizures. *Neurochem Res* **7**, 1287-98 (1982).

38. Binolfi, A., Rasia, R.M., Bertoncini, C.W., Ceolin, M., Zweckstetter, M., Griesinger, C., Jovin, T.M. & Fernandez, C.O. Interaction of alpha-synuclein with divalent metal ions reveals key differences: a link between structure, binding specificity and fibrillation enhancement. *J Am Chem Soc* **128**, 9893-901 (2006).

39. Giese, A., Levin, J., Bertsch, U. & Kretzschmar, H. Effect of metal ions on de novo aggregation of full-length prion protein. *Biochem Biophys Res Commun* **320**, 1240-6 (2004).

40. Jobling, M.F., Huang, X., Stewart, L.R., Barnham, K.J., Curtain, C., Volitakis, I., Perugini, M., White, A.R., Cherny, R.A., Masters, C.L., Barrow, C.J., Collins, S.J., Bush, A.I. & Cappai, R. Copper and zinc binding modulates the aggregation and neurotoxic properties of the prion peptide PrP106-126. *Biochemistry* **40**, 8073-84 (2001).

41. Tsenkova, R.N., Iordanova, I.K., Toyoda, K. & Brown, D.R. Prion protein fate governed by metal binding. *Biochem Biophys Res Commun* **325**, 1005-12 (2004).

42. Levin, J., Bertsch, U., Kretzschmar, H. & Giese, A. Single particle analysis of manganese-induced prion protein aggregates. *Biochem Biophys Res Commun* **329**, 1200-7 (2005).

43. Hung, Y.H., Bush, A.I. & Cherny, R.A. Copper in the brain and Alzheimer's disease. *J Biol Inorg Chem* **15**, 61-76 (2010).

44. Jomova, K., Vondrakova, D., Lawson, M. & Valko, M. Metals, oxidative stress and neurodegenerative disorders. *Mol Cell Biochem* **345**, 91-104 (2010).

45. Lumsden, A.L., Henshall, T.L., Dayan, S., Lardelli, M.T. & Richards, R.I. Huntingtin-deficient zebrafish exhibit defects in iron utilization and development. *Hum Mol Genet* **16**, 1905-20 (2007).

46. Williams, B.B., Kwakye, G.F., Wegrzynowicz, M., Li, D., Aschner, M., Erikson, K.M. & Bowman, A.B. Altered manganese homeostasis and manganese toxicity in a Huntington's disease striatal cell model are not explained by defects in the iron transport system. *Toxicol Sci* **117**, 169-79 (2010).

47. Williams, B.B., Li, D., Wegrzynowicz, M., Vadodaria, B.K., Anderson, J.G., Kwakye, G.F., Aschner, M., Erikson, K.M. & Bowman, A.B. Disease-toxicant screen reveals a neuroprotective interaction between Huntington's disease and manganese exposure. *J Neurochem* **112**, 227-37 (2010).

48. Paulsen, J.S., Zhao, H., Stout, J.C., Brinkman, R.R., Guttman, M., Ross, C.A., Como, P., Manning, C., Hayden, M.R. & Shoulson, I. Clinical markers of early disease in persons near onset of Huntington's disease. *Neurology* **57**, 658-62 (2001).

49. Harper, P.S. Huntington’s Disease. Vol. 2nd Edition (Elsevier Science, London, 1996).

50. Sari, Y. Potential Drugs and Methods for Preventing or Delaying the Progression of Huntington's Disease. *Recent Pat CNS Drug Discov* **6**, 80-90 (2011).

51. Ferrante, R.J., Kowall, N.W., Beal, M.F., Richardson, E.P., Jr., Bird, E.D. & Martin, J.B. Selective sparing of a class of striatal neurons in Huntington's disease. *Science* **230**, 561-3 (1985).

52. Ferrante, R.J., Kowall, N.W., Beal, M.F., Martin, J.B., Bird, E.D. & Richardson, E.P., Jr. Morphologic and histochemical characteristics of a spared subset of striatal neurons in Huntington's disease. *J Neuropathol Exp Neurol* **46**, 12-27 (1987).

53. de la Monte, S.M., Vonsattel, J.P. & Richardson, E.P., Jr. Morphometric demonstration of atrophic changes in the cerebral cortex, white matter, and neostriatum in Huntington's disease. *J Neuropathol Exp Neurol* **47**, 516-25 (1988).

54. Vonsattel, J.P., Myers, R.H., Stevens, T.J., Ferrante, R.J., Bird, E.D. & Richardson, E.P., Jr. Neuropathological classification of Huntington's disease. *J Neuropathol Exp Neurol* **44**, 559-77 (1985).

55. Zhang, H., Li, Q., Graham, R.K., Slow, E., Hayden, M.R. & Bezprozvanny, I. Full length mutant huntingtin is required for altered Ca2+ signaling and apoptosis of striatal neurons in the YAC mouse model of Huntington's disease. *Neurobiol Dis* **31**, 80-88 (2008).

56. Aronin, N., Chase, K., Young, C., Sapp, E., Schwarz, C., Matta, N., Kornreich, R., Landwehrmeyer, B., Bird, E., Beal, M.F. & et al. CAG expansion affects the expression of mutant Huntingtin in the Huntington's disease brain. *Neuron* **15**, 1193-201 (1995).

57. Sharp, A.H., Loev, S.J., Schilling, G., Li, S.H., Li, X.J., Bao, J., Wagster, M.V., Kotzuk, J.A., Steiner, J.P., Lo, A. & et al. Widespread expression of Huntington's disease gene (IT15) protein product. *Neuron* **14**, 1065-74 (1995).

58. Zeitlin, S., Liu, J.P., Chapman, D.L., Papaioannou, V.E. & Efstratiadis, A. Increased apoptosis and early embryonic lethality in mice nullizygous for the Huntington's disease gene homologue. *Nat Genet* **11**, 155-63 (1995).

59. Nasir, J., Floresco, S.B., O'Kusky, J.R., Diewert, V.M., Richman, J.M., Zeisler, J., Borowski, A., Marth, J.D., Phillips, A.G. & Hayden, M.R. Targeted disruption of the Huntington's disease gene results in embryonic lethality and behavioral and morphological changes in heterozygotes. *Cell* **81**, 811-23 (1995).

60. Duyao, M.P., Auerbach, A.B., Ryan, A., Persichetti, F., Barnes, G.T., McNeil, S.M., Ge, P., Vonsattel, J.P., Gusella, J.F., Joyner, A.L. & et al. Inactivation of the mouse Huntington's disease gene homolog Hdh. *Science* **269**, 407-10 (1995).

61. Dragatsis, I., Levine, M.S. & Zeitlin, S. Inactivation of Hdh in the brain and testis results in progressive neurodegeneration and sterility in mice. *Nat Genet* **26**, 300-6 (2000).

62. Cattaneo, E., Zuccato, C. & Tartari, M. Normal huntingtin function: an alternative approach to Huntington's disease. *Nat Rev Neurosci* **6**, 919-30 (2005).

63. Gusella, J.F., Wexler, N.S., Conneally, P.M., Naylor, S.L., Anderson, M.A., Tanzi, R.E., Watkins, P.C., Ottina, K., Wallace, M.R., Sakaguchi, A.Y. & et al. A polymorphic DNA marker genetically linked to Huntington's disease. *Nature* **306**, 234-8 (1983).

64. Group, H.s.D.C.R. A novel gene containing a trinucleotide repeats that is expanded and unstable on Huntington's disease chromosomes. *Cell* **72**, 971-983 (1993).

65. Bates, G.P. History of genetic disease: the molecular genetics of Huntington disease - a history. *Nat Rev Genet* **6**, 766-73 (2005).

66. Wexler, N.S. Venezuelan kindreds reveal that genetic and environmental factors modulate Huntington's disease age of onset. *PNAS* **101**, 3498-3503 (2004).

67. Brinkman, R.R., Mezei, M.M., Theilmann, J., Almqvist, E. & Hayden, M.R. The likelihood of being affected with Huntington disease by a particular age, for a specific CAG size. *Am J Hum Genet* **60**, 1202-10 (1997).

68. Telenius, H., Kremer, H.P., Theilmann, J., Andrew, S.E., Almqvist, E., Anvret, M., Greenberg, C., Greenberg, J., Lucotte, G., Squitieri, F. & et al. Molecular analysis of juvenile Huntington disease: the major influence on (CAG)n repeat length is the sex of the affected parent. *Hum Mol Genet* **2**, 1535-40 (1993).

69. Wheeler, V.C., Gutekunst, C.A., Vrbanac, V., Lebel, L.A., Schilling, G., Hersch, S., Friedlander, R.M., Gusella, J.F., Vonsattel, J.P., Borchelt, D.R. & MacDonald, M.E. Early phenotypes that presage late-onset neurodegenerative disease allow testing of modifiers in Hdh CAG knock-in mice. *Hum Mol Genet* **11**, 633-40 (2002).

70. Rubinsztein, D.C., Leggo, J., Coles, R., Almqvist, E., Biancalana, V., Cassiman, J.J., Chotai, K., Connarty, M., Crauford, D., Curtis, A., Curtis, D., Davidson, M.J., Differ, A.M., Dode, C., Dodge, A., Frontali, M., Ranen, N.G., Stine, O.C., Sherr, M., Abbott, M.H., Franz, M.L., Graham, C.A., Harper, P.S., Hedreen, J.C., Hayden, M.R. & et al. Phenotypic characterization of individuals with 30-40 CAG repeats in the Huntington disease (HD) gene reveals HD cases with 36 repeats and apparently normal elderly individuals with 36-39 repeats. *Am J Hum Genet* **59**, 16-22 (1996).

71. Georgiou, N., Bradshaw, J.L., Chiu, E., Tudor, A., O'Gorman, L. & Phillips, J.G. Differential clinical and motor control function in a pair of monozygotic twins with Huntington's disease. *Mov Disord* **14**, 320-5 (1999).

72. Anca, M.H., Gazit, E., Loewenthal, R., Ostrovsky, O., Frydman, M. & Giladi, N. Different phenotypic expression in monozygotic twins with Huntington disease. *Am J Med Genet A* **124A**, 89-91 (2004).

73. Gómez-Esteban, J.C., Lezcano, E., Zarranz, J.J., Velasco, F., Garamendi, I., Pérez, T. & Tijero , B. Monozygotic twins suffering from Huntington's disease show different cognitive and behavioural symptoms. *European Neurology* **57**, 26-30 (2007).

74. Li, J.L., Hayden, M.R., Almqvist, E.W., Brinkman, R.R., Durr, A., Dode, C., Morrison, P.J., Suchowersky, O., Ross, C.A., Margolis, R.L., Rosenblatt, A., Gomez-Tortosa, E., Cabrero, D.M., Novelletto, A., Frontali, M., Nance, M., Trent, R.J., McCusker, E., Jones, R., Paulsen, J.S., Harrison, M., Zanko, A., Abramson, R.K., Russ, A.L., Knowlton, B., Djousse, L., Mysore, J.S., Tariot, S., Gusella, M.F., Wheeler, V.C., Atwood, L.D., Cupples, L.A., Saint-Hilaire, M., Cha, J.H., Hersch, S.M., Koroshetz, W.J., Gusella, J.F., MacDonald, M.E. & Myers, R.H. A genome scan for modifiers of age at onset in Huntington disease: The HD MAPS study. *Am J Hum Genet* **73**, 682-7 (2003).

75. Djousse, L., Knowlton, B., Hayden, M., Almqvist, E.W., Brinkman, R., Ross, C., Margolis, R., Rosenblatt, A., Durr, A., Dode, C., Morrison, P.J., Novelletto, A., Frontali, M., Trent, R.J., McCusker, E., Gomez-Tortosa, E., Mayo, D., Jones, R., Zanko, A., Nance, M., Abramson, R., Suchowersky, O., Paulsen, J., Harrison, M., Yang, Q., Cupples, L.A., Gusella, J.F., MacDonald, M.E. & Myers, R.H. Interaction of normal and expanded CAG repeat sizes influences age at onset of Huntington disease. *Am J Med Genet A* **119A**, 279-82 (2003).

76. Wexler, N.S., Lorimer, J., Porter, J., Gomez, F., Moskowitz, C., Shackell, E., Marder, K., Penchaszadeh, G., Roberts, S.A., Gayan, J., Brocklebank, D., Cherny,

S.S., Cardon, L.R., Gray, J., Dlouhy, S.R., Wiktorski, S., Hodes, M.E., Conneally, P.M., Penney, J.B., Gusella, J., Cha, J.H., Irizarry, M., Rosas, D., Hersch, S., Hollingsworth, Z., MacDonald, M., Young, A.B., Andresen, J.M., Housman, D.E., De Young, M.M., Bonilla, E., Stillings, T., Negrette, A., Snodgrass, S.R., Martinez-Jaurrieta, M.D., Ramos-Arroyo, M.A., Bickham, J., Ramos, J.S., Marshall, F., Shoulson, I., Rey, G.J., Feigin, A., Arnheim, N., Acevedo-Cruz, A., Acosta, L., Alvir, J., Fischbeck, K., Thompson, L.M., Young, A., Dure, L., O'Brien, C.J., Paulsen, J., Brickman, A., Krch, D., Peery, S., Hogarth, P., Higgins, D.S., Jr. & Landwehrmeyer, B. Venezuelan kindreds reveal that genetic and environmental factors modulate Huntington's disease age of onset. *Proc Natl Acad Sci U S A* **101**, 3498-503 (2004).

77. Gusella, J.F. & MacDonald, M.E. Huntington's disease: the case for genetic modifiers. *Genome Med* **1**, 80 (2009).

78. MacDonald, M.E., Vonsattel, J.P., Shrinidhi, J., Couropmitree, N.N., Cupples, L.A., Bird, E.D., Gusella, J.F. & Myers, R.H. Evidence for the GluR6 gene associated with younger onset age of Huntington's disease. *Neurology* **53**, 1330-2 (1999).

79. Rubinsztein, D.C., Leggo, J., Chiano, M., Dodge, A., Norbury, G., Rosser, E. & Craufurd, D. Genotypes at the GluR6 kainate receptor locus are associated with variation in the age of onset of Huntington disease. *Proc Natl Acad Sci U S A* **94**, 3872-6 (1997).

80. Andresen, J.M., Gayan, J., Cherny, S.S., Brocklebank, D., Alkorta-Aranburu, G., Addis, E.A., Cardon, L.R., Housman, D.E. & Wexler, N.S. Replication of twelve association studies for Huntington's disease residual age of onset in large Venezuelan kindreds. *J Med Genet* **44**, 44-50 (2007).

81. Coppede, F., Migheli, F., Ceravolo, R., Bregant, E., Rocchi, A., Petrozzi, L., Unti, E., Lonigro, R., Siciliano, G. & Migliore, L. The hOGG1 Ser326Cys polymorphism and Huntington's disease. *Toxicology* **278**, 199-203 (2010).

82. Kovtun, I.V., Liu, Y., Bjoras, M., Klungland, A., Wilson, S.H. & McMurray, C.T. OGG1 initiates age-dependent CAG trinucleotide expansion in somatic cells. *Nature* **447**, 447-52 (2007).

83. Hockly, E., Cordery, P.M., Woodman, B., Mahal, A., van Dellen, A., Blakemore, C., Lewis, C.M., Hannan, A.J. & Bates, G.P. Environmental enrichment slows

disease progression in R6/2 Huntington's disease mice. *Ann Neurol* **51**, 235-42 (2002).

84. Lazic, S.E., Grote, H.E., Blakemore, C., Hannan, A.J., van Dellen, A., Phillips, W. & Barker, R.A. Neurogenesis in the R6/1 transgenic mouse model of Huntington's disease: effects of environmental enrichment. *Eur J Neurosci* **23**, 1829-38 (2006).

85. van Dellen, A., Cordery, P.M., Spires, T.L., Blakemore, C. & Hannan, A.J. Wheel running from a juvenile age delays onset of specific motor deficits but does not alter protein aggregate density in a mouse model of Huntington's disease. *BMC Neurosci* **9**, 34 (2008).

86. Barde, Y.A. Neurotrophins: a family of proteins supporting the survival of neurons. *Prog Clin Biol Res* **390**, 45-56 (1994).

87. Bartrup, J.T., Moorman, J.M. & Newberry, N.R. BDNF enhances neuronal growth and synaptic activity in hippocampal cell cultures. *Neuroreport* **8**, 3791-4 (1997).

88. Bartzokis, G., Cummings, J., Perlman, S., Hance, D.B. & Mintz, J. Increased basal ganglia iron levels in Huntington disease. *Arch Neurol* **56**, 569-74 (1999).

89. Simmons, D.A., Casale, M., Alcon, B., Pham, N., Narayan, N. & Lynch, G. Ferritin Accumulation in Dystrophic Microglia is an Early Event in the Development of Huntington's Disease. *Glia* **55**, 1074-1084 (2007).

90. Chen, J.C., Hardy, P.A., Kucharczyk, W., Clauberg, M., Joshi, J.G., Vourlas, A., Dhar, M. & Henkelman, R.M. MR of human postmortem brain tissue: correlative study between T2 and assays of iron and ferritin in Parkinson and Huntington disease. *AJNR Am J Neuroradiol* **14**, 275-81 (1993).

91. Boll, M.C., Alcaraz-Zubeldia, M., Montes, S. & Rios, C. Free copper, ferroxidase and SOD1 activities, lipid peroxidation and NO(x) content in the CSF. A different marker profile in four neurodegenerative diseases. *Neurochem Res* **33**, 1717-23 (2008).

92. Hilditch-Maguire, P., Trettel, F., Passani, L.A., Auerbach, A., Persichetti, F. & MacDonald, M.E. Huntingtin: an iron-regulated protein essential for normal nuclear and perinuclear organelles. *Hum Mol Genet* **9**, 2789-97 (2000).

93. Rivera-Mancia, S., Perez-Neri, I., Rios, C., Tristan-Lopez, L., Rivera-Espinosa, L. & Montes, S. The transition metals copper and iron in neurodegenerative diseases. *Chem Biol Interact* **186**, 184-99 (2010).

94. Bartzokis, G., Lu, P.H., Tishler, T.A., Fong, S.M., Oluwadara, B., Finn, J.P., Huang, D., Bordelon, Y., Mintz, J. & Perlman, S. Myelin breakdown and iron changes in Huntington's disease: pathogenesis and treatment implications. *Neurochem Res* **32**, 1655-64 (2007).

95. Bartzokis, G. Age-related myelin breakdown: a developmental model of cognitive decline and Alzheimer's disease. *Neurobiol Aging* **25**, 5-18; author reply 49-62 (2004).

96. Myers, R.H., Vonsattel, J.P., Paskevich, P.A., Kiely, D.K., Stevens, T.J., Cupples, L.A., Richardson, E.P., Jr. & Bird, E.D. Decreased neuronal and increased oligodendroglial densities in Huntington's disease caudate nucleus. *J Neuropathol Exp Neurol* **50**, 729-42 (1991).

97. Gu, M., Gash, M.T., Mann, V.M., Javoy-Agid, F., Cooper, J.M. & Schapira, A.H. Mitochondrial defect in Huntington's disease caudate nucleus. *Ann Neurol* **39**, 385-9 (1996).

98. Browne, S.E., Bowling, A.C., MacGarvey, U., Baik, M.J., Berger, S.C., Muqit, M.M., Bird, E.D. & Beal, M.F. Oxidative damage and metabolic dysfunction in Huntington's disease: selective vulnerability of the basal ganglia. *Ann Neurol* **41**, 646-53 (1997).

99. Lind, M.I., Missirlis, F., Melefors, O., Uhrigshardt, H., Kirby, K., Phillips, J.P., Soderhall, K. & Rouault, T.A. Of two cytosolic aconitases expressed in Drosophila, only one functions as an iron-regulatory protein. *J Biol Chem* **281**, 18707-14 (2006).

100. Ward, R.J., Kuhn, L.C., Kaldy, P., Florence, A., Peters, T.J. & Crichton, R.R. Control of cellular iron homeostasis by iron-responsive elements in vivo. *Eur J Biochem* **220**, 927-31 (1994).

101. Hausladen, A. & Fridovich, I. Superoxide and peroxynitrite inactivate aconitases, but nitric oxide does not. *J Biol Chem* **269**, 29405-8 (1994).

102. Tabrizi, S.J., Cleeter, M.W., Xuereb, J., Taanman, J.W., Cooper, J.M. & Schapira, A.H. Biochemical abnormalities and excitotoxicity in Huntington's disease brain. *Ann Neurol* **45**, 25-32 (1999).

103. Loeffler, D.A., LeWitt, P.A., Juneau, P.L., Sima, A.A., Nguyen, H.U., DeMaggio, A.J., Brickman, C.M., Brewer, G.J., Dick, R.D., Troyer, M.D. & Kanaley, L. Increased regional brain concentrations of ceruloplasmin in neurodegenerative disorders. *Brain Res* **738**, 265-74 (1996).

104. Chiang, M.C., Chen, H.M., Lee, Y.H., Chang, H.H., Wu, Y.C., Soong, B.W., Chen, C.M., Wu, Y.R., Liu, C.S., Niu, D.M., Wu, J.Y., Chen, Y.T. & Chern, Y. Dysregulation of C/EBPalpha by mutant Huntingtin causes the urea cycle deficiency in Huntington's disease. *Hum Mol Genet* **16**, 483-98 (2007).

105. Carter, C.J. Glutamine synthetase activity in Huntington's disease. *Life Sci* **31**, 1151-9 (1982).

106. Andreassen, O.A., Dedeoglu, A., Friedlich, A., Ferrante, K.L., Hughes, D., Szabo, C. & Beal, M.F. Effects of an inhibitor of poly(ADP-ribose) polymerase, desmethylselegiline, trientine, and lipoic acid in transgenic ALS mice. *Exp Neurol* **168**, 419-24 (2001).

107. Hurlbert, M.S., Zhou, W., Wasmeier, C., Kaddis, F.G., Hutton, J.C. & Freed, C.R. Mice transgenic for an expanded CAG repeat in the Huntington's disease gene develop diabetes. *Diabetes* **48**, 649-51 (1999).

108. Josefsen, K., Nielsen, M.D., Jorgensen, K.H., Bock, T., Norremolle, A., Sorensen, S.A., Naver, B. & Hasholt, L. Impaired glucose tolerance in the R6/1 transgenic mouse model of Huntington's disease. *J Neuroendocrinol* **20**, 165-72 (2008).

109. Andreassen, O.A., Ferrante, R.J., Dedeoglu, A., Albers, D.W., Klivenyi, P., Carlson, E.J., Epstein, C.J. & Beal, M.F. Mice with a partial deficiency of manganese superoxide dismutase show increased vulnerability to the mitochondrial toxins malonate, 3-nitropropionic acid, and MPTP. *Exp Neurol* **167**, 189-95 (2001).

110. van Dellen, A., Grote, H.E. & Hannan, A.J. Gene-environment interactions, neuronal dysfunction and pathological plasticity in Huntington's disease. *Clin Exp Pharmacol Physiol* **32**, 1007-19 (2005).

111. Friedman, J.H., Trieschmann, M.E., Myers, R.H. & Fernandez, H.H. Monozygotic twins discordant for Huntington disease after 7 years. *Arch Neurol* **62**, 995-7 (2005).

112. Garcia, M., Vanhoutte, P., Pages, C., Besson, M.J., Brouillet, E. & Caboche, J. The mitochondrial toxin 3-nitropropionic acid induces striatal neurodegeneration via a c-Jun N-terminal kinase/c-Jun module. *J Neurosci* **22**, 2174-84 (2002).

113. Milakovic, T. & Johnson, G.V. Mitochondrial respiration and ATP production are significantly impaired in striatal cells expressing mutant huntingtin. *J Biol Chem* **280**, 30773-82 (2005).

114. Trettel, F., Rigamonti, D., Hilditch-Maguire, P., Wheeler, V.C., Sharp, A.H., Persichetti, F., Cattaneo, E. & MacDonald, M.E. Dominant phenotypes produced by the HD mutation in STHdh(Q111) striatal cells. *Hum Mol Genet* **9**, 2799-809 (2000).

115. Gines, S., Ivanova, E., Seong, I.S., Saura, C.A. & MacDonald, M.E. Enhanced Akt signaling is an early pro-survival response that reflects N-methyl-D-aspartate receptor activation in Huntington's disease knock-in striatal cells. *J Biol Chem* **278**, 50514-22 (2003).

116. Dodd, C.A., Ward, D.L. & Klein, B.G. Basal Ganglia accumulation and motor assessment following manganese chloride exposure in the C57BL/6 mouse. *Int J Toxicol* **24**, 389-97 (2005).

117. Erikson, K.M., Syversen, T., Aschner, J. & Aschner, M. Interactions between excessive manganese-exposure and dietary iron-deficiency in neurodegeneration. *Environ. Toxicology and Pharmacology* **19**, 415-421 (2005).

118. Erikson, K.M. & Aschner, M. Manganese neurotoxicity and glutamate-GABA interaction. *Neurochem Int* **43**, 475-80 (2003).

119. Hurley, L.S. & Keen, C.L. Manganese. in *Trace elements in human health and animal nutrition* (eds. Underwood, E. & Mertz, W.) 185-225 (Academic Press, New York, 1987).

120. Liao, S.L. & Chen, C.J. Manganese stimulates stellation of cultured rat cortical astrocytes. *Neuroreport* **12**, 3877-81 (2001).

121. Keen, C.L., Ensunsa, J.L., Watson, M.H., Baly, D.L., Donovan, S.M., Monaco, M.H. & Clegg, M.S. Nutritional aspects of manganese from experimental studies. *Neurotoxicology* **20**, 213-23 (1999).

122. Aschner, M., Shanker, G., Erikson, K., Yang, J. & Mutkus, L.A. The uptake of manganese in brain endothelial cultures. *Neurotoxicology* **23**, 165-8 (2002).

123. Aschner, M., Guilarte, T.R., Schneider, J.S. & Zheng, W. Manganese: recent advances in understanding its transport and neurotoxicity. *Toxicol Appl Pharmacol* **221**, 131-47 (2007).

124. Prohaska, J.R. Functions of trace elements in brain metabolism. *Physiol Rev* **67**, 858-901 (1987).

125. Bowman, A.B., Erikson, K.M. & Aschner, M. Manganese - The two faces of essentiality and neurotoxicity. in *Metals and Neurodegeneration* (ed. Huang, S.) (Research Signpost, Kerala, India, 2010).

126. Morello, M., Canini, A., Mattioli, P., Sorge, R.P., Alimonti, A., Bocca, B., Forte, G., Martorana, A., Bernardi, G. & Sancesario, G. Sub-cellular localization of manganese in the basal ganglia of normal and manganese-treated rats An electron spectroscopy imaging and electron energy-loss spectroscopy study. *Neurotoxicology* **29**, 60-72 (2008).

127. Liccione, J.J. & Maines, M.D. Manganese-mediated increase in the rat brain mitochondrial cytochrome P-450 and drug metabolism activity: susceptibility of the striatum. *J Pharmacol Exp Ther* **248**, 222-8 (1989).

128. Finkelstein, Y., Milatovic, D. & Aschner, M. Modulation of cholinergic systems by manganese. *Neurotoxicology* **28**, 1003-14 (2007).

129. Aschner, M. & Aschner, J.L. Manganese neurotoxicity: cellular effects and blood-brain barrier transport. *Neurosci Biobehav Rev* **15**, 333-40 (1991).

130. USEPA. Health assessment document for manganese. (ed. agency, U.S.e.p.) (EPA, Cincinnati, 1984).

131. Tran, T.T., Chowanadisai, W., Crinella, F.M., Chicz-DeMet, A. & Lonnerdal, B. Effect of high dietary manganese intake of neonatal rats on tissue mineral

accumulation, striatal dopamine levels, and neurodevelopmental status. *Neurotoxicology* **23**, 635-43 (2002).

132. Seth, P.K. & Chandra, S.V. Neurotransmitters and neurotransmitter receptors in developing and adult rats during manganese poisoning. *Neurotoxicology* **5**, 67-76 (1984).

133. Erikson, K.M., Shihabi, Z.K., Aschner, J.L. & Aschner, M. Manganese accumulates in iron-deficient rat brain regions in a heterogeneous fashion and is associated with neurochemical alterations. *Biol Trace Elem Res* **87**, 143-56 (2002).

134. Takeda, A. Manganese action in brain function. *Brain Res Brain Res Rev* **41**, 79-87 (2003).

135. Christianson, D.W. Structural chemistry and biology of manganese mettaloenzymes. *Biophys Mol Biol* **67**, 217-52 (1997).

136. Wedler, F.C. & Denman, R.B. Glutamine synthetase: the major Mn(II) enzyme in mammalian brain. *Curr Top Cell Regul* **24**, 153-69 (1984).

137. Maciejewski, P.K. & Rothman, D.L. Proposed cycles for functional glutamate trafficking in synaptic neurotransmission. *Neurochem Int* **52**, 809-25 (2008).

138. Eid, T., Williamson, A., Lee, T.S., Petroff, O.A. & de Lanerolle, N.C. Glutamate and astrocytes--key players in human mesial temporal lobe epilepsy? *Epilepsia* **49 Suppl 2**, 42-52 (2008).

139. Ash, D.E., Cox, J.D. & Christianson, D.W. Arginase: a binuclear manganese metalloenzyme. *Met Ions Biol Syst* **37**, 407-28 (2000).

140. Estevez, A.G., Sahawneh, M.A., Lange, P.S., Bae, N., Egea, M. & Ratan, R.R. Arginase 1 regulation of nitric oxide production is key to survival of trophic factor-deprived motor neurons. *J Neurosci* **26**, 8512-6 (2006).

141. Mildvan, A.S., Scrutton, M.C. & Utter, M.F. Pyruvate carboxylase. VII. A possible role for tightly bound manganese. *J Biol Chem* **241**, 3488-98 (1966).

142. Scrutton, M.C., Utter, M.F. & Mildvan, A.S. Pyruvate carboxylase. VI. The presence of tightly bound manganese. *J Biol Chem* **241**, 3480-7 (1966).

143. Zwingmann, C., Leibfritz, D. & Hazell, A.S. Energy metabolism in astrocytes and neurons treated with manganese: relation among cell-specific energy failure, glucose metabolism, and intercellular trafficking using multinuclear NMR-spectroscopic analysis. *J Cereb Blood Flow Metab* **23**, 756-71 (2003).

144. Yu, A.C., Drejer, J., Hertz, L. & Schousboe, A. Pyruvate carboxylase activity in primary cultures of astrocytes and neurons. *J Neurochem* **41**, 1484-7 (1983).

145. Fong, N.M., Jensen, T.C., Shah, A.S., Parekh, N.N., Saltiel, A.R. & Brady, M.J. Identification of binding sites on protein targeting to glycogen for enzymes of glycogen metabolism. *J Biol Chem* **275**, 35034-9 (2000).

146. Greenberg, D.M. & Campbell, W.W. Studies in Mineral Metabolism with the Aid of Induced Radioactive Isotopes: IV-Manganese. *Proc Natl Acad Sci U S A* **26**, 448-52 (1940).

147. Pollack, S., George, J.N., Reba, R.C., Kaufman, R.M. & Crosby, W.H. The Absorption of Nonferrous Metals in Iron Deficiency. *J Clin Invest* **44**, 1470-3 (1965).

148. Klaassen, C.D. Biliary excretion of manganese in rats, rabbits, and dogs. *Toxicol Appl Pharmacol* **29**, 458-68 (1974).

149. Foradori, A.C., Bertinchamps, A., Gulibon, J.M. & Cotzias, G.C. The discrimination between magnesium and manganese by serum proteins. *J Gen Physiol* **50**, 2255-66 (1967).

150. Cotzias, G.C., Borg, D.C. & Bertinchamps, A. Clincal experiences with manganese. in *Metal binding in medicine* (eds. Seven, M.J. & Johnson, L.A.) 50-57 (Lippincott Co, Philadelphia, 1960).

151. Scheuhammer, A.M. & Cherian, M.G. The influence of manganese on the distribution of essential trace elements. II. The tissue distribution of manganese, magnesium, zinc, iron, and copper in rats after chronic manganese exposure. *J Toxicol Environ Health* **12**, 361-70 (1983).

152. Scheuhammer, A.M. & Cherian, M.G. Binding of manganese in human and rat plasma. *Biochim Biophys Acta* **840**, 163-9 (1985).

153. Mena, I., Honuchi, K. & Lopez, G. Factors enhancing entrance of manganese into brain iron deficiency and age. *J. Nucl Med* **15**(1974).

154. Rabin, O., Hegedus, L., Bourre, J.M. & Smith, Q.R. Rapid brain uptake of manganese(II) across the blood-brain barrier. *J Neurochem* **61**, 509-17 (1993).

155. Murphy, V.A., Wadhwani, K.C., Smith, Q.R. & Rapoport, S.I. Saturable transport of manganese(II) across the rat blood-brain barrier. *J Neurochem* **57**, 948-54 (1991).

156. Aschner, M. & Gannon, M. Manganese (Mn) transport across the rat blood-brain barrier: saturable and transferrin-dependent transport mechanisms. *Brain Res Bull* **33**, 345-9 (1994).

157. Gunshin, H., Mackenzie, B., Berger, U.V., Gunshin, Y., Romero, M.F., Boron, W.F., Nussberger, S., Gollan, J.L. & Hediger, M.A. Cloning and characterization of a mammalian proton-coupled metal-ion transporter. *Nature* **388**, 482-8 (1997).

158. Garrick, M.D., Dolan, K.G., Horbinski, C., Ghio, A.J., Higgins, D., Porubcin, M., Moore, E.G., Hainsworth, L.N., Umbreit, J.N., Conrad, M.E., Feng, L., Lis, A., Roth, J.A., Singleton, S. & Garrick, L.M. DMT1: a mammalian transporter for multiple metals. *Biometals* **16**, 41-54 (2003).

159. Mackenzie, B. & Hediger, M.A. SLC11 family of H+-coupled metal-ion transporters NRAMP1 and DMT1. *Pflugers Arch* **447**, 571-9 (2004).

160. Forbes, J.R. & Gros, P. Iron, manganese, and cobalt transport by Nramp1 (Slc11a1) and Nramp2 (Slc11a2) expressed at the plasma membrane. *Blood* **102**, 1884-92 (2003).

161. Au, C., Benedetto, A. & Aschner, M. Manganese transport in eukaryotes: the role of DMT1. *Neurotoxicology* **29**, 569-76 (2008).

162. Su, M.A., Trenor, C.C., Fleming, J.C., Fleming, M.D. & Andrews, N.C. The G185R mutation disrupts function of the iron transporter Nramp2. *Blood* **92**, 2157-63 (1998).

163. Fleming, M.D., Romano, M.A., Su, M.A., Garrick, L.M., Garrick, M.D. & Andrews, N.C. Nramp2 is mutated in the anemic Belgrade (b) rat: evidence of a role for Nramp2 in endosomal iron transport. *Proc Natl Acad Sci U S A* **95**, 1148-53 (1998).

164. Fleming, M.D., Trenor, C.C., 3rd, Su, M.A., Foernzler, D., Beier, D.R., Dietrich, W.F. & Andrews, N.C. Microcytic anaemia mice have a mutation in Nramp2, a candidate iron transporter gene. *Nat Genet* **16**, 383-6 (1997).

165. Fitsanakis, V.A., Zhang, N., Anderson, J.G., Erikson, K.M., Avison, M.J., Gore, J.C. & Aschner, M. Measuring brain manganese and iron accumulation in rats following 14 weeks of low-dose manganese treatment using atomic absorption spectroscopy and magnetic resonance imaging. *Toxicol Sci* **103**, 116-24 (2008).

166. Fitsanakis, V.A., Piccola, G., Aschner, J.L. & Aschner, M. Characteristics of manganese (Mn) transport in rat brain endothelial (RBE4) cells, an in vitro model of the blood-brain barrier. *Neurotoxicology* **27**, 60-70 (2006).

167. Fitsanakis, V.A., Piccola, G., Aschner, J.L. & Aschner, M. Manganese transport by rat brain endothelial (RBE4) cell-based transwell model in the presence of astrocyte conditioned media. *J Neurosci Res* **81**, 235-43 (2005).

168. Fitsanakis, V.A., Piccola, G., Marreilha dos Santos, A.P., Aschner, J.L. & Aschner, M. Putative proteins involved in manganese transport across the blood-brain barrier. *Hum Exp Toxicol* **26**, 295-302 (2007).

169. Dickinson, T.K., Devenyi, A.G. & Connor, J.R. Distribution of injected iron 59 and manganese 54 in hypotransferrinemic mice. *J Lab Clin Med* **128**, 270-8 (1996).

170. Trenor, C.C., 3rd, Campagna, D.R., Sellers, V.M., Andrews, N.C. & Fleming, M.D. The molecular defect in hypotransferrinemic mice. *Blood* **96**, 1113-8 (2000).

171. Morris, C.M., Candy, J.M., Oakley, A.E., Taylor, G.A., Mountfort, S., Bishop, H., Ward, M.K., Bloxham, C.A. & Edwardson, J.A. Comparison of the regional distribution of transferrin receptors and aluminium in the forebrain of chronic renal dialysis patients. *J Neurol Sci* **94**, 295-306 (1989).

172. Hill, J.M., Ruff, M.R., Weber, R.J. & Pert, C.B. Transferrin receptors in rat brain: neuropeptide-like pattern and relationship to iron distribution. *Proc Natl Acad Sci U S A* **82**, 4553-7 (1985).

173. Mash, D.C., Pablo, J., Flynn, D.D., Efange, S.M. & Weiner, W.J. Characterization and distribution of transferrin receptors in the rat brain. *J Neurochem* **55**, 1972-9 (1990).

174. Fujishiro, H., Doi, M., Enomoto, S. & Himeno, S. High sensitivity of RBL-2H3 cells to cadmium and manganese: an implication of the role of ZIP8. *Metallomics* (2011).

175. Himeno, S., Yanagiya, T. & Fujishiro, H. The role of zinc transporters in cadmium and manganese transport in mammalian cells. *Biochimie* **91**, 1218-22 (2009).

176. He, L., Girijashanker, K., Dalton, T.P., Reed, J., Li, H., Soleimani, M. & Nebert, D.W. ZIP8, member of the solute-carrier-39 (SLC39) metal-transporter family: characterization of transporter properties. *Mol Pharmacol* **70**, 171-80 (2006).

177. Girijashanker, K., He, L., Soleimani, M., Reed, J.M., Li, H., Liu, Z., Wang, B., Dalton, T.P. & Nebert, D.W. Slc39a14 gene encodes ZIP14, a metal/bicarbonate symporter: similarities to the ZIP8 transporter. *Mol Pharmacol* **73**, 1413-23 (2008).

178. Lucaciu, C.M., Dragu, C., Copaescu, L. & Morariu, V.V. Manganese transport through human erythrocyte membranes. An EPR study. *Biochim Biophys Acta* **1328**, 90-8 (1997).

179. Riccio, A., Mattei, C., Kelsell, R.E., Medhurst, A.D., Calver, A.R., Randall, A.D., Davis, J.B., Benham, C.D. & Pangalos, M.N. Cloning and functional expression of human short TRP7, a candidate protein for store-operated Ca2+ influx. *J Biol Chem* **277**, 12302-9 (2002).

180. Kannurpatti, S.S., Joshi, P.G. & Joshi, N.B. Calcium sequestering ability of mitochondria modulates influx of calcium through glutamate receptor channel. *Neurochem Res* **25**, 1527-36 (2000).

181. Goytain, A., Hines, R.M. & Quamme, G.A. Huntingtin-interacting proteins, HIP14 and HIP14L, mediate dual functions, palmitoyl acyltransferase and Mg2+ transport. *J Biol Chem* **283**, 33365-74 (2008).

182. Gitler, A.D., Chesi, A., Geddie, M.L., Strathearn, K.E., Hamamichi, S., Hill, K.J., Caldwell, K.A., Caldwell, G.A., Cooper, A.A., Rochet, J.C. & Lindquist, S. Alpha-synuclein is part of a diverse and highly conserved interaction network that includes PARK9 and manganese toxicity. *Nat Genet* **41**, 308-15 (2009).

183. Huang, K., Yanai, A., Kang, R., Arstikaitis, P., Singaraja, R.R., Metzler, M., Mullard, A., Haigh, B., Gauthier-Campbell, C., Gutekunst, C.A., Hayden, M.R. & El-Husseini, A. Huntingtin-interacting protein HIP14 is a palmitoyl transferase involved in palmitoylation and trafficking of multiple neuronal proteins. *Neuron* **44**, 977-86 (2004).

184. Ohyama, T., Verstreken, P., Ly, C.V., Rosenmund, T., Rajan, A., Tien, A.C., Haueter, C., Schulze, K.L. & Bellen, H.J. Huntingtin-interacting protein 14, a palmitoyl transferase required for exocytosis and targeting of CSP to synaptic vesicles. *J Cell Biol* **179**, 1481-96 (2007).

185. Singaraja, R.R., Hadano, S., Metzler, M., Givan, S., Wellington, C.L., Warby, S., Yanai, A., Gutekunst, C.A., Leavitt, B.R., Yi, H., Fichter, K., Gan, L., McCutcheon, K., Chopra, V., Michel, J., Hersch, S.M., Ikeda, J.E. & Hayden, M.R. HIP14, a novel ankyrin domain-containing protein, links huntingtin to intracellular trafficking and endocytosis. *Hum Mol Genet* **11**, 2815-28 (2002).

186. Stowers, R.S. & Isacoff, E.Y. Drosophila huntingtin-interacting protein 14 is a presynaptic protein required for photoreceptor synaptic transmission and expression of the palmitoylated proteins synaptosome-associated protein 25 and cysteine string protein. *J Neurosci* **27**, 12874-83 (2007).

187. Ramirez, A., Heimbach, A., Grundemann, J., Stiller, B., Hampshire, D., Cid, L.P., Goebel, I., Mubaidin, A.F., Wriekat, A.L., Roeper, J., Al-Din, A., Hillmer, A.M., Karsak, M., Liss, B., Woods, C.G., Behrens, M.I. & Kubisch, C. Hereditary parkinsonism with dementia is caused by mutations in ATP13A2, encoding a lysosomal type 5 P-type ATPase. *Nat Genet* **38**, 1184-91 (2006).

188. Lorkovic, H. & Feyrer, A. Manganese ions inhibit acetylcholine receptor synthesis in cultured mouse soleus muscles. *Neurosci Lett* **51**, 331-5 (1984).

189. King, R.G., Sharp, J.A. & Boura, A.L. The effects of Al3+, Cd2+ and Mn2+ on human erythrocyte choline transport. *Biochem Pharmacol* **32**, 3611-7 (1983).

190. Lockman, P.R., Roder, K.E. & Allen, D.D. Inhibition of the rat blood-brain barrier choline transporter by manganese chloride. *J Neurochem* **79**, 588-94 (2001).

191. Xiang, Z. & Burnstock, G. Expression of P2X receptors in rat choroid plexus. *Neuroreport* **16**, 903-7 (2005).

192. North, R.A. Molecular physiology of P2X receptors. *Physiol Rev* **82**, 1013-67 (2002).

193. Tanaka, N., Kawasaki, K., Nejime, N., Kubota, Y., Nakamura, K., Kunitomo, M., Takahashi, K., Hashimoto, M. & Shinozuka, K. P2Y receptor-mediated Ca(2+) signaling increases human vascular endothelial cell permeability. *J Pharmacol Sci* **95**, 174-80 (2004).

194. Crossgrove, J.S., Allen, D.D., Bukaveckas, B.L., Rhineheimer, S.S. & Yokel, R.A. Manganese distribution across the blood-brain barrier. I. Evidence for carrier-mediated influx of managanese citrate as well as manganese and manganese transferrin. *Neurotoxicology* **24**, 3-13 (2003).

195. Gunter, T.E. & Puskin, J.S. Manganous ion as a spin label in studies of mitochondrial uptake of manganese. *Biophys J.* , 625-35 (1972).

196. Liccione, J.J. & Maines, M.D. Selective vulnerability of glutathione metabolism and cellular defense mechanisms in rat striatum to manganese. *J Pharmacol Exp Ther* **247**, 156-61 (1988).

197. Gavin, C.E., Gunter, K.K. & Gunter, T.E. Manganese and calcium transport in mitochondria: implications for manganese toxicity. *Neurotoxicology* **20**, 445-53 (1999).

198. Kalia, K., Jiang, W. & Zheng, W. Manganese accumulates primarily in nuclei of cultured brain cells. *Neurotoxicology* **29**, 466-70 (2008).

199. Suzuki, H., Wada, O., Inoue, K., Tosaka, H. & Ono, T. Role of brain lysosomes in the development of manganese toxicity in mice. *Toxicol Appl Pharmacol* **71**, 422-9 (1983).

200. Yin, Z., Jiang, H., Lee, E.Y., Ni, M., Erikson, K.M., Milatovic, D., Bowman, A.B. & Aschner, M. Ferroportin is a manganese-responsive protein that decreases manganese cytotoxicity and accumulation. *J Neurochem.* **112**, 1190–1198. (2011).

201. Stupar J, Doolinsek F, Simicic J, Bizjak M & B., B. Trace element analysis of the hair of duke mirko petrovic-njegos – a possible means of clarification of his death. *Trace Elements and Electrolytes* **22**, 118-126 (2005).

202. Dale Marcy, A. & Drake, P.L. Development of a field method for measuring manganese in welding fume. *J Environ Monit* **9**, 1199-204 (2007).

203. Jarvis, K.E., Gray, A.L. & Houk, R.S. *Handbook of inductively coupled plasma mass spectrometry*, (Chapman and Hall, New York, 1992).

CHAPTER II

DEVELOPMENT OF A NOVEL HIGH-THROUGHPUT ASSAY TO ASSESS CELLULAR MANGANESE LEVELS AND TRANSPORT DYNAMICS[†]

Introduction

Manganese (Mn) is an essential ubiquitous trace element required for normal growth, development and cellular homeostasis[1]. In humans and animals, Mn functions as a required cofactor of several enzymes necessary for neuronal and glial cell function, as well as enzymes involved in neurotransmitter synthesis and metabolism[2-4]. Despite its essentiality in multiple metabolic functions, excessive levels of Mn exposure via occupational routes such as farmers exposed to Mn-based pesticides, industrial welders and miners[5-7], and dietary intake, which include high concentrations of Mn in drinking water and long-term parenteral nutrition[8], can accumulate in the brain and have been associated with dysfunction of the basal ganglia system[9]. We have previously reported decreased net Mn accumulation in a mutant ST*Hdh*$^{Q111/Q111}$ cell line model of Huntington's disease (HD) relative to wild-type ST*Hdh*$^{Q7/Q7}$ cells by GFAAS[10,11]. Given

[†] The contents of this chapter were first published as:
Gunnar F. Kwakye, Daphne Li, and Aaron B. Bowman. **Novel high-throughput assay to assess cellular manganese levels in a striatal cell line model of Huntington's disease confirms a deficit in manganese accumulation.** Neurotoxicology (2011) PMID 21238486.
Gunnar F. Kwakye, Daphne Li, Olympia Kabobel, and Aaron B. Bowman. **Cellular fura-2 Manganese Extraction Assay (CFMEA)**. Curr Protoc Toxicol Chapter 12: Unit 12:18 (2011) PMID 21553393**.**

the decreased net Mn uptake in both cellular and mouse models of HD following Mn exposure, we sought to decipher the transport mechanism underlying the decreased net Mn accumulation in mutant ST*Hdh*$^{Q111/Q111}$ cells.

Development of cellular fura-2 manganese extraction assay (CFMEA)

Available methods to measure Mn levels in cultured cells and tissues include GFAAS, radioactive trace assays and inductively coupled plasma mass spectrometry (ICP-MS). Although these techniques include multi-elemental analysis, excellent specificity, extremely high sensitivity and limited chemical interference, they are not feasible to assess Mn transport kinetics in a high-throughput manner. This is mainly due to the large number of cells required, duration of experimental analysis, and cost of analysis. Therefore, we sought to develop a high-throughput assay that enables rapid and efficient assessment of Mn transport kinetics and mechanism underlying the Mn accumulation deficit in mutant ST*Hdh* cells. After a literature search aimed at guiding the development of the high-throughput Mn assessment assay, we were intrigued by the relationship between Mn and the ratiometric calcium fluorophore fura-2, specifically, the Mn quenching properties of fura-2.

The development and utilization of the fluorescent calcium (Ca^{2+}) indicator, fura-2, by R.Y. Tsien and colleagues for both the determination of intracellular Ca^{2+} concentrations and its regulation by extracellular stimuli has improved our understanding of calcium signaling events and dysfunction in neurodegenerative diseases, including

HD[12-17]. Fura-2 is the most commonly used 1,2-bis (o-aminophenoxy) ethane-N,N,N',N'-tetraacetic acid (BAPTA) based metal-binding fluorophore for microscopy of individual loaded cells. The spectral properties of these fluorophores change upon binding to Ca^{2+} ions and are modeled after the octacoordinate binding sites of the Ca^{2+} selective chelator ethylene glycol tetraacetic acid (EGTA). In comparison to other Ca^{2+} indicators such as quin-2, fura-2 has a larger fluorophore that slightly increases its wavelengths and makes it compatible with glass microscope optics[18]. Upon Ca^{2+} binding to fura-2, the excitation spectrum shifts about 30 nm to shorter wavelengths. Hence, the ratiometric fluorescence intensity measurements obtained from the $F_{340/380}$ nm excitation pair (ratio of fluorescence yield following excitation at 340 nm over excitation at 380 nm) is considered to be a good measure of intracellular calcium concentration, and is unperturbed by variable dye content or cell thickness[12]. The green emission of fura-2 does not usually shift with calcium binding and peaks between 505 – 520 nm[19].

Published data examining the influence of metal ions on fura-2 suggest an interaction between endogenous metal ions and fura-2 loaded cells by either quenching (Mn^{2+}, Cu^{2+}, Fe^{2+}) or increasing (Zn^{2+}, Cd^{2+}) fura-2 fluorescence[12,20]. Consequently, other studies have utilized fluorescence quenching assays to assess intracellular metal ion concentration and transport in loaded cells and demonstrated a rapid and time-dependent quenching of fura-2 and calcein fluorescence following Mn^{2+}, Fe^{2+}, Co^{2+}, and Cu^{2+} exposure[12,20-24]. However, all these studies were conducted on single cultured cells, which limit high-throughput measurements of Mn levels. We reasoned that a high-throughput manganese extraction based fura-2 assay might enable efficient and accurate measurements of Mn levels in cultured cells and allow for assessment of Mn dynamics in

cellular models. Importantly, fura-2 has a Ca^{2+} isosbestic point at 360 nm, a wavelength at which fura-2 fluorescence emission properties are independent of Ca^{2+} concentration. Interestingly, Snitsarev and colleagues reported that Mn^{2+} effectively quenches fura-2 fluorescence, even at the Ca^{2+} isosbestic wavelength[20].

Development of quantitative PicoGreen assay for normalization of extracted cellular manganese levels to dsDNA

Protein detection methods (for example, Lowry and Bradford assays) have been extensively used to measure protein levels in cultured cells and animal tissues. However, their sensitivity and accuracy depends on the number of cells required for minimum detection, and are influenced by interfering agents (e.g. detergents and amino acid concentrations). Unfortunately, some cultured cells do not possess sufficient cell density in the 96 well plate format to be detected by these traditional protein assays. Quant-iT™ PicoGreen dsDNA reagent is an ultrasensitive asymmetrical fluorescent nucleic acid dye that has previously been used to quantify the concentration of dsDNA in solution[29-31]. The free dye fluoresces upon binding to dsDNA, but not RNA. Thus, alterations in RNA levels in cultured cells do not influence the sensitivity of the PicoGreen assay. Quant-iT™ PicoGreen reagent is capable of quantifying at least 25 pg/mL dsDNA with a standard fluorometric plate reader[32]. The long stability of PicoGreen to photobleaching enables longer exposure times and assay flexibility[30]. We have modified and utilized the Quant-iT™ PicoGreen dsDNA assay to measure dsDNA in cell-extracts following $MnCl_2$ exposure. This method enables normalization of extracted cellular Mn concentration to

dsDNA levels in cell-extracts following $MnCl_2$ exposure. In essence, the aim of the study was to determine if a cellular fura-2 manganese extraction assay (CFMEA) could accurately measure Mn content in $MnCl_2$ exposed striatal cells.

Materials and Methods

Chemicals, reagents, and cell culture supplies

Cell culture media and supplements were obtained from Mediatech (Manassas, VA) unless indicated. Cell lines were grown in Dulbecco's modified Eagle's medium (DMEM) with 10% fetal bovine serum (Atlanta Biologicals, Lawrenceville, GA, and Sigma, St. Louis, MO), L-glutamine, 400μg/ml G418 and Penicillin-Streptomycin. Calcium (II) chloride dihydrate ($CaCl_2 . 2H_2O$), cadmium (II) chloride heptahydrate ($CdCl_2 . 7H_2O$), cobalt (II) chloride hexahydrate ($CoCl_2 . 6H_2O$), copper (II) chloride dihydrate ($CuCl_2 . 2H_2O$), iron (II) chloride ($FeCl_2$), magnesium (II) chloride tetrahydrate ($MgCl_2 . 4H_2O$), manganese (II) chloride heptahydrate ($MnCl_2 . 7H_2O$), nickel (II) chloride hexahydrate ($NiCl_2 . 6H_2O$), lead (II) chloride ($PbCl_2$), zinc (II) chloride ($ZnCl_2$) were from Alfa Aesar (Ward Hill, MA). Ultra-pure fura-2 salt (cell-impermeable, ENZ-52007) was obtained from ENZO Biochem (New York, NY). The HEPES salt exposure buffer consisted of 25mM HEPES buffer (pH 7.2), 140mM NaCl, 5.4mM KCl, and 5mM D-glucose (Sigma). 1X ultra-pure phosphate-buffered saline (PBS), pH 7.4, without calcium and magnesium was used for post Mn exposure washes. Triton X-100 and sodium dodecyl sulfate (SDS) were obtained from Sigma.

Deoxyribonucleic acid sodium salt from salmon testes (Catalog # D1626) was obtained from Sigma (St. Louis, MO). Quant-iT™ PicoGreen dsDNA Reagent (Catalog # P7589) was obtained from Molecular Probes (Carlsbad, CA). 1x TE buffer used for the dilution of PicoGreen reagent was composed of 1 M Tris-HCl (pH 7.5) and 0.5 M EDTA (pH 8.0) prepared with DNase-free water and pH adjusted to 7.5.

Cell-free fura-2 assays

Cell-free system was composed of the indicated stock metal ions and fura-2 in either PBS with 0.1% Triton X-100 (PTx) or PBS with 0.8% SDS and assayed in a clear 96-well assay plate. After 5 seconds orbital shake, fura-2 fluorescence was measured at the Ca^{2+} isosbestic point of Ex_{360} (bandwidth of filter = ± 35 nm) and Em_{535} (bandwidth of filter = ± 25 nm) with a Beckman coulter DTX 880 multimode plate reader using multimode analysis software (version 3.2.0.6) and top read settings.

Saturation binding curve and mathematical modeling of Mn-fura-2 interaction

Saturation binding curve experiments were performed using a ten point Mn-fura-2 curve with samples containing 1 µL of different 100X stock Mn standards (0 – 100 mM) added to 99 µL of 0.5 µM fura-2 in PTx and assayed in a clear 96-well assay as described in the cell-free fura-2 assays section. The average raw fluorescence signal values (RFU) of the 0 µM Mn samples within each independent standard curve were defined as the

100% maximal fluorescence for that experiment after background subtraction. RFU of each well were then normalized as percent maximal fluorescence ($\%_{MAX}$) to this value. A one-site specific saturation-binding curve with Hill slope could be fit to $\log_{10}$ Mn concentration (x-axis) and either $\%_{MAX}$ (y-axis) or RFU (y-axis) by non-linear regression analysis using graphpad prism software (version 5.0b). As utilization of $\%_{MAX}$ rather than RFU was found to control better for the experimental variation, we preferred use of $\%_{MAX}$ for experimental determination of extracted Mn concentrations. To permit back calculations of extracted Mn levels from experimentally determined $\%_{MAX}$ values we used the trend line command in Microsoft Excel to fit power (Mn concentration = $A\bullet(\%_{MAX})^B$) and logarithmic (Mn concentration = $A\bullet\ln(\%_{MAX})+B$) equations to the standard curve data and calculated binding curve from non-linear regression analysis. Power curves were used for $\%_{MAX}$ values less than 50% and logarithmic curves for values greater than 50%, on either side of the inflection point of the saturation-binding curve plotted with Mn concentration (x-axis) and $\%_{MAX}$ (y-axis). These mathematical models used for calculating extracted Mn concentration routinely fit the saturation binding curves and standards data with r^2 values greater than 0.995.

Cell culture

The striatal cell lines – wild-type ST*Hdh*$^{Q7/Q7}$ and mutant ST*Hdh*$^{Q111/Q111}$ were a generous gift from Marcy Macdonald, PhD (Massachusetts General Hospital, Boston, MA, USA) and Gail Johnson, PhD (University of Rochester, Rochester, NY, USA) and grown at 33°C[11,25-27]. Briefly, wild-type ST*Hdh*$^{Q7/Q7}$ and mutant ST*Hdh*$^{Q111/Q111}$ cells

were plated in a clear 96 well plate at 8,000 cells per 0.32 cm^2 (surface area) respectively the evening before treatment and allowed to grow in a 33°C incubator. $MnCl_2$ was added to the complete culture media or HEPES salt exposure buffer the morning of exposure. Total extracted Mn levels were assessed by CFMEA.

Cellular fura-2 manganese extraction assay (CFMEA)

Wild-type ST*Hdh*$^{Q7/Q7}$ and mutant ST*Hdh*$^{Q111/Q111}$ were cultured in clear 96 well tissue plates and exposed to varying $MnCl_2$ concentrations. After exposure, the media was discarded and cells quickly washed three times with 200 µL PBS. The cells were extracted at 33°C for 1 hour in 100 µL PTx with 0.5 µM fura-2. Changes in fura-2 fluorescence caused by Mn quenching were measured on a plate reader as described in the cell-free fura-2 assays section. Extracted Mn concentrations from cultured cells were calculated using the logarithmic and power Mn standard curves, described in the saturation binding curve and mathematical modeling of Mn-fura-2 interaction section, with the $\%_{MAX}$ of each sample. Experimental sample $\%_{MAX}$ was determined by normalizing the RFU of each Mn-exposed sample with the RFU of vehicle-only samples (untreated), which was defined as the experimental 100% maximal fluorescence signal.

Mn-supplementation (Mn-spike) methods

Wild-type ST*Hdh*$^{Q7/Q7}$ cells were cultured and plated as described above in the cellular fura-2 manganese extraction assay (CFMEA) section. Briefly, cells were plated in a clear 96 well tissue culture plate and exposed to 0, 50, 100, and 200 μM $MnCl_2$ for 4 hours in media. Cells were washed three times with 200 μL PBS and extracted at 33°C for 1 hour in 100 μL PTx buffer containing 0.5 μM fura-2 followed by measurements of fura-2 fluorescence as described in cell-free fura-2 assays section. Cell-extracts were quickly supplemented (i.e. "spiked") with Mn and changes in fura-2 fluorescence re-measured at the aforementioned wavelengths (post-supplement). Mn concentrations in the cell extracts (pre and post-Mn spike) were computed by substituting the $\%_{MAX}$ of each experimental well after background subtraction for pre and post Mn spike measurements into a generated Mn standard curve. The difference in Mn levels in each well between pre and post Mn-spike (difference) was calculated. Alternatively, wild-type ST*Hdh*$^{Q7/Q7}$ cells were exposed to 100 μM $MnCl_2$ and extracted in known concentrations of Mn spiked fura-2 containing extraction buffers (0 μM, 250 μM, 500 μM, 1000 μM $MnCl_2$). Both the cellular and spiked Mn levels in cultured cell-extracts were measured by CFMEA. The difference in Mn levels in each well between unspiked and Mn-spiked fura-2 containing extraction buffers in vehicle exposed and Mn-exposed cultured cells (measured difference) was calculated by substituting the $\%_{MAX}$ of each experimental well after background subtraction for unspiked and Mn spiked measurements into a generated Mn standard curve. The measured difference between known and expected Mn concentrations was compared.

Graphite furnace atomic absorption spectroscopy (GFAAS)

Total Mn concentrations were measured with GFAAS (Varian Inc., AA240, Palo Alto, CA). Cultured wild-type ST*Hdh*$^{Q7/Q7}$ and mutant ST*Hdh*$^{Q111/Q111}$ cells were plated at 20,000 cells/well in clear 96 well plates and treated as described above for CFMEA. After CFMEA analysis of net cellular Mn levels in wild-type ST*Hdh*$^{Q7/Q7}$ and mutant ST*Hdh*$^{Q111/Q111}$ cells, the cell-extracts (100 µL per well) were quickly transferred into an eppendorf tube, flash-frozen and shipped on dry ice for GFAAS. To increase sensitivity for determination of Mn levels by GFAAS, six eppendorf tubes containing 100 µL cell-extracts from each set of experiment were thawed and combined together based on their genotype and exposure conditions before GFAAS analysis. For analysis, cell-extracts were digested in 200 µL ultrapure nitric acid for 24 hours in a sandbath (60°C). Mn content was determined by the following protocol: A 20 µL aliquot of the digested sample was brought to 1 ml total volume with 2% nitric acid for analysis. Bovine liver (NBS Standard Reference Material, USDC, Washington, DC) (10 µg Mn/g) was digested in ultrapure nitric acid and used as an internal standard for analysis (final concentration 5 µg Mn/L) as previously published[11,28].

PicoGreen dsDNA standard curve

PicoGreen standard curve was generated in a clear polystyrene 96 well plate by combining 100 µL salmon testes dsDNA standards (0 – 1000 µg/mL) prepared in 0.1% PTx and 50 µL of PicoGreen reagent diluted in 1x TE buffer (1:400) in a 96 well plate. In

addition, the background was determined by adding 100 µL 0.1% PTx and 50 µL 1x TE buffer. The standard curve plate was incubated at room temperature in the dark for 5 minutes and the fluorescence in each well measured with the Beckman coulter DTX 880 multimode plate reader at Ex_{485} (bandwidth of filter = ± 20 nm), Em_{535} (bandwidth of filter = ± 25 nm), and integration time of 200 ms with the indicated plate reader using multimode analysis software (version 3.2.0.6) and top read settings. The average background fluorescence read was subtracted from each of the salmon testes dsDNA PicoGreen fluorescence tested in the standard curve. The data points were plotted as average PicoGreen RFU of the DNA standards (y-axis) and their concentrations (x-axis) by non-linear regression analysis using Microsoft Excel. A standard linear regression analysis in Microsoft Excel was used to obtain a linear equation (PicoGreen Fluorescence = A•(x) + B) from the standard curve data; where A is the coefficient, rate and slope of the trend line, x is the unknown concentration of dsDNA in the cell-extract, and B is the y-intercept or where the line crosses the y-axis.

Measurement of dsDNA concentration in cell-extracts

After CFMEA analysis, 20 µL of cell-extract from each well was transferred into a clear polystyrene 96 well plate and 80 µL of 1:400 PicoGreen solution in 1x TE buffer added to each well. The cell extracts were further incubated with PicoGreen at room temperature for 5 minutes and changes in fluorescence measured as described in the PicoGreen dsDNA standard curve section. The concentration of dsDNA in each cell-extract was calculated using the linear equation generated from the salmon DNA standard

curve. In order to normalize cellular extracted Mn levels to dsDNA, we divided the calculated concentration of extracted Mn levels in each well (e.g. nanomoles) to its respective dsDNA concentration (e.g. microgram).

Statistical Analysis

Univariate and repeated-measures ANOVA tests were performed using SPSS 18 software (IBM, Inc., Chicago, IL). *Post hoc* analyses were done using Microsoft Excel (Microsoft, Redmond, WA) and assuming equal variances. Standard deviations of the mean for change in net Mn uptake or fura-2 fluorescence above basal levels or vehicle were calculated by appropriate propagation of uncertainty calculations for subtraction of sample means, with significant differences between vehicle and Mn exposed wild-type by non-overlap of the standard deviation.

Results

Establishment of essential conditions for CFMEA

To establish the basic CFMEA conditions, we first compared buffer conditions for detection of Mn-fura-2 interaction and found no significant difference between PBS and HEPES buffers (Figure II. 1.A.). Previous studies using fura-2 AM loading in single cells exhibited a temperature-dependent subcellular localization of fura-2[33-35]. Hence, we sought to determine the optimal temperature for detection of Mn quenched fura-2

fluorescence. Using a cell-free system, with varying $MnCl_2$ concentrations and fura-2, we observed a minimal influence of temperature on the Mn-fura-2 interaction (Figure II. 1.B.). Finally, we evaluated the ideal detergent concentration for maximum Mn extraction and detection by fura-2 from the striatal cells following a 100 μM $MnCl_2$ exposure. Maximal extraction was indicated by the greatest degree of fura-2 fluorescence quenching (i.e. decrease in RFU relative to the fura-2 containing detergent-buffer alone). After 45 minutes $MnCl_2$ exposure, cells were extracted in different concentrations of SDS or Triton X-100 in PBS for 1 hour at 33°C. RFU of fura-2 after the cell extraction (Mn extraction) and the baseline control (RFU of fura-2 containing buffer prior to extraction) were plotted for the different concentrations of detergent (Figure II. 1.C. and 1.D.). In the absence of detergent, fluorescence quenching was not observed, indicating the post-exposure PBS washes were sufficient to remove fura-2 detectable extracellular Mn. As little as 0.001% Triton X-100 or 0.01% SDS was sufficient to extract Mn from Mn-exposed cells. Although 0.01% SDS exhibited the greatest quenching following extraction of Mn-exposed cells, we selected 0.1% Triton X-100 in PBS for subsequent Mn extraction experiments in the cultured striatal cell line based on its maximal quenching and relatively minor changes in baseline RFU compared with SDS. SDS exhibited a dramatic phasic response in average RFU following Mn extraction of exposed cells. Moreover, we observed a concentration-dependent influence of both detergents on the baseline control fura-2 fluorescence. Specifically, SDS exhibited ~170 to 250% increase in control baseline RFU between 0.001 and 1% SDS. Triton X-100 showed a 10 to 20% increase in control baseline RFU at concentrations below 0.1 and 30% decrease at 1% Triton X-100. Furthermore, we observed an increase in control and Mn-exposed

baseline fluorescence for both detergents at concentrations above 1% (data not shown). These results elucidated the optimal buffer, temperature, and detergent concentration for CFMEA in the striatal cells.

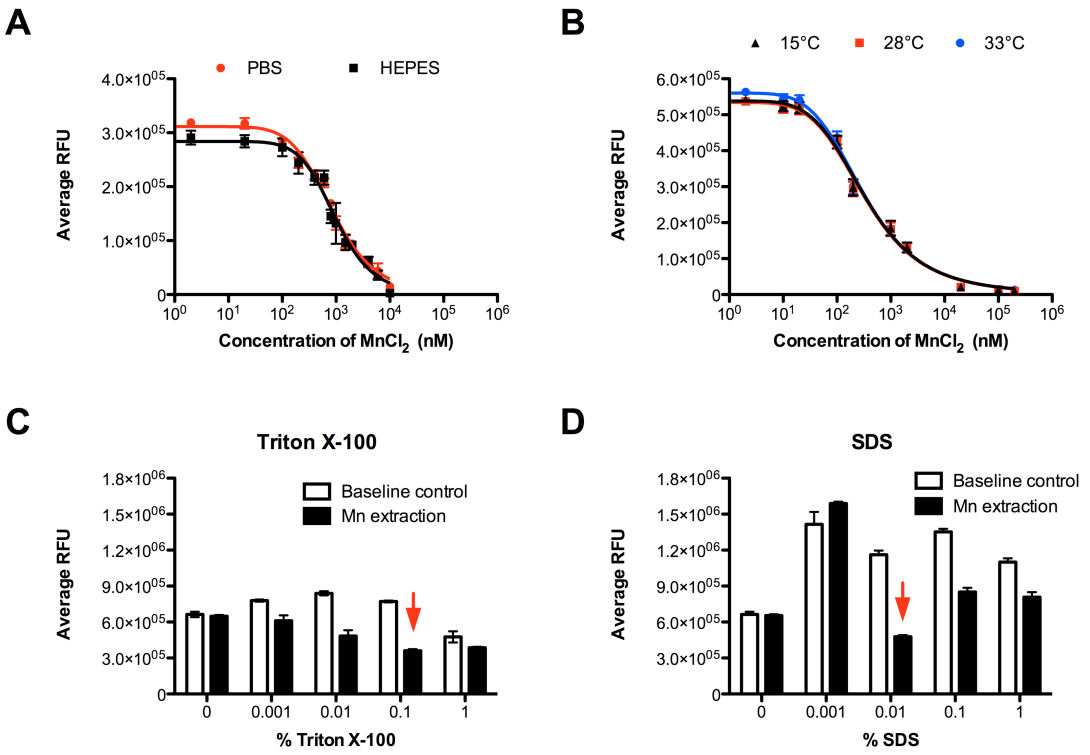

Figure II. 1. Optimization of buffer, temperature, and detergent for CFMEA. (**A**) No significant difference in two commonly used buffers (PBS and HEPES) on Mn-fura-2 fluorescence quenching. (**B**) Minimal influence of temperature (15, 28, and 33°C) on Mn-fura-2 fluorescence quenching. Data is represented as RFU (y-axis) versus transformed $\log_{10}$ Mn concentration on a linear scale (x-axis). A one-site specific saturation-binding curve with Hill slope was fit to $\log_{10}$ Mn concentration (x-axis). N=3; 8 wells/experiment. Mean levels are indicated as ± standard deviation for (A) and (B). Fura-2 concentrations for (A) and (B) are 0.05 µM and 0.5 µM respectively. Cellular Mn was extracted with different concentrations of (**C**) Triton X-100 or (**D**) SDS in PBS containing 0.5 µM fura-2. Arrow (red) indicates the maximum intracellular Mn extracted by each buffer. Data is represented as RFU of baseline control (fura-2 containing buffer with the indicated concentration of detergents) and Mn exposed cell-extracts (Mn-extraction). N=3; 4 wells/experiment. Mean levels are indicated as ± standard deviation.

Relationship between fura-2 concentration and Mn detection

In order to explore the optimal fura-2 concentration for detection of Mn, we utilized the aforementioned cell-free system with PTx and 0.5 μM fura-2. Owing to the sigmoidal nature of the fura-2 fluorescence response to Mn, we defined the optimal detection range for Mn by fura-2 to be between 10% and 85% the maximal baseline control fura-2 fluorescence. The detection range for Mn by fura-2 was explored by examining concentration-response curves for Mn at three fura-2 concentrations (0.05, 0.5, and 2 μM), and then fitting one-site specific binding curves to RFU values and Mn concentration by non-linear regression (Figure II. 2.). Specifically, 0.05 μM and 2 μM fura-2 accurately detected extracted Mn concentrations between about 50 nM – 6,000 nM and 300 nM – 10,000 nM respectively while 0.5 μM fura-2 detected Mn concentrations between about 70 nM – 10,000 nM (Table II. 1.). Although 0.05 μM fura-2 was capable of detecting lower Mn concentrations (50 nM), the lower absolute RFU values led to an inferior signal to noise ratio. Based on the signal to noise ratio, detection range, and expected concentration of Mn in cellular extracts, we selected 0.5 μM fura-2 as the optimal concentration for detection of extracted Mn from striatal cell lines.

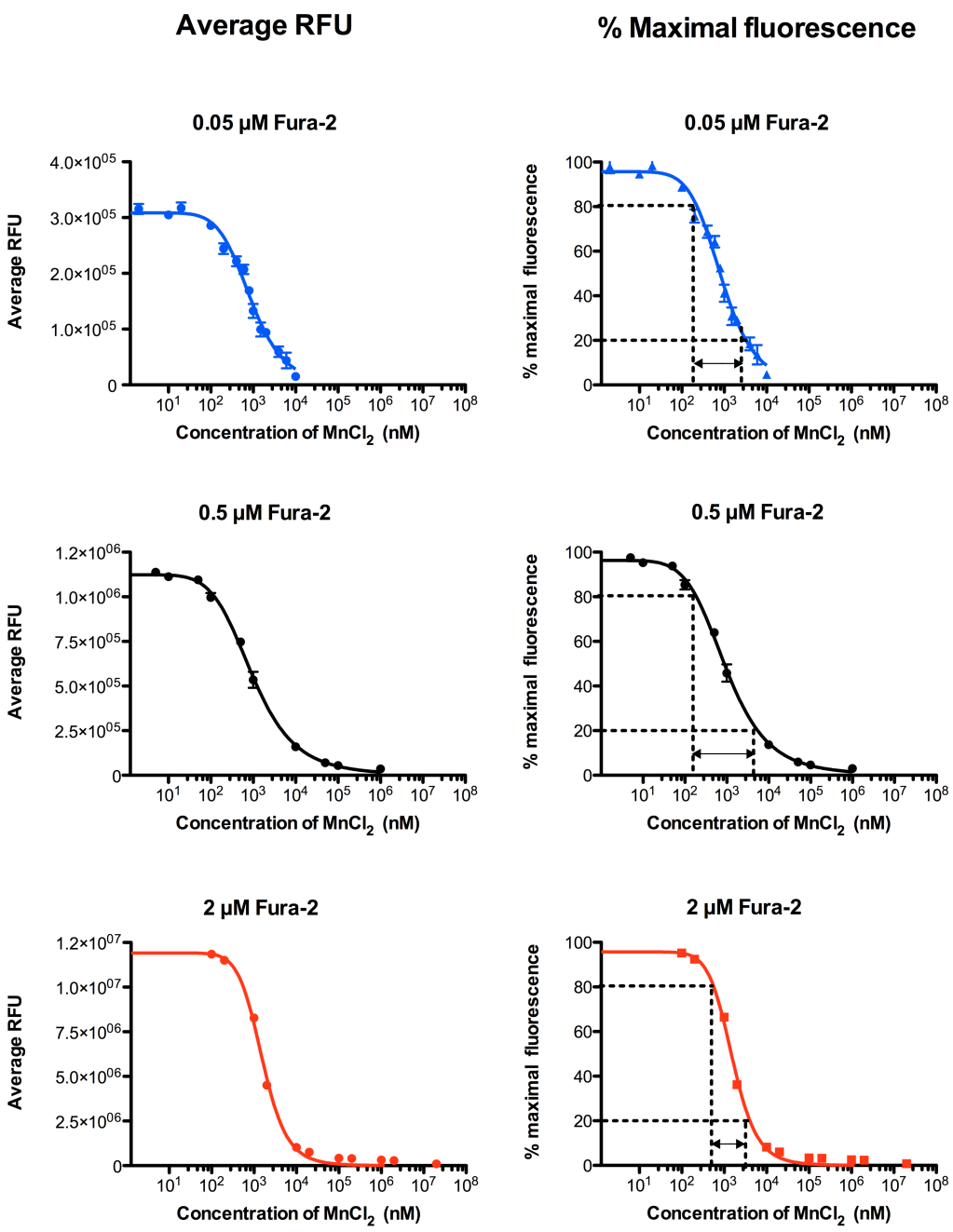

Figure II. 2. Optimal fura-2 concentration for CFMEA. The detection range for Mn concentration by fura-2 was explored by examining concentration-response curves for Mn at three fura-2 concentrations (0.05, 0.5, and 2 µM) in a cell-free system. Dotted lines represent the estimated Mn detection range of each fura-2 concentration and were chosen based on an arbitrary 10 to 85 % maximal fluorescence intensity range. The width of arrowhead line also indicates fura-2 detection range. Mn-fura-2 concentration-response curves are analyzed by nonlinear regression to fit one-site specific binding curves with

Hill slope, and plotted as RFU, left column, or normalized to unbound fura-2 ($\%_{MAX}$), right column, versus transformed $\log_{10}$ Mn concentration on a linear scale for each fura-2 concentration. N=3; 8 wells/experiment. Mean levels are indicated as ± standard deviation.

Fura-2 concentration (μM)	~ Optimal Mn^{2+} detection range (nM)
0.05	50 - 6,000
0.5	100 - 10,000
2	300 - 10,000

Table II. 1. Optimal Mn detection concentrations by fura-2. These concentrations were calculated based upon the defined 10% - 85% range extrapolated from each % maximal fura-2 concentration response curve shown in Figure II. 2.

Quantitative relationship between Mn concentration and fura-2 fluorescence

To generate a Mn-fura-2 standard curve for back calculation of total extracted Mn levels from cultured cells, we utilized the cell-free system described in the methods and materials (cell-free fura-2 assays). Eight independent Mn-fura-2 standard curves generated over an extended period of time exhibited a fairly consistent relationship between absolute RFU values and Mn concentration across experiments, with higher variability in the absolute values of the low Mn concentration samples (Figure II. 3.A.). To minimize this variability, we averaged the RFU values of the 0 μM Mn samples within each independent standard curve and defined this value as the 100% maximal fluorescence for that experiment. RFU of each well were then normalized as $\%_{MAX}$ to this value and plotted as $\%_{MAX}$ (y-axis) by non-linear regression analysis (Figure II. 3.B.). Importantly, we observed significantly less experimental variability in the standard

curves when represented as $\%_{MAX}$ rather than RFU (y-axis). To explore the binding relationship between Mn and fura-2 in our standard curves, we generated a one-site specific saturation-binding curve with Hill slope as discussed in methods and materials (saturation binding curve and mathematical modeling of Mn-fura-2 interaction), which tightly fit four averaged independent cell-free system experiments (Figure II. 3.C.). Binding curve data was fit to exponential and logarithmic curves to enable back calculation of extracted Mn levels from experimentally determined $\%_{MAX}$ values. These curves could be generated alongside Mn-exposure experiments to accurately quantify extracted Mn levels, and consistently demonstrated nearly identical Mn-fura-2 saturation binding curves and equations (Figure II. 3.B.).

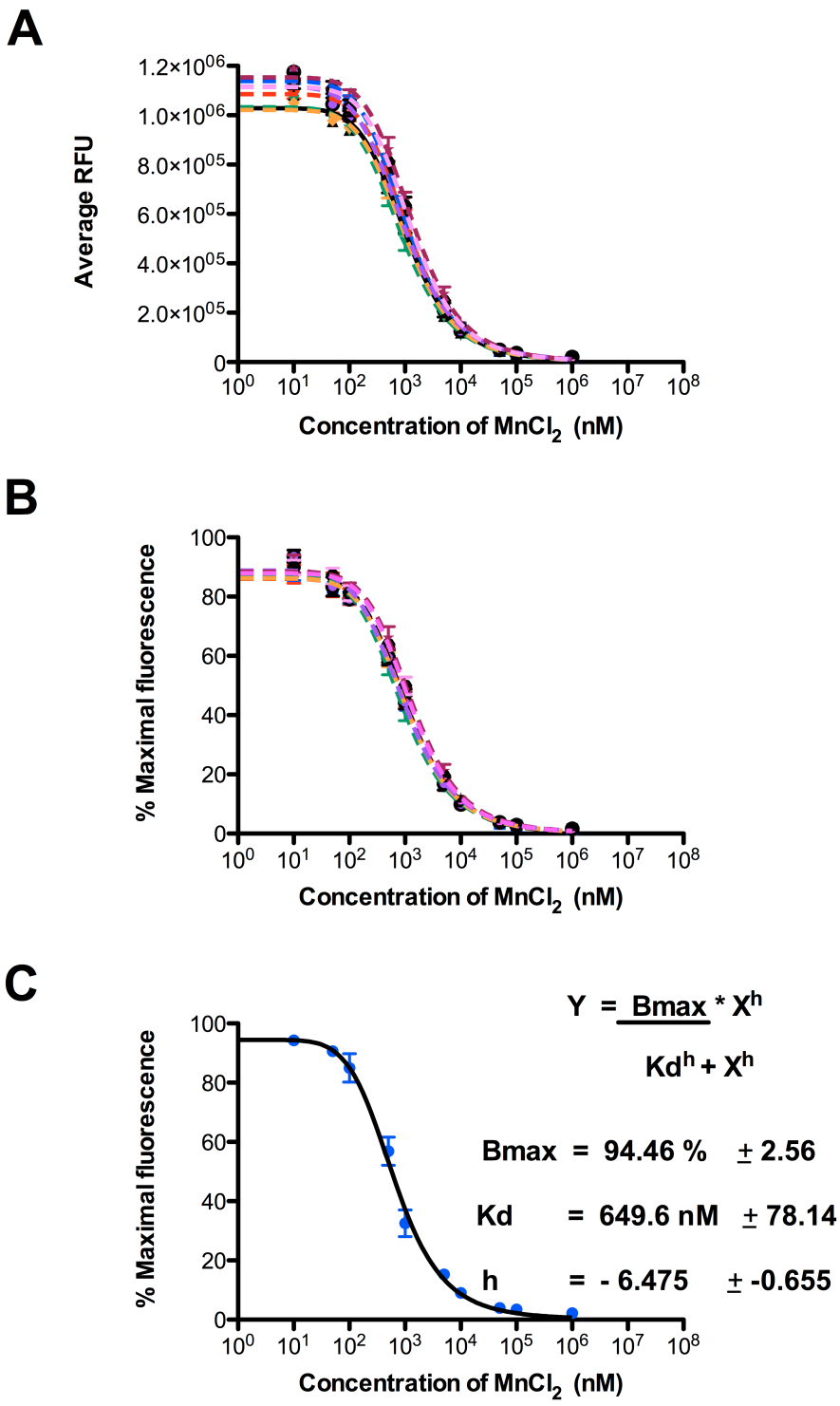

Figure II. 3. Mn-fura-2 standard curves. Mn-fura-2 standard curves were generated using a cell-free system with 0.5 μM fura-2 in PTx at Ex_{360}/Em_{535}. (**A**) Eight independent

fura-2 standard curves were generated over an extended period of time (> 1 year). Data is plotted as RFU versus $\log_{10}$ transformed Mn concentration on a linear scale. (**B**) The same curves as shown in (**A**) were plotted instead as $\%_{MAX}$ versus $\log_{10}$ transformed Mn concentration on a linear scale. Data in (**A**) and (**B**) were used to fit one-site specific binding curves with Hill slope (dashed lines). Mean values for (**A**) and (**B**) are indicated as ± standard deviation, N=3; 8 wells/experiment. (**C**) A one-site specific binding curve with Hill slope (black, equation indicated on plot) was fit by non-linear regression to $\%_{MAX}$ values obtained from four independent cell-free experiments (blue). The 95% confidence interval of the calculated binding curve constants are indicated on the plot. N=4; 4 wells/exposure condition. Mean levels are indicated as ± standard deviation.

Effect of metal ions on fura-2 fluorescence at Ex_{360}

Previous studies investigating the effect of metal ions on fura-2 fluorescence have demonstrated that other metal ions influence fura-2 fluorescence (increase or decrease) at the $F_{340/380}$ excitation/emission wavelengths[12,20-23]. In addition, Snitsarev and colleagues have shown that Zn^{2+}, Ca^{2+}, and Mn^{2+} influence fura-2 fluorescence between 300 nm and 400 nm excitation wavelengths[20]. To evaluate the potential of other metal ions to influence CFMEA, we examined the effect of other metal ions on our fura-2 cell-free system. Specifically, we generated Ex_{360}/Em_{535} concentration-response curves for different metal ions with 0.5 μM fura-2 in PTx buffer. The influence of these metal ions on fura-2 fluorescence was measured and fitted by nonlinear regression analysis to a one-site competitive binding curve (Figure II. 4.). We determined the approximate $\%_{MAX}$ at saturated metal binding of fura-2 (B_{max}) and half maximal effective concentration (EC_{50}) values for each metal ion from the one-site binding curves (Table II. 2.). Here, we show that while Mn^{2+}, Fe^{2+}, Co^{2+}, Ni^{2+}, Cu^{2+}, and Cd^{2+} quenched fura-2 fluorescence at varying concentrations, Pb^{2+}, Ca^{2+}, and Mg^{2+} had no effect on fura-2 fluorescence at the Ca^{2+} isosbestic wavelength. Furthermore, we observed an increase in fura-2 fluorescence in

the presence of Zn^{2+}. This suggests a need to control for the influence of some of these intracellular metal ions on CFMEA.

Metal	Fluorescence (Ex_{360} , Em_{535}) nm	EC_{50} (μM)	% Fluorescence at Bmax
Cd^{2+}	Decrease	0.3	70%
Co^{2+}	Decrease	0.7	0%
Cu^{2+}	Decrease	0.02	5%
Fe^{2+}	Decrease	80	0%
Mn^{2+}	Decrease	0.3	0%
Ni^{2+}	Decrease	4	15%
Zn^{2+}	Increase	~100	120%
Ca^{2+}	No effect *	N/A	N/A
Mg^{2+}	No effect	N/A	N/A
Pb^{2+}	No effect	N/A	N/A

Table II. 2. Effect of metals on fura-2 fluorescence at Ex_{360}/Em_{535}. Examination of approximate $\%_{MAX}$ at saturated metal binding of fura-2 (B_{max}) and half maximal effective concentration (EC_{50}) values for each metal ion extrapolated from the one-site binding curves (Figure IV.2.). (~) Indicates approximated value extrapolated from the one-site competition binding curves (Figure IV.2.). (*) Represents decrease effect on fura-2 fluorescence at concentrations above 10 μM.

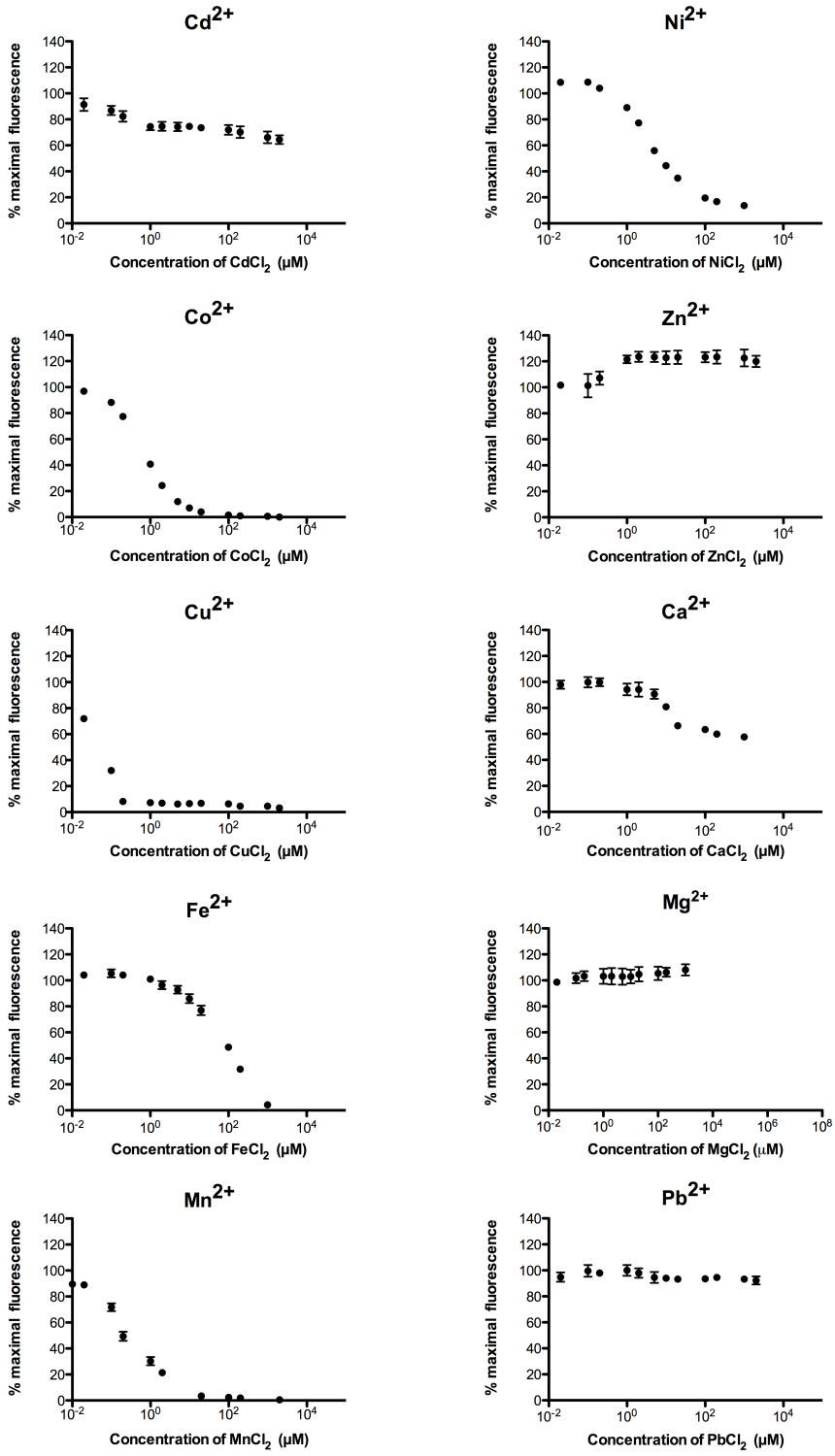

Figure II. 4. Effect of metal ions on fura-2 fluorescence at Ex_{360}/Em_{535}. Concentration-response curves were generated for 10 different divalent metal cations

with 0.5 μM fura-2 in PTx. The influence of these metal ions on fura-2 fluorescence was measured and fitted by nonlinear regression analysis to a one-site competitive binding curve. Mn concentrations were transformed to $\log_{10}$ Mn concentration versus normalized response curves and represented as transformed $\log_{10}$ Mn concentration on a linear scale. N=3; 8 wells/exposure condition. Mean levels are indicated ± standard deviation.

Competitive influence of metal ions on CFMEA

Although our experiments above and previous experimental reports suggest that intracellular metal ions could influence fura-2 fluorescence, it was unclear whether the concentrations of abundant endogenous cellular metal ions [12] would competitively influence Mn quantification by fura-2 in CFMEA. Therefore, we assessed the competitive influence of the two most abundant cellular metal ions, Ca^{2+} and Mg^{2+}, on the Mn-fura-2 interaction at the Ca^{2+} isosbestic wavelength of 360 nm using a cell-free system with varying concentrations of either $CaCl_2$ or $MgCl_2$ at different $MnCl_2$ levels. We observed no competitive influence of either Ca^{2+} or Mg^{2+} ions on Mn induced fura-2 quenching at concentrations of 10 μM or lower for all tested Mn concentrations (Figure II. 5.A. and 5.B.). However, we observed a competitive quenching effect on fura-2 fluorescence with increasing Ca^{2+} concentrations above 10 μM Ca^{2+} for all tested Mn concentrations (data not shown). Given the considerable affinity of Co^{2+}, Cu^{2+}, and Fe^{2+} for fura-2, we examined the possible competitive interference of the aforementioned metal ions on the Mn-fura-2 interaction at the Ca^{2+} isosbestic wavelength of 360 nm using a cell-free system with varying concentrations of either $CoCl_2$, $CuCl_2$, and $FeCl_2$ at different $MnCl_2$ levels. We observed a concentration-dependent quenching effect of all three metals on fura-2 fluorescence at the Ca^{2+} isosbestic wavelength of 360 nm.

However, there was no significant competitive influence of Co^{2+} concentrations below 1 µM on Mn induced fura-2 quenching at 0.05 µM and 0.2 µM $MnCl_2$. Importantly we observed minimal competitive quenching influence of the differently tested Co^{2+} concentrations on 2 µM and 20 µM $MnCl_2$ concentrations (Figure II. 5.C.). Moreover, we observed a similar effect of Cu^{2+} on Mn-fura-2 interaction (data not shown). In addition, Fe^{2+} demonstrated a minimal additive quenching effect on Mn-Fura-2 interaction at all the tested concentrations (Figure II. 5.D.).

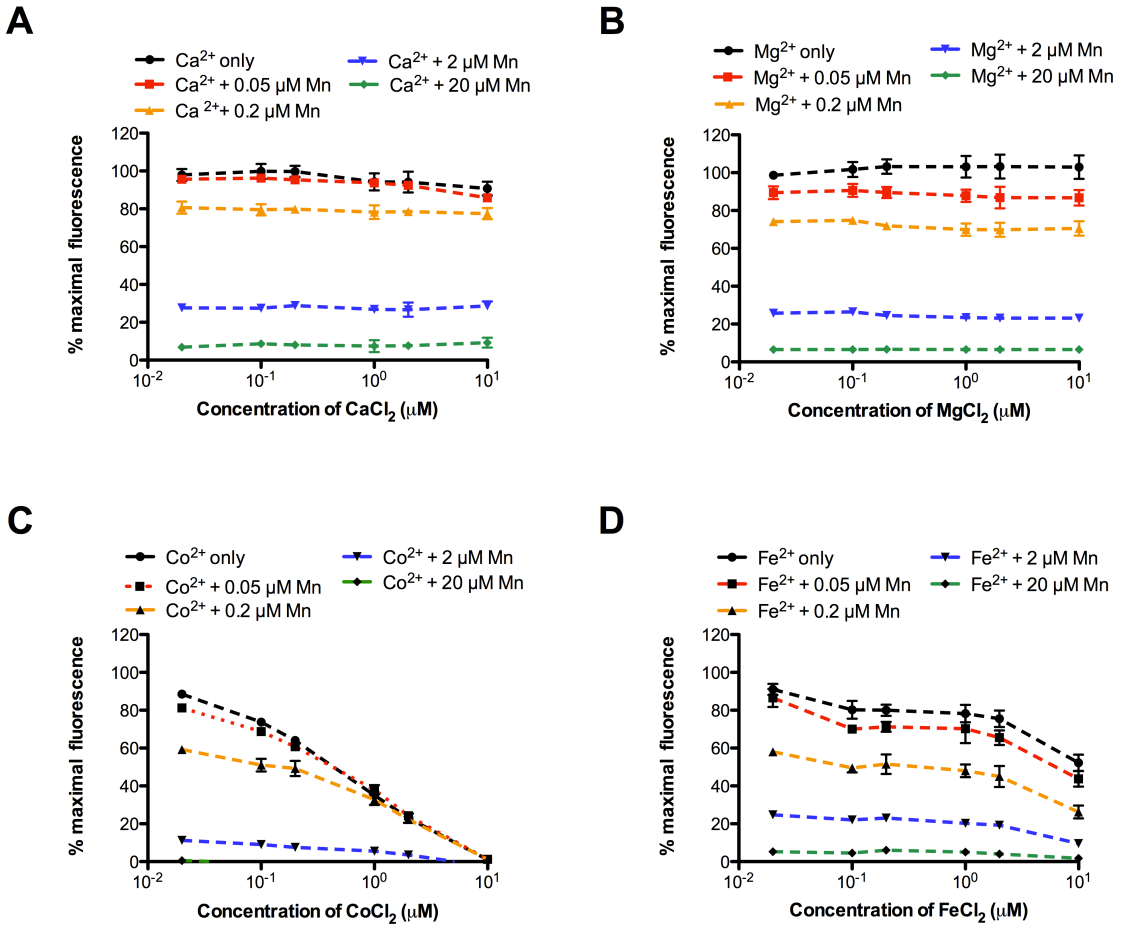

Figure II. 5. Competitive interference of metal ions on CFMEA. To examine the competitive interference of metal ions that have considerable affinity for fura-2 on CFMEA, we utilized 0.5 µM fura-2 in PTx and different concentrations of (**A**) $CaCl_2$

(**B**) $MgCl_2$, (**C**) $CoCl_2$ and (**D**) $FeCl_2$ with or without different concentrations of $MnCl_2$. N=3; 8 wells/exposure condition. Mean levels are indicated ± standard deviation.

Validation of CFMEA by Mn supplementation

To determine if other metal ions present in cultured striatal cells influence the specificity and accuracy of CFMEA, we validated the accuracy of Mn determination by a Mn supplementation test (Mn spike method 1). This method measures Mn levels in extracts of $MnCl_2$ exposed cultured cells before (pre) and after (post) the addition of a fixed concentration of Mn to the cell extract. We reasoned that if metal ions other than Mn present in the cultured cells have a significant influence on measured Mn concentrations, then the different concentrations of Mn and other ions in the cell-extracts following exposure would impede our ability to accurately measure a known quantity of Mn spiked into the samples ("post" minus "pre"). Upon comparison of measured Mn levels in the cultured striatal cell-extracts following $MnCl_2$ exposure, pre, and post-Mn spike, we observed a concentration-dependent increase in measured Mn levels in pre and post Mn-spiked conditions. However, there was no statistically significant difference in the calculated concentration of supplemented Mn measured over the full range of $MnCl_2$ exposure conditions. This data suggests that CFMEA is capable of accurately measuring Mn concentrations in extracted cultured cells over a two $\log_{10}$ scale concentration range of extracted Mn (Figure II. 6.A. and 6.B.). Conversely, we validated the accuracy of CFMEA by an alternative Mn supplementation method (Mn spike method 2). This method measures Mn levels in cultured cells extracted in differently spiked (0 μM, 250 μM, 500 μM, and 1000 μM $MnCl_2$) fura-2 containing extraction buffer. We reasoned that

if endogenous cellular metal ions other than Mn present in the cultured cells would competitively influence measured Mn concentrations, then CFMEA would be incapable of accurately measuring both the known concentration of Mn spiked into the fura-2 containing extraction buffer and cellular Mn levels. Upon comparison of the difference in Mn levels in each well containing cell-extract between unexposed and Mn-exposed cultured cells extracted in unspiked or Mn-spiked (measured difference) fura-2 containing extraction buffers, we observed an increase in measured Mn levels under all Mn-spiked conditions. Moreover, we observed no statistically significant difference between the known and measured Mn concentration difference at all the tested Mn spike concentrations (Figure II. 6.C. and 6.D.). The findings in both Mn spike methods (1 and 2) suggest that CFMEA is proficient in accurately and specifically measuring Mn concentrations in both Mn spiked extracted cultured cells and fura-2 containing extraction buffer.

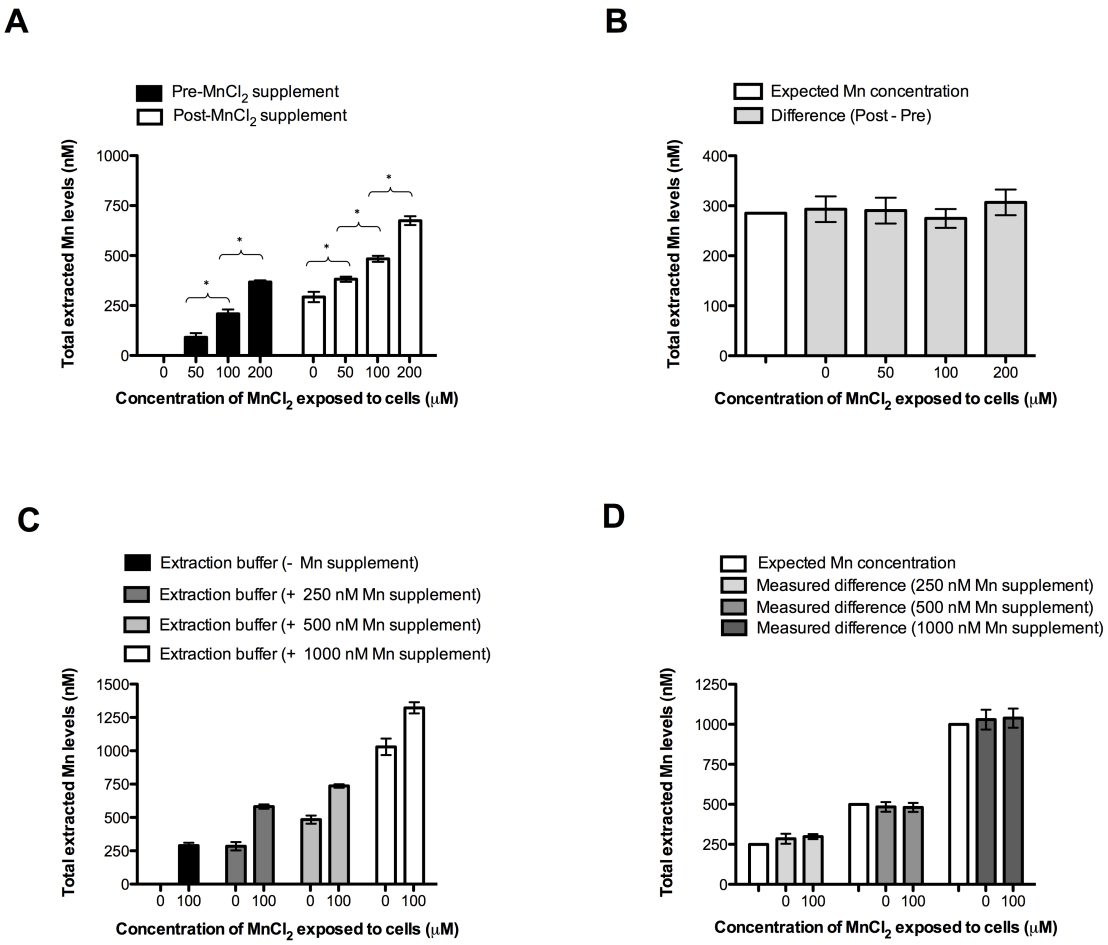

Figure II. 6. Validation of CFMEA by Mn-supplementation. Mn-spike methods accurately measured supplemented Mn levels in cultured wild-type neuronal cells. (**A**) Wild-type striatal cells were exposed to $MnCl_2$ and cellular Mn levels measured by CFMEA. Cell-extracts were quickly supplemented/spiked with Mn (~285 nM final Mn concentration) and changes in fura-2 fluorescence re-measured (post-supplement). (**B**) The difference in Mn levels in each well between pre and post Mn-spike (difference) was calculated. N=3; 4 wells/exposure condition. Mean levels are indicated $\pm$ standard deviation. (*) Indicates a significant concentration-dependent net Mn uptake ($p < 0.0001$, post-hoc t-test) in wild-type striatal cell lines. (**C**) Wild-type striatal cells were exposed to $MnCl_2$ and extracted in 0 μM, 250 μM, 500 μM, and 1000 μM $MnCl_2$ spiked fura-2 containing extraction buffers and total Mn levels assessed by CFMEA. (**D**) The difference in Mn levels in each well between unspiked and Mn-spiked (measured difference) fura-2 containing extraction buffers was calculated and compared to the known and expected Mn concentration. N=4; 4 wells/exposure condition. Mean levels are indicated $\pm$ standard deviation.

Validation of CFMEA by GFAAS

To further validate the accuracy and specificity of CFMEA, we measured and compared Mn levels in HD striatal cells by both CFMEA and GFAAS following 30 minutes $MnCl_2$ exposure in HEPES salt buffer. We observed a close-agreement in the measured intracellular Mn levels between CFMEA and GFAAS (Figure II. 7.). Repeated measures ANOVA showed a significant decrease in mutant ST*Hdh*$^{Q111/Q111}$ Mn accumulation compared to wild-type ST*Hdh*$^{Q7/Q7}$ cells ($p < 0.0001$) when assayed by both CFMEA and GFAAS. Importantly, we did not observe a significant difference in the levels of Mn measured between CFMEA and GFAAS in either wild-type or mutant cells. In addition, we did not observe a genotype by assay effect. This data suggest that both CFMEA and GFAAS exhibit similar sensitivity and are capable of accurately and specifically measuring cellular Mn levels.

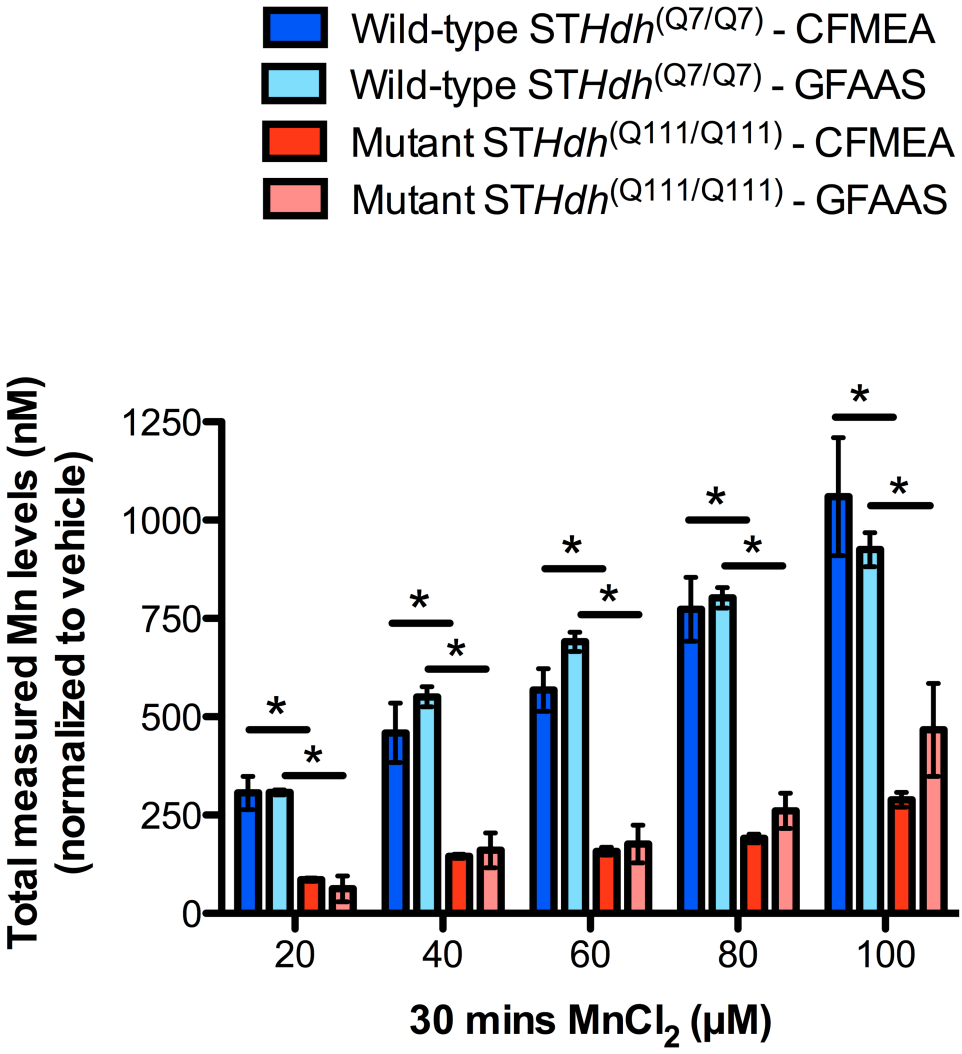

Figure II. 7. Close-agreement between CFMEA and GFAAS in the measured net intracellular Mn levels in cultured HD striatal cells. Wild-type ST*Hdh*$^{Q7/Q7}$ (blue) and mutant ST*Hdh*$^{Q111/Q111}$ (red) cells were cultured in a 96 well tissue culture plate and exposed to the indicated $MnCl_2$ concentrations for 30 minutes in HEPES salt buffer and total extractable Mn levels measured by CFMEA and GFAAS. N = 3; 6 wells/exposure condition. Note: 1 nM (nanomolar/L) = 0.001 nanomoles per mL. The mean total Mn levels (±SEM) are plotted as indicated. (*) Indicates a significant effect of genotype on net Mn uptake ($p < 0.0001$, repeated measures ANOVA) between wild-type ST*Hdh*$^{Q7/Q7}$ and mutant ST*Hdh*$^{Q111/Q111}$ cells assessed with either CFMEA or GFAAS.

PicoGreen standard curve

We observed that cultured striatal cells plated at cell densities below 20,000 cells per well in a 96-well tissue culture plate had insufficient protein levels to be detected by standard protein assays, including Bradford and Lowry. Hence, we generated a PicoGreen standard curve using a cell-free system (Figure II. 8.A) as detailed in Table II. 3 and a striatal cell-extract system (Figure II. 8.B.) using the PicoGreen assay (described in methods and materials section) to enable efficient and accurate normalization of cellular Mn levels in the cell-extracts to dsDNA content (Figure II. 8.A) or cell number (Figure II. 8.B.) following CFMEA analysis. We observed a linear relationship between the concentrations of dsDNA, cell number and PicoGreen fluorescence. Importantly, the concentrations of dsDNA in the striatal cells pre and post Mn exposure were within the lower and upper limits of the PicoGreen standard curve.

Well number on 96-well plate	**Stock [DNA] (µg/ml)**	**DNA stock (µl)**	**PicoGreen solution (µl)**
A1, B1, C1, D1	0.00381	100	50
A2, B2, C2, D2	0.00763	100	50
A3, B3, C3, D3	0.01526	100	50
A4, B4, C4, D4	0.03052	100	50
A5, B5, C5, D5	0.06104	100	50
A6, B6, C6, D6	0.12207	100	50
A7, B7, C7, D7	0.24414	100	50
A8, B8, C8, D8[a]	0	(100 µl extraction buffer)	(50 µl 1x TE buffer)

Table II. 3. Format to generate a PicoGreen dsDNA standard curve. *a*Represents wells used for PicoGreen background subtraction.

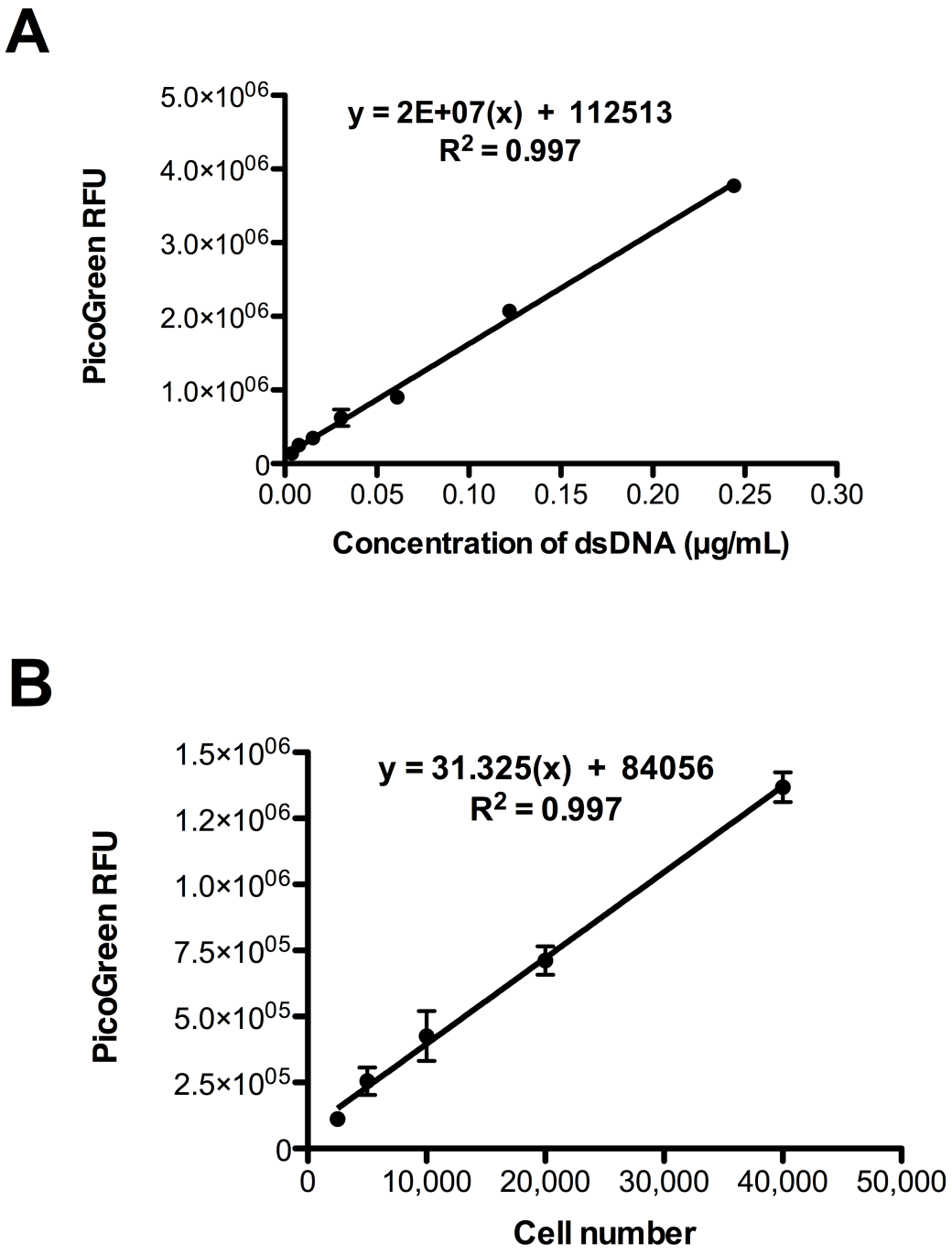

Figure II. 8. Quantitative relationship between PicoGreen fluorescence, concentration of dsDNA, and cell number. (**A**) A seven-point PicoGreen standard was generated using a cell-free system composed of a 1:400 dilution of PicoGreen reagent in 1x TE buffer and varying salmon testes dsDNA concentrations and measured at

Ex_{485}/Em_{535} nm. (**B**) A five-point PicoGreen fluorescence versus number of cells standard curve was generated using striatal cells extracted in 0.1% PTx containing 0.5μM final concentration of fura-2. N = 4 wells/dsDNA concentration or cell number for (**A**) and (**B**) respectively. Mean levels are indicated as 95% confidence intervals.

Examination of endogenous cellular Mn levels in HD striatal cells

To investigate the basal levels of Mn in vehicle exposed wild-type ST*Hdh*$^{Q7/Q7}$ and mutant ST*Hdh*$^{Q111/Q111}$ cells, we measured changes in fura-2 fluorescence and utilized a Mn-fura-2 standard curve (as depicted in Figure II. 3.) to calculate for total extracted cellular Mn levels following 1 hour exposure to vehicle (0 μM $MnCl_2$) in HEPES salt buffer. To enable efficient normalization of net dsDNA levels in the striatal cells, we used the PicoGreen assay (described above) and PicoGreen standard curve (depicted in Figure II. 8). We observed ~ 5-10 % quenching in both wild-type ST*Hdh*$^{Q7/Q7}$ and mutant ST*Hdh*$^{Q111/Q111}$ cells (Figure II. 9.A.). Furthermore, there were no statistical differences in the quantified total endogenous Mn levels expressed in nanomolar (nM) between wild-type ST*Hdh*$^{Q7/Q7}$ and mutant ST*Hdh*$^{Q111/Q111}$ cells (Figure II. 9.B.). In addition, both genotypes exhibited equivalent dsDNA levels (Figure II. 9.C.) and similar net Mn levels following normalization by dsDNA (Figure II. 9.C.).

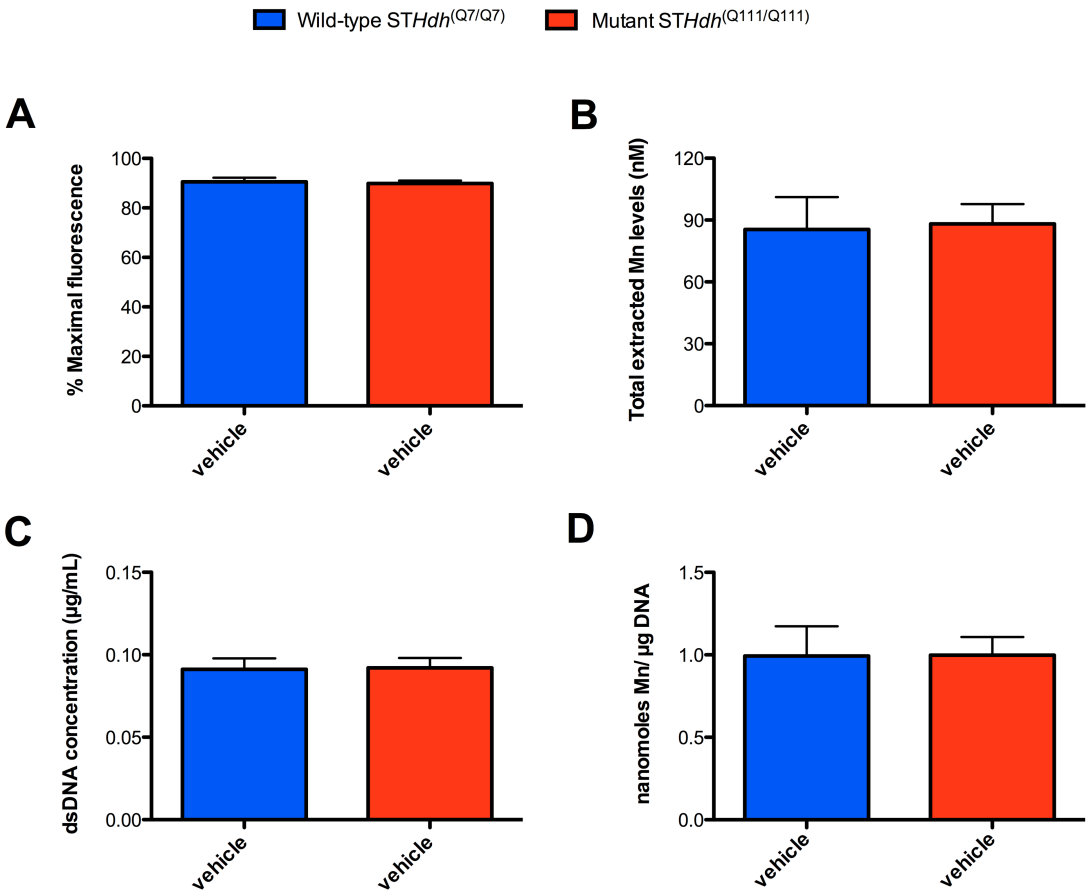

Figure II. 9. Assessment of endogenous Mn levels in HD striatal cells. Wild-type ST*Hdh*$^{Q7/Q7}$ (blue) and mutant ST*Hdh*$^{Q111/Q111}$ (red) cells were cultured in a 96 well tissue culture plate and exposed to vehicle (0 µM $MnCl_2$) for 30 minutes in HEPES salt buffer. CFMEA was used to measure (**A**) changes in % maximal fura-2 fluorescence and (**B**) total extracted cellular Mn levels expressed in nanomolar (nM) concentration. (**C**) dsDNA levels in the same striatal cells were assessed by PicoGreen assay. (**D**) Net Mn levels in each well/experiment were normalized to their corresponding dsDNA content. Note: 1 nM (nanomolar/L) = 0.001 nanomoles per mL. N = 11; 6 wells/experiment. The mean levels are indicated as 95 % confidence interval.

Conclusions

We have developed a high-throughput fluorescence quenching assay, CFMEA, by establishing the critical extraction and assay conditions (e.g. extraction buffer, temperature, and fura-2 concentration) required for quantitative detection of extracted Mn from cultured striatal cell lines by fura-2. The assay utilizes changes in fura-2 fluorescence as an indirect read-out of intracellular Mn concentrations. In contrast to the typical usage of fura-2 following cell loading, this high-throughput and cost-effective assay extracts intracellular Mn in cultured striatal cells following $MnCl_2$ exposure and allows for rapid assessment of Mn dynamics. In this assay, cultured cells are thoroughly washed following Mn exposure and intracellular Mn is extracted by detergent solubilization in the presence of fura-2. Fluorescence is then measured at Ex_{360}/Em_{535}. We have shown that a Mn standard curve, based on saturation one-site specific binding kinetics, can be generated to enable back calculation of Mn concentration from Mn quenching of fura-2 fluorescence. We have also examined the influence of other metal ions on CFMEA at this Ca^{2+} isosbestic wavelength (Ex_{360}/Em_{535}). In addition, we have also developed a quantitative PicoGreen assay for accurate and efficient normalization of cellular Mn levels in cell-extracts following Mn exposure.

We report that the ideal detergent concentration for Mn extraction from the striatal cell lines is 0.1% Triton X-100 (Figure II. 1.C.). Furthermore, detergent was required for detection of fura-2 quenching by CFMEA, suggesting that extracellular Mn is not a significant component of the Mn detected by this assay. We observed minimal influence of Triton X-100 on baseline fura-2 fluorescence relative to SDS. In addition,

the unexpected biphasic increase in fura-2 RFU of both baseline control and cell extracts from 0 to 1% SDS may possibly be due to an interaction between SDS and fura-2. Interestingly, previous experimental evidence suggests that SDS can exist either as monomers or micellar aggregates in aqueous solutions depending on the total concentration, ionic strength, and temperature. Moreover, increasing total concentration of SDS at a given ionic strength impedes the ability to measure increases in monomer concentration above the critical micelle concentration (CMC)[36]. The phasic Mn quenching observed in both SDS and Triton X-100 at higher concentrations might be due to alterations in the CMC of both detergents used for Mn extraction in the cultured striatal cells.

The generation of a Mn-fura-2 standard curve enabled back calculation of Mn levels in cultured striatal cells. However, we observed experimental variability in RFU between independent standard curves generated over an extended period of time. This variability may be due to experimental differences in fura-2 concentration, fluorometric plate reader sensitivity, and detection of Mn quenched fura-2. Thus, the use of $\%_{MAX}$ to calculate Mn levels in cell extracts may improve the accuracy of Mn determination across experiments. We observed agreement in the quantitative relationship between Mn concentration and fura-2 fluorescence in the eight independent standard curves, which had a tight fit to a one-site specific binding curve with Hill slope (Figure II. 3.). This data argues for the possibility of using a single Mn-fura-2 standard curve for multiple independent experiments to facilitate high throughput analysis.

Owing to the published effect of metal ions on fura-2 fluorescence at the $F_{340/380}$ excitation ratio wavelengths [12,20-23], we examined and demonstrated a similar influence of Mn^{2+}, Fe^{2+}, Co^{2+}, Ni^{2+}, Cu^{2+}, Ca^{2+}, Mg^{2+}, Pb^{2+}, and Zn^{2+} on fura-2 fluorescence in our cell-free system at Ex_{360}/Em_{535} (Figure II. 4. and Table II. 1) and published data that used single cell loaded fura-2 AM at $F_{340/380}$ nm excitation ratio[12,20,37,38]. However, in contrast to published evidence of an increase in fura-2 fluorescence by Cd^{2+} at the $F_{340/380}$ ratio [12,20], we observed a quenching effect at high Cd^{2+} concentrations with an EC_{50} of 0.3 μM (Figure II. 4. and Table II. 1). In addition, we observed an unexpected fura-2 quenching effect (~10%) with Ca^{2+} concentrations above 10 μM, regardless of the concentration of Mn present in the cell-free system (data not shown). It is possible that the competitive quenching effect of Ca^{2+} may be due to detection limits of the plate reader or changes in fura-2 and Mn binding stoichiometry that would induce molecular crowding of fura-2 by Ca^{2+} ions and decrease fura-2 fluorescence. Furthermore, we demonstrated that not only do Co^{2+} and Cu^{2+} quench fura-2 fluorescence in a concentration-dependent manner, but also they can competitively interfere with Mn-fura-2 interaction at concentrations above 1 μM (Figure II. 5.C. and data not shown). Although Fe^{2+} quenched fura-2 in a concentration-dependent manner, it had minimal influence on the Mn-fura-2 interaction (Figure II. 5.D.). However, we did not observe any significant influence of basal cellular metal ions on the quantified Mn levels in the striatal cell extracts by the CFMEA assay. This may be due in part to the fact that cells were extracted in a large volume of fura-2 detergent-based extraction buffer (100 μL) that reduced the concentration of endogenous metal ions that might otherwise influence the assay. However, CFMEA may fail to provide accurate measurements of cellular Mn levels following exposure to mixtures of

toxicants containing multiple fura-2 binding metals if levels reach concentrations high enough to influence fura-2 fluorescence. On the other hand, given the substantial affinity of Cu^{2+}, Co^{2+}, Ni^{2+}, and Fe^{2+} for fura-2, it is likely that CFMEA could be adapted for studies examining the cellular uptake of these other metals.

We observed approximately 5 - 10% quenching effect of endogenous metal ions in untreated cell-extracts (Figure II. 9.A.). To account for the potential effect of endogenous metal ions in the striatal cells on fura-2 fluorescence, we defined the fluorescence of untreated cells as the 100% maximal fluorescence rather than the fura-2 fluorescence value obtained from the cell-free system. The Mn-spike validation assays (Mn-spike methods 1 and 2) strongly suggest a minimal influence of endogenous metal ions on the accuracy of CFMEA. Specifically, the Mn-spike methods revealed that irrespective of the basal metal levels in cells exposed to different $MnCl_2$ concentrations or extracted in different Mn-spiked fura-2 containing extraction buffer, CFMEA is capable of accurately measuring a known quantity of supplemented Mn over a wide range of measured Mn concentrations (Figure II 6.A. – 6.D.). In addition, the Mn-spike method B demonstrated that Mn spiking of the fura-2 containing extraction buffer before cellular Mn extraction did not saturate the fura-2 metal binding sites.

We observed a close-agreement in the measured Mn levels between CFMEA and GFAAS (Figure II. 7.). We demonstrate that while both assays are specific and accurate in the detection of reduced Mn accumulation in mutant HD striatal cells compared to wild-type over a wide-range of concentrations, we did not observe a genotype by assay effect. We observed a substantial difference in the time required for measurement of

extracted cellular Mn and data acquisition between both assays. Specifically, the high-throughput nature of CFMEA enabled for feasible assessment of Mn levels in cultured wild-type ST*Hdh*$^{Q7/Q7}$ and mutant ST*Hdh*$^{Q111/Q111}$ cells within two hours following exposure to Mn. Conversely, independent cell-extracts had to be pooled together for GFAAS measurements and analysis, which required several weeks.

We observed that cultured striatal cells plated at lower cell densities (<20,000 cells/well on a 96 well plate) were undetectable my traditional protein detection assays. Thus, we developed a quantitative PicoGreen assay that enabled efficient normalization of cellular Mn levels in the striatal cell following CFMEA analysis. Importantly, we demonstrated a linear relationship between PicoGreen fluorescence and either the concentrations of dsDNA (Figure II 8.A.) or cell number (Figure II 8.B.) in the striatal cell-extracts. Moreover, the concentrations of dsDNA in the striatal cells pre and post Mn exposure were within the lower and upper limits of the PicoGreen standard curve. We demonstrated that both wild-type ST*Hdh*$^{Q7/Q7}$ and mutant ST*Hdh*$^{Q111/Q111}$ cells exhibit similar dsDNA levels after vehicle exposure (Figure II. 9.C.). In addition, pre and post normalization of net extracted Mn levels in vehicle exposed striatal cells to dsDNA levels does not change the net Mn levels between both genotypes (Figure II. 9.B. and 9.D.).

It is possible that the extraction conditions and fura-2 concentration of CFMEA could be modified and applied to rapidly assess different metal ion levels and dynamics in other cells and animal tissues. Furthermore CFMEA has the potential to provide Mn kinetic measurements (i.e. B_{max}, EC_{50}, K_m) in cells and tissues. This approach has the potential to extend our understanding of Mn transport kinetics and homeostasis. In

conclusion, we have developed, optimized, validated and applied a functional high-throughput fluorescence-quench extraction assay (CFMEA) to accurately assess Mn levels in a striatal cell line. Importantly, CFMEA provides a rapid means to evaluate Mn transport kinetics in cellular toxicity and disease models. Given the close-relationship in measured Mn levels, similarities in sensitivity, accuracy, specificity between CFMEA and GFAAS, and most importantly, the high-throughput nature of CFMEA, we used CFMEA as the preferred assay to investigate the Mn transport dynamics underlying decreased Mn accumulation in mutant HD striatal cells.

References

1. Erikson, K.M., Syversen, T., Aschner, J. & Aschner, M. Interactions between excessive manganese-exposure and dietary iron-deficiency in neurodegeneration. *Environ. Toxicology and Pharmacology* **19**, 415-421 (2005).

2. Erikson, K.M. & Aschner, M. Manganese neurotoxicity and glutamate-GABA interaction. *Neurochem Int* **43**, 475-80 (2003).

3. Butterworth, J. Changes in nine enzyme markers for neurons, glia, and endothelial cells in agonal state and Huntington's disease caudate nucleus. *J Neurochem* **47**, 583-7 (1986).

4. Hurley, L.S. & Keen, C.L. Manganese. in *Trace elements in human health and animal nutrition* (eds. Underwood, E. & Mertz, W.) 185-225 (Academic Press, New York, 1987).

5. Roth, J.A. & Garrick, M.D. Iron interactions and other biological reactions mediating the physiological and toxic actions of manganese. *Biochem Pharmacol* **66**, 1-13 (2003).

6. Olanow, C.W. Manganese-induced parkinsonism and Parkinson's disease. *Ann N Y Acad Sci* **1012**, 209-23 (2004).

7. Dobson, A.W., Erikson, K.M. & Aschner, M. Manganese neurotoxicity. *Ann N Y Acad Sci* **1012**, 115-28 (2004).

8. Ensing, J.G. Bazooka: cocaine-base and manganese carbonate. *J Anal Toxicol* **9**, 45-6 (1985).

9. Aschner, M., Guilarte, T.R., Schneider, J.S. & Zheng, W. Manganese: recent advances in understanding its transport and neurotoxicity. *Toxicol Appl Pharmacol* **221**, 131-47 (2007).

10. Williams, B.B., Kwakye, G.F., Wegrzynowicz, M., Li, D., Aschner, M., Erikson, K.M. & Bowman, A.B. Altered manganese homeostasis and manganese toxicity in a Huntington's disease striatal cell model are not explained by defects in the iron transport system. *Toxicol Sci* **117**, 169-79 (2010).

11. Williams, B.B., Li, D., Wegrzynowicz, M., Vadodaria, B.K., Anderson, J.G., Kwakye, G.F., Aschner, M., Erikson, K.M. & Bowman, A.B. Disease-toxicant screen reveals a neuroprotective interaction between Huntington's disease and manganese exposure. *J Neurochem* **112**, 227-37 (2010).

12. Grynkiewicz, G., Poenie, M. & Tsien, R.Y. A new generation of Ca2+ indicators with greatly improved fluorescence properties. *The Journal of Biological Chemistry* **260**, 3440 - 3450 (1985).

13. Cobbold, P.H. & Rink, T.J. Fluorescence and bioluminescence measurement of cytoplasmic free calcium. *Biochem J.* **248**, 313-328 (1987).

14. Tsien, R.W. & Malinow, R. Changes in presynaptic function during long-term potentiation. *Ann N Y Acad Sci* **635**, 208-20 (1991).

15. Oliveira, J.M.A., Chen, S., Almeida, S., Riley, R., Goncalves, J., Oliveira, C.R., Hayden, M.R., Nicholls, D.G., Ellerby, L.M. & Christina Rego, A. Mitochondrial-dependent Ca2+ handling in Huntington's disease striatal cells: Effect of histone deacetylase inhibitors. . *The Journal of Neuroscience* **26**, 11174 - 11186 (2006).

16. Lim, D., Feedrizzi, L., Tartari, M., Zuccato, C., Cattaneo, E., Brini, M. & Carafoli, E. Calcium homeostasis and mitochondrial dysfunction in striatal neurons of Huntington disease. *The Journal of Biological Chemistry* **283**, 5780–5789 (2007).

17. Tang, T.S., Tu, H., Chan, E.Y., Maximov, A., Wang, Z., Wellington, C.L., Hayden, M.R. & Bezprozvanny, I. Huntingtin and huntingtin-associated protein 1 influence neuronal calcium signaling mediated by inositol-(1,4,5) triphosphate receptor type 1. *Neuron* **39**, 227-39 (2003).

18. Tsien, R. & Pozzan, T. Measurement of cytosolic free Ca2+ with quin2. *Methods Enzymol* **172**, 230-62 (1989).

19. Tsien, R.Y. Fluorescent probes of cell signaling. *Annual Review of Neuroscience* **12**, 227-253 (1989).

20. Snitsarev, V.A., McNulty, T.J. & Taylor, C.W. Endogenous heavy metal ions perturb fura-2 measurements of basal and hormone-evoked Ca2+ signals. *Biophys J* **71**, 1048-56 (1996).

21. Forbes, J.R. & Gros, P. Iron, manganese, and cobalt transport by Nramp1 (Slc11a1) and Nramp2 (Slc11a2) expressed at the plasma membrane. *Blood* **102**, 1884-92 (2003).

22. Merritt, J.E., Jacob, R. & Hallam, T.J. Use of manganese to discriminate between calcium influx and mobilization from internal stores in stimulated human neutrophils. *J Biol Chem* **264**, 1522-7 (1989).

23. Picard, V., Govoni, G., Jabado, N. & Gros, P. Nramp 2 (DCT1/DMT1) expressed at the plasma membrane transports iron and other divalent cations into a calcein-accessible cytoplasmic pool. *J Biol Chem* **275**, 35738-45 (2000).

24. Xu, B., Xu, Z.F. & Deng, Y. Effect of manganese exposure on intracellular Ca2+ homeostasis and expression of NMDA receptor subunits in primary cultured neurons. *Neurotoxicology* **30**, 941-9 (2009).

25. Cattaneo, E. & Conti, L. Generation and characterization of embryonic striatal conditionally immortalized ST14A cells. *J Neurosci Res* **53**, 223-34 (1998).

26. Milakovic, T. & Johnson, G.V. Mitochondrial respiration and ATP production are significantly impaired in striatal cells expressing mutant huntingtin. *J Biol Chem* **280**, 30773-82 (2005).

27. Trettel, F., Rigamonti, D., Hilditch-Maguire, P., Wheeler, V.C., Sharp, A.H., Persichetti, F., Cattaneo, E. & MacDonald, M.E. Dominant phenotypes produced by the HD mutation in STHdh(Q111) striatal cells. *Hum Mol Genet* **9**, 2799-809 (2000).

28. Anderson, J.G., Fordahl, S.C., Cooney, P.T., Weaver, T.L., Colyer, C.L. & Erikson, K.M. Extracellular norepinephrine, norepinephrine receptor and transporter protein and mRNA levels are differentially altered in the developing rat brain due to dietary iron deficiency and manganese exposure. *Brain Res* **1281**, 1-14 (2009).

29. Enger, Ø. Use of the fluorescent dye PicoGreen™ for quantification of PCR products after agarose gel electrophoresis. *Biotechniques* **21**, 372-374 (1996).

30. Ahn, S.J., Costa, J. & Emanuel, J.R. PicoGreen quantitation of DNA: effective evaluation of samples pre- or post-PCR. *Nucleic Acids Res* **24**, 2623-5 (1996).

31. Seville, M., West, A.B. & McHenry, C.S. Fluorometric assay for DNA polymerases and reverse transcriptase. *Biotechniques* **21**, 664-672 (1996).

32. Molecular Probes, I. Picogreen dsDNA Quantitation Reagent and Kit instruction. (USA, 1996).

33. Poenie, M., Alderton, J., Steinhardt, R. & Tsien, R.Y. Calcium rises abruptly and briefly throughout the cell at the onset of anaphase. *Science* **233**(1986).

34. Malgaroli, A., Milani, D., Meldolesi, J. & Pozzan, T. Fura-2 measurement of cytosolic free Ca2+ in monolayers and suspensions of various types of animal cells. *J Cell Biol* **105**, 2145-55 (1987).

35. Plieth, C. & Hansen, U. Methodological aspects of pressure loading of fura-2 into characean cells. *Journal of Experimental Botany* **47**, 1601-1612 (1996).

36. Reynolds, J.A. & Tanford, C. Binding of dodecyl sulfate to proteins at high binding ratios. Possible implications for the state of proteins in biological membranes. *Proc Natl Acad Sci U S A* **66**, 1002-7 (1970).

37. Coyle, P., Zalewski, P.D., Philcox, J.C., Forbes, I.J., Ward, A.D., Lincoln, S.F., Mahadevan, I. & Rofe, A.M. Measurement of zinc in hepatocytes by using a fluorescent probe, Zinquin: relationship to me- tallothionein and intracellular zinc. *Biochem J.* **303**, 781-786 (1994).

38. Hughes, M.N. In comprehensive coordination chemistry. The synthesis, reactions, properties and applications of coordination compounds. in *Coordination Compounds in Biology.* , Vol. 6 (eds. Wilkinson, G., Gillard, R.D. & McCleverty, J.A.) (Pergamon Press, Oxford, 1987).

CHAPTER III

ASSESSMENT OF MANGANESE TRANSPORT KINETICS TO FUNCTIONALLY CHARACTERIZE THE DECREASED MANGANESE ACCUMULATION IN MUTANT COMPARED TO WILD-TYPE ST*Hdh* CELLS

Introduction

Manganese (Mn) is stringently regulated in the brain and necessary for normal growth, cellular homeostasis, and development. However, excessive levels through dietary intake and occupational routes can accumulate in the brain and alter the basal ganglia function to induce neuron dysfunction and neurodegeneration[1-4]. Impairment in metal ions and metal-dependent enzymes has been reported in HD. For example, Dexter and colleagues have provided evidence for elevated Cu and Fe levels in the corpus striatum of postmortem human brain tissues[5,6]. Moreover, emerging reports have elucidated striking similarities in the pathophysiological mechanisms between HD and metal toxicity[3,7-11].

Several modes of Mn uptake transport across the blood brain barrier have been reported and suggested to occur via facilitated diffusion, active transport through DMT1, voltage-regulated and stored operated Ca^{2+} channels, ZIP8, citrate, and the TfR transporters[3]. Approximately 80% of Mn in plasma is bound to proteins and a smaller

fraction bound to Tf, an iron-binding protein[12]. Mn transport through TfR is exclusively present in the trivalent oxidation-state[13]. Intracellular Mn^{2+} is sequestered into the mitochondria of brain and liver via the Ca^{2+} uniporter[14,15]. However, there has been conflicting reports to support either the mitochondria or nuclei as the cellular organelle that accumulates the primary pool of Mn in the cell[16-18]. The efflux mechanism of cellular mitochondrial Mn^{2+} is mediated preferentially through an active, but slow Na^{+}-independent mechanism with minimal transport over the Na^{+}-dependent efflux mechanism[19]. This slow Mn efflux has been suggested to account for the net Mn accumulation in the mitochondria. Nevertheless, the cytoplasmic Fe^{2+} exporter, ferroportin-1, has been hypothesized and reported to be a candidate Mn exporter because its surface localization and protein expression is perturbed following Mn exposure[20].

In spite of the numerous reports implicating altered metal homeostasis in *in vitro* and *in vivo* models of HD, it is still unclear the nature of the metal transport dynamics that underlie the altered metal homeostasis observed in HD. However, two independent studies have examined Mn transport in glia cells (astrocytes) using radiotracer $^{54}Mn(II)$ and reported discrete modes of Mn transport dynamics[21,22]. In fact, while Wedler and Aschner have demonstrated that astrocytes can efficiently transport Mn through specific transporter systems that are inhibited by excess extracellular Ca^{2+}, they also show that astrocytes exhibit saturation kinetics and accumulate Mn. Furthermore, Mn efflux in astrocytes is biphasic and comprised of a slow and rapid efflux modules[21,22]. Nevertheless, we have previously reported and described a disease-toxicant screen that was performed using a neuronal striatal cell line model of HD (wild-type ST*Hdh*$^{(Q7/Q7)}$ and mutant ST*Hdh*$^{(111/Q111)}$). The screen revealed a gene-environment interaction between

mutant HTT and Mn. Specifically; expression of mutant HTT decreased net Mn accumulation in mutant ST*Hdh*$^{(Q111/Q111)}$ cells and the striatum of a mouse model of HD. In addition, the decreased Mn accumulation correlated with diminished vulnerability to Mn induced cytoxicity[23,24].

In chapter II, we reported the establishment, development, and validation of a novel fluorescence-based Mn detection assay (CFMEA). This assay accurately measures cellular Mn levels in cultured HD striatal cells following Mn exposure (Figure II. 6. and 7.). The discovery of the HD-Mn disease-toxicant interaction further supports the need to investigate the Mn transport kinetics that underlies the Mn accumulation deficit in mutant HTT striatal cells. Based on the unique transport dynamics reported in glia cells and the alterations in metal homeostasis caused by expression of mutant HTT protein, we hypothesized that expression of mutant HTT impairs Mn homeostasis to cause decreased Mn accumulation via alterations in Mn transport kinetic mechanisms, specifically; uptake, cellular storage, or efflux. Importantly, these three possible transport mechanisms are not mutually exclusive. The Mn transport dynamics in wild-type ST*Hdh*$^{(Q7/Q7)}$ and mutant ST*Hdh*$^{(111/Q111)}$ cells was assessed with CFMEA and the traditional fura-2 loaded Mn-quenching kinetic assays. Finally, other studies have previously utilized the traditional fura-2 loaded Mn-quenching assays to assess intracellular metal ion concentration and transport in loaded cells and demonstrated a rapid and time-dependent quenching of fura-2 fluorescence following metals, including Mn exposure[25-30].

Materials and Methods

Chemicals, reagents, and cell culture supplies

Unless indicated, cell culture media and supplements were obtained from Mediatech (Manassas, VA). Cell lines were grown in Dulbecco's modified Eagle's medium (DMEM) with 10% fetal bovine serum (Atlanta Biologicals, Lawrenceville, GA, and Sigma, St. Louis, MO), L-glutamine, 400μg/ml G418 and Penicillin-Streptomycin. Manganese (II) chloride heptahydrate ($MnCl_2 . 7H_2O$) was from Alfa Aesar (Ward Hill, MA). Ultra-pure fura-2 salt (cell impermeable, ENZ-52007) and fura-2 AM salt (cell permeable, ALX-620-005) were obtained from ENZO Biochem (New York, NY). The HEPES salt exposure buffer consisted of 25mM HEPES buffer (pH 7.2), 140mM NaCl, 5.4mM KCl, and 5mM D-glucose (Sigma). The Krebs-Ringers (KR) buffer consisted of 135mM NaCl, 5mM KCl, 0.4mM KH_2PO_4, 1.8mM $CaCl_2$, 1mM $MgSO_4$, 20mM HEPES, and 5.5mM D-glucose, pH 7.4 (Sigma). 1X ultra-pure phosphate-buffered saline (PBS), pH 7.4, without calcium and magnesium was used for post Mn exposure washes. Triton X-100 was obtained from Sigma. Deoxyribonucleic acid sodium salt from salmon testes (Catalog # D1626) was obtained from Sigma (St. Louis, MO). Quant-iT™ PicoGreen dsDNA Reagent (Catalog # P7589) was obtained from Molecular Probes (Carlsbad, CA). 1x TE buffer used for the dilution of PicoGreen reagent was composed of 1 M Tris-HCl (pH 7.5) and 0.5 M EDTA (pH 8.0) prepared with DNase-free water and pH adjusted to 7.5.

Cell culture

Wild-type ST*Hdh*$^{(Q7/Q7)}$ and mutant ST*Hdh*$^{(111/Q111)}$ were grown as previously described [24,31-33]. In brief, wildtype ST*Hdh*$^{Q7/Q7}$ and mutant ST*Hdh*$^{Q111/Q111}$ cells were plated in a clear polystyrene 96 well plate at 20,000 cells per 0.32 cm^2 (surface area) respectively the evening before treatment and allowed to grow in a 33°C incubator. $MnCl_2$ was added to the KR buffer, complete culture media, or HEPES salt exposure buffer the morning of exposure. Total extracted cellular Mn levels were assessed by CFMEA or the traditional fura-2 loaded Mn-quenching kinetic assay.

Mn-fura-2 standard curve

Cell-free Mn-fura-2 saturation binding curve was generated using a ten point Mn-fura-2 curve with samples containing 1 µL of different 100X stock Mn standards (0 – 100 mM) added to 99 µL of 0.5 µM fura-2 in PBS with 0.1% Triton X-100 (PTx) and assayed in a clear polystyrene 96-well assay. After 5 seconds orbital shake, fura-2 fluorescence was measured at the Ca^{2+} isosbestic point of Ex_{360} (bandwidth of filter = ± 35 nm) and Em_{535} (bandwidth of filter = ± 25 nm) with a Beckman coulter DTX 880 multimode plate reader using multimode analysis software (version 3.2.0.6) and top read settings. The average raw fluorescence signal values (RFU) of the 0 µM Mn samples within each independent standard curve were defined as the 100% maximal fluorescence for that experiment after background subtraction. RFU of each well was then normalized as percent maximal fluorescence ($\%_{MAX}$) to this value. A one-site specific saturation-

binding curve with Hill slope could be fit to $\log_{10}$ Mn concentration (x-axis) and either $\%_{MAX}$ (y-axis) or RFU (y-axis) by non-linear regression analysis using graphpad prism software (version 5.0b). As utilization of $\%_{MAX}$ rather than RFU was found to control better for the experimental variation, we preferred use of $\%_{MAX}$ for experimental determination of extracted Mn concentrations. To permit back calculations of extracted Mn levels from experimentally determined $\%_{MAX}$ values we used the trend line command in Microsoft Excel to fit power (Mn concentration = $A\bullet(\%_{MAX})^B$) and logarithmic (Mn concentration = $A\bullet\ln(\%_{MAX})+B$) equations to the standard curve data and calculated binding curve from non-linear regression analysis. Power curves were used for $\%_{MAX}$ values less than 50% and logarithmic curves for values greater than 50%, on either side of the inflection point of the saturation-binding curve plotted with Mn concentration (x-axis) and $\%_{MAX}$ (y-axis). These mathematical models used for calculating extracted Mn concentration routinely fit the saturation binding curves and standards data with r^2 values greater than 0.995.

Quantification of net cellular Mn levels in cultured cell-extracts by CFMEA

Wildtype ST*Hdh*$^{Q7/Q7}$ and mutant ST*Hdh*$^{Q111/Q111}$ were cultured in clear polystyrene 96 well plates and exposed to varying $MnCl_2$ concentrations. After exposure, the media was discarded and cells quickly washed three times with 200 µL PBS. The cells were extracted at 33°C for 1 hour in 100 µL PTx with 0.5 µM fura-2. Changes in fura-2 fluorescence caused by Mn quenching were measured on a plate reader as described in the Mn-fura-2 standard curve section. Extracted Mn concentrations from

cultured cells were calculated using the logarithmic and power Mn standard curve (generated in the cell-free Mn-fura-2 standard curve section) with the $\%_{MAX}$ of each sample. Experimental sample $\%_{MAX}$ was determined by normalizing the RFU of each Mn-exposed sample with the RFU of vehicle-only samples (untreated), which was defined as the experimental 100% maximal fluorescence signal.

PicoGreen dsDNA standard curve

PicoGreen standard curve was generated as previously published[34] and described in chapter II. In brief, 100 µL salmon testes dsDNA standards (0 – 1000 µg/mL) prepared in 0.1% PTx was added to 50 µL of PicoGreen reagent diluted in 1x TE buffer (1:400) in a 96 well plate. In addition, the background was determined by adding 100 µL 0.1% PTx and 50 µL 1x TE buffer. The standard curve plate was incubated at room temperature in the dark for 5 minutes and the fluorescence in each well measured with a plate reader at Ex_{485} (bandwidth of filter = ± 20 nm), Em_{535} (bandwidth of filter = ± 25 nm), and integration time of 200 ms with the indicated plate reader using multimode analysis software (version 3.2.0.6) and top read settings. The average background fluorescence read was subtracted from each of the salmon testes dsDNA PicoGreen fluorescence tested in the standard curve. A standard linear regression analysis in Microsoft Excel was used to obtain a linear equation from the standard curve data.

Normalization of cellular Mn levels to dsDNA

Following CFMEA analysis, 50 µL of 1:400 PicoGreen solution in 1x TE buffer was added to each well containing cell-extract (100 µL). The cell extracts were further incubated and changes in fluorescence measured as described in the PicoGreen dsDNA standard curve section. The concentration of dsDNA in each cell-extract was calculated using the linear equation generated from the salmon DNA standard curve and normalized to Mn levels in the cell-extracts.

Traditional fura-2 loaded Mn-quenching kinetic assay

Wild-type ST*Hdh*$^{(Q7/Q7)}$ and mutant ST*Hdh*$^{(111/Q111)}$ cells were plated in a clear polystyrene 96 well plate at 20,000 cells per 0.32 cm^2 (surface area) the evening before exposure. Cells were washed three times with 200 µL KR buffer to remove residual culture media. To obtain equal loading of the high affinity cell permeable Ca^{2+} probe fura-2 AM in both genotypes, wildtype and mutant striatal cells were loaded with 100 µL of 5 and 10 µM fura-2 AM dissolved in KR buffer at room temperature, respectively. After 30 minutes loading in the dark, cultured HD striatal cells were washed three times with 200 µL KR buffer and allowed to de-esterify in 100 µL KR buffer for an additional 15 minutes at room temperature and stored in the dark. Following completion of de-esterification in the cultured HD striatal cells, the buffer was replaced with fresh KR buffer. The baseline intracellular fura-2 fluorescence was measured for both genotypes at the Ca^{2+} isosbestic point (Ex_{360}) and emission (Em_{535}) nm with a plate reader using top

read and 33°C settings. The cultured HD striatal cells were exposed with 100 µL of 0, 100, or 250 µM $MnCl_2$ prepared in KR buffer. Changes in fura-2 fluorescence induced by intracellular Mn quenching was measured at an integration time of 200 ms in increments of 1 minute for up to 30 minutes at the Ca^{2+} isosbestic point (Ex_{360}) and emission (Em_{535}) nm and compared to vehicle. The vehicle fluorescence was subtracted from each $MnCl_2$ exposed cell sample within the same increment read. The difference in fura-2 quenching (ΔF) in each cell sample was calculated as $([F_{(i)}- F_{(o)}]/F_{(i)})$ and averaged across six replicates for each genotype per exposure concentration. $F_{(i)}$ is the initial fluorescence following $MnCl_2$ exposure and $F_{(o)}$ is the second increment fluorescence read of the same well. The $F_{(i)}$ and $F_{(o)}$ from each well on the 96 well plate decreases over the exposure duration. Thus, enabling for indirect assessment of Mn uptake and cellular storage properties.

Statistical Analysis

Univariate and repeated-measures ANOVA tests were performed using SPSS 18 software (IBM, Inc., Chicago, IL). *Post hoc* analysis and pairwise comparisons were done using Microsoft Excel (Microsoft, Redmond, WA) by Student's *t*-tests (two tailed) or testing for nonoverlap of the 95% confidence interval for normalized ratios; error bars are expressed as standard error of the mean (SEM). Standard deviations (SDEVs) for the difference in net Mn levels were calculated by appropriate propagation of uncertainty calculations for subtraction of sample means, with significant differences between wildtype and mutant cells evaluated by non-overlap of the 95% confidence interval.

Results

Mutant HTT expression impairs net Mn accumulation in a broad concentration- and time-dependent manner

To determine if CFMEA was capable of detecting net Mn accumulation deficit in mutant ST*Hdh*$^{(Q111/Q111)}$ cells previously identified by GFAAS [23,24], we exposed cultured wild-type ST*Hdh*$^{(Q7/Q7)}$ and mutant ST*Hdh*$^{(Q111/Q111)}$ cells to different $MnCl_2$ concentrations for 27 hours in media. After Mn exposure, net Mn accumulation was measured with CFMEA. We observed a concentration-dependent increase in net Mn accumulation in both wild-type ST*Hdh*$^{(Q7/Q7)}$ and mutant ST*Hdh*$^{(111/Q111)}$ cells (Figure III. 1.A.). Repeated-measures ANOVA showed a significant main effect of Mn-exposure ($F_{(3, 12)} = 176.84$, $p<0.0001$) and genotype ($F_{(1, 4)} = 14.02$, $p = 0.02$), as well as exposure by genotype interaction ($F_{(3, 12)} = 5.215$, $p< 0.02$). To explore the minimum duration required for the detection of mutant Mn accumulation deficit, we exposed wild-type ST*Hdh*$^{(Q7/Q7)}$ and mutant ST*Hdh*$^{(111/Q111)}$ to 100 μM $MnCl_2$ for 6 and 27 hrs and measured net Mn accumulation with CFMEA. Repeated-measures ANOVA showed a significant main effect of duration ($F_{(1, 4)} = 100.4$, $p = 0.001$) and genotype ($F_{(1, 4)} = 19.93$ $p = 0.01$) on Mn accumulation (Figure III. 1.B.). However, the magnitude difference in net Mn accumulation between wild-type and mutant cells was substantially enhanced after 6 hrs exposure compared to 27 hrs. This data confirms a concentration- and time-dependent Mn accumulation deficit in mutant HD striatal cells. In addition, it suggests that future studies aimed at understanding the mutant Mn transport defect could be performed at earlier time points other than 27 hrs.

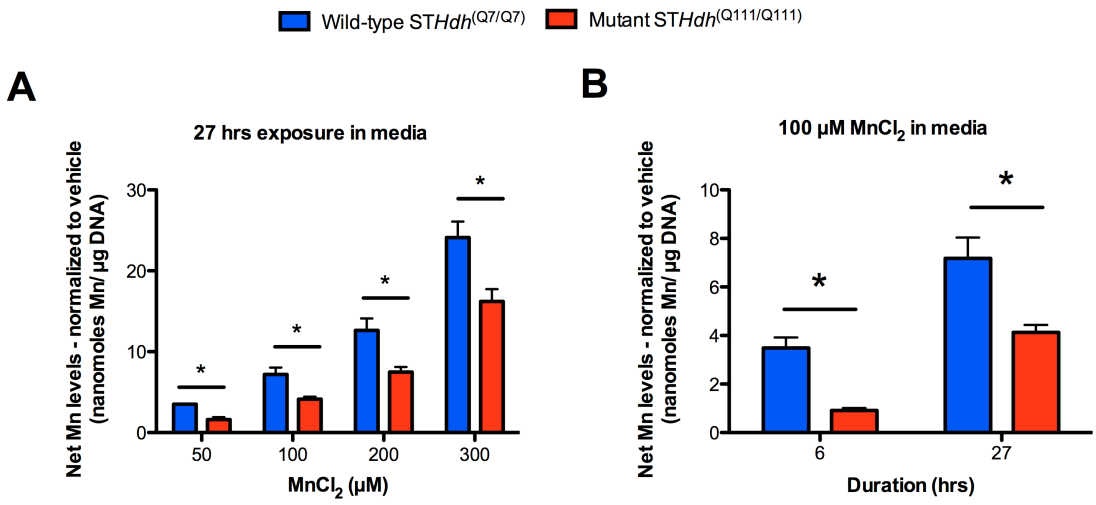

Figure III. 1. Mutant HTT striatal cells exhibit defect in net Mn accumulation across a broad exposure concentration and duration range. (A) Wild-type ST*Hdh*$^{Q7/Q7}$ (blue) and mutant ST*Hdh*$^{(Q111)/(Q111)}$ (red) cells were exposed to $MnCl_2$ for 27 hrs in media. **(B)** Wild-type ST*Hdh*$^{Q7/Q7}$ and mutant ST*Hdh*$^{(Q111)/(Q111)}$ cells were exposed to 100 µM $MnCl_2$ for 6 and 27 hrs in media. Net Mn accumulation in (A) and (B) were measured with CFMEA. Changes in Mn levels following Mn exposure were first normalized to vehicle and further normalized to dsDNA levels on a per well basis. N=3; 8 wells/exposure condition. Mean levels are indicated ± SEM. (*) Indicates significant main effect of exposure and genotype on Mn accumulation in wild-type ST*Hdh*$^{(Q7/Q7)}$ and mutant ST*Hdh*$^{(111/Q111)}$.

Di-/or trivalent metal ions and serum proteins are not required for the decreased Mn accumulation phenotype in mutant HTT striatal cells

To examine the requirement of metal binding proteins and co-transporter ions in the Mn accumulation deficit observed in mutant HTT striatal cells, we exposed wild-type ST*Hdh*$^{(Q7/Q7)}$ and mutant ST*Hdh*$^{(Q111/Q111)}$ cells to different $MnCl_2$ concentrations for 1 hour in HEPES salt buffer (Figure III. 2.). We reasoned that if mutant striatal cells' Mn accumulation deficit is solely dependent on di-/or trivalent metals, serum proteins, and

known Mn co-transporters present in culture media, then Mn exposure in a HEPES salt buffer lacking the aforementioned media components would abolish the decreased Mn accumulation deficit in mutant ST*Hdh*$^{(Q111/Q111)}$ cells. After 1 hr Mn exposure in HEPES salt buffer, repeated-measures ANOVA showed a significant main effect of Mn-exposure ($F_{(2, 8)} = 172.4$, $p < 0.001$) and genotype ($F_{(1, 4)} = 14.51$, $p = 0.02$), as well as exposure by genotype interaction ($F_{(2, 8)} = 7.582$, $p < 0.01$) (Figure III. 2.A.). However, similar exposure concentrations in media resulted in ~ 2 – 3 fold decrease in net Mn accumulation in both genotypes. Importantly, mutant HD striatal cells accumulated less Mn levels as compared to wild-type (Figure 2. B.). Additionally, repeated measures ANOVA showed a significant main effect of Mn ($F_{(2, 8)} = 175.2$, $p < 0.001$), genotype ($F_{(1, 4)} = 14.58$, $p < 0.05$), and Mn * genotype interactions ($F_{(2, 8)} = 7.707$, $p < 0.05$) following $MnCl_2$ exposure in media containing di-/or trivalent metals, serum proteins, and known Mn co-transporters. This data strongly suggest that the components of media are not required for diminished Mn accumulation in mutant HTT striatal cells. In addition, our data indicates that the components of media may bind to extracellular Mn and decrease its availability for cellular uptake.

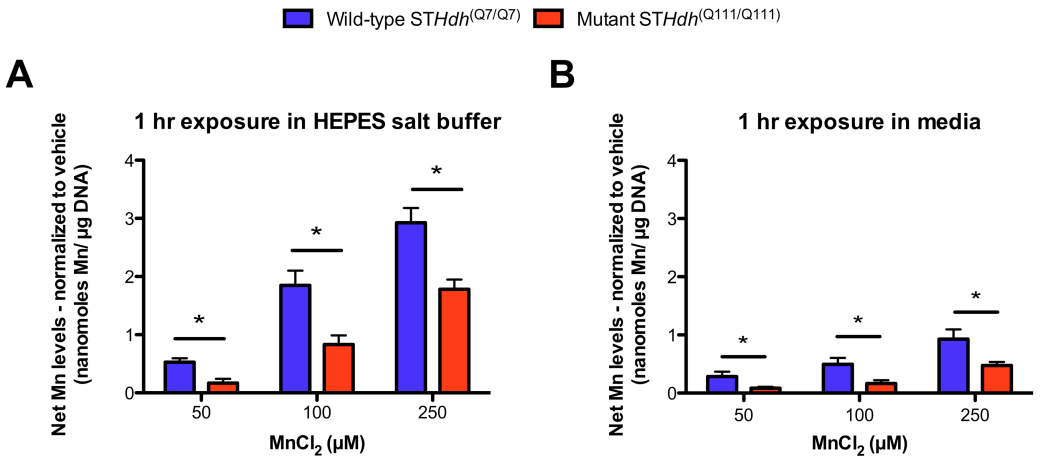

Figure III. 2. Di-/or trivalent metals, serum proteins, and known Mn co-transporters are not required for mutant HTT Mn accumulation deficit. Wild-type ST*Hdh*$^{(Q7/Q7)}$ (blue) and mutant ST*Hdh*$^{(Q111/Q111)}$ (red) cells were exposed to $MnCl_2$ in (**A**) HEPES salt buffer or (**B**) media and cellular Mn levels measured by CFMEA. N=3; 8 wells/exposure condition. Mean levels are indicated $\pm$ SEM. (*) Indicates significant effect of genotype on net accumulation of Mn ($p < 0.05$, repeated measures ANOVA) between wild-type ST*Hdh*$^{(Q7/Q7)}$ and mutant ST*Hdh*$^{(Q111/Q111)}$ cells.

Mutant HTT alters instantaneous Mn uptake kinetics and cellular storage properties

To investigate the effect of mutant HTT expression on instantaneous Mn uptake kinetics in wild-type ST*Hdh*$^{(Q7/Q7)}$ and mutant ST*Hdh*$^{(Q111/Q111)}$ cells, we utilized the traditional fura-2 loaded Mn-quenching kinetic assay. We show that after equivalent loading of cultured wild-type ST*Hdh*$^{(Q7/Q7)}$ and mutant ST*Hdh*$^{(Q111/Q111)}$ cells with the cell-permeable fura-2 dye (fura-2 AM) and exposure to 100 and 250 µM $MnCl_2$ in KR buffer, the instantaneous Mn uptake kinetics in mutant ST*Hdh*$^{(Q111/Q111)}$ cells is significantly decreased ($p<0.0001$, *post hoc t*-test) compared to wild-type ST*Hdh*$^{(Q7/Q7)}$ (Figure III. 3.A.). In addition, the decreased instantaneous Mn uptake was evident as

early as 2 minutes following Mn exposure (Figure III. 3.A.). Furthermore, we observed that the decreased instantaneous Mn uptake kinetics in wild-type ST*Hdh*$^{(Q7/Q7)}$ and mutant ST*Hdh*$^{(Q111/Q111)}$ cells was independent of the concentration of $MnCl_2$ used for the exposure (Figure III. 3A.). Importantly, we observed significant differences ($p<0.001$) in the initial slope of Mn uptake kinetics between wild-type and mutant HTT striatal cells during the first 5 minutes following exposure to 100 and 250 μM $MnCl_2$ (Table III. 2.).

Interestingly, we observed a striking concentration-dependent difference in the cellular Mn saturation rates or cellular storage between wild-type ST*Hdh*$^{(Q7/Q7)}$ and mutant ST*Hdh*$^{(Q111/Q111)}$ cells (Figure III. 3.A.). We show that the difference in cellular Mn storage in both genotypes commences approximately 15 minutes following exposure to 100 and 250 μM $MnCl_2$ (Figure III. 3.A.). In addition, we demonstrate that mutant HTT cells exhibit a concentration- and time-dependent impairment in the instantaneous Mn uptake and cellular storage properties. Furthermore, we examined the uptake and cellular storage kinetics in wild-type ST*Hdh*$^{(Q7/Q7)}$ and mutant ST*Hdh*$^{(Q111/Q111)}$ cells using one-site specific binding curves and observed a significant decrease in the maximum quenching of fura-2 by Mn (Bmax) in mutant ST*Hdh*$^{(Q111/Q111)}$ compared to wild-type ST*Hdh*$^{(Q7/Q7)}$ cells. In addition, the duration required for mutant to exert half maximal effect on fura-2 quenching after Mn uptake (Kd) was substantially decreased compared to wild-type cells (Table III. 1.).

To determine the predominant cellular Mn pools, cytosolic versus total (organelles and cytosolic), that contributes to the diminished cellular Mn storage in mutant ST*Hdh*$^{(Q111/Q111)}$ cells, we exposed cultured wild-type ST*Hdh*$^{(Q7/Q7)}$ and mutant

ST*Hdh*$^{(111/Q111)}$ cells to the same Mn concentrations as used in the kinetic studies (100 and 250 μM $MnCl_2$) for 30 minutes and measured net cellular Mn storage by CFMEA. We reasoned that fura-2 loaded Mn-quenching assay might only measure cytosolic Mn levels and exclude the contribution of organelle-specific Mn storage properties in the cells. Thus, CFMEA would be capable of detecting total extractable Mn levels in the cells (cytosolic and organelles) following Mn exposure. After 30 minutes $MnCl_2$ exposure in KR buffer and CFMEA analysis, repeated-measures ANOVA showed a significant main effect of exposure ($F_{(1, 6)} = 67.13$, $p < 0.001$) and genotype ($F_{(1, 6)} = 177.1$ $p = 0.02$) on net cellular Mn storage (Figure III. 3.B.). This data suggests that mutant HTT expression impairs instantaneous Mn uptake kinetics and total cellular Mn storage properties to cause the observed Mn accumulation deficit in mutant HTT striatal cells.

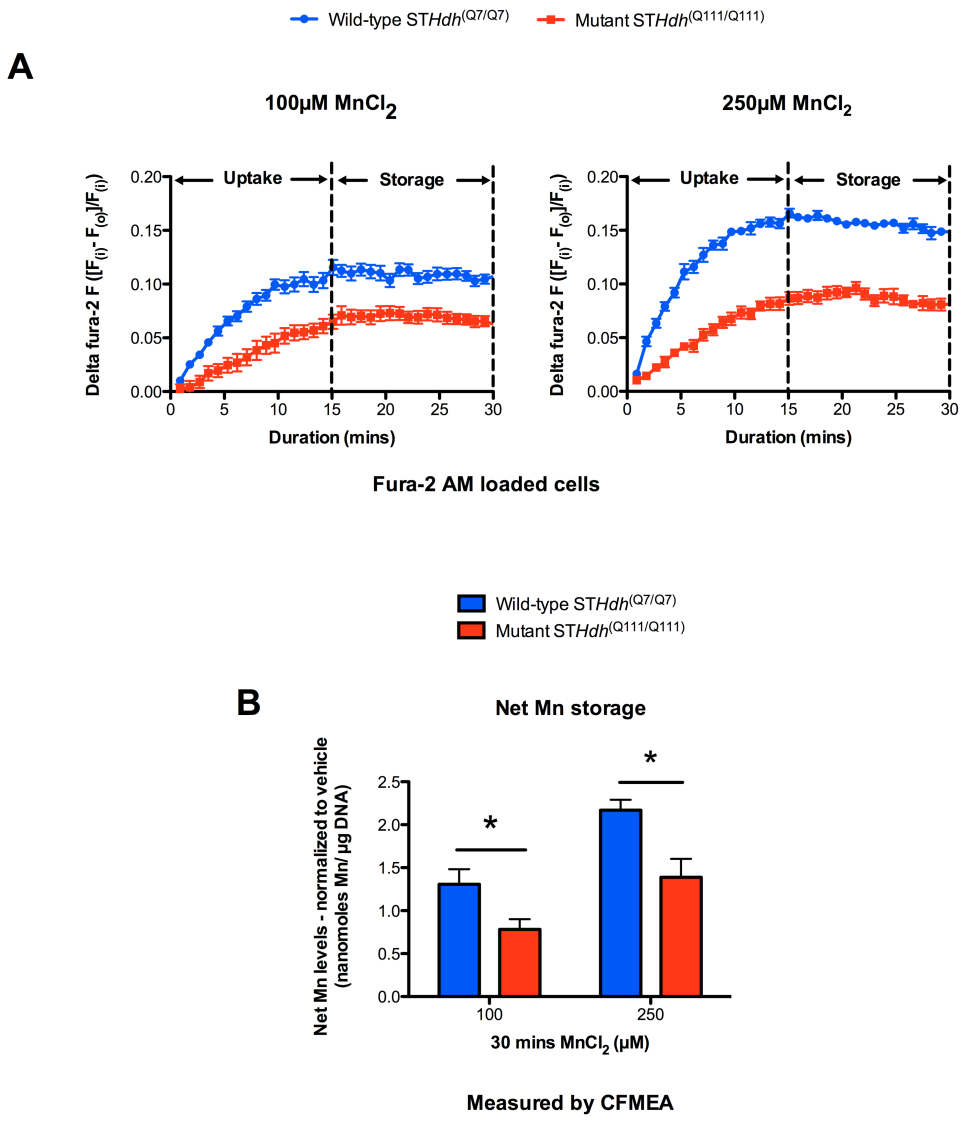

Figure III. 3. Expression of mutant HTT impairs instantaneous Mn uptake kinetics and cellular storage properties in striatal cells. Concentration and time-dependent differences in instantaneous Mn uptake and cellular storage between wild-type ST*Hdh*$^{(Q7/Q7)}$ (blue) and mutant ST*Hdh*$^{(Q111/Q111)}$ (red) cells. Striatal cells were equally loaded with fura-2 AM and exposed to 100 and 250 μM $MnCl_2$ for 30 minutes. Changes in intracellular fura-2 fluorescence by Mn quenching were assessed by fura-2 loaded Mn-quenching kinetic assay. (**B**) Total cellular Mn storage is impaired in mutant HTT expressing striatal cells. Wild-type and mutant HTT striatal cells were exposed to the indicated $MnCl_2$ for 30 mins in HEPES salt buffer and Mn levels measured with CFMEA. N=3; 8 wells/exposure condition. Mean levels are indicated ± SEM. (*) Indicates significant effect of genotype on net cellular Mn storage between wild-type ST*Hdh*$^{Q7/Q7}$ and mutant ST*Hdh*$^{Q111/Q111}$ cells.

Genotype	[$MnCl_2$] µM	Bmax (RFU)	Kd (mins)
Wild-type ST*Hdh*$^{(Q7/Q7)}$	100	0.1095 - 0.1187	3.8900 – 4.6790
Mutant ST*Hdh*$^{(Q111/Q111)}$	100	0.0673 - 0.0799	6.3370 – 8.2670
Wild-type ST*Hdh*$^{(Q7/Q7)}$	250	0.1579 – 0.1646	3.2010 – 3.6020
Mutant ST*Hdh*$^{(Q111/Q111)}$	250	0.0872 - 0.0978	5.0330 – 6.2300

Table III. 1. Summary of instantaneous Mn uptake and cellular storage kinetic properties in HD striatal cells. Examination of instantaneous Mn uptake and cellular storage kinetics using the 95% confidence interval values of saturated Mn binding of fura-2 (B_{max}) and half maximal effective duration (Kd) values for Mn uptake extrapolated from the one-site specific binding curves (Figure III. 3A.).

Genotype	Duration of Exposure (mins)	[$MnCl_2$] µM	Slope	p-value
Wild-type ST*Hdh*$^{(Q7/Q7)}$	0 - 5	100	0.0106 – 0.0144	
Mutant ST*Hdh*$^{(Q111/Q111)}$	0 - 5	100	0.0022 – 0.0085	* <0.001
Wild-type ST*Hdh*$^{(Q7/Q7)}$	6 - 10	100	0.0044 – 0.0114	
Mutant ST*Hdh*$^{(Q111/Q111)}$	6 - 10	100	-0.0003 – 0.0112	* 0.3019
Wild-type ST*Hdh*$^{(Q7/Q7)}$	10 - 15	100	-0.0004 – 0.0066	
Mutant ST*Hdh*$^{(Q111/Q111)}$	10 - 15	100	-0.0007 – 0.0669	* 0.8865
Wild-type ST*Hdh*$^{(Q7/Q7)}$	0 - 5	250	0.0179 – 0.0232	
Mutant ST*Hdh*$^{(Q111/Q111)}$	0 - 5	250	0.0056 – 0.0092	* <0.001
Wild-type ST*Hdh*$^{(Q7/Q7)}$	6 - 10	250	0.0049 – 0.0124	
Mutant ST*Hdh*$^{(Q111/Q111)}$	6 - 10	250	0.0032 – 0.0109	* 0.5551
Wild-type ST*Hdh*$^{(Q7/Q7)}$	10 - 15	250	0.0008 – 0.0054	
Mutant ST*Hdh*$^{(Q111/Q111)}$	10 - 15	250	0.0003 – 0.0059	* 0.9711

Table III. 2. Comparison of instantaneous Mn uptake kinetic slopes following $MnCl_2$ exposure between wild-type and mutant HD striatal cells. Assessment of instantaneous Mn uptake slopes using the 95% confidence interval slope values extrapolated from linear regression analyses in Microsoft Excel of the uptake curves (Figure III. 3A.).

Wild-type and mutant HTT striatal cells exhibit similar net Mn efflux following equal intracellular Mn levels

To explore the efflux kinetics in HTT striatal cells following $MnCl_2$ exposure, wild-type ST*Hdh*$^{(Q7/Q7)}$ and mutant ST*Hdh*$^{(Q111/Q111)}$ cells were equally loaded with fura-2 AM and exposed to 500 μM $MnCl_2$ in KR buffer. After 30 minutes exposure, the cultured cells were quickly rinsed with Mn-free KR buffer and allowed to efflux in extracellular Mn-free KR buffer for an additional 30 minutes. Efflux kinetics was assessed by changes in fura-2 fluorescence and measured by the traditional fura-2 loaded Mn-quenching kinetic assay. We observed a substantial time-dependent increase in Mn efflux kinetics in the wild-type ST*Hdh*$^{(Q7/Q7)}$ compared to mutant ST*Hdh*$^{(Q111/Q111)}$ cells (Figure III. 4.A.). However, this enhanced Mn efflux was mainly due to a two-fold elevated net accumulated Mn levels in wild-type ST*Hdh*$^{(Q7/Q7)}$ and mutant ST*Hdh*$^{(Q111/Q111)}$ cells (Figure III. 4.A.). Hence, we examined Mn efflux kinetics after similar net Mn accumulation levels in the wild-type ST*Hdh*$^{(Q7/Q7)}$ and mutant ST*Hdh*$^{(Q111/Q111)}$ cells. After exposure of cultured HTT striatal cells to 300 and 500 μM $MnCl_2$ respectively for 6 hours in media, net accumulated cellular Mn levels was immediately measured (prior to efflux) or allowed to efflux in fresh Mn-free media that was changed every 5 minutes for 1 hour (post 1 hour Mn efflux) (Figure III. 4.A.). Net Mn accumulation levels in the prior and post Mn efflux were measured with CFMEA. The rationale behind this experiment was to change the equilibrium potential between intra and extra-cellular Mn conditions, which would induce the shuttling of Mn from cellular storage pools into the fresh extracellular Mn-free media. Thus, decreasing the net accumulated Mn levels in the HTT striatal cells. After equivalent cellular Mn loading between wild-type ST*Hdh*$^{(Q7/Q7)}$ and

mutant ST*Hdh*$^{(Q111/Q111)}$ cells, we observed no difference in net Mn efflux between both genotypes (Figure III. 4.B.) This data shows that wild-type and mutant cells have similar efflux kinetics after equivalent intracellular Mn levels and also suggest that the Mn accumulation deficit in mutant HTT expressing striatal cells is not due to an efficient efflux mechanism in mutant ST*Hdh*$^{(Q111/Q111)}$ compared to wild-type ST*Hdh*$^{(Q7/Q7)}$ cells.

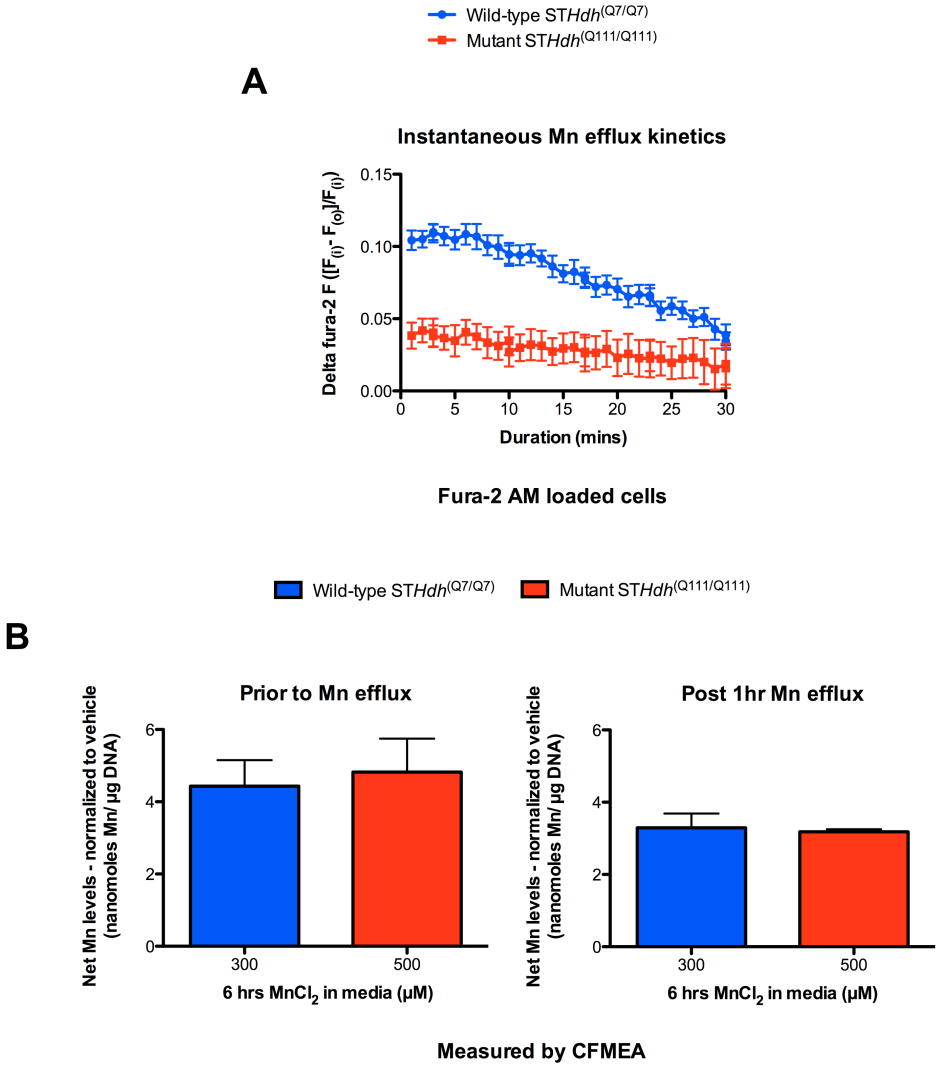

Figure III. 4. Wild-type and mutant HTT striatal cells exhibit similar Mn efflux kinetics following equivalent intracellular Mn levels. (**A**) The instantaneous Mn efflux kinetics graph shows efficient Mn efflux in ST*Hdh*$^{(Q7/Q7)}$ (blue) compared to mutant

ST*Hdh*$^{(Q111/Q111)}$ (red) cells following unequal cellular Mn levels. Wild-type and mutant cells were equally loaded with fura-2 AM and exposed to 500 μM $MnCl_2$ for 30 minutes. Post Mn exposure, intracellular Mn was allowed to efflux in Mn-free KR buffer for 30 minutes. Changes in fluorescence were assessed with fura-2 loaded Mn-quenching kinetic assay. (**B**) Wild-type ST*Hdh*$^{(Q7/Q7)}$ (blue) and mutant ST*Hdh*$^{(Q111/Q111)}$ (red) cells were exposed to 300 μM and 500 μM $MnCl_2$ respectively in media for 6 hours to obtain equivalent intracellular Mn levels. Cellular Mn was extracted (prior to Mn efflux) or allowed to efflux in Mn-free media that was replaced every 5 minutes for 1 hr (post 1hr Mn efflux) before extraction and Mn measurements with CFMEA. N = 3; 6 wells/exposure condition. Mean total Mn efflux levels for (**A**) and (**B**) are indicated ±SDEV.

Conclusions

We tested the hypothesis that alterations in manganese transport kinetics (uptake, cellular storage, and efflux) by expression of mutant HTT contributes to the decreased net Mn accumulation deficit in mutant ST*Hdh*$^{(Q111/Q111)}$ compared to wild-type ST*Hdh*$^{(Q7/Q7)}$ cells following $MnCl_2$ exposure. We demonstrate that expression of mutant HTT significantly reduces both the instantaneous Mn uptake kinetics and cellular Mn storage properties in mutant ST*Hdh*$^{(Q111/Q111)}$ compared to wild-type ST*Hdh*$^{(Q7/Q7)}$ cells following Mn exposure (Figure III. 3.A. and 3.B.). We show that wild-type ST*Hdh*$^{(Q7/Q7)}$ and mutant ST*Hdh*$^{(Q111/Q111)}$ cells exhibit similar Mn efflux rates following equivalent cellular Mn loading (Figure III. 3.A. and 3.B.). In addition, we demonstrate that mutant striatal cells exhibit a broad concentration and time-dependent defect in Mn uptake and accumulation (Figure III 1.A. and 1.B. and Figure III. 3.A.). Finally, we show that di/or trivalent metals, serum proteins, and known Mn co-factors are not required for mutant Mn uptake and cellular storage deficit (Figure III. 2.A.).

Owing to the previously reported concentration and time-dependent Mn uptake and accumulation in glial cells (astrocytes)[21,22], we examined and demonstrated a similar influence of broad Mn concentration and time-dependency on Mn accumulation in the neuronal striatal HTT cells (Figure III. 1.A. and 1.B.). We observed a significant concentration-dependent increase in net Mn accumulation in both wild-type ST*Hdh*$^{(Q7/Q7)}$ and mutant ST*Hdh*$^{(Q111/Q111)}$ cells. However, we noticed a significant decrease in net Mn accumulation in mutant ST*Hdh*$^{(Q111/Q111)}$ compared to wild-type ST*Hdh*$^{(Q7/Q7)}$ cells at all the tested Mn concentrations (Figure III. 1.A.). This data further support the previously published decreased net Mn accumulation in mutant ST*Hdh*$^{(Q111/Q111)}$ cells by GFAAS[24]. Given that the decreased Mn accumulation phenotype observed in mutant ST*Hdh*$^{(Q111/Q111)}$ cells was solely dependent on mutant HTT expression, we reasoned that the difference in Mn accumulation would be observed at an earlier exposure time point other than 27 hrs. Thus, we examined and demonstrated that the mutant Mn accumulation deficit is detectable by CFMEA as early as 6 hrs following exposure to 100μM $MnCl_2$ in media (Figure III. 1.B.). Interestingly, we observed a substantial increase in the magnitude difference between wild-type ST*Hdh*$^{(Q7/Q7)}$ and mutant ST*Hdh*$^{(111/Q111)}$ cells after 6 hrs compared to 27 hrs exposure with 100 μM $MnCl_2$ in media. This enhanced magnitude difference in net Mn accumulation between wild-type ST*Hdh*$^{(Q7/Q7)}$ and mutant ST*Hdh*$^{(Q111/Q111)}$ cells at 6 hrs strongly argues for future assessment of Mn transport dynamics in media or other buffers at earlier time points. This would enable efficient characterization of Mn transport kinetics in the striatal HTT cells. It is possible that during longer Mn exposure duration, other known or putative Mn transporters that are not impaired by mutant HTT expression may be activated via compensatory

mechanisms to increase Mn uptake, intracellular trafficking, and accumulation in the mutant ST*Hdh*$^{(Q111/Q111)}$ cells. Thus, decreasing the magnitude of Mn accumulation between wild-type ST*Hdh*$^{(Q7/Q7)}$ and mutant ST*Hdh*$^{(Q111/Q111)}$ cells. Moreover, the compensatory Mn transporter activation system is highly unlikely regulated directly by mutant HTT expression, albeit it could potentially mask discrete Mn transport kinetics and transporter functions between wild-type ST*Hdh*$^{(Q7/Q7)}$ and mutant ST*Hdh*$^{(Q111/Q111)}$ cells.

Metal ions, carrier proteins, and co-transporters ions have been reported to influence Mn uptake[35-38]. We examined and demonstrated that di-/or trivalent metals, other small anions such as nitrate (NO_3^-) and sulfate (SO_4^{2-}), serum proteins, and known Mn co-transporters are not required for decreased Mn accumulation in mutant HD striatal cells compared to wild-type (Figure III. 2.A.). We report that 1 hr exposure of cultured striatal HTT cells with at least 50 μM $MnCl_2$ in HEPES salt buffer containing NaCl, KCl, and glucose is sufficient to detect a significant decrease in mutant ST*Hdh*$^{(Q111/Q111)}$ Mn accumulation compared to wild-type ST*Hdh*$^{(Q7/Q7)}$ cells (Figure III. 2.A.). Moreover, similar Mn exposure concentrations and duration in media yielded ~ 2 – 3 fold decrease in Mn accumulation in both genotypes when compared to the HEPES salt buffer exposure conditions (Figure III. 2.A. and 2.B.). Importantly, we observed significant differences in net Mn accumulation between wild-type and mutant HTT striatal cells at all the tested $MnCl_2$ exposure concentrations in media (Figure III. 2.B.). The 2 – 3 fold decrease in Mn accumulation in the HD striatal cells in media versus HEPES salt buffer exposure conditions may likely be due to the binding or association of extracellular Mn with high-affinity serum proteins, for example; albumin and beta$_1$-globulin, other

proteins, small anions such as nitrate (NO_3^-) and sulfate (SO_4^{2-}), which decreases the availability and concentration of extracellular Mn for cellular uptake.

The premise behind the traditional fura-2 loaded Mn-quenching assay is that as Mn influxes into cultured HTT striatal cells, it quenches the loaded fura-2 fluorescence. Change in fluorescence over time is inversely correlated with Mn uptake and saturation levels. Thus, we combined both CFMEA and the traditional fura-2 loaded Mn-quenching to functionally discriminate Mn transport kinetics in wild-type ST*Hdh*$^{(Q7/Q7)}$ and mutant ST*Hdh*$^{(Q111/Q111)}$ cells. We characterized the Mn^{2+} uptake and saturation in the HTT striatal cells by measuring the instantaneous rate and time-dependence, as well as net cellular Mn storage into cultured HTT striatal cells. We report that expression of mutant HTT impedes the instantaneous Mn uptake kinetics as early as 2 minutes following $MnCl_2$ exposure (Figure III. 3.A. and Table III. 1.). In addition, we show that the maximum Mn uptake or saturation rate in the HD striatal cells exposed with $MnCl_2$ in KR buffer was observed between 15 and 30 minutes. In spite of the differences in concentration and time-dependence uptake between wild-type ST*Hdh*$^{(Q7/Q7)}$ and mutant ST*Hdh*$^{(Q111/Q111)}$ cells, we demonstrate that they exhibit similar duration (~15 minutes) in the initiation of Mn saturation (Figure III. 3.A.). Importantly, we show that mutant ST*Hdh*$^{(Q111/Q111)}$ cells have decreased Mn saturation rate or cellular storage compared to wild-type ST*Hdh*$^{(Q7/Q7)}$ cells following $MnCl_2$ exposure (Figure III. 3.A. and Table III. 1.). Importantly, examination of the Mn transport kinetics showed a significant decrease in the instantaneous Mn uptake and cellular storage properties between wild-type ST*Hdh*$^{(Q7/Q7)}$ and mutant ST*Hdh*$^{(Q111/Q111)}$ cells as shown by the non-overlapping 95% confidence intervals (Table III. 1.). Furthermore, we demonstrated that the Mn uptake

kinetic slopes between wild-type ST*Hdh*$^{(Q7/Q7)}$ and mutant ST*Hdh*$^{(Q111/Q111)}$ cells is significantly different during the first 5 minutes following $MnCl_2$ exposure (Figure III. 3.A. and Table III. 2.). This data suggest that decreased Mn accumulation in mutant striatal cells may be due in part due to an impaired primary Mn uptake transport system that is inherit to mutant HTT expressing striatal cells. Our data also suggest that during the latter $MnCl_2$ exposure duration (5- 15 minutes), other compensatory/secondary Mn uptake transporter systems may be similarly activated to facilitate Mn uptake in both genotypes. Although these compensatory/secondary Mn uptake transport system are capable of abolishing the difference in Mn uptake kinetics slope between wild-type ST*Hdh*$^{(Q7/Q7)}$ and mutant ST*Hdh*$^{(Q111/Q111)}$ cells, they are incapable of rescuing the phenotypic Mn accumulation deficit observed in mutant HTT striatal cells (Figure III. 3.A. and Table III. 2.). Previous studies have reported that Mn accumulates in organelles, including mitochondria[14,39], nucleus[16], and golgi[40]. Interestingly, it has been suggested that loaded fura-2 may not be efficiently sequestered into organelles, but only measures changes in cytosolic metal ion concentrations, including Mn. Based on the ability of Mn to be sequestered into organelles that may not be detected by the traditional fura-2 loaded Mn quenching assay, we examined the cellular Mn pools that contributes to the diminished cellular Mn storage in mutant ST*Hdh*$^{(Q111/Q111)}$ cells. We explored and demonstrated that the prevalent cellular Mn pool that involved in the diminished cellular Mn storage properties in mutant ST*Hdh*$^{(Q111/Q111)}$ cells encompasses both cytosolic and organelle-accumulated Mn. This was determined by the ability of CFMEA to detect both the cytosolic and organelle (total) accumulated Mn levels. Interestingly, we observed an approximately two-fold decrease in net Mn accumulation Mn in mutant ST*Hdh*$^{(Q111/Q111)}$

compared to wild-type ST*Hdh*$^{(Q7/Q7)}$ cells after 30 minutes exposure to 100 and 250 μM $MnCl_2$ in KR buffer and Mn levels measured by both the traditional fura-2 loaded Mn quenching and CFMEA assays (Figure III. 3.A. and 3.B.). In addition, we observed similar net cellular Mn storage between wild-type ST*Hdh*$^{(Q7/Q7)}$ and mutant ST*Hdh*$^{(Q111/Q111)}$ cells exposed to 100 μM and 250 μM $MnCl_2$ in KR buffer for 30 minutes (Figure III. 3.B.). The instantaneous Mn uptake difference between wild-type ST*Hdh*$^{(Q7/Q7)}$ and mutant ST*Hdh*$^{(Q111/Q111)}$ cells strongly suggests a defective primary Mn transporter system in mutant ST*Hdh*$^{(Q111/Q111)}$ cells. It is highly unlikely that the observed similar Mn saturation time points for both genotypes (~15 minutes) was due to (i) maximal saturation of the loaded fura-2 dye with intracellular Mn because both wild-type ST*Hdh*$^{(Q7/Q7)}$ and mutant ST*Hdh*$^{(111/Q111)}$ cells were equally loaded and possess distinct Mn influx rates; or (ii) increased mutant HTT sequestration of the fura-2 dye into cellular organelles, which would decrease its availability for Mn quenching. Finally, we demonstrate that mutant HTT expression impairs instantaneous Mn uptake kinetics and total cellular Mn storage properties to cause the observed Mn accumulation deficit in mutant ST*Hdh*$^{(Q111/Q111)}$ cells.

We explored the role of Mn efflux kinetics in the mutant Mn accumulation deficit phenotype. After examination of Mn efflux rates with the traditional fura-2 Mn-quenching assay, we observed a substantial time-dependent increase in wild-type ST*Hdh*$^{(Q7/Q7)}$ Mn efflux rates compared to mutant ST*Hdh*$^{(Q111/Q111)}$ cells following exposure to 500 μM $MnCl_2$ (Figure III. 4.A.). However, we reasoned that the increased Mn efflux rates in wild-type ST*Hdh*$^{(Q7/Q7)}$ compared to mutant ST*Hdh*$^{(Q111/Q111)}$ cells might be due to difference in net Mn accumulation levels in the cells prior to assessment

of Mn efflux kinetics. Furthermore, after equal loading of wild-type ST*Hdh*$^{(Q7/Q7)}$ and mutant ST*Hdh*$^{(Q111/Q111)}$ cells with 300 μM and 500 μM $MnCl_2$ respectively in media, we assessed the net Mn efflux after 1 hr. We report that both wild-type ST*Hdh*$^{(Q7/Q7)}$ and mutant ST*Hdh*$^{(Q111/Q111)}$ cells exhibit similar net Mn efflux kinetics after equal intracellular Mn levels (Figure III. 4.B.). Unfortunately, the precise nature of Mn efflux mechanism in the HD striatal cells during the 1 hr Mn-free extracellular KR buffer efflux is unknown. However, previous reports have postulated that distinct Mn cellular pools exist[21,22]. These discrete cellular Mn pools have been speculated to be involved in the fast phase of Mn efflux, slow equilibrium, and irreversibly bound Mn that are unavailable for efflux. In addition, biphasic Mn efflux kinetic profiles have been reported to exist in cultured astrocytes[21,22]. Thus, it is possible that both wild-type ST*Hdh*$^{(Q7/Q7)}$ and mutant ST*Hdh*$^{(Q111/Q111)}$ cells possess similar Mn efflux pools. However, the cellular Mn efflux pools that contribute to the biphasic Mn efflux kinetics may have occurred during the constant 5 minutes interval changes of extracellular Mn-free media and therefore was undetectable after 1 hr Mn efflux. Moreover, it is known that a fairly large proportion of Mn uptake into chick glial cells (68%) and hepatocytes (60%) associate predominantly with proteins in the cytosol that are unable to be dissociated via membrane permeabilization with dextran sulfate[21,22,41]. Furthermore, we observed similar net Mn efflux between wild-type ST*Hdh*$^{(Q7/Q7)}$ and mutant ST*Hdh*$^{(Q111/Q111)}$ cells following equal cellular Mn loading. This further supports the view that cytosolic Mn association with proteins is not influenced by expression of mutant HTT. Importantly, the equilibrium between cytosolic Mn associations with proteins may dictate the available cellular Mn pools for efflux. Nevertheless, our data supports the previously published evidence of

unchanged protein levels in the suggested Mn exporter, ferroportin-1, in both wild-type ST*Hdh*$^{(Q7/Q7)}$ and mutant ST*Hdh*$^{(Q111/Q111)}$ cells following $MnCl_2$ exposure[23].

In summary, our findings provide the framework for understanding the Mn^{2+} transport kinetics underlying the Mn accumulation deficit in mutant ST*Hdh*$^{(Q111/Q111)}$ cells. Furthermore, our data supports the postulated and accepted criteria of Mn transport mechanism in cells, including; Mn uptake via facilitated diffusion or active metal transporters, cellular Mn storage indicated by the saturation kinetics, and the ability of proteins and metal ions to associate with Mn and influence its transport dynamics. Importantly, our data elucidates a discrete nature of mutant HTT modulation of Mn transport kinetics as well as the need to control for equal cellular Mn levels when assessing Mn efflux rates in different genotypes and cell-types. The discussed findings above substantiate the importance of investigating the transporter system(s) underlying the mutant Mn uptake and cellular storage deficits.

References

1. Dobson, A.W., Erikson, K.M. & Aschner, M. Manganese neurotoxicity. *Ann N Y Acad Sci* **1012**, 115-28 (2004).

2. Olanow, C.W. Manganese-induced parkinsonism and Parkinson's disease. *Ann N Y Acad Sci* **1012**, 209-23 (2004).

3. Aschner, M., Guilarte, T.R., Schneider, J.S. & Zheng, W. Manganese: recent advances in understanding its transport and neurotoxicity. *Toxicol Appl Pharmacol* **221**, 131-47 (2007).

4. Ensing, J.G. Bazooka: cocaine-base and manganese carbonate. *J Anal Toxicol* **9**, 45-6 (1985).

5. Dexter, D.T., Carayon, A., Javoy-Agid, F., Agid, Y., Wells, F.R., Daniel, S.E., Lees, A.J., Jenner, P. & Marsden, C.D. Alterations in the levels of iron, ferritin and other trace metals in Parkinson's disease and other neurodegenerative diseases affecting the basal ganglia. *Brain* **114 (Pt 4)**, 1953-75 (1991).

6. Dexter, D.T., Jenner, P., Schapira, A.H. & Marsden, C.D. Alterations in levels of iron, ferritin, and other trace metals in neurodegenerative diseases affecting the basal ganglia. The Royal Kings and Queens Parkinson's Disease Research Group. *Ann Neurol* **32 Suppl**, S94-100 (1992).

7. Fox, J.H., Kama, J.A., Lieberman, G., Chopra, R., Dorsey, K., Chopra, V., Volitakis, I., Cherny, R.A., Bush, A.I. & Hersch, S. Mechanisms of copper ion mediated Huntington's disease progression. *PLoS One* **2**, e334 (2007).

8. Molina-Holgado, F., Hider, R.C., Gaeta, A., Williams, R. & Francis, P. Metals ions and neurodegeneration. *Biometals* **20**, 639-54 (2007).

9. Wright, R.O. & Baccarelli, A. Metals and neurotoxicology. *J Nutr* **137**, 2809-13 (2007).

10. Choi, C.J., Anantharam, V., Martin, D.P., Nicholson, E.M., Richt, J.A., Kanthasamy, A. & Kanthasamy, A.G. Manganese upregulates cellular prion protein and contributes to altered stabilization and proteolysis: relevance to role of metals in pathogenesis of prion disease. *Toxicol Sci* **115**, 535-46 (2010).

11. Firdaus, W.J., Wyttenbach, A., Giuliano, P., Kretz-Remy, C., Currie, R.W. & Arrigo, A.P. Huntingtin inclusion bodies are iron-dependent centers of oxidative events. *FEBS J* **273**, 5428-41 (2006).

12. Foradori, A.C. The discrimination between magnesium and manganese by serum proteins. *J Gen Physiol* **50** 2255-2266 (1967).

13. Aisen, P., Aasa, R. & Redfield, A.G. The chromium, manganese, and cobalt complexes of transferrin. *J Biol Chem* **244**, 4628-33 (1969).

14. Gunter, T.E. & Puskin, J.S. Manganous ion as a spin label in studies of mitochondrial uptake of manganese. *Biophys J.* , 625-35 (1972).

15. Liccione, J.J. & Maines, M.D. Selective vulnerability of glutathione metabolism and cellular defense mechanisms in rat striatum to manganese. *J Pharmacol Exp Ther* **247**, 156-61 (1988).

16. Kalia, K., Jiang, W. & Zheng, W. Manganese accumulates primarily in nuclei of cultured brain cells. *Neurotoxicology* **29**, 466-70 (2008).

17. Gavin, C.E., Gunter, K.K. & Gunter, T.E. Manganese and calcium transport in mitochondria: implications for manganese toxicity. *Neurotoxicology* **20**, 445-53 (1999).

18. Zwingmann, C., Leibfritz, D. & Hazell, A.S. Energy metabolism in astrocytes and neurons treated with manganese: relation among cell-specific energy failure, glucose metabolism, and intercellular trafficking using multinuclear NMR-spectroscopic analysis. *J Cereb Blood Flow Metab* **23**, 756-71 (2003).

19. Bowman, A.B., Erikson, K.M. & Aschner, M. Manganese - The two faces of essentiality and neurotoxicity. in *Metals and Neurodegeneration* (ed. Huang, S.) (Research Signpost, Kerala, India, 2010).

20. Yin, Z., Jiang, H., Lee, E.Y., Ni, M., Erikson, K.M., Milatovic, D., Bowman, A.B. & Aschner, M. Ferroportin is a manganese-responsive protein that decreases manganese cytotoxicity and accumulation. *J Neurochem.* **112**, 1190–1198. (2011).

21. Aschner, M., Gannon, M. & Kimelberg, H.K. Manganese uptake and efflux in cultured rat astrocytes. *J Neurochem* **58**, 730-5 (1992).

22. Wedler, F.C., Ley, B.W. & Grippo, A.A. Manganese(II) dynamics and distribution in glial cells cultured from chick cerebral cortex. *Neurochem Res* **14**, 1129-35 (1989).

23. Williams, B.B., Kwakye, G.F., Wegrzynowicz, M., Li, D., Aschner, M., Erikson, K.M. & Bowman, A.B. Altered manganese homeostasis and manganese toxicity in a Huntington's disease striatal cell model are not explained by defects in the iron transport system. *Toxicol Sci* **117**, 169-79 (2010).

24. Williams, B.B., Li, D., Wegrzynowicz, M., Vadodaria, B.K., Anderson, J.G., Kwakye, G.F., Aschner, M., Erikson, K.M. & Bowman, A.B. Disease-toxicant screen reveals a neuroprotective interaction between Huntington's disease and manganese exposure. *J Neurochem* **112**, 227-37 (2010).

25. Fasolato, C., Hoth, M. & Penner, R. Multiple mechanisms of manganese-induced quenching of fura-2 fluorescence in rat mast cells. *Pflugers Arch* **423**, 225-31 (1993).

26. Grynkiewicz, G., Poenie, M. & Tsien, R.Y. A new generation of Ca2+ indicators with greatly improved fluorescence properties. *The Journal of Biological Chemistry* **260**, 3440 - 3450 (1985).

27. Forbes, J.R. & Gros, P. Iron, manganese, and cobalt transport by Nramp1 (Slc11a1) and Nramp2 (Slc11a2) expressed at the plasma membrane. *Blood* **102**, 1884-92 (2003).

28. Merritt, J.E., Jacob, R. & Hallam, T.J. Use of manganese to discriminate between calcium influx and mobilization from internal stores in stimulated human neutrophils. *J Biol Chem* **264**, 1522-7 (1989).

29. Picard, V., Govoni, G., Jabado, N. & Gros, P. Nramp 2 (DCT1/DMT1) expressed at the plasma membrane transports iron and other divalent cations into a calcein-accessible cytoplasmic pool. *J Biol Chem* **275**, 35738-45 (2000).

30. Snitsarev, V.A., McNulty, T.J. & Taylor, C.W. Endogenous heavy metal ions perturb fura-2 measurements of basal and hormone-evoked Ca2+ signals. *Biophys J* **71**, 1048-56 (1996).

31. Cattaneo, E. & Conti, L. Generation and characterization of embryonic striatal conditionally immortalized ST14A cells. *J Neurosci Res* **53**, 223-34 (1998).

32. Milakovic, T. & Johnson, G.V. Mitochondrial respiration and ATP production are significantly impaired in striatal cells expressing mutant huntingtin. *J Biol Chem* **280**, 30773-82 (2005).

33. Trettel, F., Rigamonti, D., Hilditch-Maguire, P., Wheeler, V.C., Sharp, A.H., Persichetti, F., Cattaneo, E. & MacDonald, M.E. Dominant phenotypes produced by the HD mutation in STHdh(Q111) striatal cells. *Hum Mol Genet* **9**, 2799-809 (2000).

34. Kwakye, G.F., Li, D., Kabobel, O.A. & Bowman, A.B. Cellular fura-2 Manganese Extraction Assay (CFMEA). *Curr Protoc Toxicol* **Chapter 12**, Unit12 18 (2011).

35. Mackenzie, B., Loo, D.D., Fei, Y., Liu, W.J., Ganapathy, V., Leibach, F.H. & Wright, E.M. Mechanisms of the human intestinal H+-coupled oligopeptide transporter hPEPT1. *J Biol Chem* **271**, 5430-7 (1996).

36. Yokel, R.A. Brain uptake, retention, and efflux of aluminum and manganese. *Environ Health Perspect* **110 Suppl 5**, 699-704 (2002).

37. Steel, A., Nussberger, S., Romero, M.F., Boron, W.F., Boyd, C.A. & Hediger, M.A. Stoichiometry and pH dependence of the rabbit proton-dependent oligopeptide transporter PepT1. *J Physiol* **498 (Pt 3)**, 563-9 (1997).

38. Chen, N., Luo, T., Wellington, C., Metzler, M., McCutcheon, K., Hayden, M.R. & Raymond, L.A. Subtype-specific enhancement of NMDA receptor currents by mutant huntingtin. *J Neurochem* **72**, 1890-8 (1999).

39. Gunter, T.E., Miller, L.M., Gavin, C.E., Eliseev, R., Salter, J., Buntinas, L., Alexandrov, A., Hammond, S. & Gunter, K.K. Determination of the oxidation states of manganese in brain, liver, and heart mitochondria. *J Neurochem* **88**, 266-80 (2004).

40. Mukhopadhyay, S. & Linstedt, A.D. Identification of a gain-of-function mutation in a Golgi P-type ATPase that enhances Mn2+ efflux and protects against toxicity. *Proc Natl Acad Sci U S A* **108**, 858-63 (2011).

41. Schramm, V.L. & Brandt, M. The manganese(II) economy of rat hepatocytes. *Fed Proc* **45**, 2817-20 (1986).

CHAPTER IV

FUNCTIONAL DISSECTION AND EXAMINATION OF METAL TRNSPORTERS UNDERLYING MUTANT HTT-MANGANESE INTERACTION

Introduction

Huntington's disease (HD) is a progressive autosomal dominant neurodegenerative disorder that is caused by an expansion of a glutamine-encoding triplet repeat (CAG) in the Huntingtin gene (*HTT*)[1-4]. A pathologic feature of HD is selective degeneration of the medium spiny neurons (MSNs) in the corpus striatum. Unfortunately, the molecular mechanisms underlying the selective degeneration are still not fully understood. However, several cellular mechanisms including alterations in metal homeostasis and oxidative injury have been implicated in the neuropathology of HD[5-9]. Although HD is monogenetic, both genetic and environmental factors have been reported to contribute to the variability in age of disease onset and progression in humans and animal models[10-15]. Previous research utilizing *in vitro* and *in vivo* models of HD have provided experimental evidence for altered Mn homoeostasis in the striatum[16,17].

Mn is stringently regulated within the brain and necessary for normal growth, cellular homeostasis, and development. Under normal physiological conditions, Mn is efficiently transported across the blood-brain barrier (BBB) in both the developing fetus

and adults[18,19]. Over the past two decades, different Mn transporter systems have been identified; including active and facilitated diffusion modes of Mn transport[20-22]. Emerging reports have indicated that Mn can be transported via the divalent metal transporter 1 (DMT1), transferrin receptor (TfR), calcium, zinc, magnesium, Park9, HIP14 channels/transporters, and others. While the tissue-specific expression of each of the aforementioned Mn transporters is yet to be determined, it is likely that the optimal tissue Mn levels are maintained through the involvement of all the above and other unknown Mn transporters. Of all the above listed polyvalent transporters, TfR and DMT1 are the most extensively documented[22]. Intracellular Mn^{2+} is sequestered into the mitochondria of brain and liver via the Ca^{2+} uniporter[23,24]. However, there has been conflicting reports to support either the mitochondria or nuclei as the cellular organelle that accumulates the primary pool of Mn in the cell[25-27]. Mn exposure occludes oxidative phosphorylation and causes cellular oxidative damage in the brain. In addition, Mn^{2+} oxidation to Mn^{3+} in the mitochondria mediates cellular oxidative injury via the oxidation of essential cellular components[28-30]. Interestingly, mutant HTT modulates the sensitivity of metal-induced opening of the mitochondrial permeability transition pore (mPTP)[31]. Nevertheless, emerging reports have implicated the peroxisome proliferator-activated receptor gamma (PPARγ) as an important pathway for mitochondrial regulation of metal homeostasis via modulation of mitochondrial membrane potential and reactive oxygen species (ROS) production[31,32]. Finally, there are similarities in the pathophysiological mechanisms, for example: oxidative injury, impaired metal homeostasis, and mitochondria dysfunction, between HD and metal toxicity[33-38]. Not only has these similarities been suggested to underlie the neurotoxicity implicated in HD and metal

overexposure, but also they indicate that metals are the prime environmental candidates to modulate HD pathophysiology.

In chapter I, I discussed the discovery of a gene-environment interaction between mutant HTT and Mn. Specifically, expression of mutant HTT decreased net Mn accumulation in mutant ST*Hdh*$^{(Q111/Q111)}$ compared to wild-type ST*Hdh*$^{(Q7/Q7)}$ cell line model of HD. The decreased net Mn uptake in the mutant ST*Hdh*$^{(Q111/Q111)}$ cell was confirmed using the high-throughput Mn detection assay, CFMEA that was discussed in chapter II[39]. Moreover, the decreased Mn accumulation correlated with diminished vulnerability to Mn induced cytoxicity[16,17].

In chapter III, I demonstrated discrete modes of Mn transport kinetics in the neuronal HD striatal cells. Specifically, I showed that expression of mutant HTT impairs instantaneous Mn uptake kinetics and cellular Mn storage properties, yet has no significant effect on Mn efflux dynamics following similar intracellular Mn levels between wild-type ST*Hdh*$^{(Q7/Q7)}$ and mutant ST*Hdh*$^{(Q111/Q111)}$ cells (Figure III. 4.B.). Moreover, we have previously reported that the Fe transport system is insufficient to explain the mutant HTT resistance and decreased Mn accumulation in the HD striatal cells[16]. Recognizing the promiscuous modes of Mn transport across and within cells, decreased instantaneous Mn uptake, diminished cellular Mn storage, and the availability of CFMEA, we sought to systematically dissect and examine known and putative Mn transporter system functions in Mn transport and identify their contribution to the mutant Mn accumulation deficit. In addition, we examined the functional relationship between the accumulated cellular Mn pools and oxidative injury in the HD striatal cells.

Materials and Methods

Chemicals, reagents, and cell culture supplies

Neuronal striatal cell lines were grown in Dulbecco's modified Eagle's medium (DMEM) with 10% fetal bovine serum (Atlanta Biologicals, Lawrenceville, GA, and Sigma, St. Louis, MO), L-glutamine, 400μg/ml G418 and Penicillin-Streptomycin was obtained from Mediatech (Manassas, VA). Dispase (catalog # 17105), 10% heat-inactivated hoarse serum (catalog # 26050), and CM-H2DCFDA (catalog # C6827) were obtained from Invitrogen, Carlsbad, CA. Cadmium (II) chloride heptahydrate ($CdCl_2 . 7H_2O$), manganese (II) chloride heptahydrate ($MnCl_2 . 7H_2O$), magnesium (II) chloride tetrahydrate ($MnCl_2 . 4H_2O$), calcium (II) chloride dihydrate ($CaCl_2 . 2H_2O$), and strontium (II) chloride hexahydrate ($SrCl_2 . 6H_2O$) were from Alfa Aesar (Ward Hill, MA). Ultra-pure fura-2 salt (cell-impermeable fura-2, catalog # ENZ-52007), rosiglitazone (Roz) [catalog # ALX-350-125], and GW9662 (catalog # BML-GR234) were obtained from ENZO Biochem (New York, NY). 2-Aminoethoxydiphenyl borate (2-APB) [catalog # 42810] and ruthenium red (RuR) [catalog # R2751] were obtained from Sigma, St. Louis, MO. 30% hydrogen peroxide (H_2O_2) [catalog # H323-500] was obtained from Thermo Fisher Scientific Inc, Hanover Park, IL. Ferristatin/ NSC306711 and NSC75600 were generous gift from the Developmental Therapeutics Program NCI/NIH, Bethesda, MD. The HEPES salt buffer consisted of 25mM HEPES, 140mM NaCl, 5.4mM KCl, and 5mM D-glucose, pH 7.4 (Sigma). The Krebs-Ringers (KR) buffer consisted of 135mM NaCl, 5mM KCl, 0.4mM KH_2PO_4, 1.8mM $CaCl_2$, 1mM $MgSO_4$, 20mM HEPES, and 5.5mM D-glucose, pH 7.4 (Sigma). 1X ultra-pure phosphate-

buffered saline (PBS), pH 7.4, without calcium and magnesium was used for post Mn exposure washes. Triton X-100 was obtained (catalog # 17105) from Sigma. Deoxyribonucleic acid sodium salt from salmon testes (Catalog # D1626) was obtained from Sigma (St. Louis, MO). Quant-iT™ PicoGreen dsDNA Reagent (Catalog # P7589) was obtained from Molecular Probes (Carlsbad, CA). 1x TE buffer used for the dilution of PicoGreen reagent was composed of 1 M Tris-HCl (pH 7.5) and 0.5 M EDTA (pH 8.0) prepared with DNase-free water and pH adjusted to 7.5. 1X Tris-buffered saline and Tween 20 (TBST) comprised of 50 mM Tris, 150 mM NaCl and 0.05% Tween, pH 7.6. The 3-(4,5-dimethylthiazol-2-yl)- 2,5-diphenyltetrazolium bromide (MTT) salt (catalog # 6494) and dimethyl sulfoxide (DMSO) (catalog # 472301) were obtained from Sigma. Sorenson's buffer consisted of 0.1 M glycine, 0.1 M NaCl, pH=10.5.

Cell culture

Neuronal HD striatal cells

HD striatal cell lines were cultured as previously described[17,40-42]. In brief, wild-type ST*Hdh*$^{(Q7/Q7)}$ and mutant ST*Hdh*$^{(Q111/Q111)}$ cells were plated in a 96 well plate at either 10,000 or 20,000 cells per well depending on the experiment and allowed to grow at 33°C in a 95% air/5% CO_2 incubator overnight. $MnCl_2$ exposure buffer was prepared in media or HEPES salt exposure buffer immediately before exposure.

Primary rat cortical astrocyte cultures

Astrocytic cultures from rat cerebral cortices of newborn (1-day-old) Sprague–Dawley rats were established as previously described[43]. Briefly, rat pups were sacrificed and the cerebral cortices removed. The meninges were carefully removed and the cerebral cortices digested with bacterial neutral protease (dispase). Repeated removal of dissociated cells from cultured brain tissues enabled astrocyte recovery. To preserve the adhering astrocytes and eliminate the neurons and oligodendrocytes, the media was changed 24 hours after the initial plating in clear polysterne 24-well plates. The cultures were maintained at 37 °C in a 95% air/5% CO_2 incubator for 3–4 weeks in minimal essential medium (MEM) with Earle's salts supplemented with 10% heat-inactivated horse serum, 100 U/ml penicillin and 100 μg/ml streptomycin. The media was changed twice per week.

Mn-fura-2 saturation binding curve

In vitro cell-free Mn-fura-2 standard curve was generated using a ten point Mn-fura-2 curve with samples containing 1 μL of different 100X stock Mn standards (0 – 100 mM) added to 99 μL of 0.5 μM fura-2 in PBS with 0.1% Triton X-100 (PTx) and assayed in a 96-well assay. A change in fura-2 fluorescence was measured at the Ca^{2+} isosbestic point of Ex_{360} and Em_{535} after 5 seconds orbital shake with a plate reader. The average raw fluorescence signal values (RFU) of the 0 μM Mn samples within each independent standard curve were defined as the 100% maximal fluorescence for that experiment after

background subtraction. RFU of each well were then normalized as percent maximal fluorescence ($\%_{MAX}$) to this value. A one-site specific saturation-binding curve with Hill slope could be fit to $\log_{10}$ Mn concentration (x-axis) and either $\%_{MAX}$ (y-axis) or RFU (y-axis) by non-linear regression analysis. To permit back calculations of extracted Mn levels from experimentally determined $\%_{MAX}$ values, we used the trend line command in Microsoft Excel to fit power (Mn concentration = $A\bullet(\%_{MAX})^{B}$) and logarithmic (Mn concentration = $A\bullet\ln(\%_{MAX})+B$) equations to the standard curve data and calculated binding curve from non-linear regression analysis. Power curves were used for $\%_{MAX}$ values less than 50% and logarithmic curves for values greater than 50%, on either side of the inflection point of the saturation-binding curve plotted with Mn concentration (x-axis) and $\%_{MAX}$ (y-axis).

Assessment of Mn levels in cell-extracts

Primary rat cortical astrocytes, wildtype ST*Hdh*$^{Q7/Q7}$ and mutant ST*Hdh*$^{Q111/Q111}$ cells were cultured in clear polystyrene 96 well tissue plates and exposed to varying $MnCl_2$ concentrations. After exposure, the media or exposure buffer was discarded and cells quickly washed three times with 200 µL PBS. The cells were extracted at 33°C for 1 hour in 100 µL PTx with 0.5 µM fura-2. Changes in fura-2 fluorescence caused by Mn quenching were measured on a plate reader as described in the Mn-fura-2 standard curve section. Extracted Mn concentrations from cultured cells were calculated using the logarithmic and power Mn standard curve (generated in the Mn-fura-2 saturation binding curve section) with the $\%_{MAX}$ of each sample. Experimental sample $\%_{MAX}$ was

determined by normalizing the RFU of each Mn-exposed sample with the RFU of vehicle-only samples (untreated), which was defined as the experimental 100% maximal fluorescence signal.

Generation of dsDNA standard curve

The PicoGreen reagent was used to generate a dsDNA standard curve as previously described in chapter II. Briefly, a twelve point salmon testes dsDNA curve with samples containing 100 µL dsDNA standards (0 – 1000 µg/mL) prepared in 0.1% PTx added to 50 µL PicoGreen reagent diluted in 1x TE buffer (1:400). Changes in fluorescence were measured at Ex_{485} and Em_{535} with a plate reader. Average background fluorescence was subtracted from each of the dsDNA containing PicoGreen fluorescence in the standard curve. A linear regression analysis in Microsoft Excel was used to obtain a linear equation from the standard curve data.

Normalization of cellular Mn levels to dsDNA

After CFMEA analysis, 100 µL of cell-extract (astrocytes and the neuronal HD striatal cells) per well was added to 50 µL of 1:400 PicoGreen solution in 1x TE buffer added to each well. The fluorescence was measured as described in the PicoGreen dsDNA standard curve section. The concentration of dsDNA in each cell-extract was

calculated using the linear equation generated from the salmon DNA standard curve and normalized to Mn levels in the cell-extracts.

Westerns blot analysis

Wildtype ST*Hdh*$^{Q7/Q7}$ and mutant ST*Hdh*$^{Q111/Q111}$ cells were equally plated at 360,000 cells per 10cm^2 plate, exposed with $MnCl_2$ for 27 hours, and harvested by trypsinization. Cells were spun at 5,000 rpm for 5-10 minutes to pellet and lysed in RIPA buffer comprised of 50mM Tris, 1.0% Nonidet 40, 150mM $NaCl_2$, 12mM deoxcholic acid, 0.1% SDS, 1x phosphatase inhibitor cocktails I and II (Sigma, St. Louis), and 1x protease inhibitor cocktail (Sigma, St. Louis). Lysed pellets were loaded by equal protein for SDS-PAGE analysis. Western blots were blocked with 5% milk prepared in TBST for 3-4 hrs at room temperature and incubated with the primary antibodies, HIP14 (Sigma, St. Louis), and β-actin (Developmental Studies Hybridoma Bank, Iowa City, IA) in 5% milk in TBST at 1:2,000 and 1:100,000 dilutions respectively overnight at 4 °C. The peroxidase-conjugated secondary IgG mouse and IgG rabbit were obtained from Jackson Immunoresearch Laboratories (West Grove, PA) and diluted at 1:10,000 in 5% milk for incubation of the western blots at room temperature for 2 hrs. The Western blots were visualized with Supersignal West Dura Extended Duration Chemiluminescent Substrate (Thermo Scientific Pierce Waltham, MA) on an Ultralum Omega 12iC (Claremont, CA). ImageJ (NIH) was used to quantify the integrated density of protein bands and background correction computed using a signal ratio error model, as previously

described[44]. The quantified relative signals from the protein bands were normalized to untreated or vehicle-exposed wild-type sample for each set.

Determination of cell viability in neuronal HD striatal cells

Wildtype ST*Hdh*$^{Q7/Q7}$ and mutant ST*Hdh*$^{Q111/Q111}$ cells were plated in a clear polystyrene 96 well plate at 5,000 cells per well the evening before exposure and allowed to grow and maintained at 33°C in a 95% air/5% CO_2 incubator overnight. On the day of the experiment, striatal HD cells were exposed to freshly prepared $MnCl_2$, $CaCl_2$, $MgCl_2$, and $SrCl_2$ in media for 27 hrs at 33°C. Cell viability was assessed by MTT assay as previously described in the established protocol[45] with subtle modifications. In brief, culture media was removed after exposure and 100 µL of 0.5% MTT salt prepared in MEM containing fetal bovine serum and penicillin–streptomycin was added to each well and incubated at 33°C in a 95% air/5% CO_2 incubator for 3 hrs. The MTT reagent containing minimal essential medium was gently aspirated. 100 µL of freshly prepared Sorenson's buffer in DMSO (Sorenson's buffer diluted 1 mL into 10 mL of DMSO) was added to the 96 well plate containing cultured and exposed striatal HD cells to dissolve the precipitate. The plates were incubated at 33°C until all the MTT salt precipitate could no longer be visualized under a microscope. The absorbance in each well on the 96 well was read at 570 nm with a plate reader. To calculate cell survival, the absorbance readings obtained from the survival data were normalized by genotype to the control (vehicle-only exposed) included in each independent sample set.

Assessment of oxidative stress in cultured HD striatal cells

Wild-type ST*Hdh*$^{(Q7/Q7)}$ and mutant ST*Hdh*$^{(Q111/Q111)}$ cells were plated in a 96 well plate at 20,000 cells per well the evening before exposure and allowed to grow and maintained at 33°C in a 95% air/5% CO_2 incubator overnight. The neuronal HD striatal cells were washed twice with 200 µL KR buffer to remove residual media followed by equal loading with 100 µL of 5 µM CM-H2DCFDA dye. After 30 minutes incubation in the dark, the cells were washed twice with 200 µL KR buffer. The baseline fluorescence was measured for both genotypes at excitation (Ex_{485}) and emission (Em_{535}) nm with a plate reader using top read and 33°C settings followed by removal of the KR-buffer. Cultured HD striatal cells were exposed to 100 µL HEPES salt buffer containing $MnCl_2$, $CdCl_2$, H_2O_2 for 5, 15, and 30 minutes in the plate reader set at 33°C. Changes in fluorescence was measured at an integration time of 200 ms at Ex_{485} and Em_{535} and compared to vehicle-only. Difference in DCF fluorescence (ΔF) after exposure was calculated as $([F_{(o)}- F_{(i)}]/F_{(i)})$, where $F_{(i)}$ is the initial fluorescence following Mn exposure and $F_{(o)}$ is the subsequent fluorescence read of the same well. The $F_{(i)}$ and $F_{(o)}$ from each well on the 96 well plate increases over the exposure duration.

Statistical Analysis

Univariate and repeated measures ANOVA tests were performed using SPSS 18 software (IBM, Inc., Chicago, IL). *Post hoc* analysis and pairwise comparisons were done using Microsoft Excel (Microsoft, Redmond, WA) by Student's *t*-tests (two tailed)

or testing for nonoverlap of the 95% confidence interval for normalized ratios; error bars are expressed as standard error of the mean (SEM). Standard deviations (SDEVs) for the difference in net Mn levels were calculated by appropriate propagation of uncertainty calculations for subtraction of sample means, with significant differences between wildtype and mutant cells evaluated by non-overlap of the 95% confidence interval.

Results

Influence of temperature on net Mn transport in HTT striatal cells

To investigate the effect of temperature on net Mn transport in the HTT striatal cells, we assessed changes in net Mn uptake levels in wild-type ST*Hdh*$^{(Q7/Q7)}$ and mutant ST*Hdh*$^{(Q111/Q111)}$ cells following exposure to $MnCl_2$ at 33°C (normal growth temperature) or 4°C (on ice) by CFMEA. The premise behind this experiment was that changes in temperature conditions would decrease the activity and function of the major Mn transport system(s), as well as decrease cellular ATP production. Moreover, if the major Mn transporter system that contribute to the decreased Mn uptake in mutant compared to wild-type HTT striatal cells was temperature-sensitive, then a decrease in the exposure-temperature conditions (from 33°C to 4°C) would abolish the net Mn uptake difference between wild-type ST*Hdh*$^{(Q7/Q7)}$ and mutant ST*Hdh*$^{(Q111/Q111)}$ cells or substantially decrease net Mn uptake levels in both genotypes. After 1 hr exposure of HTT striatal cells to 100 and 250 μM $MnCl_2$ in HEPES salt buffer at 33°C or 4°C (on ice), we observed an overall ~ 4 – 6 fold or 50 - 80% decrease in net Mn uptake in both genotypes

at 4°C and 33°C $MnCl_2$ exposures (Figure IV. 1A. and 1.B.). Additionally, repeated measures ANOVA with two within subject factors (Mn concentration and temperature) and one between subject factor (genotype) showed a significant main effect of genotype, Mn concentration, and temperature on net Mn uptake in the HD striatal cells (Table IV. 1.). Moreover, there was no two-way interaction between Mn concentration * genotype, temperature * genotype, or a three-way interaction between Mn concentration * temperature * genotype effects on net Mn accumulation in the HD striatal cells (Table IV. 1.). Importantly, we did not observe gross cytotoxicity of the HD striatal cells upon visual inspection following $MnCl_2$ exposure at 33°C or 4°C (on ice). This data suggest that the major Mn transport system(s) responsible for decreased net Mn accumulation in the HD striatal cells functions in a temperature-dependent manner. Furthermore, wild-type and mutant HD striatal cells respond similarly in their modes of Mn uptake and flux following changes in temperature conditions and possibly energy status (Figure IV. 1.A. and 1.B.).

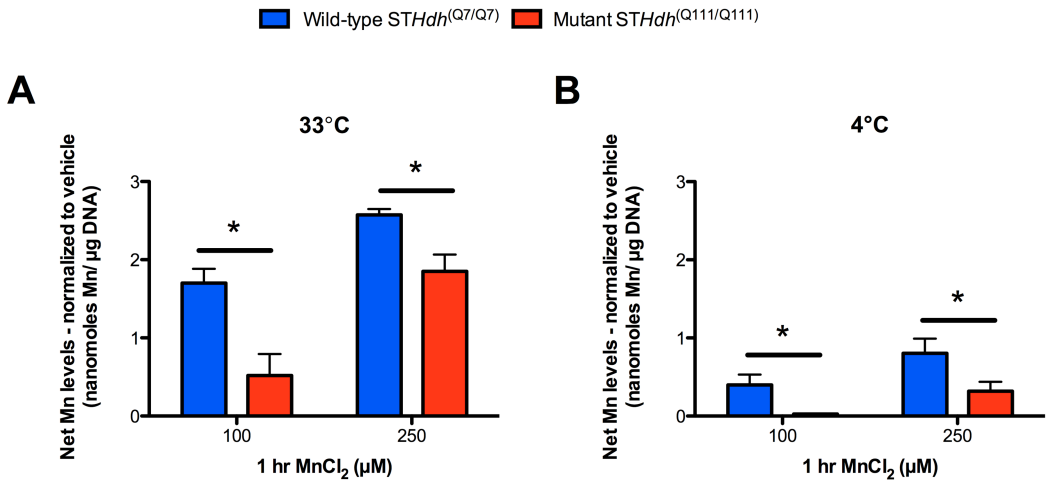

Figure IV. 1. Temperature dependence of Mn accumulation in HD striatal cells. Wild-type ST*Hdh*$^{(Q7/Q7)}$ (blue) and mutant ST*Hdh*$^{(Q111/Q111)}$ (red) cells were exposed to 100 µM and 250 µM $MnCl_2$ in HEPES salt buffer at (**A**) 33°C or (**B**) 4°C (on ice) for 1 hr. N= 4; 4 wells/exposure condition. Changes in Mn levels following Mn exposure were first normalized to vehicle and further normalized to dsDNA levels on a per well basis. (*) Indicates a significant effect of genotype on net Mn uptake ($p<0.01$, repeated measures ANOVA). Mean total Mn levels (±SEM) for (A) and (B) are plotted as indicated.

ANOVA	F	p-value
Genotype	$F_{(1,6)} = 25.65$	**<0.01**
Mn	$F_{(1,6)} = 116.4$	**<0.001**
Genotype * Mn	$F_{(1,6)} = 1.685$	0.242
Temperature	$F_{(1,6)} = 58.35$	**<0.001**
Genotype * temperature	$F_{(1,6)} = 2.466$	0.167
Mn * temperature	$F_{(1,6)} = 22.90$	**<0.01**
Genotype * Mn * temperature	$F_{(1,6)} = 3.252$	0.121

Table IV. 1. Repeated measures ANOVA results for temperature-dependence of net Mn uptake and cellular storage in HD striatal cells (Figure IV. 1.).

Role of DMT1 in the Mn transport kinetics deficit observed in mutant HD striatal cells

To examine the contribution of DMT1 in the Mn transport kinetics and cellular storage deficit observed in mutant HD striatal cells, we used the specific small molecule DMT1 inhibitor, ferristatin/NSC306711 to inhibit Mn uptake into cultured wild-type ST*Hdh*$^{(Q7/Q7)}$ and mutant ST*Hdh*$^{(Q111/Q111)}$ cells. Although ferristatin/NSC306711 has been previously reported to exhibit specific, reversible, and competitive inhibition of iron uptake in a cell line that stably overexpresses DMT1[46], we further tested the specificity of NSC306711 on cultured primary rat cortical astrocytes that have been previously reported to facilitate Mn uptake primarily through DMT1[47-50]. After 30 minutes pre-incubation with 1 and 5 μM NSC306711, cultured astrocytes were co-exposed to 100 μM $MnCl_2$ with or without NSC306711 in media for 6 hours. Additionally, repeated measures ANOVA showed a significant inhibition of Mn uptake ($F_{(2, 4)} = 49.11$, $p=0.002$) in the primary astrocytes. *Post hoc* analysis by *t*-test found a significant concentration-dependent NSC306711 inhibition ($p<0.01$) of DMT1-mediated Mn uptake in astrocytes (Figure IV. 2.A.). However, we observed no significant inhibition of Mn uptake in the neuronal wild-type ST*Hdh*$^{(Q7/Q7)}$ and mutant ST*Hdh*$^{(Q111/Q111)}$ cells (Figure IV. 2.B.). Furthermore, a comparison of Mn accumulation levels between both genotypes by repeated measures ANOVA revealed a significant decrease in mutant ST*Hdh*$^{(Q111/Q111)}$ Mn accumulation ($p<0.001$) compared to wild-type ST*Hdh*$^{(Q7/Q7)}$ cells with or without the inhibitor. In addition, we observed similar effects with another small molecule DMT1 inhibitor (NSC75600) on Mn uptake in the neuronal HD striatal cells and primary cortical astrocyte cultures (data not show). Although the tested concentrations of the inhibitor had no effect on Mn levels in the neuronal HD striatal cells, we noticed a trend towards an

increase in net Mn accumulation levels for both wild-type ST*Hdh*$^{(Q7/Q7)}$ and mutant ST*Hdh*$^{(Q111/Q111)}$ cells. After comparison of the net accumulated Mn levels in the neuronal HD striatal cells and primary cortical astrocytes following 100 μM $MnCl_2$ exposure, we observed a subtle but significant decrease ($p < 0.05$, *t-test*) in net Mn accumulation levels in primary astrocytes compared to wild-type ST*Hdh*$^{(Q7/Q7)}$ cells. Furthermore, we noticed a significant increase ($p < 0.05$, *t-test*) in net Mn accumulation levels in primary astrocytes compared to mutant ST*Hdh*$^{(Q111/Q111)}$ cells (Figure IV. 2.A. and 2.B.). These data suggest that DMT1 is not involved in the mutant Mn accumulation deficit and further supports our previously described equal DMT1 protein expression levels between wild-type ST*Hdh*$^{(Q7/Q7)}$ and mutant ST*Hdh*$^{(Q111/Q111)}$ cells[16]. Furthermore, our data suggest that DMT1 is not responsible for a significant amount of Mn uptake in these HD striatal cells.

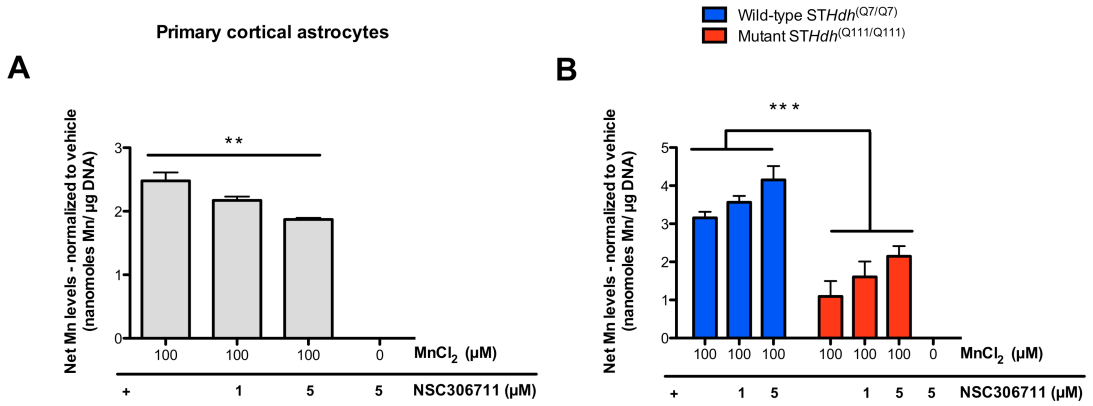

Figure IV. 2. The small molecule DMT-1 inhibitor (NSC306711) exhibits opposite effects on net Mn uptake and cellular storage between primary cortical astrocytes and neuronal HD striatal cells. (**A**) Cultured primary rat cortical astrocytes (gray) were plated in 96 well plates, pre-incubated for 30 mins and exposed to 100µM $MnCl_2$ with or without the indicated concentrations of NSC306711 for 6 hours. N = 3; 12 wells/exposure condition. (*) Indicates a significant effect of inhibitor on net Mn uptake levels ($p<0.01$, *post hoc* t-test). Mean total Mn levels (±SDEV) are plotted as indicated. (**B**) Wild-type ST*Hdh*$^{(Q7/Q7)}$ (blue) and mutant ST*Hdh*$^{(Q111/Q111)}$ (red) cells were pre-incubated and exposed to 100µM $MnCl_2$ with or without the indicated concentrations of NSC306711 for 6 hours. N = 3; 6 wells/exposure condition. Mean total Mn levels (±SEM) are plotted as indicated. Mn levels in (**A**) and (**B**) were normalized to dsDNA content on a per well basis. (*) Indicates a significant effect of genotype on net Mn uptake ($p < 0.001$, repeated measures ANOVA).

Broad calcium channels, mPTP, and PPARγ modulators show minimal effect on Mn uptake and cellular storage properties in neuronal HD striatal cells

Previous studies examining Mn-transporters in mammalian cells have demonstrated or suggested that Ca^{2+} channels such as voltage- and ligand-gated, store-operated Ca^{2+} channels, and the mitochondrial Ca^{2+} uniporter contribute to cellular Mn uptake[26,47,51-56]. Furthermore, expression of mutant HTT induces altered Ca^{2+} homeostasis via modulation of calcium channels[57-60]. Based on the link between Ca^{2+}-mediated Mn uptake and mutant HTT effects on Ca^{2+} channels, we reasoned that broad-based Ca^{2+}

channel blockers, 2-APB and RuR would exhibit a stronger inhibition of Mn uptake in wild-type ST*Hdh*$^{(Q7/Q7)}$ compared to mutant ST*Hdh*$^{(Q111/Q111)}$ cells if the hypothesis that decreased Ca^{2+} channel activity is the basis for the Mn accumulation deficit observed in mutant HD striatal cells. After 30 minutes pre-treatment of neuronal HD striatal cells with 2-APB and RuR and 6 hours $MnCl_2$ exposure with or without the indicated Ca^{2+} channel blockers in media, we observed minimal effect of the inhibitors on Mn accumulation (Figure IV. 3.A. and 3.B.). In addition, the PPARγ pathway has been indicated to regulate mitochondrial function via modulation of mitochondrial membrane potential and reactive oxygen species (ROS) production[29,30]. Furthermore, the mitochondrial function in mutant ST*Hdh*$^{(Q111/Q111)}$ cells has also been reported to be impaired[31,32,61-65]. Thus, we hypothesized that expression of mutant HTT would impair the mitochondrial regulatory function of metal homeostasis via the PPARγ mediated pathway and/or mPTP. To test this hypothesis, we utilized a PPARγ agonist (Roz) and antagonist (GW9662), as well as mPTP antagonist (CsA) as previously described for 2-APB and RuR and failed to observe an influence of either the PPARγ mediated pathway and mPTP on mutant Mn uptake and accumulation deficit (Figure IV. 3.C. and 3.D.). However, a comparison of Mn accumulation levels between genotypes by repeated measures ANOVA revealed a significant decrease in mutant ST*Hdh*$^{(Q111/Q111)}$ Mn accumulation ($p<0.001$) compared to wild-type ST*Hdh*$^{(Q7/Q7)}$ cells with or without the inhibitors. (Figure IV. 3.A. - 3.D.). These data suggest that 2-APB, RuR, CsA, Roz, and GW9962 blockable channels are not involved in the impaired Mn uptake and cellular storage phenotype observed in mutant ST*Hdh*$^{(Q111/Q111)}$ cells.

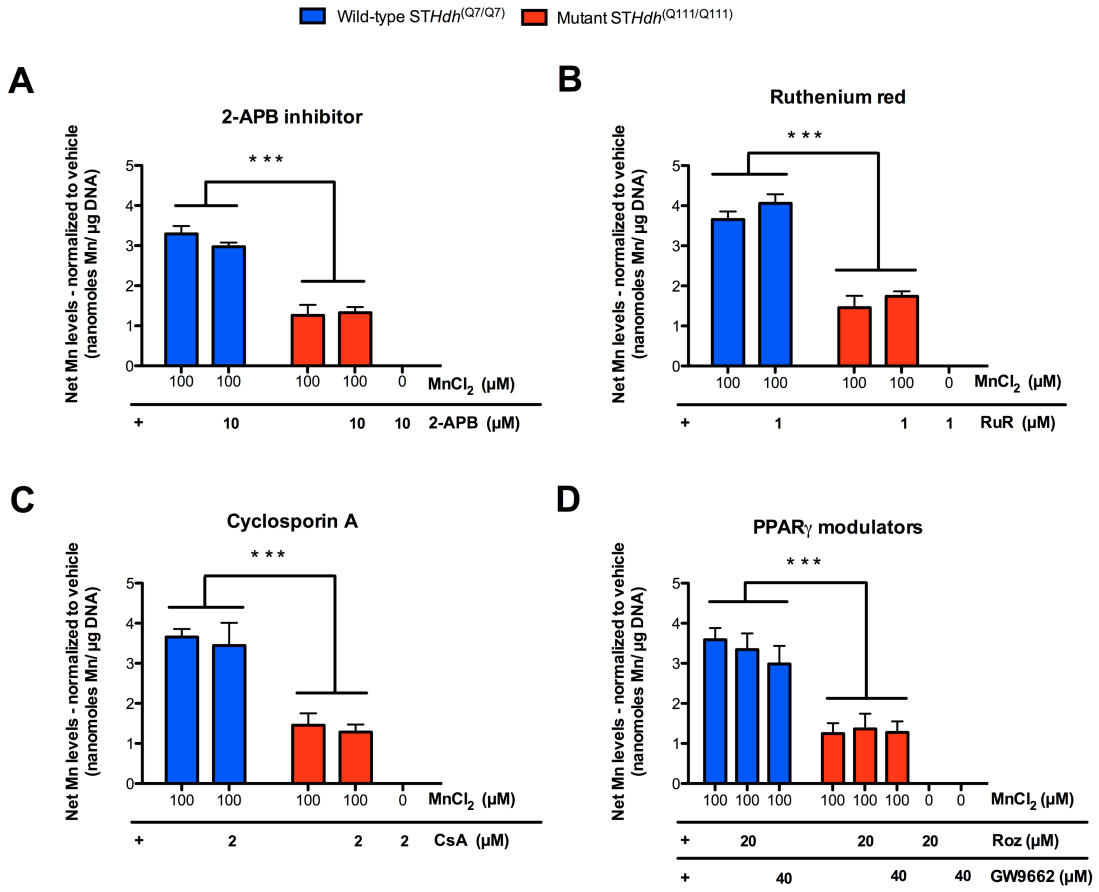

Figure IV. 3. Metal transporter modulators show minimal effect on Mn uptake and accumulation in neuronal HD striatal cells despite strong Mn uptake deficit in mutant cells. Cultured wild-type ST*Hdh*$^{(Q7/Q7)}$ (blue) and mutant ST*Hdh*$^{(Q111/Q111)}$ (red) cells were exposed to 100µM $MnCl_2$ with or without (**A**) 10 µM 2-APB, (**B**) 1 µM RuR, (**C**) 2 µM CsA, and (**D**) 20 µM Roz and 40 µM GW9662 inhibitors for 6 hours. N = 3; 6 wells/exposure condition. (*) Indicates a significant effect of genotype on net Mn uptake ($p < 0.001$, repeated measures ANOVA). Mean total Mn levels (±SEM) for (**A**), (**B**), (**C**), and (**D**) are plotted as indicated.

Examination of the putative Mn transporter, HIP14, protein levels in HD striatal cells

Based on the minimal contribution of known Mn transporters, including DMT1, TfR, and others in the diminished mutant Mn uptake and cellular storage phenotype, we

sought to investigate the functions of other putative Mn transporter systems in the mutant Mn phenotype. Importantly, the HIP14 transporter mediates Mn and other divalent metal transport and is modulated by mutant HTT expression[66,67]. Based on the intriguing relationship between Mn affinity for the HIP14 transporter and the regulatory effects of mutant HTT on HIP14 function, we examined the protein expression levels of HIP14 in wild-type ST*Hdh*$^{(Q7/Q7)}$ and mutant ST*Hdh*$^{(Q111/Q111)}$ cells following $MnCl_2$ exposure. We found a significant main effect of genotype on HIP14 protein levels by ANOVA (Table IV. 2.). In addition, we demonstrate a significant decrease (approximately 40%) in basal mutant ST*Hdh*$^{(Q111/Q111)}$ HIP14 protein expression levels ($p<0.05$, t-test) compared to wild-type ST*Hdh*$^{(Q7/Q7)}$ cells. Finally, we observed a non-statistical trend towards down-regulation of HIP14 protein levels in wild-type ST*Hdh*$^{(Q7/Q7)}$ cells following increasing exposure concentrations of $MnCl_2$. (Figure IV. 4.A.).

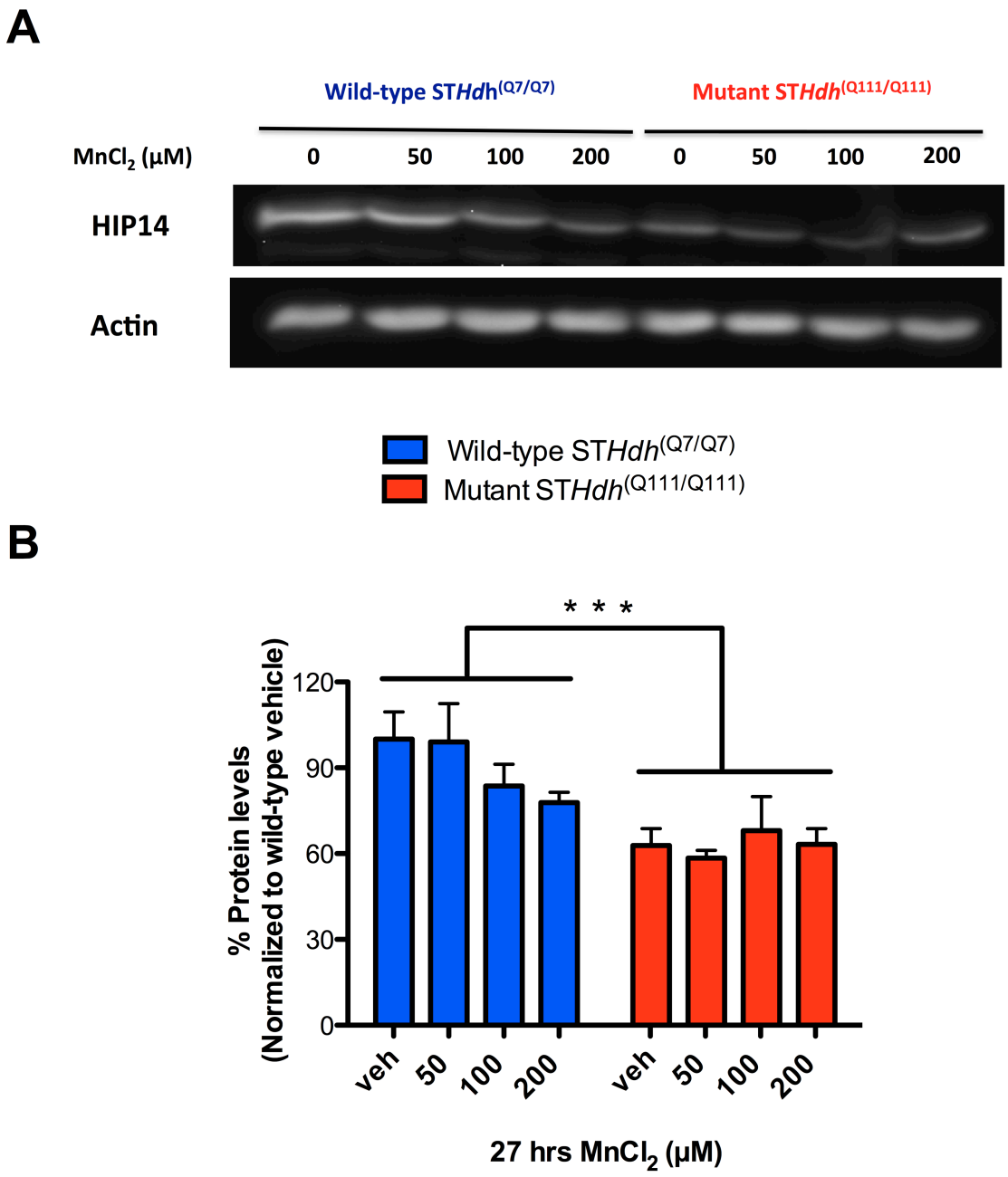

Figure IV. 4. Mutant HD striatal cells exhibit significant decrease in HIP14 protein levels compared to wild-type. Wild-type ST*Hdh*$^{(Q7/Q7)}$ (blue) and mutant ST*Hdh*$^{(Q111/Q111)}$ (red) cell lysates were harvested after 27 hrs exposure to the indicated $MnCl_2$ concentrations versus vehicle control and analyzed by western blot for HIP14 and β-actin. (**A**) Representative blots of each genotype-exposure group are shown. (**B**) Quantification of HIP14 protein levels in the HD striatal cells are represented as a bar graph. N = 3 sets per genotype per exposure groups. Mean levels (±SEM) are normalized

to β-actin as a percent of the untreated wild-type vehicle (N = 3). (*) Indicates significant differences in HIP14 expression levels between the wild-type and mutant cells ($p < 0.001$, Univariate ANOVA)

ANOVA	F	p-value
Genotype	$F_{(1,16)} = 21.01$	<0.001
Mn	$F_{(3,16)} = 0.627$	0.608
Genotype * Mn	$F_{(3,16)} = 1.375$	0.280

Table IV. 2. Repeated measures ANOVA results of HIP14 protein levels in striatal HD cells (Figure IV. 4.).

HD striatal cells are resistant to Mg^{2+}, Sr^{2+}, and Ca^{2+} induced cytotoxicity

We have previously excluded a role for the transferrin-mediated metal transporter pathway as a major transporter underlying the Mn accumulation deficit in mutant HD cells by using saturated Fe^{3+} levels to outcompete Mn uptake via the transferrin pathway in cultured HD striatal cells[16]. To further characterize the metal transporter/channel defect in mutant HD striatal cells, we utilized excess levels of the divalent metals, Mg^{2+}, Sr^{2+}, and Ca^{2+}, which share similar transport systems with Mn^{2+}[66]. Prior to investigation of the competitive effects of excess Mg^{2+}, Sr^{2+}, and Ca^{2+} on Mn transport, we examined the potential cytotoxic effects of the above divalent metals on the striatal HTT cells. The premise behind this experiment was to identify the optimal concentrations of Mg^{2+}, Sr^{2+}, and Ca^{2+} levels that when used in excess amounts would exhibit no toxicity, but outcompete Mn for its shared transporter with Mg^{2+}, Sr^{2+}, and Ca^{2+} in the HD striatal

cells. We exposed the HD striatal cells to 1 and 10 mM Mg^{2+}, Sr^{2+}, and Ca^{2+} based on the reported concentrations of the above divalent metal ions to influence other metal ion transport[68-72]. Following 27 hrs exposure of HD striatal cells to 1 and 10 mM Mg^{2+}, Sr^{2+}, and Ca^{2+}, we observed no effect on cell viability between wild-type ST*Hdh*$^{(Q7/Q7)}$ and mutant ST*Hdh*$^{(Q111/Q111)}$ cells (Figure IV. 5.). In addition, we observed no significant differences in cell survival for both genotypes when compared to vehicle-exposed (Figure IV. 5.). Importantly, we confirmed that wild-type HD striatal cells are significantly ($p < 0.001$, repeated measures ANOVA) more susceptible to Mn-induced toxicity than mutants following 50 μM $MnCl_2$ exposure and when compared to vehicle-exposed cells (Figure IV. 5.). This data indicates that the chosen concentrations of excess Mg^{2+}, Sr^{2+}, and Ca^{2+} do not exhibit cytotoxic effects and are optimal for its usage as divalent metal ion inhibitors and competitors of Mn uptake and cellular storage properties in the HD striatal cells.

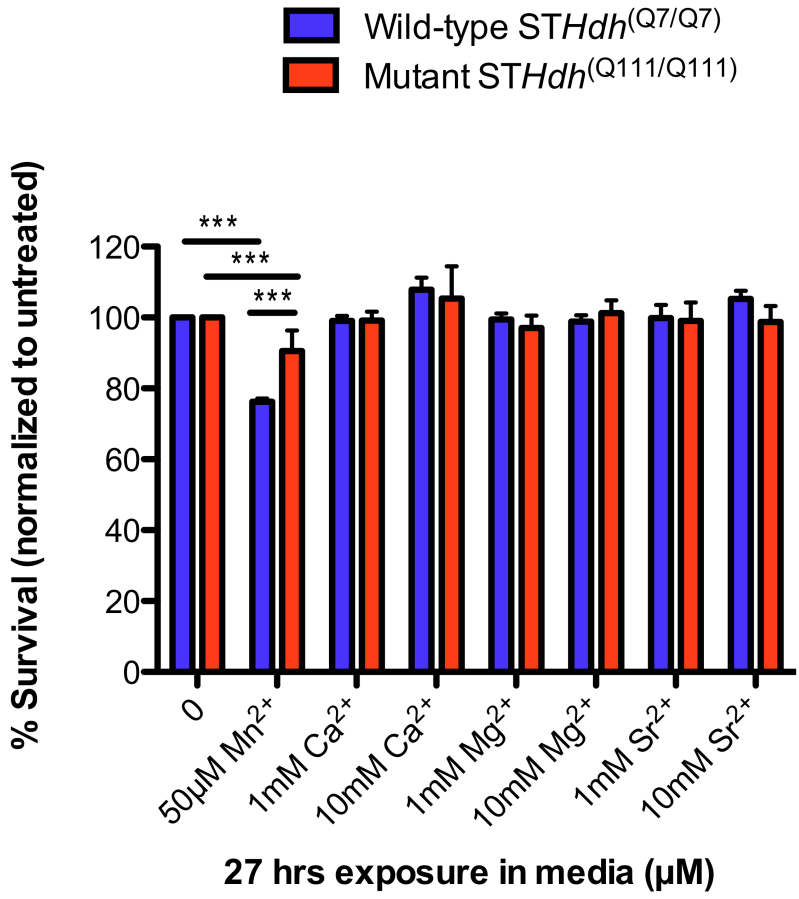

Figure IV. 5. High levels of Ca^{2+}, Mg^{2+}, and Sr^{2+} are not toxic in HD striatal cells. Wild-type ST*Hdh*$^{(Q7/Q7)}$ (blue) and mutant ST*Hdh*$^{(Q111/Q111)}$ (red) cells were exposed to different concentrations of the indicated metal ions for 27 hrs in media. N = 3; 6 wells/exposure condition. (*) Indicates a significant effect of genotype as well as Mn exposure on net Mn uptake ($p < 0.001$, repeated measures ANOVA). Mean total Mn levels of the 95% confidence interval are plotted as indicated.

Excess Mg^{2+}, Sr^{2+}, and Ca^{2+} substantially inhibit Mn uptake and accumulation

To further characterize the metal transporter/channel defect in mutant HD striatal cells, we utilized the non-toxic divalent metals, Mg^{2+}, Sr^{2+}, and Ca^{2+}, which share similar transport systems with Mn^{2+}[66]. We reasoned that if expression of mutant HTT impairs the function of a known or novel transporter/channel shared between Mg^{2+}, Sr^{2+}, Ca^{2+}, and

Mn^{2+}, then co-exposure of Mn and excess levels of Mg^{2+}, Sr^{2+}, or Ca^{2+} would outcompete Mn for its shared transporter. Thus, decreasing Mn uptake and accumulation in wild-type HTT expressing cells to similar levels found in mutant HTT expressing cells, as well as potentially decrease mutant Mn uptake and accumulation. After 1 hr co-exposure of wild-type and mutant HTT cells to 100 μM $MnCl_2$ with or without 1 and 10 mM $MgCl_2$ in HEPES salt buffer, repeated-measures ANOVA showed a significant main effect of Mg^{2+} ($F_{(2, 8)} = 43.705$, $p<0.001$) and genotype ($F_{(1, 4)} = 52.47$, $p <0.01$), but not an genotype by Mg^{2+} interaction ($F_{(2, 8)} = 1.101$, $p<0.378$) (Figure IV. 6.A. and Table IV. 3.A.). Nevertheless, we found similar inhibitory effects on net Mn uptake and cellular storage with excess Sr^{2+} and Ca^{2+} in wild-type ST*Hdh*$^{(Q7/Q7)}$ and mutant ST*Hdh*$^{(Q111/Q111)}$ cells. In fact repeated measures ANOVA showed a significant main effect of Sr^{2+} ($F_{(2, 8)} = 103.1$, $p<0.001$), genotype ($F_{(1, 4)} = 13.03$, $p <0.05$), and an exposure by genotype interaction ($F_{(2, 8)} = 10.40$, $p<0.01$) (Figure IV. 6.B. and Table IV. 3.B.) on Mn uptake and storage. In addition, we observed a main effect of Ca^{2+} ($F_{(2, 8)} = 101.6$, $p<0.001$) and genotype by Ca^{2+} interaction ($F_{(2, 8)} = 19.66$, $p <0.01$), but no genotype effect ($F_{(1, 4)} = 0.038$, $p = 0.191$) on Mn uptake and cellular storage (Figure IV. 6.C. and Table IV. 3.C.) by repeated measures ANOVA. Interestingly, we demonstrate that at least 1 mM Mg^{2+} and Sr^{2+} co-exposed with 100 μM $MnCl_2$ is sufficient to occlude and diminish Mn uptake in wild-type ST*Hdh*$^{(Q7/Q7)}$ to similar levels observed in mutant ST*Hdh*$^{(Q111/Q111)}$ cells following 100μM $MnCl_2$ exposure (Figure III. 6.A. and 6.B.). Nevertheless, we observed an approximately 4-fold inhibitory effect of 1mM Ca^{2+} and 100 μM $MnCl_2$ on wild-type Mn uptake and storage, albeit no effect on mutant Mn uptake and cellular storage (Figure IV. 6.C.). In fact, co-exposure of wild-type ST*Hdh*$^{(Q7/Q7)}$ and mutant ST*Hdh*$^{(Q111/Q111)}$

cells to 1mM Ca^{2+} and 100 μM $MnCl_2$ completely abolished the observed Mn uptake and cellular storage differences between wild-type ST*Hdh*$^{(Q7/Q7)}$ and mutant ST*Hdh*$^{(Q111/Q111)}$ cells (Figure IV. 6.C.). In general, we show a substantial inhibition of Mn uptake and accumulation in wild-type ST*Hdh*$^{(Q7/Q7)}$ and mutant ST*Hdh*$^{(Q111/Q111)}$ cells following exposure to Mn and excess, but non-toxic levels of Mg^{2+}, Sr^{2+}, or Ca^{2+} ions.

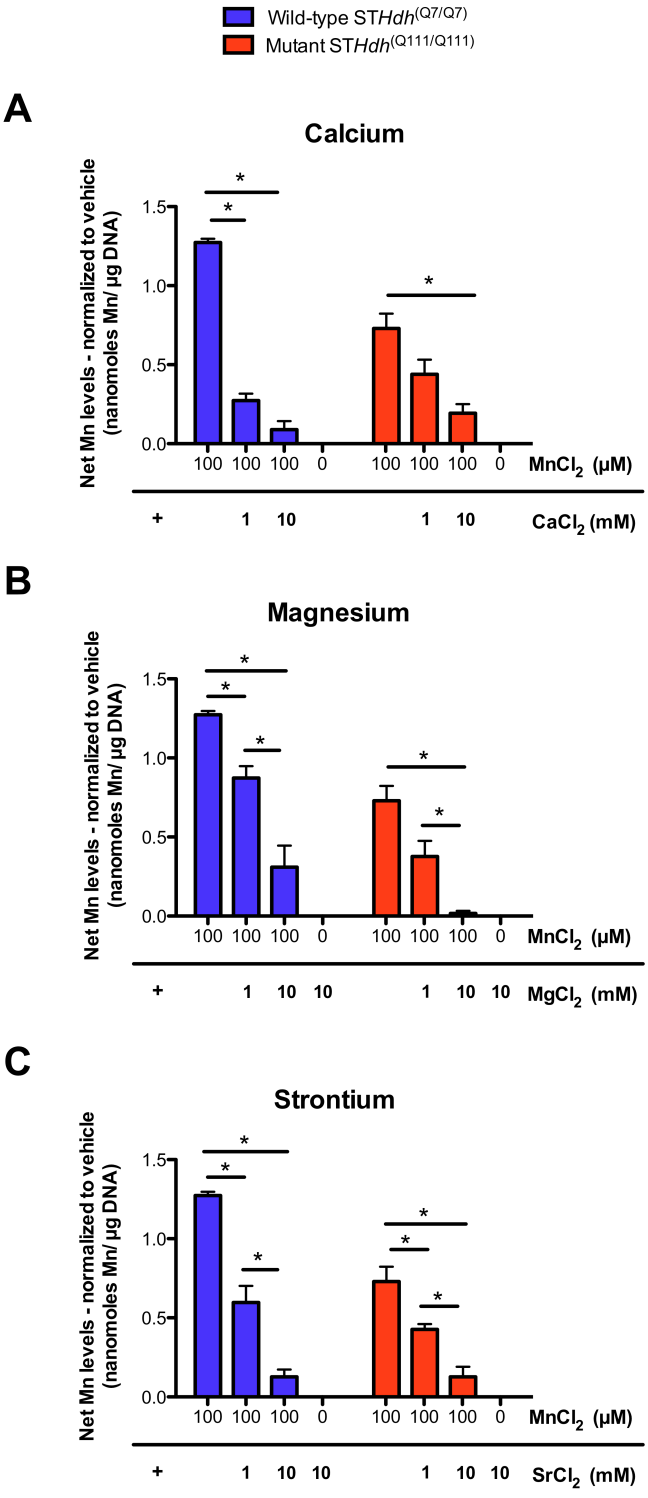

Figure IV. 6. Excess Mg^{2+}, Sr^{2+}, and Ca^{2+} substantially inhibit Mn uptake and accumulation in neuronal HD striatal cells. Wild-type ST*Hdh*$^{(Q7/Q7)}$ (blue) and mutant

ST*Hdh*$^{(Q111/Q111)}$ (red) cells were cultured in a 96 well tissue culture plate and exposed to 100 µM $MnCl_2$ with or without (**A**) 1 mM and 10mM $MgCl_2$, (**B**) 1 mM and 10mM $SrCl_2$ and (**C**) 1 mM and 10mM $CaCl_2$ in HEPES salt buffer for 1 hr. Net Mn uptake and accumulation was assessed by CFMEA. Mean total Mn levels (±SEM) are plotted as indicated. N = 3; 6 wells/exposure condition. (*) Indicates a significant effect of the tested excess metal ion on net Mn uptake ($p < 0.005$, repeated measures ANOVA).

A.

ANOVA	F	p-value
Genotype	$F_{(1, 4)} = 0.038$	0.191
Ca^{2+}	$F_{(2, 8)} = 101.6$	**<0.001**
Genotype * Ca^{2+}	$F_{(2, 8)} = 19.66$	**<0.01**

B.

ANOVA	F	p-value
Genotype	$F_{(1, 4)} = 52.47$	**<0.01**
Mg^{2+}	$F_{(2, 8)} = 43.71$	**<0.001**
Genotype * Mg^{2+}	$F_{(2, 8)} = 1.101$	0.378

C.

ANOVA	F	p-value
Genotype	$F_{(1,16)} = 13.03$	**<0.05**
Sr^{2+}	$F_{(3,16)} = 103.1$	**<0.001**
Genotype * Sr^{2+}	$F_{(3,16)} = 10.40$	**<0.01**

Table IV. 3. Repeated measures ANOVA results of excess Mg^{2+}, Sr^{2+}, and Ca^{2+} ions effects on net Mn uptake and cellular storage in striatal HTT cells (Figure IV. 6.).

Functional relationship between differential Mn uptake, cellular Mn pools, and oxidative injury in neuronal HD striatal cells

We have previously reported that expression of mutant HTT decreases Mn cytotoxicty compared to wild-type HD striatal cells over a wide range of concentrations[17]. Moreover, we have provided experimental evidence in chapter III for differential cellular Mn storage between wild-type ST*Hdh*$^{(Q7/Q7)}$ and mutant ST*Hdh*$^{(Q111/Q111)}$ cells following Mn exposure (Figure III. 3.). To examine the functional relationship between cellular Mn pools and the temporal induction of oxidative stress that may underlie the differences in Mn-induced cytotoxicity in the HD striatal cells, we utilized the DCF assay to measure changes in ROS levels following $MnCl_2$ exposure. Following equal loading of wild-type ST*Hdh*$^{(Q7/Q7)}$ and mutant ST*Hdh*$^{(Q111/Q111)}$ cells with DCF and exposure to vehicle, $MnCl_2$, $CdCl_2$, and H_2O_2 for 5, 15, and 30 minutes, the mean vehicle-only ROS level for each genotype at the indicated exposure duration was compared to the $MnCl_2$, $CdCl_2$, and H_2O_2 induced ROS levels at the respective exposure durations. We observed a significant increase in ROS production ($p<0.05$; *post hoc* t-test) induced by $MnCl_2$, $CdCl_2$, and H_2O_2 above baseline levels at all the evaluated time points with the exception of wild-type H_2O_2 ROS levels at 30 minutes (Figure IV. 7.C.) After 5 minutes $MnCl_2$ exposure in HEPES salt buffer, repeated-measures ANOVA showed a significant main effect of Mn ($F_{(1, 4)} = 41.31$, $p<0.01$), genotype ($F_{(1, 4)} = 12.49$, $p <0.05$), and genotype by Mn interaction ($F_{(1, 4)} = 30.17$, $p<0.01$) on ROS production (Figure IV. 7.A and Table IV. 4.A.). In addition, we demonstrate a significant main effect of Mn ($F_{(1, 4)} = 83.06$, $p<0.01$), genotype ($F_{(1, 4)} = 119.4$, $p <0.001$), and genotype by Mn interaction ($F_{(1, 4)} = 39.20$, $p<0.05$) following 15 minutes exposure and by repeated measures

ANOVA (Figure IV. 7.B. and Table IV. 4.B.). Moreover, 30 minutes $MnCl_2$ exposure showed a main effect of Mn ($F_{(1, 4)} = 46.94$, $p<0.01$), genotype ($F_{(1, 4)} = 121.2$, $p <0.001$), and genotype by Mn interaction ($F_{(1, 4)} = 12.93$, $p<0.05$); repeated measures ANOVA (Figure IV. 7.C. and Table IV. 4.C.). Conversely, we observed a time-dependent increase in vehicle-only/basal ROS levels ($p<0.01$, *post hoc* t-test) (Figure IV. 7.A. – 7.C.). Nevertheless, we noticed a time-dependent increase in mutant ST*Hdh*$^{(Q111/Q111)}$ to H_2O_2 stimulated ROS generation ($p<0.01$) when compared to wild-type ST*Hdh*$^{(Q7/Q7)}$ cells (Figure IV. 7.A. – 7.C.). Moreover, we did not observe a genotypic difference in $CdCl_2$ induced ROS production at 5, 15, or 30 minutes exposure. In addition, we noticed no difference in ROS levels between wild-type ST*Hdh*$^{(Q7/Q7)}$ and mutant ST*Hdh*$^{(Q111/Q111)}$ cells following exposure to $CoCl_2$ for 5, 15, and 30 minutes (data not shown).

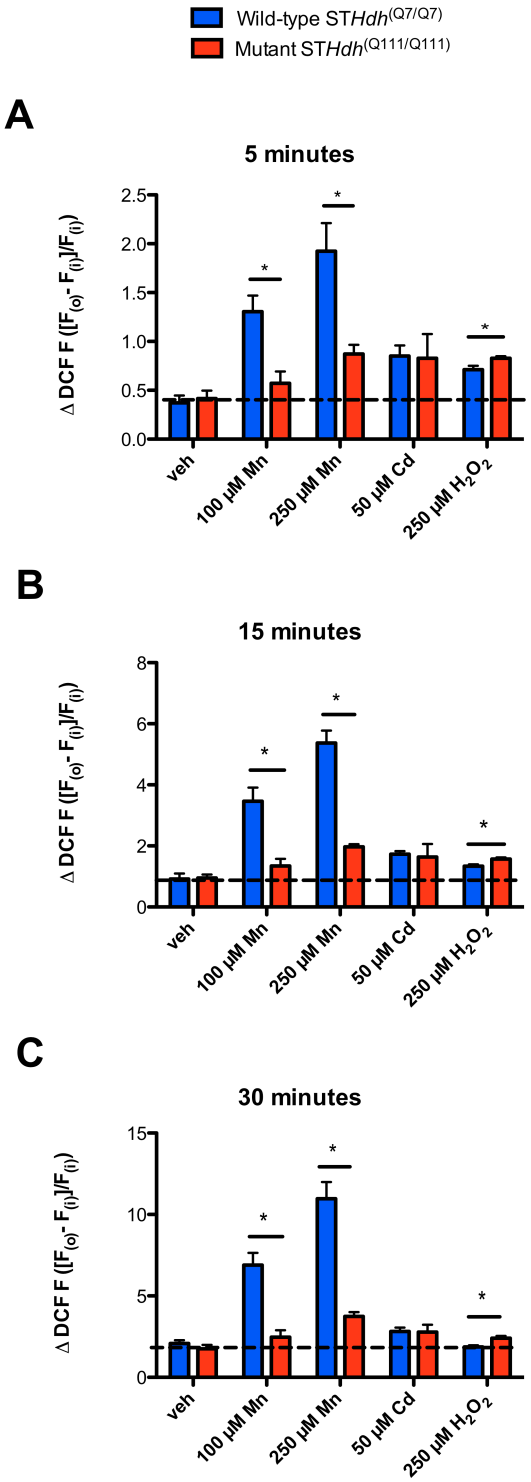

Figure IV. 7. Temporal- and concentration-dependent Mn uptake in HD striatal cells is functionally related to the cellular Mn pools that contribute to oxidative

stress. Wild-type ST*Hdh*$^{(Q7/Q7)}$ (blue) and mutant ST*Hdh*$^{(Q111/Q111)}$ (red) cells were cultured in a 96 well tissue culture plate, and equally loaded with DCF. Cells were exposed to $MnCl_2$, $CdCl_2$, and H_2O_2 in HEPES salt buffer for (**A**) 5, (**B**) 15, and (**C**) 30 minutes. The effects of $MnCl_2$, $CdCl_2$, and H_2O_2 induced oxidative stress were assessed by DCF assay. Dashed horizontal line (---) represents baseline/vehicle-only ROS levels at each time point. N = 3; 6 wells/exposure condition. Mean ROS levels (±SDEV) are plotted as indicated.

A.

ANOVA	F	p-value
Genotype	$F_{(1, 4)} = 12.49$	<0.05
Mn^{2+}	$F_{(1, 4)} = 41.31$	<0.01
Genotype * Mn^{2+}	$F_{(1, 4)} = 30.17$	<0.01

B.

ANOVA	F	p-value
Genotype	$F_{(1, 4)} = 119.4$	<0.001
Mn^{2+}	$F_{(1, 4)} = 83.06$	<0.01
Genotype * Mn^{2+}	$F_{(1, 4)} = 39.20$	<0.01

C.

ANOVA	F	p-value
Genotype	$F_{(1, 4)} = 121.2$	<0.001
Mn^{2+}	$F_{(1, 4)} = 46.94$	<0.01
Genotype * Mn^{2+}	$F_{(1, 4)} = 12.93$	<0.05

Table IV. 4. Repeated measures ANOVA results of functional relationship between differential cellular Mn pools and oxidative stress levels in striatal HTT cells (Figure IV. 7.). Vehicle, $MnCl_2$, $CdCl_2$, and H_2O_2 exposures of striatal HTT cells for (**A**) 5 minutes, (**B**) 15 minutes, and (**C**) 30 minutes.

Conclusions

We systematically dissected and functionally examined the role of known and putative Mn transporters in the diminished Mn uptake and cellular storage deficits in mutant HD striatal cells. Our data strongly suggest that Mn transport dynamics in the HD striatal cells are temperature-dependent (Figure IV. 1.). Moreover, we have provided experimental evidence to suggest that the mutant ST*Hdh*$^{(Q111/Q111)}$ Mn transport kinetic deficits are independent of the known Mn transporters, including; DMT1, 2-APB, RuR, mPTP, Roz, and GW9662 blockable transporters/channels (Figure IV. 2 and 3). Nevertheless, we demonstrate that the putative Mn transporter, HIP14 is significantly decreased in mutant ST*Hdh*$^{(Q111/Q111)}$ compared to wild-type ST*Hdh*$^{(Q7/Q7)}$ cells. In addition, we show a significant reduction in basal HIP14 protein levels in mutant ST*Hdh*$^{(Q111/Q111)}$ compared to wild-type ST*Hdh*$^{(Q7/Q7)}$ cells (Figure IV. 4. and Table IV. 2.). Moreover, excess non-toxic levels of Mg^{2+}, Sr^{2+}, and Ca^{2+} significantly impedes Mn uptake and cellular storage in the HD striatal cells (Figure IV. 5., 6.A. – 6.C., and Table IV. 3.). Importantly, we show that excess levels of at least 1 mM Sr^{2+} and Ca^{2+} are sufficient to abolish the phenotypic Mn uptake and cellular storage differences between wild-type ST*Hdh*$^{(Q7/Q7)}$ and mutant ST*Hdh*$^{(Q111/Q111)}$ cells (Figure IV. 6.B. and 6.C.). Finally, we demonstrate that the time-dependent differences in Mn uptake and cellular storage properties discussed in chapter III as well as the differential vulnerability to Mn-induced cytotoxicity between wild-type ST*Hdh*$^{Q7/Q7}$ and mutant ST*Hdh*$^{Q111/Q111}$ cells[17] are functionally related to the cellular Mn pools that contribute to oxidative stress (Figure IV. 7.A. – 7.C.).

Our data demonstrate the influence of temperature on net Mn transport dynamics (uptake, storage, and efflux) in the neuronal HD striatal cells and is in agreement with the previously reported temperature-dependence on Mn uptake and flux across the blood brain barrier[73]. Indeed, the overall ~ 4 – 6 fold or 50-80% decrease in net Mn uptake transport dynamics for both genotypes at 4°C and 33°C following 1 hr $MnCl_2$ exposure (Figure IV. 1A. and 1.B.) provides further evidence that the Mn influx across the plasma membranes of HD striatal cells is not mediated by a simple diffusion transport process, but rather an active protein-mediated transport system. Importantly, it is highly unlikely that the temperature-dependent effect on Mn uptake and cellular storage in the HD striatal cells were mainly due to changes in the random movements of Mn^{2+} particles across the membrane due to modifications in the kinetic energy of our exposure system (Brownian motion) at 4°C. Indeed, the kinetic energy in our exposure system can be calculated using the following equation: $E = (3\ kT)/2$, where E, K, and T are the kinetic energy, Boltzman constant, and temperature. If the temperature-dependent effects that we observed in the HD striatal cells were solely based on changes in the kinetic energy of Mn^{2+} particles in our system, we would have expected a ~15% decrease, rather than the 50-80% diminished Mn transport dynamics. Furthermore, the similar effects of temperature on Mn uptake and cellular storage in both wild-type and mutant HD striatal cells suggest that the impaired major Mn transport system in mutant HD striatal cells is not a temperature-sensitive metal transporter. Although we did not directly investigate the energy-dependence on Mn transport in the HD striatal cells by using mitochondrial complex or ATP synthetase inhibitors, it is likely that changes in temperature conditions would decrease cellular ATP production in a Mn concentration- and genotype-dependent

manner in the HD striatal cells.

We have previously demonstrated that DMT1 protein levels are unchanged[16] as well as similar Cu^{2+}, Co^{2+}, Fe^{3+}, Ni^{2+}, Pb^{2+}, and Zn^{2+} induced cytoxicity between wild-type ST*Hdh*$^{Q7/Q7}$ and mutant ST*Hdh*$^{Q111/Q111}$ cells[17]. In fact, the aforementioned metals are substrates for DMT1 with either lower or higher affinities than Mn (II)[49]. We examined and demonstrate that inhibition of DMT1 function with the small molecule inhibitor, NSC306711[46], fail to impede the Mn uptake and cellular storage differences between wild-type ST*Hdh*$^{(Q7/Q7)}$ and mutant ST*Hdh*$^{(Q111/Q111)}$ cells (Figure IV. 2.B.). Moreover, we observed a non-significant trend towards an increase in Mn uptake in both genotypes following co-exposure with $MnCl_2$ and NSC306711 (Figure IV. 2.B.). Conversely, we report that NSC306711 inhibits Mn uptake in a concentration-dependent manner in primary rat astrocyte cultures (Figure IV. 2.A.). In addition, we observed similar modulatory effects on net Mn uptake and cellular storage properties in the HD striatal cells and primary astrocytes using another small molecule DMT1 inhibitor, NSC75600 (data not shown). It is unlikely that the opposite effects of the DMT1 inhibitors on Mn uptake and cellular storage in the neuronal HD striatal cells compared to primary astrocytes was due to cell-type specific inhibitory actions. The most likely explanation is that neurons and glial (astrocytes) may utilize different modes and Mn transporters/channels for Mn uptake. Interestingly, we demonstrated a subtle but significant decrease in net Mn accumulation levels in primary astrocytes compared to wild-type neuronal HD striatal cells (Figure IV. 2.A. and 2.B.). Although the difference in Mn accumulation levels between neuronal HD striatal cells and glial (astrocytes) was assessed at a single Mn concentration and exposure time-point, it is possible that *in vivo*

glial cells (astrocytes) might be regulating the amount of Mn that accumulates in neurons by sequestering Mn as a neuroprotective mechanism. Thus, this may explain the previously reported increased Mn accumulation levels observed in astrocytes following Mn exposure[71,72]. In spite of the similar DMT1 protein expression levels in the neuronal HD striatal cells[16], it is still unknown if the DMT1 expressed is functional. We find that mutant Mn uptake and cellular storage deficits are independent of 2-APB and RuR blockable channels such as store-operated calcium channel and the Ca^{2+} uniporter (Figure IV. 2.A. and 2.B.). Furthermore, we report that the altered Mn uptake and cellular storage difference between wild-type ST*Hdh*$^{(Q7/Q7)}$ and mutant ST*Hdh*$^{(Q111/Q111)}$ cells is likely not due to deranged regulation of Mn homeostasis via the PPARγ pathway or the mPTP (Figure IV. 2.C. and 2.D.).

Emerging experimental evidence has elucidated the role of novel candidate metal transporters, such as HIP14, HIP14L proteins, and others in mediating Mn^{2+} and other divalent metals (Mg^{2+}, Sr^{2+}, and others) transport[66,67]. Here we report that HIP14 protein levels is significantly decreased in mutant ST*Hdh*$^{(Q111/Q111)}$ cells compared to wild-type ST*Hdh*$^{(Q7/Q7)}$ (Figure IV. 5.A. and 5.B and Table IV. 2.). In addition we show that the basal HIP14 protein levels in mutant ST*Hdh*$^{(Q111/Q111)}$ is significantly diminished compared to wild-type ST*Hdh*$^{(Q7/Q7)}$ cells (Figure IV. 5.A., 5.B., and Table IV. 2.). Moreover, we observed a non-statistical trend towards down regulation of HIP14 protein expression levels in response to increasing $MnCl_2$ exposure (Figure IV. 5.A. and 5.B). Interestingly, previous experimental evidence has demonstrated reduced interaction between mutant HTT and HIP14 proteins and significant inhibition of the HIP14 transporter function by excess Ca^{2+} levels[66]. Thus, we examined the cytotoxic effects and

influence of excess levels of the two highest affinity cations (Mg^{2+}, Sr^{2+}) for the HIP14 transporter and the specific HIP14 cation inhibitor (Ca^{2+}) on Mn uptake and storage. We demonstrate that excess levels of Mg^{2+}, Sr^{2+}, and Ca^{2+} are not toxic to the HD striatal cells (Figure IV. 5.) and significantly inhibit Mn uptake (Figure IV. 6 and Table IV. 3.). Importantly we show that excess levels (1 and 10 mM) of Mg^{2+}, Sr^{2+}, and Ca^{2+} do not induce cytotoxicity in the HD striatal cells (Figure IV. 4.). Moreover, the Mn uptake and cellular storage differences between wild-type ST*Hdh*$^{(Q7/Q7)}$ and mutant ST*Hdh*$^{(Q111/Q111)}$ cells is completely eliminated with either 10 mM Mg^{2+}, 1mM Sr^{2+} or 1mMCa^{2+} (Figure IV. 6.A – 6.C and Table IV. 3.). Furthermore, we demonstrate that the magnitude of excess Ca^{2+} inhibition of Mn uptake in wild-type cells is substantially greater than that of mutant cells. Our findings from the HIP14 protein expression and the influence of excess metals on Mn uptake and cellular storage suggest that the major Mn transporter underlying decreased Mn uptake and cellular storage in mutant HD striatal cells is a shared transporter between Mn^{2+}, Mg^{2+}, Sr^{2+}, and Ca^{2+}. Finally, the metal transporter(s) involved in the mutant Mn uptake and cellular storage properties are efficiently blockable by excess Mg^{2+}, Sr^{2+}, and Ca^{2+} and possess higher affinity for Mg^{2+}, Sr^{2+}, and Ca^{2+} compared to Mn^{2+}. Given the structural and cation selectivity similarities between HIP14 and HIP14L and reduced interaction between mutant HTT and HIP14 proteins[66], it is possible that the mutant ST*Hdh*$^{(Q111/Q111)}$ Mn uptake and cellular storage deficit may be due to mutant HTT induced impairment in HIP14 and/or HIP14L transporter function.

Williams and colleagues have previously demonstrated that when the cellular Mn uptake levels are the same between wild-type ST*Hdh*$^{(Q7/Q7)}$ and mutant ST*Hdh*$^{(Q111/Q111)}$ cells, the degree of Mn induced toxicity is matched[16]. However, the relationship between

cellular Mn pools and the differential Mn induced cytotoxicity between wild-type ST*Hdh*$^{(Q7/Q7)}$ and mutant ST*Hdh*$^{(Q111/Q111)}$ cells is still unknown. Furthermore, there is evidence to support and suggest that metal ions can induce the generation of ROS through the Fenton-Harber Weiss reactions to cause cell death[74,75]. We demonstrate that wild-type ST*Hdh*$^{(Q7/Q7)}$ and mutant ST*Hdh*$^{(Q111/Q111)}$ cells significantly generate ROS levels in a time-dependent manner and above baseline levels following exposure to $MnCl_2$ and H_2O_2 (Figure IV. 7.A. – 7.C.). We observed a concentration- and time-dependent decrease in Mn stimulated ROS generation in mutant ST*Hdh*$^{(Q111/Q111)}$ compared to wild-type cells using the DCF assay (Figure IV. 7.A. - 7.C. and Table IV. 4.). In addition, we have previously demonstrated a concentration- and time-dependent decrease in mutant Mn uptake kinetics and cellular Mn storage compared to wild-type ST*Hdh*$^{(Q7/Q7)}$ cells (Figure III. 3.A. and 3.B.). Interestingly, MacDonald and colleagues utilized a chemiluminescent H_2O_2 detection kit to monitor intracellular H_2O_2 concentrations as a read-out of ROS production in the same HD striatal cells and reported a significant reduction in mutant ST*Hdh*$^{Q111/Q111}$ ROS levels compared to wild-type ST*Hdh*$^{(Q7/Q7)}$ cells[9]. However, we observed the opposite effect at 5, 15, and 30 minutes exposure to H_2O_2 (Figure IV. 7.A. - 7.C.). This difference may possibly be due to the specificity and detection limits of the assays been used for ROS assessment. Specifically, the DCF assay is a fluorometric assay that does not discriminate between the types of free radicals generated in the cell to cause changes in ROS levels. However, the cheluminescent assay is a luminescent assay that specifically measures intracellular H_2O_2 concentration as a direct correlation of intracellular ROS levels. In spite of the time-dependent increase in H_2O_2 stimulated ROS production in wild-type cells at 5,15, and 30

minutes, we did not observe a significant increase in ROS levels above baseline at 30 minutes (Figure IV. 7.C.). This may be due to maximal ROS production in the wild-type ST*Hdh*$^{(Q7/Q7)}$ cells and unlikely due to saturation of free intracellular DCF molecules for free radical binding. Moreover, mutant ST*Hdh*$^{Q111/Q111}$ cells that were equally loaded with DCF dye exhibited increased ROS levels above baseline after 30 minutes exposure to H_2O_2. Finally, this data suggest that the differential- and temporal-dependent Mn uptake, and net cellular Mn pools between wild-type ST*Hdh*$^{(Q7/Q7)}$ and mutant ST*Hdh*$^{(Q111/Q111)}$ cells may be functionally related to the rate of oxidative injury induction. This phenomenon may underlie the differential vulnerability of Mn-induced cytoxicity between wild-type and mutant HD striatal cells. It is noteworthy that the functional relationship between cellular Mn pools and oxidative injury demonstrated in the HD striatal cells might not be the primary mechanism underlying striatal specific degeneration of medium spiny neurons in HD patients. In fact, it is highly likely that a combination of diminished cellular Mn levels, impaired Mn-dependent and other antioxidant activities, altered mitochondrial function, oxidative injury, diminished ATP levels, decreased neuroprotective roles of glial cells, protein aggregation, and upregulation of cell death mechanisms might underlie the *in vivo* mutant HTT expressing striatal-specific degeneration.

References

1. Bates, G.P. History of genetic disease: the molecular genetics of Huntington disease - a history. *Nat Rev Genet* **6**, 766-73 (2005).

2. Walker, F.O. Huntington's disease. *Lancet* **369**, 218-28 (2007).

3. Group, H.s.D.C.R. A novel gene containing a trinucleotide repeats that is expanded and unstable on Huntington's disease chromosomes. *Cell* **72**, 971-983 (1993).

4. Cowan, C.M. & Raymond, L.A. Selective neuronal degeneration in Huntington's disease. *Curr Top Dev Biol* **75**, 25-71 (2006).

5. Borrell-Pages, M., Zala, D., Humbert, S. & Saudou, F. Huntington's disease: from huntingtin function and dysfunction to therapeutic strategies. *Cell Mol Life Sci* **63**, 2642-60 (2006).

6. Dexter, D.T., Carayon, A., Javoy-Agid, F., Agid, Y., Wells, F.R., Daniel, S.E., Lees, A.J., Jenner, P. & Marsden, C.D. Alterations in the levels of iron, ferritin and other trace metals in Parkinson's disease and other neurodegenerative diseases affecting the basal ganglia. *Brain* **114 (Pt 4)**, 1953-75 (1991).

7. Dexter, D.T., Jenner, P., Schapira, A.H. & Marsden, C.D. Alterations in levels of iron, ferritin, and other trace metals in neurodegenerative diseases affecting the basal ganglia. The Royal Kings and Queens Parkinson's Disease Research Group. *Ann Neurol* **32 Suppl**, S94-100 (1992).

8. Lumsden, A.L., Henshall, T.L., Dayan, S., Lardelli, M.T. & Richards, R.I. Huntingtin-deficient zebrafish exhibit defects in iron utilization and development. *Hum Mol Genet* **16**, 1905-20 (2007).

9. Lee, J.M., Ivanova, E.V., Seong, I.S., Cashorali, T., Kohane, I., Gusella, J.F. & MacDonald, M.E. Unbiased gene expression analysis implicates the huntingtin polyglutamine tract in extra-mitochondrial energy metabolism. *PLoS Genet* **3**, e135 (2007).

10. Gómez-Esteban, J.C., Lezcano, E., Zarranz, J.J., Velasco, F., Garamendi, I., Pérez, T. & Tijero , B. Monozygotic twins suffering from Huntington's disease show different cognitive and behavioural symptoms. *European Neurology* **57**, 26-30 (2007).

11. Georgiou, N., Bradshaw, J.L., Chiu, E., Tudor, A., O'Gorman, L. & Phillips, J.G. Differential clinical and motor control function in a pair of monozygotic twins with Huntington's disease. *Mov Disord* **14**, 320-5 (1999).

12. Friedman, J.H., Trieschmann, M.E., Myers, R.H. & Fernandez, H.H. Monozygotic twins discordant for Huntington disease after 7 years. *Arch Neurol* **62**, 995-7 (2005).

13. Anca, M.H., Gazit, E., Loewenthal, R., Ostrovsky, O., Frydman, M. & Giladi, N. Different phenotypic expression in monozygotic twins with Huntington disease. *Am J Med Genet A* **124A**, 89-91 (2004).

14. Garcia, M., Vanhoutte, P., Pages, C., Besson, M.J., Brouillet, E. & Caboche, J. The mitochondrial toxin 3-nitropropionic acid induces striatal neurodegeneration via a c-Jun N-terminal kinase/c-Jun module. *J Neurosci* **22**, 2174-84 (2002).

15. van Dellen, A., Grote, H.E. & Hannan, A.J. Gene-environment interactions, neuronal dysfunction and pathological plasticity in Huntington's disease. *Clin Exp Pharmacol Physiol* **32**, 1007-19 (2005).

16. Williams, B.B., Kwakye, G.F., Wegrzynowicz, M., Li, D., Aschner, M., Erikson, K.M. & Bowman, A.B. Altered manganese homeostasis and manganese toxicity in a Huntington's disease striatal cell model are not explained by defects in the iron transport system. *Toxicol Sci* **117**, 169-79 (2010).

17. Williams, B.B., Li, D., Wegrzynowicz, M., Vadodaria, B.K., Anderson, J.G., Kwakye, G.F., Aschner, M., Erikson, K.M. & Bowman, A.B. Disease-toxicant screen reveals a neuroprotective interaction between Huntington's disease and manganese exposure. *J Neurochem* **112**, 227-37 (2010).

18. Mena, I., Honuchi, K. & Lopez, G. Factors enhancing entrance of manganese into brain iron deficiency and age. *J. Nucl Med* **15**(1974).

19. Aschner, M. & Aschner, J.L. Manganese neurotoxicity: cellular effects and blood-brain barrier transport. *Neurosci Biobehav Rev* **15**, 333-40 (1991).

20. Rabin, O., Hegedus, L., Bourre, J.M. & Smith, Q.R. Rapid brain uptake of manganese(II) across the blood-brain barrier. *J Neurochem* **61**, 509-17 (1993).

21. Murphy, V.A., Wadhwani, K.C., Smith, Q.R. & Rapoport, S.I. Saturable transport of manganese(II) across the rat blood-brain barrier. *J Neurochem* **57**, 948-54 (1991).

22. Aschner, M. & Gannon, M. Manganese (Mn) transport across the rat blood-brain barrier: saturable and transferrin-dependent transport mechanisms. *Brain Res Bull* **33**, 345-9 (1994).

23. Gunter, T.E. & Puskin, J.S. Manganous ion as a spin label in studies of mitochondrial uptake of manganese. *Biophys J.* , 625-35 (1972).

24. Liccione, J.J. & Maines, M.D. Selective vulnerability of glutathione metabolism and cellular defense mechanisms in rat striatum to manganese. *J Pharmacol Exp Ther* **247**, 156-61 (1988).

25. Kalia, K., Jiang, W. & Zheng, W. Manganese accumulates primarily in nuclei of cultured brain cells. *Neurotoxicology* **29**, 466-70 (2008).

26. Gavin, C.E., Gunter, K.K. & Gunter, T.E. Manganese and calcium transport in mitochondria: implications for manganese toxicity. *Neurotoxicology* **20**, 445-53 (1999).

27. Zwingmann, C., Leibfritz, D. & Hazell, A.S. Energy metabolism in astrocytes and neurons treated with manganese: relation among cell-specific energy failure, glucose metabolism, and intercellular trafficking using multinuclear NMR-spectroscopic analysis. *J Cereb Blood Flow Metab* **23**, 756-71 (2003).

28. Archibald, F.S. & Tyree, C. Manganese poisoning and the attack of trivalent manganese upon catecholamines. *Arch Biochem Biophys* **256**, 638-50 (1987).

29. Gunter, T.E., Miller, L.M., Gavin, C.E., Eliseev, R., Salter, J., Buntinas, L., Alexandrov, A., Hammond, S. & Gunter, K.K. Determination of the oxidation

states of manganese in brain, liver, and heart mitochondria. *J Neurochem* **88**, 266-80 (2004).

30. Gunter, K.K., Aschner, M., Miller, L.M., Eliseev, R., Salter, J., Anderson, K. & Gunter, T.E. Determining the oxidation states of manganese in NT2 cells and cultured astrocytes. *Neurobiol Aging* **27**, 1816-26 (2006).

31. Quintanilla, R.A., Jin, Y.N., Fuenzalida, K., Bronfman, M. & Johnson, G.V. Rosiglitazone treatment prevents mitochondrial dysfunction in mutant huntingtin-expressing cells: possible role of peroxisome proliferator-activated receptor-gamma (PPARgamma) in the pathogenesis of Huntington disease. *J Biol Chem* **283**, 25628-37 (2008).

32. Glass, C.K. & Ogawa, S. Combinatorial roles of nuclear receptors in inflammation and immunity. *Nat Rev Immunol* **6**, 44-55 (2006).

33. Aschner, M., Guilarte, T.R., Schneider, J.S. & Zheng, W. Manganese: recent advances in understanding its transport and neurotoxicity. *Toxicol Appl Pharmacol* **221**, 131-47 (2007).

34. Fox, J.H., Kama, J.A., Lieberman, G., Chopra, R., Dorsey, K., Chopra, V., Volitakis, I., Cherny, R.A., Bush, A.I. & Hersch, S. Mechanisms of copper ion mediated Huntington's disease progression. *PLoS One* **2**, e334 (2007).

35. Molina-Holgado, F., Hider, R.C., Gaeta, A., Williams, R. & Francis, P. Metals ions and neurodegeneration. *Biometals* **20**, 639-54 (2007).

36. Wright, R.O. & Baccarelli, A. Metals and neurotoxicology. *J Nutr* **137**, 2809-13 (2007).

37. Choi, C.J., Anantharam, V., Martin, D.P., Nicholson, E.M., Richt, J.A., Kanthasamy, A. & Kanthasamy, A.G. Manganese upregulates cellular prion protein and contributes to altered stabilization and proteolysis: relevance to role of metals in pathogenesis of prion disease. *Toxicol Sci* **115**, 535-46 (2010).

38. Firdaus, W.J., Wyttenbach, A., Giuliano, P., Kretz-Remy, C., Currie, R.W. & Arrigo, A.P. Huntingtin inclusion bodies are iron-dependent centers of oxidative events. *FEBS J* **273**, 5428-41 (2006).

39. Kwakye, G.F., Li, D. & Bowman, A.B.B. Novel high-throughput assay to assess cellular manganese levels in a striatal cell line model of Huntington's disease confirms a deficit in manganese accumulation. *Neurotoxicology* (2011).

40. Cattaneo, E. & Conti, L. Generation and characterization of embryonic striatal conditionally immortalized ST14A cells. *J Neurosci Res* **53**, 223-34 (1998).

41. Milakovic, T. & Johnson, G.V. Mitochondrial respiration and ATP production are significantly impaired in striatal cells expressing mutant huntingtin. *J Biol Chem* **280**, 30773-82 (2005).

42. Trettel, F., Rigamonti, D., Hilditch-Maguire, P., Wheeler, V.C., Sharp, A.H., Persichetti, F., Cattaneo, E. & MacDonald, M.E. Dominant phenotypes produced by the HD mutation in STHdh(Q111) striatal cells. *Hum Mol Genet* **9**, 2799-809 (2000).

43. Aschner, M., Mullaney, K.J., Wagoner, D., Lash, L.H. & Kimelberg, H.K. Intracellular glutathione (GSH) levels modulate mercuric chloride (MC)- and methylmercuric chloride (MeHgCl)-induced amino acid release from neonatal rat primary astrocytes cultures. *Brain Res* **664**, 133-40 (1994).

44. Kreutz, C., Bartolome Rodriguez, M.M., Maiwald, T., Seidl, M., Blum, H.E., Mohr, L. & Timmer, J. An error model for protein quantification. *Bioinformatics* **23**, 2747-53 (2007).

45. Ehrich, M. & Sharova, L. In vitro methods for detecting cyto-toxcity. *Curr. Protoc. Toxicol.* **3**, 6.2.11-6.2.12 (2000).

46. Buckett, P.D. & Wessling-Resnick, M. Small molecule inhibitors of divalent metal transporter-1. *Am J Physiol Gastrointest Liver Physiol* **296**, G798-804 (2009).

47. Au, C., Benedetto, A. & Aschner, M. Manganese transport in eukaryotes: the role of DMT1. *Neurotoxicology* **29**, 569-76 (2008).

48. Erikson, K.M. & Aschner, M. Increased manganese uptake by primary astrocyte cultures with altered iron status is mediated primarily by divalent metal transporter. *Neurotoxicology* **27**, 125-30 (2006).

49. Gunshin, H., Mackenzie, B., Berger, U.V., Gunshin, Y., Romero, M.F., Boron, W.F., Nussberger, S., Gollan, J.L. & Hediger, M.A. Cloning and characterization of a mammalian proton-coupled metal-ion transporter. *Nature* **388**, 482-8 (1997).

50. Bowman, A.B., Erikson, K.M. & Aschner, M. Manganese - The two faces of essentiality and neurotoxicity. in *Metals and Neurodegeneration* (ed. Huang, S.) (Research Signpost, Kerala, India, 2010).

51. Shibuya, I. & Douglas, W.W. Calcium channels in rat melanotrophs are permeable to manganese, cobalt, cadmium, and lanthanum, but not to nickel: evidence provided by fluorescence changes in fura-2-loaded cells. *Endocrinology* **131**, 1936-41 (1992).

52. Heilig, E.A., Thompson, K.J., Molina, R.M., Ivanov, A.R., Brain, J.D. & Wessling-Resnick, M. Manganese and iron transport across pulmonary epithelium. *Am J Physiol Lung Cell Mol Physiol* **290**, L1247-59 (2006).

53. Riccio, A., Mattei, C., Kelsell, R.E., Medhurst, A.D., Calver, A.R., Randall, A.D., Davis, J.B., Benham, C.D. & Pangalos, M.N. Cloning and functional expression of human short TRP7, a candidate protein for store-operated Ca2+ influx. *J Biol Chem* **277**, 12302-9 (2002).

54. Gavin, C.E., Gunter, K.K. & Gunter, T.E. Manganese and calcium efflux kinetics in brain mitochondria. Relevance to manganese toxicity. *Biochem J* **266**, 329-34 (1990).

55. Kazuhiko, N., Kawasaki, F. & Kita, H. Mn and Mg influxes through Ca channels of motor nerve terminals are prevented by verapamil in frogs. *Brain Research* **510**, 289-295 (1990).

56. Fukuda, J. & Kawa, K. Permeation of manganese, cadmium, zinc, and beryllium through calcium channels of an insect muscle membrane. *Science* **190**, 309-311 (1977).

57. Bezprozvanny, I. Inositol 1,4,5-tripshosphate receptor, calcium signalling and Huntington's disease. *Subcell Biochem* **45**, 323-35 (2007).

58. Williams, A., Sarkar, S., Cuddon, P., Ttofi, E.K., Saiki, S., Siddiqi, F.H., Jahreiss, L., Fleming, A., Pask, D., Goldsmith, P., O'Kane, C.J., Floto, R.A. & Rubinsztein, D.C. Novel targets for Huntington's disease in an mTOR-independent autophagy pathway. *Nat Chem Biol* **4**, 295-305 (2008).

59. Tang, T.S., Tu, H., Chan, E.Y., Maximov, A., Wang, Z., Wellington, C.L., Hayden, M.R. & Bezprozvanny, I. Huntingtin and huntingtin-associated protein 1 influence neuronal calcium signaling mediated by inositol-(1,4,5) triphosphate receptor type 1. *Neuron* **39**, 227-39 (2003).

60. Panov, A.V., Gutekunst, C.A., Leavitt, B.R., Hayden, M.R., Burke, J.R., Strittmatter, W.J. & Greenamyre, J.T. Early mitochondrial calcium defects in Huntington's disease are a direct effect of polyglutamines. *Nat Neurosci* **5**, 731-6 (2002).

61. Mazziotta, J.C., Phelps, M.E., Pahl, J.J., Huang, S.C., Baxter, L.R., Riege, W.H., Hoffman, J.M., Kuhl, D.E., Lanto, A.B., Wapenski, J.A. & et al. Reduced cerebral glucose metabolism in asymptomatic subjects at risk for Huntington's disease. *N Engl J Med* **316**, 357-62 (1987).

62. Coles, C.J., Edmondson, D.E. & Singer, T.P. Inactivation of succinate dehydrogenase by 3-nitropropionate. *J Biol Chem* **254**, 5161-7 (1979).

63. Beal, M.F. Huntington's disease, energy, and excitotoxicity. *Neurobiol Aging* **15**, 275-6 (1994).

64. Lesort, M., Tucholski, J., Zhang, J. & Johnson, G.V. Impaired mitochondrial function results in increased tissue transglutaminase activity in situ. *J Neurochem* **75**, 1951-61 (2000).

65. Alston, T.A., Mela, L. & Bright, H.J. 3-Nitropropionate, the toxic substance of Indigofera, is a suicide inactivator of succinate dehydrogenase. *Proc Natl Acad Sci U S A* **74**, 3767-71 (1977).

66. Goytain, A., Hines, R.M. & Quamme, G.A. Huntingtin-interacting proteins, HIP14 and HIP14L, mediate dual functions, palmitoyl acyltransferase and Mg2+ transport. *J Biol Chem* **283**, 33365-74 (2008).

67. Gitler, A.D., Chesi, A., Geddie, M.L., Strathearn, K.E., Hamamichi, S., Hill, K.J., Caldwell, K.A., Caldwell, G.A., Cooper, A.A., Rochet, J.C. & Lindquist, S. Alpha-synuclein is part of a diverse and highly conserved interaction network that includes PARK9 and manganese toxicity. *Nat Genet* **41**, 308-15 (2009).

68. Bond, G.H. & Hudgins, P.M. Inhibition of human red cell Nak-ATPase by magnesium and potassium. *Biochem Biophys Res Commun* **66**, 645-50 (1975).

69. Plishker, G.A. Effects of cadmium and zinc on calcium uptake in human red blood cells. *Am J Physiol* **247**, C143-9 (1984).

70. Shawki, A. & Mackenzie, B. Interaction of calcium with the human divalent metal-ion transporter-1. *Biochem Biophys Res Commun* **393**, 471-5 (2010).

71. Wedler, F.C., Ley, B.W. & Grippo, A.A. Manganese(II) dynamics and distribution in glial cells cultured from chick cerebral cortex. *Neurochem Res* **14**, 1129-35 (1989).

72. Aschner, M., Gannon, M. & Kimelberg, H.K. Manganese uptake and efflux in cultured rat astrocytes. *J Neurochem* **58**, 730-5 (1992).

73. Fitsanakis, V.A., Piccola, G., Aschner, J.L. & Aschner, M. Characteristics of manganese (Mn) transport in rat brain endothelial (RBE4) cells, an in vitro model of the blood-brain barrier. *Neurotoxicology* **27**, 60-70 (2006).

74. Milatovic, D., Yin, Z., Gupta, R.C., Sidoryk, M., Albrecht, J., Aschner, J.L. & Aschner, M. Manganese induces oxidative impairment in cultured rat astrocytes. *Toxicol Sci* **98**, 198-205 (2007).

75. Zhang, P., Hatter, A. & Liu, B. Manganese chloride stimulates rat microglia to release hydrogen peroxide. *Toxicol Lett* **173**, 88-100 (2007).

CHAPTER V

DISCUSSION AND FUTURE DIRECTIONS

Discussion

The novel findings of these studies include (1) development, optimization, and validation of a high-throughput assay, CFMEA, to measure Mn levels and transport dynamics in cultured HD striatal cells, (2) development of an efficient quantitative normalization assay, PicoGreen assay, to measure dsDNA levels in cultured cells post CFMEA analyses, (3) functional characterization and identification of the impaired Mn transport kinetics (uptake, cellular storage, and efflux) in mutant HD striatal cells, (4) dissection of metal transporter systems and identification of a putative Mn transporter that may underlie the disrupted Mn homeostasis in mutant HD striatal cells, and (5) determination of the relationship between Mn uptake, cellular Mn pools, Mn induced cytotoxicity, and oxidative stress in wild-type and mutant HD striatal cells.

Development of CFMEA and PicoGreen assays

In our quest to develop CFMEA, we optimized the essential assay conditions and parameters required for efficient and accurate detection of the detergent-extracted cellular Mn levels in cultured cells. Contrary to the previous reports of a temperature–dependent

subcellular localization of fura-2 in cells loaded with fura-2 AM and measured at $F_{340/380}$ ratio[1-3], we report minimal influence of temperature on Mn-fura-2 interaction at the Ca^{2+} isosbestic wavelength, excitation at 360 nm (Ex_{360}) in a cell-free system (Figure II. 1.B.). The disparity between our findings and that of the single-cell loaded fura-2 studies may be due to the following: (i) diminished activity of intracellular esterases to cleave the AM portion of the fura-2 dye at lower temperatures and not necessarily a direct influence of temperature on the Ca^{2+}-fura-2 interaction; (ii) temperature-dependent sequestration of fura-2 dye into organelles[4,5] that would decrease the availability of free cytosolic fura-2 dye to be detected; (iii) differences in the excitation wavelengths used to measure the temperature-dependent effects on fura-2 fluorescence, for example: Ex_{360} versus $Ex_{340/380}$ nm. In fact, measurements of intracellular Ca^{2+} levels using $Ex_{340/380}$ nm excitation ratio has been suggested to decrease the variability induced by differences in cellular fura-2 loading, disparities in the thickness of cells, and potential dye leakage during detection of intracellular Ca^{2+} concentrations in cells[1,4]. Based on the photochemical properties of fura-2 and changes in membrane potential, it is likely that the temperature-dependent changes previously reported in the fura-2 loaded cells might be due in part by (a) photodegradation or bleaching of fura-2 dye that may be interpreted as temperature-induced decrease in fura-2 fluorescence or (b) rupturing of membranes and efficient fura-2 dye leakage into the extracellular milieu.

Given the unique quenching relationship between fura-2 concentration, Mn detection limits, and the expected cellular Mn levels in cultured cells following $MnCl_2$ exposure, it was crucial for us to examine the optimal fura-2 concentration required for

the precise and accurate detection limits of extracted cellular Mn levels in the cells. This was achieved by (a) estimation of the maximum Mn concentration that could possibly be present in the cultured cells or animal tissues following $MnCl_2$ exposure for the preferred duration and (b) generation of Mn-fura-2 standard curves that spanned the expected cellular Mn concentration, which enabled efficient back calculation of extracted Mn levels in cells or tissues following $MnCl_2$ exposure. Although the recommended Mn detection window by fura-2 is applicable to any generated Mn-fura-2 standard curves, the experimenter may modify the recommended detection window (10% - 85%). However, it is important that the newly defined Mn detection window obtained by extrapolating the minimum and maximum $\%_{MAX}$ values on the Mn-fura-2 standard curve fit within the optimal detection range of the sigmoidal Mn-fura-2 standard curve. Importantly, it is critical to ensure that the number of cultured cells used in the experiment is above the minimum number of cells (~ 5,000 cells per well in a 96 tissue culture plate, empirically determined by us) required for Mn detection by CFMEA. The quantitative relationship between Mn and fura-2 fits with a Michaelis-Menten one-site specific saturation-binding kinetics[6]. However, to enable efficient back calculation of Mn concentrations from changes in fura-2 fluorescence, it is necessary to switch the axes of the Mn-standard curve and represent $\%_{MAX}$ fura-2 values and Mn concentration on the x and y-axes, respectively. The binding curve data obtained when the axes are switched tightly fit to exponential and logarithmic curves generated using Microsoft excel non-linear regression analysis. Thus, enabling a direct back calculation of extracted Mn levels from experimentally determined $\%_{MAX}$ values. Conversely, other curves (polynomial, linear, etc) may also be used to model the mathematical relationship between Mn and fura-2

depending on the range of Mn concentrations used to generate the Mn-fura-2 standard curve. In fact, it is necessary to generate Mn-fura-2 standard curve alongside Mn-exposure experiments to accurately quantify extracted cellular Mn levels using the same fura-2 containing extraction buffer. This will decrease any experimental variability caused by changes in the concentration or volume of fura-2 added during the preparation of the extraction buffer. Interestingly, low Mn concentration samples (1 – 100 nM) used to generate Mn-fura-2 standard curves between independent experiments demonstrated moderate variability (Figure II. 3.A.). This might be due to low sensitivity of the plate reader at those concentrations. This variability can be minimized by averaging the RFU values of the 0 μM Mn samples within each independent standard curve and defining this value as the 100% maximal fluorescence for that experiment. In addition, normalization of the RFU values of each well as $\%_{MAX}$ to the 100% maximal fluorescence value for representation on the Mn-fura-2 standard curve decreases experimental variability.

We have shown that the ideal detergent concentration for Mn extraction from the cultured HD striatal cell is 0.1% Triton X-100 (Figure II. 1C.). Furthermore, we have demonstrated that detergent is required for the detection of fura-2 quenching by CFMEA, suggesting that extracellular Mn is not a significant component of the Mn detected by CFMEA. However, we observed minimal influence of Triton X-100 on baseline fura-2 fluorescence relative to SDS. In addition, the unexpected biphasic increase in fura-2 RFU of both baseline control and cell extracts from 0 to 1% SDS may possibly be due to an interaction between SDS and fura-2. Interestingly, previous experimental evidence has suggested that SDS can exist either as monomers or micellar aggregates in aqueous

solutions depending on the total concentration, ionic strength, and temperature. Moreover, increasing total concentration of SDS at a given ionic strength impedes the ability to measure increases in monomer concentration above the critical micelle concentration[7]. The lack of a concentration-response relationship observed in SDS might be due to alteration in the critical micelle concentration used for Mn extraction in the cultured HD striatal cells (Figure II. 1.B). The cellular Mn extraction conditions that we have demonstrated are ideal for many cultured cells including primary cultured astrocytes (Figure IV. 1.A.). However, if the experimenter chooses to optimize the extraction conditions for the cultured cells used for cellular Mn uptake and transport kinetic studies due to known physical, chemical, or other interferences with the described cellular Mn extraction conditions, it is important to consider the critical micelle concentration of the chosen detergent concentration. For example higher concentrations of Triton X-100 and SDS (>1%) impedes efficient cellular Mn extraction from the cultured cells[8].

The quenching effect of metal ions other than Mn^{2+} on fura-2 and the ability of Zn^{2+} to increase fura-2 fluorescence at the Ca^{2+} isosbestic wavelength, 360 nm (Figure II. 4. and II. 5., Table II. 2.) that we identified may be caused by (i) similar or higher affinities of those metals for the fura-2 molecule, (ii) the bandwidth of filter [Ex_{360} (bandwidth of filter = ± 35 nm)] overlapping with known wavelengths of fura-2 that are influenced by other metal ions, or (iii) molecular crowding theory of metal ions on fura-2 molecules. Endogenous heavy metal ions are known to influence fura-2 fluorescence (increase or decrease) in single cell loaded fura-2 AM at $Ex_{340/380}$ excitation ratio[9-15]. Although theoretically metal ions are not supposed to have any effect on fura-2

fluorescence at the Ca^{2+} isosbestic wavelength, we observed that Fe^{2+}, Co^{2+}, Ni^{2+}, Cu^{2+}, and Cd^{2+} quenched while Zn^{2+} increased the fura-2 fluorescence in an *in vitro* cell-free assay. Zn^{2+} binds to fura-2 molecule with a high affinity (Kd = 1.5 nM)[16] and induce similar but increased shifts in the isosbestic excitation wavelength to 376 nm[10]. This may explain why we observed ~20% maximum increase with 100 μM Zn^{2+} in our studies. Our findings of other metal ions, excluding Mn, to quench fura-2 fluorescence at the Ca^{2+} isosbestic wavelength support the previously reported effects of heavy metal ions including, Mn^{2+}, Fe^{2+}, and Cu^{2+} to quench fura-2 fluorescence over a wide excitation wavelengths (300 – 400 nm) range including the Ca^{2+} isosbestic wavelength (360 nm) in single cell loaded fura-2 AM[10]. However, Snitsarev and colleagues did not examine the contribution of Ni^{2+}, Co^{2+}, and Cd^{2+} on fura-2 fluorescence at 360 nm. This may be due to their low abundance or affinity for fura-2 in cells. Our data identify the influence of other metal ions on fura-2 fluorescence at 360 nm. Secondly, we used an excitation filter of 360 nm with a bandwidth of ± 35 nm that overlaps with the excitation wavelengths (340 and 380 nm) of fura-2, which can be potentially influenced by metal ions. Thirdly, molecular crowding is thought to occur when metal ions cluster around metal-bound fluorophores, such as fura-2, and occlude the fluorescence to cause decrease in fluorescence. We have observed an unexpected fura-2 quenching effect (~10%) with Ca^{2+} concentrations above 10 μM regardless of the concentration of Mn present in the assay. It is possible that the competitive quenching effect of Ca^{2+} may be due to changes in the fura-2 and Mn binding stoichiometry that would induce molecular crowding of fura-2 by Ca^{2+} ions and decreases its fluorescence. In addition, we have demonstrated a

concentration-dependent decrease in the relationship between Ca^{2+} bound fura-2 at the isosbestic wavelength (Figure II. 5.A.).

Not only do Co^{2+} and Cu^{2+} quench fura-2 fluorescence in a concentration-dependent manner, but also they competitively interfere with Mn-fura-2 interaction at concentrations above 1 μM (Figure II. 5.C. and data not shown). Interestingly, other metal ions (for, example Zn^{2+} that mimics Ca^{2+} binding to the fura-2 molecule) have been reported to compete with Ca^{2+} for binding to fura-2 and decrease the affinity of fura-2 for Ca^{2+} binding in single cell loaded fura-2 AM at $F_{340/380}$ excitation ratio[10]. Chelation of Zn^{2+} abolishes the competitive effect of Zn^{2+} on the Ca^{2+}-fura-2 interaction and enhances Ca^{2+} induced amplitude changes in fura-2 fluorescence[10]. This suggests the need to control for endogenous metal ions from cell-extracts used in CFMEA analysis. Due to that fact that a metal chelator capable of chelating all other metal ions with the exception of Mn is currently not available, we extract Mn from cultured cells in a large volume of fura-2 detergent-based extraction buffer (100 μL) and this substantially reduces the concentration of endogenous metal ions that may competitively influence Mn-fura-2 interaction. In addition, we normalize extracted cellular Mn levels from $MnCl_2$ exposed cells to vehicle-only before further normalization of extracted cellular Mn levels to dsDNA on a per well basis using PicoGreen assay. Thus, accounting for possible changes in basal metal ion influence on the accuracy and specificity of CFMEA to measure Mn levels.

Given that other metal ions influenced fura-2 fluorescence at the Ca^{2+} isosbestic wavelength, we were cognizant about their effects on the accuracy and specificity of Mn

detection by CFMEA. We have validated the accuracy and specificity of CFMEA by two alternative Mn supplementation assays (Figure II. 6.A. and 6.B.) and the gold standard technique for detecting Mn levels, GFAAS (Figure II. 7.). Importantly, we showed that both CFMEA and GFAAS were capable of detecting comparable changes in net Mn levels in cultured HD striatal cells and exhibited similar Mn detection sensitivities at the tested concentrations. In addition, our findings from the Mn supplementation tests indicate that CFMEA is proficient in accurately and specifically measuring Mn concentrations in both Mn spiked extracted cultured HD striatal cells and fura-2 containing extraction buffer. In addition, CFMEA validation by GFAAS further suggests that the above-discussed metal ions' influence on fura-2 fluorescence is substantially decreased under the optimized cellular Mn extraction conditions. Nevertheless, it is noteworthy that CFMEA may fail to provide accurate measurements of cellular Mn levels following exposure to mixtures of toxicants containing multiple fura-2 binding metals if levels reach concentrations high enough to influence fura-2 fluorescence. On the other hand, given the substantial affinity of Cu^{2+}, Co^{2+}, Ni^{2+}, and Fe^{2+} for fura-2, it is likely that CFMEA could be adapted for studies examining the cellular uptake of these other metals.

Due to insufficient protein levels to be detected by standard protein assays, we developed the PicoGreen assay (described in chapter II) to enable normalization of cellular Mn levels to dsDNA post CFMEA analyses. Although the emission spectra of fura-2 and PicoGreen overlapped, we observed no effect of fura-2 on PicoGreen fluorescence (data not shown). It is important that the solution is prepared in a plastic container instead of glass surfaces as this may cause absorption of the PicoGreen reagent.

Given that PicoGreen reagent is susceptible to photodegradation, the working solution must be covered in foil to protect from light or store in the dark. In addition, 96 well tissue culture plates containing cell-extracts and dsDNA standard curve must be protected from light. During the preparation of dsDNA standards for PicoGreen normalization assay, it is important that the components of the extraction buffer used to prepare the dsDNA standards and for extraction of cellular Mn cells are treated the same and contain similar levels of contaminants. Although the CFMEA and PicoGreen assays described in this thesis was used to measure and normalize cellular Mn uptake and transport kinetics in striatal cells and primary astrocyte cells cultured in 96 well plate format to dsDNA, the parameters of the assays can be modified to assess cellular Mn transport dynamics using different culture plate formats, cultured cell densities, and cell types. Specifically, to assess cellular Mn uptake and transport dynamics in larger cell densities, cultured cells can be plated on 12 or 48 wells tissue culture plates. This would enable the usage of standard protein detection methods to normalize extracted cellular Mn levels to protein levels instead of utilization of the PicoGreen dsDNA assay.

The amount of time required to measure cellular Mn uptake and transport dynamics in cultured cells by CFMEA can be divided into five phases: (1) biological preparation, (2) transport incubations, (3) generation of Mn-fura-2 standard curve, (4) normalization, and (5) data analysis. The first phase requires significantly more time than the other four phases. The preparation of cultured cells, which includes trypsinization, cell counting, and plating in the 96 well tissue culture plates require ~ 10 - 15 minutes per 96 well plate. If Mn uptake and transport dynamics are assessed in cells that grow in

suspension, this time would vary depending on the method being used to prepare the cells. The transport incubations typically require ~ 5 - 10 minutes preparation of working $MnCl_2$ solutions from stocks. Cultured cells exposed to $MnCl_2$ in HEPES salt exposure buffer or Krebs Ringers buffer require ~ 3 - 5 minutes per 96 well plate pre-wash two times with 200 μL of either of the indicated serum-free exposure buffers. In contrast to the duration necessary for the first phase and preparatory steps of the second phase, the actual Mn transport incubations are done in real time. The duration required for metal transport incubation could be as early as 5 minutes and dependent on the type of cultured cells, experimental design, exposure buffer, and concentration of $MnCl_2$ used for exposure. Furthermore, generation of a cell-free Mn-fura-2 standard curve necessitates ~ 5 minutes per experiment. It takes ~ 2 minutes per 96 well plate per assay to measure changes in fura-2 fluorescence in the fluorometric plate reader. The PicoGreen assay requires ~ 5 minutes to load a 96 well plate with DNA standards and ~ 5 minutes incubation of standards with PicoGreen reagent. In addition, an ~ 2 - 4 minutes per 96 well tissue culture plate is required to transfer cell extracts into a new 96 well plate before incubation with PicoGreen reagent for ~ 5 minutes and ~ 2 minutes per 96 well tissue culture plate to measure PicoGreen fluorescence with a fluorometric plate reader. The duration of the fifth phase is flexible and depends on practice, experimenter's speed of data analysis and familiarity to Microsoft excel linear regression analysis. It typically takes ~ 5 - 7 minutes per 96 well plate for complete analysis of cellular Mn levels and normalization by DNA. Depending on the experimental set-up, duration and concentration of $MnCl_2$, and familiarity with Microsoft Excel non-linear regression analysis, approximately ten to twenty 96-well plates can be assayed and scored in one

day. In comparison, GFAAS and other traditional Mn detection assays can take several days to weeks (*personal communication*) to analyze the same experimental samples. Finally, we report that CFMEA provides a high-throughput, feasible, accurate, and inexpensive assessment of cellular Mn levels in cultured cells. This assay provided a rapid means to evaluate Mn transport kinetics in cellular toxicity and disease models.

Manganese transport dynamics in HD striatal cells

We have found that expression of mutant HTT protein significantly reduces net Mn accumulation in a broad concentration-[17] and time-dependent manner compared to wild-type ST*Hdh*$^{(Q7/Q7)}$ cells using CFMEA analysis (Figure III.1.A. and B.). The concentration-dependent decrease in mutant ST*Hdh*$^{(Q111/Q111)}$ cells further supports the previously published decreased net Mn accumulation in mutant ST*Hdh*$^{(Q111/Q111)}$ cells compared to wild-type by GFAAS[18]. In addition, other studies using radiotracer ^{54}Mn have demonstrated that Mn uptake and accumulation in glial cells (astrocytes) occurs in a concentration- and time-dependent manner. Moreover, cultured astrocytes not only proficiently transports Mn, but contain glutamine synthetase (an astrocyte specific manganoprotein) which accounts for ~ 80% of net Mn levels in the brain[19-21]. To the best of my knowledge, no studies have directly and simultaneously measured Mn accumulation levels in astrocytes versus neurons cultured from the same animal in the same or different brain tissue. The current evidence to support substantial Mn uptake in astrocytes were all conducted in primary astrocytic cultures. However, our current

findings showed a subtle but significant increase in net Mn accumulation in the neuronal wild-type HD striatal cells compared to the primary astrocytes following 100 μM $MnCl_2$ exposure in media for 6 hrs (Figure IV. 2.). The incongruities between our findings and the previously reported bulk astrocytic Mn accumulation following Mn exposure might be due to (a) differences in species – murine neuronal HD cells versus rat primary astrocytes, (b) brain-region specificity and affinity for Mn accumulation – striatum versus cortex, and (c) immortalized HD cell line versus primary astrocytes. It is likely that under *in vivo* conditions, glial cells (astrocytes) might be regulating the amount of Mn that accumulates in neurons via the sequestration of Mn into intracellular compartments. However, in the absence of astrocytes, neurons lose their neuroprotective mechanism against Mn induced toxicity. Thus, resulting in excess Mn accumulation compared to astrocytes. In fact, we demonstrated that the decreased Mn accumulation in mutant HD striatal cells can be observed as early as 1 hr following 50 μM $MnCl_2$ exposure in HEPES salt buffer and media (Figure III. 2.A. and 2.B.). Interestingly, we found an increase in the magnitude of net Mn accumulation between wild-type ST*Hdh*$^{(Q7/Q7)}$ and mutant ST*Hdh*$^{(111/Q111)}$ cells exposed for 6 hrs compared to 27 hrs exposure (Figure III. 1.B.). The enhanced magnitude might possible be due to temporal activation of known and putative Mn transporters[22]. Nevertheless, other studies not directly assessing metals have demonstrated that dopamine transporters regulate effective concentrations of dopamine at the synaptic cleft in a time-dependent activation manner[23,24]. In essence, it is possible that during the first couple of hours following $MnCl_2$ exposure, only the primary/major Mn transporters are activated to mediate Mn transport. However, by 27 hrs $MnCl_2$ exposure, other secondary and tertiary Mn

transporter systems may also be activated to compensate for the significant decrease in mutant Mn uptake. It is possible that by 27 hrs $MnCl_2$ exposure, wild-type ST*Hdh*$^{(Q7/Q7)}$ cells might be approaching their maximum cellular Mn storage capacity. Thus, activation of the secondary or tertiary Mn transporter may only be substantially beneficial in mediating the latent mutant ST*Hdh*$^{(Q111/Q111)}$ Mn uptake and eventually decrease the fold difference in Mn accumulation when compared to wild-type ST*Hdh*$^{(Q7/Q7)}$ cells. It is unlikely that the decreased magnitude of net Mn accumulation between wild-type ST*Hdh*$^{(Q7/Q7)}$ and mutant ST*Hdh*$^{(111/Q111)}$ cells exposed for 27 hrs is due to the effects of cell debris following Mn accumulation and concomitant cell death on the accuracy of CFMEA and PicoGreen assays. This is mainly because cultured and exposed cells are efficiently washed three times with 200 μL PBS before cellular Mn extraction is performed by CFMEA and subsequent dsDNA using PicGreen normalization. Our data strongly argues for future assessment of Mn transport dynamics in media or other buffers at earlier time points. This would enable efficient characterization of Mn transport kinetics in the HD striatal cells. Moreover, the compensatory Mn transport system activation is unlikely directly regulated by mutant HTT expression, albeit it could potentially mask discrete Mn transport kinetics and transporter functions between wild-type ST*Hdh*$^{(Q7/Q7)}$ and mutant ST*Hdh*$^{(Q111/Q111)}$ cells.

We have combined both CFMEA and the traditional fura-2 loaded Mn-quenching assays to examine Mn transport kinetics in the HD striatal cells. The characterization of Mn^{2+} uptake and saturation in the HD striatal cells by measurements of instantaneous kinetics and time-dependency, as well as net cellular Mn storage in the cultured HD

striatal cells (Figure III. 3.A, 3.B., Table III. 1., and Table III. 2.) have further elucidated the transport dynamics in the HD striatal cells. Specifically, we have shown that expression of mutant HTT decreases the instantaneous and net Mn uptake kinetics as early as 2 minutes following $MnCl_2$ exposure (Figure III. 3.A., Table III. 1., and Table III. 2.). In addition, our findings demonstrated that the maximum Mn uptake or saturation rate in the mutant ST*Hdh*$^{(Q111/Q111)}$ cells is observed between 15 and 30 minutes. Moreover, both wild-type and mutant HD striatal cells exhibit a similar initiation of Mn saturation time point (~15 minutes) (Figure III.3.A.). Importantly, we found significant differences ($p<0.001$) in the initial slope of Mn uptake kinetics between wild-type and mutant HTT striatal cells during the first 5 minutes following exposure to 100 and 250 μM $MnCl_2$ (Table III. 2.). The above findings from the uptake kinetics in the HD striatal cells strongly points to impaired Mn uptake in mutant ST*Hdh*$^{(Q111/Q111)}$ cells compared to wild-type ST*Hdh*$^{(Q7/Q7)}$. Moreover, we have demonstrated that mutant ST*Hdh*$^{(Q111/Q111)}$ cells have decreased Mn saturation rate or storage capacity compared to wild-type ST*Hdh*$^{(Q7/Q7)}$ following $MnCl_2$ exposure (Figure III. 3.A. and Table III. 1.). Our findings are consistent with the previously reported time-dependence of Mn uptake and saturation kinetics using radiotracer ^{54}Mn (II) in cultured primary astrocytes[19,20,25,26]. In fact, a recent study conducted in human intestinal Caco-2 cell line and Mn levels and transport kinetics measured by the atomic absorption spectrophotometer reported similar findings to what we observed in the HD striatal cells[22]. Specifically, the authors demonstrated a substantial time- and concentration-dependent increase in Mn uptake. In addition, they demonstrated a biphasic Mn transport kinetic; first slow phase that lasted for ~ 45 minutes followed by a faster linear phase, which exhibited ~ 5-fold increase in Mn uptake

by 3.5 hrs compared to the slow phase following exposure with 100 μM $MnCl_2$. Furthermore, they observed a preliminary lagged period or Mn saturation transport kinetics in the Caco-2 Mn exposed cells between 15 and 30 minutes[22]. All the above mentioned and discussed studies fit with our findings of Mn uptake and cellular Mn storage in the HD striatal cells. In addition, the faster linear phase Mn transport reported by Leblondel and colleagues[22] further supports our idea of a time-dependent activation of Mn transporters (Figure III. 1.B.). On the other hand, it was unclear whether the changes we observed in Mn uptake and cellular storage were mainly due to changes in cytosolic Mn as the loaded fura-2 dye may not be efficiently sequestered into organelles to detect Mn levels. Moreover, Tsien and colleagues have suggested a temperature-dependent sequestration of fura-2 into organelles[4,5]. Thus, our data demonstrates that the prevalent cellular Mn pool involved in the diminished cellular Mn storage in mutant HD striatal cells compared to wild-type encompasses both cytosolic and net organelle-accumulated Mn (Figure III. 3.B.).

Despite the previous reports that Mn accumulates in brain organelles including mitochondria[27,28], nucleus[29], lysosomes[30], and golgi[31], it is still unknown how mutant HTT modulates Mn sequestration into the aforementioned organelles. However, recent studies have suggested that wild-type HTT is necessary for normal regulation of the transferrin receptor, crucial for iron homeostasis, recycling of endosomes, associates and regulates trafficking of nuclei and perinuclear membrane organelles (endoplasmic reticulum, golgi, mitochondria, and endosomes)[32,33]. Based on our findings of decreased instantaneous Mn uptake kinetics and cellular Mn storage in mutant HD striatal cells

compared to wild-type, the aforementioned relationship amongst wild-type HTT, metal homeostasis, and trafficking of organelles that accumulate Mn, it is possible that the mutant HTT protein may be functioning in the following ways to result in the decreased Mn uptake and cellular storage deficits; (a) protein level: mutant HTT may directly or indirectly associate with a primary/major Mn transporter on the plasma membrane or known Mn accumulation organelle(s) and down-regulate its function by changing its conformational state, which would result in reduced Mn uptake and cellular storage, (b) messenger RNA level: mutant HTT may impair the translation of major Mn transporter transcript levels, (c) protein interactions: mutant HTT may associate and impair the trafficking of known Mn accumulation organelles, and (d) proteasomal function: expression of mutant HTT may result in the upregulation of the activity and function of the proteasome, which would in turn result in uncontrolled degradation of a known or putative Mn transporters as well as other essential proteins. Thus, decreasing the efficiency of the HD striatal cells to uptake, accumulate, and efflux Mn when exposed to identical Mn concentrations as wild-type. We demonstrated a critical need to equally ascertain that both wild-type and mutant HD striatal cells have similar intracellular Mn levels prior to assessment of Mn efflux kinetics. We demonstrated a substantial time-dependent increase in wild-type ST*Hdh*$^{(Q7/Q7)}$ Mn efflux kinetics compared to mutant ST*Hdh*$^{(Q111/Q111)}$ cells following exposure to identical concentrations of $MnCl_2$ (Figure III. 4.A.). However, after similar intracellular Mn levels of wild-type ST*Hdh*$^{(Q7/Q7)}$ and mutant ST*Hdh*$^{(Q111/Q111)}$ cells, we showed that both wild-type ST*Hdh*$^{(Q7/Q7)}$ and mutant ST*Hdh*$^{(Q111/Q111)}$ cells exhibit similar net Mn efflux kinetics (Figure III. 4.B.). Unfortunately, the precise nature of Mn efflux mechanism in the HD striatal cells is

unknown. However, previous reports have suggested the existence of discrete cellular Mn pools[19,20]. The cellular Mn pools involved in Mn efflux can be categorized into 3 different classes: (i) fast phase, (ii) slow equilibrium, and (iii) irreversibly bound Mn efflux that are unavailable for efflux.

Furthermore, Aschner and Wedler have demonstrated biphasic Mn efflux kinetic profiles in cultured astrocytes[19,20]. Thus, it is possible that both wild-type ST*Hdh*$^{(Q7/Q7)}$ and mutant ST*Hdh*$^{(Q111/Q111)}$ cells possess similar Mn efflux pools following equal intracellular Mn levels. However, at different intracellular Mn levels, wild-type HD striatal cells may efficiently efflux more Mn compared to mutant. This may possibly be the means by which wild-type HD striatal cells efficiently regulate net Mn uptake and cellular storage, which is impaired in mutant HTT striatal cells (Figure III. 3, Table III. 1., and Table III. 2.). It is likely that we did not observe the previously reported biphasic relationship in Mn efflux[19,20] in the HD striatal cells due to rapid efflux and loss of detectable cellular Mn pools that contribute to the biphasic Mn efflux kinetics during the repeated media changes aspect of the efflux experiment. Moreover, our data is consistent with the previously reported evidence of predominant interactions between Mn and cytosolic proteins in hepatocytes and chick glial cells studies[19,20,34]. In fact, approximately 80% of plasma Mn is bound to beta$_1$-globulin protein[35]. Although there has been discrepancies in the affinity of Mn and other metals such as Cd and Zn to preferentially bind to albumin[36,37] our current findings suggest that extracellular Mn binds with high-affinity to serum proteins, for example; albumin and beta$_1$-globulin, other proteins, small anions such as nitrate (NO_3^-) and sulfate (SO_4^{2-}), in the extracellular Mn

exposure media and decrease the availability and concentration of extracellular Mn for cellular uptake (Figure III. 2.B.). Hence, it is unlikely that expression of mutant HTT may modify the interactions between cytosolic Mn and proteins to decrease their availability for Mn efflux as we observed similar effects on net Mn uptake and cellular storage in both genotypes following exposure in HEPES salt buffer (Figure III. 2.A.). Nevertheless, our efflux data following similar intracellular Mn levels further supports the previously published evidence of similar ferroportin-1 (the suggested Mn exporter) protein levels in both genotypes. Based on the Mn uptake, cellular storage, and similar efflux following equivalent intracellular Mn levels in the HD striatal cells, our data indicate and suggest that the decreased Mn accumulation in mutant HD striatal cells compared to mutant (Figure III. 2.A. and 2.B.) is due to decreased Mn uptake, diminished cellular Mn storage, and not efficient efflux compared to wild-type ST*Hdh*$^{(Q7/Q7)}$ cells.

The nature, types, and roles of known and putative Mn transporters in neuronal HD striatal cells' Mn transport

In our quest to investigate the Mn transporter implicated in the mutant HD striatal Mn transport deficits, we explored the nature of Mn transport by comparing the net Mn uptake and cellular Mn storage following $MnCl_2$ exposure at 33°C or 4°C (on ice). Our data is consistent with the previously reported decreased net Mn accumulation at 4°C versus 33°C[19]. Specifically, 50 – 80 % decrease in net Mn uptake and cellular Mn storage between 4°C and 33°C (Figure IV. 1.A. and 1.B.). Furthermore, our findings indicate that the major Mn transport system(s) in the HD striatal cells is temperature-responsive

(Figure IV. 1.A. and 1.B.). In fact, our temperature-dependence on Mn uptake suggest that Mn influx across the plasma membranes of HD striatal cells is not mediated by a simple diffusion transport process, but rather an active protein-mediated transport system. Importantly, it is highly unlikely that the temperature-dependent effect on Mn uptake and cellular storage in the HD striatal cells were mainly due to changes in the random movements of Mn^{2+} particles across the membrane due to modifications in the kinetic energy of our exposure system (Brownian motion) at 4°C. Finally, the phenotypic differences in Mn uptake and cellular storage in both wild-type and mutant HD striatal cells following a change in temperature suggest that the major dysfunctional Mn transporter in mutant HD striatal cells is not a temperature-sensitive metal transporter.

Our findings suggest that DMT1, 2-APB, RuR, mPTP, Roz, and GW9662 blockable transporters/channels are not responsible for the mutant ST*Hdh*$^{(Q111/Q111)}$ Mn transport kinetic deficits (Figure IV. 2.B., and 3.). In fact, we have previously demonstrated that DMT1 protein levels are unchanged[18]. Despite the differential affinities of DMT1 for other metal transport, including Cu^{2+}, Co^{2+}, Fe^{3+}, Ni^{2+}, Pb^{2+}, and Zn^{2+}[38], none of these metals showed differences in cytoxicity between wild-type ST*Hdh*$^{Q7/Q7}$ and mutant ST*Hdh*$^{Q111/Q111}$ cells[18]. For example, we demonstrated that while the specific DMT1 inhibitor, NSC306711[39], occluded Mn uptake and accumulation in a concentration-dependent manner in primary astrocytes, it failed to inhibit Mn uptake and cellular Mn storage in the neuronal HD striatal cells (Figure IV. 2.A.). The opposite effects of the inhibitor on Mn uptake and cellular Mn storage may possibly be due to distinct Mn transporter systems in neurons and glial (astrocytes). In spite of the similar

DMT1 protein expression levels in the neuronal HD striatal cells[18], it is unknown if the expressed DMT1 transporter is functional. Our current and previously reported data[18] suggest that DMT1 may not be the major Mn transporter impaired in mutant expressing HTT striatal cells

SOCCs have been reported to transport Mn in cells[40]. Interestingly, mutant HTT associates with the inositol triphosphate 3 receptor (IP3R) and increases the sensitivity of the receptor pore opening permeability, which causes excess calcium release and altered mitochondrial function to cause cell death[41,42]. However, we demonstrated that utilization of 2-APB, which inhibits both SOCCs and inositol triphosphate receptor showed no effect on Mn uptake and cellular Mn storage in either wild-type or mutant cells (Figure IV. 2A.) Conversely, RuR has been used to occlude the Ca^{2+} uniporter function on isolated mitochondria[43,44]. However, it is unknown if RuR crosses the plasma membrane to exert its actions on the Ca^{2+} uniporter. It is possible that RuR may modulate other transporters on the plasma membrane that do not participate in Mn uptake. This may explain why RuR had no effect on the Mn transport and storage capacity in the HD striatal cells (Figure IV. 2.B.). The mitochondria have been suggested to regulate metal ion homeostasis through the PPARγ pathway by modulating the mitochondrial membrane potential and reactive oxygen species (ROS) production[45,46]. However, neither the PPARγ antagonist (GW9662) nor agonist (Roz) altered Mn uptake and storage capacity in either wild-type or mutant cells (Figure IV. 2.D.) Previous studies that utilized the PPARγ modulators in the HD striatal cells measured changes in the mitochondrial activity following incubation with or without GW9662, Roz, and mitochondrial toxins for 24-48

hrs. However, we observed an ~ 40% and ~ 60% cell survival in mutants and wild-type cells, respectively when compared to vehicle-only and following 27 hrs exposure with identical concentrations of GW9662 (40 μM) in the same HD striatal cells (data not shown). Furthermore, we found an opposite vulnerability effect with 20 μM Roz on wild-type (~75%) and mutant (55%) cell survival after 27 hrs exposure (data not shown). Although our Mn uptake studies with the PPARγ modulators were conducted at 6 hrs, it is likely that these modulators may be acting on other pathways rather than the proposed. In addition, the toxicity induced by the PPARγ modulators is of great concern for future studies aimed at utilizing them to understand mitochondrial regulation of metal homeostasis or function. Nevertheless, CsA was incapable of mitigating the decreased Mn uptake and storage deficits in mutant HD striatal cells (Figure IV. 2. C.) Based on our findings, it is possible to suggest that the mitochondrial may be involved in minor roles or uninvolved in the mutant Mn accumulation deficit.

Emerging experimental evidence have identified and suggested HIP14 and HIP14L as candidate proteins/metal transporters of Mn and other metal ions transport in cells. In addition, both HIP14 and HIP14L have different affinities for different metal ions[47,48]. HIP14 and HIP14L are palmitoyl transferases implicated in Mn^{2+} and other metals (Mg^{2+}, Sr^{2+}, Ni^{2+}, Cu^{2+}, Ba^{2+}, Zn^{2+}, Fe^{2+}, Co^{2+}, Ca^{2+} transport[47,48]. In fact, HIP14 is primarily expressed in neurons and on membranes of the golgi and endoplasmic reticulum, organelles that are known to accumulate Mn[47]. Furthermore, expression of mutant HTT is known to decrease HIP14 interaction with HTT and its ability to palmitoylate the HTT protein[47]. We have shown that HIP14 protein levels is significantly

reduced in mutant ST*Hdh*$^{(Q111/Q111)}$ cells compared to wild-type ST*Hdh*$^{(Q7/Q7)}$ (Figure IV. 4.A. and 4.B). In addition, we have revealed significantly diminished (~40%) basal HIP14 protein levels in mutant ST*Hdh*$^{(Q111/Q111)}$ compared to wild-type ST*Hdh*$^{(Q7/Q7)}$ cells (Figure IV. 4.A. and 4.B.). Interestingly, previous reports have demonstrated significant inhibition of the HIP14 transporter function by excess (2 mM) Ca^{2+} levels[47]. We have shown that excess levels (1 and 10 mM) of the two highest HIP14 affinity cations (Mg^{2+}, Sr^{2+}) and Ca^{2+} (specific HIP14 inhibitor cation) are not toxic in both genotypes (Figure IV. 5.) and inhibit Mn uptake and cellular Mn storage in the HD striatal cells (Figure IV. 6. and Table Iv. 3.). We examined the influence of excess levels of the low affinity cations for HIP14 such as Cu^{2+} and Co^{2+} and observed similar quenching effect in both wild-type and mutant HD striatal cells (data not shown). However, Cu^{2+} and Co^{2+} substantially quenched fura-2 fluorescence making it impossible to quantify their effects on Mn uptake and cellular Mn storage in the HD striatal cells. Our findings from the HIP14 protein expression levels and the influence of excess metals on Mn uptake and cellular Mn storage indicate that the impaired Mn transporter underlying mutant Mn uptake and storage capacity deficit is a shared transporter between Mn^{2+}, Mg^{2+}, Sr^{2+} and Ca^{2+}. Furthermore, the altered Mn transporter is efficiently blocked by excess Mg^{2+}, Sr^{2+}, and Ca^{2+} and possesses higher affinity for Mg^{2+}, Sr^{2+}, and Ca^{2+} compared to Mn^{2+}. Given the structural and cation selectivity, similarities between HIP14 and HIP14L, and reduced interaction between mutant HTT and HIP14 proteins[47], it is possible that the mutant ST*Hdh*$^{(Q111/Q111)}$ Mn uptake and cellular storage deficit may be due to mutant HTT induced impairment in HIP14 and/or HIP14L transporter function. It is still unclear at what level of Mn transport does HIP14 possibly modulate. It is possible that HIP14 may

be functioning in a dual Mn regulation mechanism; (a) HIP14 may be expressed on the plasma membrane of cells to mediate the Mn uptake into cells. (b) Upon Mn influx into cells, HIP14 may associate with HTT and palmitolyate it for its normal functions in metal homeostasis. However mutant HTT could possibly decrease the palmitoylation of HTT and further decrease the intracellular trafficking of Mn dependent proteins to cause the decreased net Mn uptake and accumulation.

Relationship between Mn uptake, cellular Mn pools, and oxidative stress

Metals including Cu^{2+} and Mn^{2+} are known to be modifiers of PD by either accumulating in the brain and causing PD-like symptoms or increasing the risk of developing the disease[49,50]. Exposure to metals increase the risk of neurodegenerative diseases via the production of ROS by the Fenton-Harber Weiss reactions to cause oxidative stress, which damages lipids, proteins, DNA, and further depletes ATP to cause cell death[51-53]. It was unclear how the demonstrated differences in Mn uptake and storage capacity (Figure III. 3.) are functionally related to the previously reported cytoxicity difference between wild-type ST*Hdh*$^{(Q7/Q7)}$ and mutant ST*Hdh*$^{(Q111/Q111)}$ cells[18]. We have shown that although wild-type ST*Hdh*$^{(Q7/Q7)}$ and mutant ST*Hdh*$^{(Q111/Q111)}$ cells significantly generate ROS levels in a time-dependent manner and above baseline levels following exposure to $MnCl_2$, mutant ST*Hdh*$^{(Q111/Q111)}$ cells exhibited decreased Mn induced ROS production compared to wild-type (Figure IV. 7.A. – 7.C., and Table IV. 4.). In addition, we have also demonstrated a concentration- and time-dependent decrease

in mutant Mn uptake kinetics and cellular Mn storage compared to wild-type ST*Hdh*$^{(Q7/Q7)}$ cells (Figure III. 3.A. and 3.B. and Figure III. 1.A. and 1.B.). Our findings suggest a functional relationship between Mn uptake, cellular Mn pools that could directly or indirectly induce Mn-induced ROS production to cause cell death. This phenomenon may cause the differential vulnerability of Mn-induced cytoxicity between wild-type ST*Hdh*$^{(Q7/Q7)}$ and mutant ST*Hdh*$^{(Q111/Q111)}$ cells[18]. However, our findings do not directly provide the underlying mechanism for striatal specific degeneration of medium spiny neurons in HD brains.

Nevertheless, mutant HTT expression[54-61] and Mn exposure[62-66] have been previously reported to increase ROS production in the brain. Furthermore, MacDonald and colleagues have previously utilized a chemiluminescent H_2O_2 detection kit to monitor intracellular H_2O_2 concentrations as a read-out of ROS production in HD striatal cells and reported a significant reduction in mutant ST*Hdh*$^{Q111/Q111}$ ROS levels compared to wild-type ST*Hdh*$^{(Q7/Q7)}$ cells[67]. However, we observed the opposite effect at 5, 15, and 30 minutes exposure to H_2O_2. The discrepancy between our findings and the previour report might possibly be due to the following: (i) specificity and detection limits of assays been used for ROS detection. Specifically, the DCF assay does not distinguish between the types of free radicals generated in the cell to cause changes in ROS levels. However, the cheluminescent assay is a luminescent assay that specifically measures intracellular H_2O_2 concentration as a direct correlation of intracellular ROS levels. In addition, other factors that may cause the differences between the two assays used to monitor ROS levels in cells may be due to (ii) type of oxidative stress biomarkers measured. For example, 8-

hydroxy-2-deoxyguanosine (OH(8)dG[54] versus isoprostanes[62], (iii) Differences in the cell-types used to examine oxidative stress[63,64], and (iii) Mode of ROS stimulation in *in vivo* HD models (chemically induced 3-nitropropionic acid or malonate inhibitors)[56] versus metals. Despite the known link between metals and ROS production, and the relationship between mutant HTT and ROS generation, none of the above studies have examined a combinatorial effect of both; specifically, the synergistic effect of metals (Mn) and mutant HTT expression on ROS production in cells. It is noteworthy that the functional relationship between cellular Mn pools and oxidative injury demonstrated in the HD striatal cells might not be the primary mechanism underlying striatal specific degeneration of medium spiny neurons in HD patients. In fact, it is highly likely that a combination of diminished cellular Mn levels, impaired Mn-dependent and other antioxidant activities, altered mitochondrial function, oxidative injury, diminished ATP levels, decreased neuroprotective roles of glial cells, protein aggregation, and upregulation of cell death mechanisms might underlie the *in vivo* mutant HTT expressing striatal-specific degeneration. Despite the decreased Mn uptake and accumulation in mutant ST*Hdh*$^{Q111/Q111}$ cell lines and YAC128 mouse models of HD, diminished susceptibility of mutant ST*Hdh*$^{Q111/Q111}$ cell lines to Mn induced cytotoxicity, and reduced ROS levels in mutant HD striatal cell lines compared to wild-type[18], the striatum in animal models and HD patients are the most vulnerable in the disease. Given that the enzymatic activities of several manganoproteins have been reported to be reduced in HD patients and animal models[68-73] as well as Dexter and colleagues reporting no change in Mn levels in HD postmortem brains due to a small sample size[74], it is possible that the neuroprotective effects of Mn *in vivo* may be regulated by other factors including, cell

types (astrocytes, microglial), age of disease onset, and changes in other metal homeostasis that are difficult to control in our *in vitro* HD striatal cells. Prior to the clinical manifestation of HD, the brain tightly regulates metal ions including Mn^{2+}, Cu^{2+}, and Fe^{2+} that may be required as cofactors for enzymatic functions necessary for medium spiny neuron function and survival in the striatum. However, as the disease progresses, mutant HTT protein might aberrantly via direct or indirect means regulate metal homeostasis that would result in the reported increase in Fe^{2+} (56%) and Cu^{2+} (48%) levels in the brain[70]. If the demands of Mn^{2+} as a cofactor for manganoproteins in the striatum were substantially higher than other brain regions, then the dysregulated metal ions including Mn^{2+} in the brain would eventually cause decreased neuroprotection of medium spiny neurons in the striatum. Furthermore, the Mn-dependent antioxidants (Mn-SOD2, arginase)[68,71], astrocyte specific Mn-dependent enzyme (glutamine synthetase)[69,70], and Mn-dependent energy production enzyme (pyruvate carboxylase)[72,73] would be altered as reported. It is possible that the substantial changes in Fe^{2+} (56%) and Cu^{2+} (48%) levels in HD brain[70] may directly induce ROS production through the Fenton-Harber Weiss reactions to cause oxidative stress, which would damage lipids, proteins, DNA, and further depletes ATP to cause cell death[51-53] or indirectly alter mitochondrial function, induce protein aggregation, and down-regualate the activity and function of the proteasome. In the neuronal HD striatal cell lines that lack the *in vivo* neuroprotective functions of astrocytes, they might possibly be regulating metal ion homeostasis in a completely different manner compared to what exists *in vivo*. For example, mutant HD striatal cells that lack the *in vivo* astrocyte sequestration of excess Mn may downregulate HIP14 or other putative Mn transporters as a defensive response

to increased Mn above endogenous levels. This would explain the decreased Mn uptake and cellular storage, diminished basal HIP14 protein levels, and reduced ROS production in mutant HD striatal cells compared to wild-type.

Future directions

To completely understand the disease-toxicant interaction between HD and Mn and translate our findings as beneficial or detrimental to the variability in age of disease onset, severity, disease progression, and selective neuropathology of HD, further studies would have to be conducted. Future studies would have to examine the contribution of other putative Mn transporters in the HD-Mn interaction. Given that our findings ruled out several known Mn transporters as culprits of the decreased Mn uptake and storage capacity deficits in mutant HTT expressing cells, it would be essential to examine the role of the suggested putative Mn transporters HIP14L, PARK9, and others in Mn uptake. Based on our findings of decreased HIP14 protein levels in mutant HD striatal cells and inhibition of the Mn uptake and cellular Mn storage by the non-toxic two highest affinity cations (Mg^{2+}, Sr^{2+}) of the HIP14 transporter and its selective cation inhibitor (Ca^{2+}), future studies would have to knockdown HIP14 and or HIP14L levels in wild-type neuronal HD striatal cells to determine if that phenocopies the decreased basal expression of HIP14 in mutant HD strital cells. In addition, changes in Mn uptake, cellular storage and efflux kinetics in the HIP14 knockdown wild-type HD striatal cells should be examined and compared to the controls (wild-type and mutant HD striatal cells).

Furthermore, overexpression of HIP14 and/or HIP14L in mutant HD striatal cells would have to be performed to further substantiate the role of HIP14 in the diminished Mn transport dynamics in mutant expressing HTT striatal cells. Furthermore, previous studies have demonstrated an inverse correlation between the polyQ repeat length in the HTT protein and HIP14 interaction[47,75]. Moreover, HIP14 is known to palmitolyate the HTT and other proteins[75]. Future studies would have to investigate the effect of Mn exposure on HIP14 transcript levels in the neuronal HD striatal cells. Interestingly, what is also not known is the effect of metals, for example Mn on HIP14 palmitoylation activity. It would be important to explore the effects of Mn on the temporal and spatial localization of HIP14 and HTT proteins at the cellular level, as well as their interactions by performing immunostaining and other biochemical assays. Although previous studies have reported HIP14 localization on the golgi and endoplasmic reticulum membrane[47,75], they did not show HIP14 expression on the plasma membrane. It is still unclear whether HIP14 and/or HIP14L proteins are expressed on the plasma membrane. Future studies should perform biotinylation assays to determine HIP14 and HIP14L expression on the plasma membrane. Finally, with the current availability of specific HIP14 inhibitors[76,77], the functions of HIP14 in metal transport and homeostasis in other neurodegenerative diseases can be efficiently investigated.

On the other hand, Gitler and colleagues have implicated PARK9 as a Mn transporter in a yeast model of PD[48]. However, it is still unknown whether PARK9 mediates Mn uptake in *in vitro* and *in vivo* models. Future studies would have to ascertain PARK9 as a Mn transporter in other *in vitro* (neuronal HD striatal cells) and *in vivo*

animal models of HD (YAC128, BAC225) and other neurodegenerative diseases. In addition, understanding the effect of Mn on PARK9 protein and transcript expression levels would further support PARK9 as a Mn-responsive gene. Once PARK9 has been confirmed as a Mn-responsive gene, future experiments would have to modulate its expression and function to test its role in the HD-Mn interaction. This would be achieved through PARK9 overexpression and knockdown studies. Furthermore, development of small molecules that modulate PARK9 activity and function would enable future studies to screen for the role of PARK9 in metal transport and homeostasis, as well as other pathophysiological pathways implicated in neurodegenerative diseases. Although the exact function of PARK9 is unknown, it is generally thought to be a transmembrane cationic metal transporter that shuttles cations, including Mn across the cell. Biochemical studies have demonstrated that the highest and lowest PARK9 mRNA levels are localized within the substantia nigra and cerebellum respectively[78]. However, it is still unknown if PARK9 is expressed on the plasma membrane of cells. Future studies should investigate PARK9 expression on membranes and if Mn exposure alters the localization and function of PARK9 protein in the neuronal HD striatal cells.

It is likely that the above discussed putative transporters and other yet to be identified metal transporters may underlie the decreased Mn uptake and cellular storage in mutant HD striatal cells. However, an important aspect for better understanding of the disease-toxicant interaction and metal transporters would require the combination of both *in* vitro and *in vivo* animal models. In the case of HIP14 and PARK9 functions as metal transporters in *in vivo* animal models, future studies should examine similar experimental

ideas as discussed above for the neuronal HD striatal cells. The recently developed transgenic mouse model (YAC128-HIP14 knock out) of HD[79] permits the investigation of the mutant HTT-Mn interaction in the context of a mouse model that lacks HIP14. This would enable future studies to ascertain whether HIP14 is the primary Mn transporter underlying decreased Mn accumulation in the HD striatal cells and striatum of YAC128 mouse model of HD. Moreover, future studies should actively consider generating transgenic animal models of HIP14L and PARK9 to better examine metals, for example, Mn transport and homeostasis. In addition, it would important to understand whether the CAG repeat length modulates Mn transport dynamics in the context of HIP14, HIP14L, and PARK9 expression levels in both *in vitro* and *in vivo* mouse models of HD. Given the affinity of HIP14 for other divalent metals (Mg^{2+}, Sr^{2+}, Ni^{2+}, Ca^{2+}, Ba^{2+}, Zn^{2+}), it is possible that HIP14 may mediate metal induced toxicity in other neurodegenerative diseases. Future studies should also consider examining the role of other putative Mn transporters, such as TRPM7, homomeric purinoreceptors, and the citrate transporters in both the neuroal HD striatal cells and in vivo animal models of HD (YAC128, BAC225). Importantly, future studies shown explore the sequential or simultaneous contribution of multiple known or putative Mn transporters in the mutant HTT-Mn interaction.

Availability of the high-throughput assay (CFMEA) has enabled for efficient dissection of Mn transporter systems and Mn transport dynamics in the neuronal HD striatal cells. However, we still don't know the nature of the impaired Mn transporter. Thus, future experiments should use CFMEA, traditional fura-2 loaded kinetic assays,

and biochemical techniques to investigate whether the impaired transporter is energy-dependent and modulated by changes in pH. Findings from these studies in addition to our findings of similar response of wild-type and mutant HD striatal cells to net Mn uptake and cellular storage following changes in temperature (Figure IV. 1.) would enable future studies to focus on known metal transporters that fall within those categories. Furthermore, we have demonstrated decreased net cellular Mn storage in mutant HD striatal cells compared to wild-type following Mn exposure (Figure III. 3.A. and 3.B.). However, we still do not know the cellular compartments responsible for the Mn deficit. Given the conflicting reports to support either the mitochondria or nuclei as the cellular organelle that accumulates the primary pool of Mn in the cell [29,43,80], future studies should consider performing subcellular fractionation experiments in the neuronal HD striatal cells and the striatum of YAC128 mouse models of HD. In these experiments organelles, such as mitochondria, endoplasmic reticulum, and nuclei would have to be fractionated either pre and post Mn exposures. It is crucial that the experimenters consider the integrity of the organelles during subcellular fraction. For example, while other studies have shown that it is essential to add substrates, such as pyruvate, during subcellular fractionation of the mitochondria, other researchers have argued against it. It is important that future studies perform their subcellular fractionation by either adding or excluding substrates. Finally, future studies should also examine the temporal and spatial Mn accumulation in the brain of mouse models of HD.

It is still unclear if the selective neuropathology in the striatum of HD brains is caused by oxidative stress, mitochondrial dysfunction, protein aggregation, or altered

metal homeostasis. It is possible that all these pathways converge to exacerbate the phenotypic variabilities in HD. Future studies should consider examining other biomarkers of oxidative stress, such as isoprostanes following Mn exposure in the neuronal HD striatal cells and YAC128 mouse model of HD. Secondly, understanding how Mn exposure may alter mitochondrial function through membrane fragmentation, production of ROS, or decreasing ATP levels would provide great insights into the initiating factors and the understanding of how mutant HTT may modulate these pathways to cause striatal specific degeneration. In addition future experiments should assess ROS production in primary neuronal, astrocytic, and mixed cultures to investigate cell-type specific response to Mn exposure. Moreover, examination of the mitochondrial integrity following Mn exposure would be important in understanding the differential vulnerability in Mn induced cytotoxicity between wild-type and mutant neuronal HD strial cells. These studies could be performed alongside other Mn transport kinetic studies and assessed by CFMEA.

Given the promising future of induced pluripotent stem (IPS) cell research, it would be very important for future studies to translate our findings in the neuronal HD striatal cells and YAC128 mouse model into patients. The generation of medium spiny neurons from HD patient skin biopsy would enable for high-throughput screening of metals and other toxicants that exhibit gene-environment interaction with mutant HTT. In addition, these studies may elucidate some primary pathophysiological mechanisms in HD neuropathology that has not yet been observed in *in vitro* and *in vivo* animal models.

An important long-term goal would be to provide therapeutic interventions for HD patients from our findings. However, there are some crucial hurdles that must be overcome prior to our ability to recommend low concentrations of Mn for HD patients. (i) We would need to ascertain the appropriate Mn exposure concentrations that are capable of retarding medium spiny neuron degeneration, disease progression, symptoms, and decrease age of onset without possessing toxic effects in animal models of HD. (ii) Investigate the required and physiologically relevant concentrations of Mn that can be used in development of a drug to ameliorate the phenotypic symptoms of HD and most importantly not have major side effects in HD patients. (iii) We would need to certify that the newly developed Mn-rich drugs when administered in the brain would be efficiently metabolized and not end up accumulating in the basal ganglia regions or other known Mn accumulation organs and cause Manganism, (iv) Determine the optimal drug efficacy window in HD patients - pre versus during onset of disease symptomology, and (ii) types of HD - juvenile versus adult; as the cerebellum that does not accumulate Mn also degenerates in juvenile HD.

References

1. Poenie, M., Alderton, J., Steinhardt, R. & Tsien, R.Y. Calcium rises abruptly and briefly throughout the cell at the onset of anaphase. *Science* **233**(1986).

2. Malgaroli, A., Milani, D., Meldolesi, J. & Pozzan, T. Fura-2 measurement of cytosolic free Ca2+ in monolayers and suspensions of various types of animal cells. *J Cell Biol* **105**, 2145-55 (1987).

3. Plieth, C. & Hansen, U. Methodological aspects of pressure loading of fura-2 into characean cells. *Journal of Experimental Botany* **47**, 1601-1612 (1996).

4. Tsien, R.Y. Fluorescent probes of cell signaling. *Annual Review of Neuroscience* **12**, 227-253 (1989).

5. Tsien, R.Y., Rink, T.Y. & Poenie, M. Measurement of cytosolic free Ca2+ in individual small cells using fluorescence microscopy with dual excitation wavelengths. *Cell Calcium* **6**, 145 - 157 (1985).

6. Kwakye, G.F., Li, D. & Bowman, A.B.B. Novel high-throughput assay to assess cellular manganese levels in a striatal cell line model of Huntington's disease confirms a deficit in manganese accumulation. in *NeuroToxicology* (Vanderbilt University, Nashville, 2010, manuscript under review).

7. Reynolds, J.A. & Tanford, C. Binding of dodecyl sulfate to proteins at high binding ratios. Possible implications for the state of proteins in biological membranes. *Proc Natl Acad Sci U S A* **66**, 1002-7 (1970).

8. Kwakye, G.F., Li, D., Kabobel, O.A. & Bowman, A.B. Cellular fura-2 Manganese Extraction Assay (CFMEA). *Curr Protoc Toxicol* **Chapter 12**, Unit12 18 (2011).

9. Grynkiewicz, G., Poenie, M. & Tsien, R.Y. A new generation of Ca2+ indicators with greatly improved fluorescence properties. *The Journal of Biological Chemistry* **260**, 3440 - 3450 (1985).

10. Snitsarev, V.A., McNulty, T.J. & Taylor, C.W. Endogenous heavy metal ions perturb fura-2 measurements of basal and hormone-evoked Ca2+ signals. *Biophys J* **71**, 1048-56 (1996).

11. Merritt, J.E., Jacob, R. & Hallam, T.J. Use of manganese to discriminate between calcium influx and mobilization from internal stores in stimulated human neutrophils. *J Biol Chem* **264**, 1522-7 (1989).

12. Picard, V., Govoni, G., Jabado, N. & Gros, P. Nramp 2 (DCT1/DMT1) expressed at the plasma membrane transports iron and other divalent cations into a calcein-accessible cytoplasmic pool. *J Biol Chem* **275**, 35738-45 (2000).

13. Forbes, J.R. & Gros, P. Iron, manganese, and cobalt transport by Nramp1 (Slc11a1) and Nramp2 (Slc11a2) expressed at the plasma membrane. *Blood* **102**, 1884-92 (2003).

14. Hughes, M.N. In comprehensive coordination chemistry. The synthesis, reactions, properties and applications of coordination compounds. in *Coordination Compounds in Biology.* , Vol. 6 (eds. Wilkinson, G., Gillard, R.D. & McCleverty, J.A.) (Pergamon Press, Oxford, 1987).

15. Coyle, P., Zalewski, P.D., Philcox, J.C., Forbes, I.J., Ward, A.D., Lincoln, S.F., Mahadevan, I. & Rofe, A.M. Measurement of zinc in hepatocytes by using a fluorescent probe, Zinquin: relationship to me- tallothionein and intracellular zinc. *Biochem J.* **303**, 781-786 (1994).

16. Hechtenberg, S. & Beyersmann, D. Differential control of free calcium and free zinc levels in isolated bovine liver nuclei. *Biochem J* **289 (Pt 3)**, 757-60 (1993).

17. Kwakye, G.F., Li, D. & Bowman, A.B.B. Novel high-throughput assay to assess cellular manganese levels in a striatal cell line model of Huntington's disease confirms a deficit in manganese accumulation. *Neurotoxicology* (2011).

18. Williams, B.B., Li, D., Wegrzynowicz, M., Vadodaria, B.K., Anderson, J.G., Kwakye, G.F., Aschner, M., Erikson, K.M. & Bowman, A.B. Disease-toxicant screen reveals a neuroprotective interaction between Huntington's disease and manganese exposure. *J Neurochem* **112**, 227-37 (2010).

19. Wedler, F.C., Ley, B.W. & Grippo, A.A. Manganese(II) dynamics and distribution in glial cells cultured from chick cerebral cortex. *Neurochem Res* **14**, 1129-35 (1989).

20. Aschner, M., Gannon, M. & Kimelberg, H.K. Manganese uptake and efflux in cultured rat astrocytes. *J Neurochem* **58**, 730-5 (1992).

21. Wedler, F.C. & Denman, R.B. Glutamine synthetase: the major Mn(II) enzyme in mammalian brain. *Curr Top Cell Regul* **24**, 153-69 (1984).

22. Leblondel, G. & Allain, P. Manganese transport by Caco-2 cells. *Biol Trace Elem Res* **67**, 13-28 (1999).

23. Giros, B. & Caron, M.G. Molecular characterization of the dopamine transporter. *Trends Pharmacol Sci* **14**, 43-9 (1993).

24. Chen, R., Wu, X., Wei, H., Han, D.D. & Gu, H.H. Molecular cloning and functional characterization of the dopamine transporter from Eloria noyesi, a caterpillar pest of cocaine-rich coca plants. *Gene* **366**, 152-60 (2006).

25. Bressler, J.P., Olivi, L., Cheong, J.H., Kim, Y., Maerten, A. & Bannon, D. Metal transporters in intestine and brain: their involvement in metal-associated neurotoxicities. *Hum Exp Toxicol* **26**, 221-9 (2007).

26. Erikson, K.M. & Aschner, M. Increased manganese uptake by primary astrocyte cultures with altered iron status is mediated primarily by divalent metal transporter. *Neurotoxicology* **27**, 125-30 (2006).

27. Gunter, T.E. & Puskin, J.S. Manganous ion as a spin label in studies of mitochondrial uptake of manganese. *Biophys J.* , 625-35 (1972).

28. Gunter, T.E., Miller, L.M., Gavin, C.E., Eliseev, R., Salter, J., Buntinas, L., Alexandrov, A., Hammond, S. & Gunter, K.K. Determination of the oxidation states of manganese in brain, liver, and heart mitochondria. *J Neurochem* **88**, 266-80 (2004).

29. Kalia, K., Jiang, W. & Zheng, W. Manganese accumulates primarily in nuclei of cultured brain cells. *Neurotoxicology* **29**, 466-70 (2008).

30. Suzuki, H., Wada, O., Inoue, K., Tosaka, H. & Ono, T. Role of brain lysosomes in the development of manganese toxicity in mice. *Toxicol Appl Pharmacol* **71**, 422-9 (1983).

31. Mukhopadhyay, S. & Linstedt, A.D. Identification of a gain-of-function mutation in a Golgi P-type ATPase that enhances Mn2+ efflux and protects against toxicity. *Proc Natl Acad Sci U S A* **108**, 858-63 (2011).

32. Lumsden, A.L., Henshall, T.L., Dayan, S., Lardelli, M.T. & Richards, R.I. Huntingtin-deficient zebrafish exhibit defects in iron utilization and development. *Hum Mol Genet* **16**, 1905-20 (2007).

33. Hilditch-Maguire, P., Trettel, F., Passani, L.A., Auerbach, A., Persichetti, F. & MacDonald, M.E. Huntingtin: an iron-regulated protein essential for normal nuclear and perinuclear organelles. *Hum Mol Genet* **9**, 2789-97 (2000).

34. Schramm, V.L. & Brandt, M. The manganese(II) economy of rat hepatocytes. *Fed Proc* **45**, 2817-20 (1986).

35. Foradori, A.C., Bertinchamps, A., Gulibon, J.M. & Cotzias, G.C. The discrimination between magnesium and manganese by serum proteins. *J Gen Physiol* **50**, 2255-66 (1967).

36. Scheuhammer, A.M. & Cherian, M.G. The influence of manganese on the distribution of essential trace elements. II. The tissue distribution of manganese, magnesium, zinc, iron, and copper in rats after chronic manganese exposure. *J Toxicol Environ Health* **12**, 361-70 (1983).

37. Scheuhammer, A.M. & Cherian, M.G. Binding of manganese in human and rat plasma. *Biochim Biophys Acta* **840**, 163-9 (1985).

38. Gunshin, H., Mackenzie, B., Berger, U.V., Gunshin, Y., Romero, M.F., Boron, W.F., Nussberger, S., Gollan, J.L. & Hediger, M.A. Cloning and characterization of a mammalian proton-coupled metal-ion transporter. *Nature* **388**, 482-8 (1997).

39. Buckett, P.D. & Wessling-Resnick, M. Small molecule inhibitors of divalent metal transporter-1. *Am J Physiol Gastrointest Liver Physiol* **296**, G798-804 (2009).

40. Au, C., Benedetto, A. & Aschner, M. Manganese transport in eukaryotes: the role of DMT1. *Neurotoxicology* **29**, 569-76 (2008).

41. Bezprozvanny, I. Inositol 1,4,5-tripshosphate receptor, calcium signalling and Huntington's disease. *Subcell Biochem* **45**, 323-35 (2007).

42. Bezprozvanny, I. & Hayden, M.R. Deranged neuronal calcium signaling and Huntington disease. *Biochem Biophys Res Commun* **322**, 1310-7 (2004).

43. Gavin, C.E., Gunter, K.K. & Gunter, T.E. Manganese and calcium transport in mitochondria: implications for manganese toxicity. *Neurotoxicology* **20**, 445-53 (1999).

44. Gavin, C.E., Gunter, K.K. & Gunter, T.E. Manganese and calcium efflux kinetics in brain mitochondria. Relevance to manganese toxicity. *Biochem J* **266**, 329-34 (1990).

45. Quintanilla, R.A., Jin, Y.N., Fuenzalida, K., Bronfman, M. & Johnson, G.V. Rosiglitazone treatment prevents mitochondrial dysfunction in mutant huntingtin-expressing cells: possible role of peroxisome proliferator-activated receptor-gamma (PPARgamma) in the pathogenesis of Huntington disease. *J Biol Chem* **283**, 25628-37 (2008).

46. Glass, C.K. & Ogawa, S. Combinatorial roles of nuclear receptors in inflammation and immunity. *Nat Rev Immunol* **6**, 44-55 (2006).

47. Goytain, A., Hines, R.M. & Quamme, G.A. Huntingtin-interacting proteins, HIP14 and HIP14L, mediate dual functions, palmitoyl acyltransferase and Mg2+ transport. *J Biol Chem* **283**, 33365-74 (2008).

48. Gitler, A.D., Chesi, A., Geddie, M.L., Strathearn, K.E., Hamamichi, S., Hill, K.J., Caldwell, K.A., Caldwell, G.A., Cooper, A.A., Rochet, J.C. & Lindquist, S. Alpha-synuclein is part of a diverse and highly conserved interaction network that includes PARK9 and manganese toxicity. *Nat Genet* **41**, 308-15 (2009).

49. Gorell, J.M., Johnson, C.C., Rybicki, B.A., Peterson, E.L., Kortsha, G.X., Brown, G.G. & Richardson, R.J. Occupational exposure to manganese, copper, lead, iron, mercury and zinc and the risk of Parkinson's disease. *Neurotoxicology* **20**, 239-47 (1999).

50. Mergler, D., Huel, G., Bowler, R., Iregren, A., Belanger, S., Baldwin, M., Tardif, R., Smargiassi, A. & Martin, L. Nervous system dysfunction among workers with long-term exposure to manganese. *Environ Res* **64**, 151-80 (1994).

51. Olafsdottlr, K., Pascoe, G.A. & Reed, D.J. Mitochondnal glutamate status dunng Ca2+ ionophore induced injury to isolated hepatocytes. *Arch Biochem Blophys* **263**, 226-235 (1988).

52. Aschner, M. & Aschner, J.L. Manganese neurotoxicity: cellular effects and blood-brain barrier transport. *Neurosci Biobehav Rev* **15**, 333-40 (1991).

53. Leonard, S.S., Harris, G.K. & Shi, X. Metal-induced oxidative stress and signal transductionstar, open. *Free Radical Biology and Medicine* **37**(2004).

54. Bogdanov, M.B., Andreassen, O.A., Dedeoglu, A., Ferrante, R.J. & Beal, M.F. Increased oxidative damage to DNA in a transgenic mouse model of Huntington's disease. *J Neurochem* **79**, 1246-9 (2001).

55. Browne, S.E., Bowling, A.C., MacGarvey, U., Baik, M.J., Berger, S.C., Muqit, M.M., Bird, E.D. & Beal, M.F. Oxidative damage and metabolic dysfunction in Huntington's disease: selective vulnerability of the basal ganglia. *Ann Neurol* **41**, 646-53 (1997).

56. Gu, M., Gash, M.T., Mann, V.M., Javoy-Agid, F., Cooper, J.M. & Schapira, A.H. Mitochondrial defect in Huntington's disease caudate nucleus. *Ann Neurol* **39**, 385-9 (1996).

57. Mann, V.M., Cooper, J.M., Javoy-Agid, F., Agid, Y., Jenner, P. & Schapira, A.H. Mitochondrial function and parental sex effect in Huntington's disease. *Lancet* **336**, 749 (1990).

58. Perez-Severiano, F., Santamaria, A., Pedraza-Chaverri, J., Medina-Campos, O.N., Rios, C. & Segovia, J. Increased formation of reactive oxygen species, but no changes in glutathione peroxidase activity, in striata of mice transgenic for the Huntington's disease mutation. *Neurochem Res* **29**, 729-33 (2004).

59. Perluigi, M., Poon, H.F., Maragos, W., Pierce, W.M., Klein, J.B., Calabrese, V., Cini, C., De Marco, C. & Butterfield, D.A. Proteomic analysis of protein

expression and oxidative modification in r6/2 transgenic mice: a model of Huntington disease. *Mol Cell Proteomics* **4**, 1849-61 (2005).

60. Tabrizi, S.J., Scahill, R.I., Durr, A., Roos, R.A., Leavitt, B.R., Jones, R., Landwehrmeyer, G.B., Fox, N.C., Johnson, H., Hicks, S.L., Kennard, C., Craufurd, D., Frost, C., Langbehn, D.R., Reilmann, R. & Stout, J.C. Biological and clinical changes in premanifest and early stage Huntington's disease in the TRACK-HD study: the 12-month longitudinal analysis. *Lancet Neurol* **10**, 31-42 (2011).

61. Tabrizi, S.J., Cleeter, M.W., Xuereb, J., Taanman, J.W., Cooper, J.M. & Schapira, A.H. Biochemical abnormalities and excitotoxicity in Huntington's disease brain. *Ann Neurol* **45**, 25-32 (1999).

62. Benedetto, A., Au, C., Avila, D.S., Milatovic, D. & Aschner, M. Extracellular dopamine potentiates mn-induced oxidative stress, lifespan reduction, and dopaminergic neurodegeneration in a BLI-3-dependent manner in Caenorhabditis elegans. *PLoS Genet* **6**(2010).

63. dos Santos, A.P., Milatovic, D., Au, C., Yin, Z., Batoreu, M.C. & Aschner, M. Rat brain endothelial cells are a target of manganese toxicity. *Brain Res* **1326**, 152-61 (2010).

64. Milatovic, D., Yin, Z., Gupta, R.C., Sidoryk, M., Albrecht, J., Aschner, J.L. & Aschner, M. Manganese induces oxidative impairment in cultured rat astrocytes. *Toxicol Sci* **98**, 198-205 (2007).

65. Milatovic, D., Zaja-Milatovic, S., Gupta, R.C., Yu, Y. & Aschner, M. Oxidative damage and neurodegeneration in manganese-induced neurotoxicity. *Toxicol Appl Pharmacol* **240**, 219-25 (2009).

66. Zhang, P., Hatter, A. & Liu, B. Manganese chloride stimulates rat microglia to release hydrogen peroxide. *Toxicol Lett* **173**, 88-100 (2007).

67. Lee, J.M., Ivanova, E.V., Seong, I.S., Cashorali, T., Kohane, I., Gusella, J.F. & MacDonald, M.E. Unbiased gene expression analysis implicates the huntingtin polyglutamine tract in extra-mitochondrial energy metabolism. *PLoS Genet* **3**, e135 (2007).

68. Chiang, M.C., Chen, H.M., Lee, Y.H., Chang, H.H., Wu, Y.C., Soong, B.W., Chen, C.M., Wu, Y.R., Liu, C.S., Niu, D.M., Wu, J.Y., Chen, Y.T. & Chern, Y. Dysregulation of C/EBPalpha by mutant Huntingtin causes the urea cycle deficiency in Huntington's disease. *Hum Mol Genet* **16**, 483-98 (2007).

69. Carter, C.J. Glutamine synthetase activity in Huntington's disease. *Life Sci* **31**, 1151-9 (1982).

70. Butterworth, J. Changes in nine enzyme markers for neurons, glia, and endothelial cells in agonal state and Huntington's disease caudate nucleus. *J Neurochem* **47**, 583-7 (1986).

71. Andreassen, O.A., Ferrante, R.J., Dedeoglu, A., Albers, D.W., Klivenyi, P., Carlson, E.J., Epstein, C.J. & Beal, M.F. Mice with a partial deficiency of manganese superoxide dismutase show increased vulnerability to the mitochondrial toxins malonate, 3-nitropropionic acid, and MPTP. *Exp Neurol* **167**, 189-95 (2001).

72. Hurlbert, M.S., Zhou, W., Wasmeier, C., Kaddis, F.G., Hutton, J.C. & Freed, C.R. Mice transgenic for an expanded CAG repeat in the Huntington's disease gene develop diabetes. *Diabetes* **48**, 649-51 (1999).

73. Josefsen, K., Nielsen, M.D., Jorgensen, K.H., Bock, T., Norremolle, A., Sorensen, S.A., Naver, B. & Hasholt, L. Impaired glucose tolerance in the R6/1 transgenic mouse model of Huntington's disease. *J Neuroendocrinol* **20**, 165-72 (2008).

74. Dexter, D.T., Carayon, A., Javoy-Agid, F., Agid, Y., Wells, F.R., Daniel, S.E., Lees, A.J., Jenner, P. & Marsden, C.D. Alterations in the levels of iron, ferritin and other trace metals in Parkinson's disease and other neurodegenerative diseases affecting the basal ganglia. *Brain* **114 (Pt 4)**, 1953-75 (1991).

75. Huang, K., Yanai, A., Kang, R., Arstikaitis, P., Singaraja, R.R., Metzler, M., Mullard, A., Haigh, B., Gauthier-Campbell, C., Gutekunst, C.A., Hayden, M.R. & El-Husseini, A. Huntingtin-interacting protein HIP14 is a palmitoyl transferase involved in palmitoylation and trafficking of multiple neuronal proteins. *Neuron* **44**, 977-86 (2004).

76. Ducker, C.E., Griffel, L.K., Smith, R.A., Keller, S.N., Zhuang, Y., Xia, Z., Diller, J.D. & Smith, C.D. Discovery and characterization of inhibitors of human palmitoyl acyltransferases. *Mol Cancer Ther* **5**, 1647-59 (2006).

77. Gupta, S., Misra, G., Pant, M.C. & Seth, P.K. Prediction of a new surface binding pocket and evaluation of inhibitors against huntingtin interacting protein 14: an insight using docking studies. *J Mol Model* (2011).

78. Ramirez, A., Heimbach, A., Grundemann, J., Stiller, B., Hampshire, D., Cid, L.P., Goebel, I., Mubaidin, A.F., Wriekat, A.L., Roeper, J., Al-Din, A., Hillmer, A.M., Karsak, M., Liss, B., Woods, C.G., Behrens, M.I. & Kubisch, C. Hereditary parkinsonism with dementia is caused by mutations in ATP13A2, encoding a lysosomal type 5 P-type ATPase. *Nat Genet* **38**, 1184-91 (2006).

79. Singaraja, R.R., Huang, K., Sanders, S.S., Milnerwood, A.J., Hines, R., Lerch, J.P., Franciosi, S., Drisdel, R.C., Vaid, K., Young, F.B., Doty, C., Wan, J., Bissada, N., Henkelman, R.M., Green, W.N., Davis, N.G., Raymond, L.A. & Hayden, M.R. Altered palmitoylation and neuropathological deficits in mice lacking HIP14. *Hum Mol Genet* (2011).

80. Zwingmann, C., Leibfritz, D. & Hazell, A.S. Energy metabolism in astrocytes and neurons treated with manganese: relation among cell-specific energy failure, glucose metabolism, and intercellular trafficking using multinuclear NMR-spectroscopic analysis. *J Cereb Blood Flow Metab* **23**, 756-71 (2003).